REPUBLIC OF TURKEY
YILDIZ TECHNICAL UNIVERSITY
GRADUATE SCHOOL OF NATURAL AND APPLIED SCIENCES

WET CHEMICAL SYNTHESIS OF ZnO PARTICLES AND INCORPORATION INTO PHBV MATRIX

TUĞÇE BEKAT

PhD. THESIS
DEPARTMENT OF CHEMICAL ENGINEERING
PROGRAM OF CHEMICAL ENGINEERING

ADVISER
PROF. DR. MUALLA ÖNER

İSTANBUL, 2018

REPUBLIC OF TURKEY

YILDIZ TECHNICAL UNIVERSITY

GRADUATE SCHOOL OF NATURAL AND APPLIED SCIENCES

WET CHEMICAL SYNTHESIS OF ZnO PARTICLES AND INCORPORATION INTO PHBV MATRIX

A thesis submitted by Tuğçe BEKAT in partial fulfillment of the requirements for the degree of **PHILOSOPHY OF DOCTORAL** is approved by the committee on 07.06.2018 in Department of Chemical Engineering, Chemical Engineering Program.

Thesis Adviser

Prof. Dr. Mualla ÖNER

Yıldız Technical University

Approved By the Examining Committee

Prof. Dr. Mualla ÖNER

Yıldız Technical University _____

Prof. Dr. Sema BAYKARA, Member

Yıldız Technical University _____

Prof. Dr. Ş. Birgül TANTEKİN ERSOLMAZ, Member

İstanbul Technical University _____

Doç. Dr. Emek MÖRÖYDOR DERUN, Member

Yıldız Technical University _____

Prof. Dr. Süheyla ÇEHRELİ, Member

İstanbul University _____

This study was supported by the Yildiz Technical University Scientific Research Projects Council (BAPK) Grant No: 2015-07-01-DOP03.

ACKNOWLEDGEMENTS

I would like to express my gratitude to my supervisor Prof. Dr. Mualla Öner for her guidance and support during my PhD studies, and for his patience, motivation, encouragement and immense knowledge. I also would like to thank my mother Serap Hiçyılmaz for supporting me throughout my life.

June, 2018

Tuğçe BEKAT

TABLE OF CONTENTS

Page

LIST OF SYMBOLS viii

LIST OF ABBREVIATIONS x

LIST OF FIGURES xii

LIST OF TABLES xvi

ABSTRACT xviii

ÖZET xx

CHAPTER 1

INTRODUCTION 1

1.1 Literature Review 1
1.2 Objective of the Thesis 1
1.3 Hypothesis 1

CHAPTER 2

GENERAL INFORMATION 2

2.1 Biopolymers 3
2.1.1 Polyhydroxyalkanoates (PHA) 5
2.1.1.1 Applications of PHA 9
2.1.2 Recent Advances in PHA 10
2.1.3 ZnO As Nanofiller For PHA 18
2.2 Synthesis and Properties of ZnO Particles 22
2.2.1 Chemical Precipitation Method for ZnO Synthesis 24
2.2.2 Surface modification of ZnO Particles 29

CHAPTER 3

EXPERIMENTAL 31

3.1 Synthesis of ZnO Particles 31
3.1.1 Addition of CMI as Growth Modifier 34
3.1.2 Ultrasound Assisted Synthesis 35

3.2 Surface Modification of Synthesized ZnO Particles 36
3.3 Ultrasonic Dispersion of ZnO Particles 39
3.4 Characterization of ZnO Particles 40
3.4.1 Measurement of the Surface Area by BET Method 40
3.4.2 X-Ray Diffraction Analysis of ZnO Particles 41
3.4.3 Scanning Electron Microscopy of ZnO Particles 43
3.4.4 Fourier Transform Infrared Spectroscopy of ZnO Particles 44
3.5 Incorporation of ZnO Particles into PHBV Matrix 46
3.6 Characterization of PHBV/ZnO Nanocomposites 48
3.6.1 Structural Characterization of PHBV/ZnO Nanocomposites 49
3.6.2 Thermal Characterization of PHBV/ZnO Nanocomposites 49
3.6.2.1 Thermal Stability of the PHBV/ZnO Nanocomposites 50
3.6.2.2 Melting and Crystallization Behavior of the PHBV/ZnO Nanocomposites 50
3.6.3 Mechanical Properties of PHBV/ZnO Nanocomposites 52

CHAPTER 4

RESULTS AND DISCUSSION 56

4.1 Synthesis of ZnO Particles 56
4.1.1 Effect of Precursors Concentration 57
4.1.2 Effect of Reaction Temperature 63
4.1.3 Effect of Reactor Volume 65
4.1.4 Structural Analysis of ZnO-2L-95C Particles by XRD Analysis 68
4.1.5 FTIR Study of ZnO-2L-95C Particles 70
4.2 Ultrasonic Dispersion of ZnO Particles 72
4.3 Surface Modification of ZnO-2L-95C Particles 75
4.3.1 Determination of the Surface Area of ZnO-2L-95C Particles by BET Analysis 76
4.3.2 Calculation of the Required MPS for Monolayer Coverage 78
4.3.3 FTIR Study of the MPS-Treated ZnO-2L-95C Particles 79
4.3.4 Ultrasonic Dispersion of the MPS-Treated ZnO-2L-95C Particles 82
4.4 Effect of CMI as a Growth Inhibitor 83
4.4.1 XRD Analysis of ZnO Particles Synthesized in Presence of CMI 92
4.4.2 FTIR Study of the ZnO Particles Synthesized in Presence of CMI 95
4.5 Ultrasound Assisted Synthesis of ZnO Particles 97
4.5.1 XRD Analysis of the ZnO-2L-95C-UB40 Particles 101
4.5.2 FTIR Study of the ZnO-2L-95C-UB40 Particles 104
4.5.3 Surface Modification of the ZnO-2L-95C-UB40 Particles 105
4.5.3.1 Calculation of the Required Amount of OTES for Monolayer Coverage 106
4.5.3.2 FTIR Study of OTES-Modified ZnO-2L-95C-UB40 Particles 107
4.6 Development and Characterization of PHBV/ZnO Nanocomposites 109
4.6.1 PHBV/ZnO Nanocomposites Fabricated by ZnO-2L-95C Particles 109
4.6.1.1 Structural Characterization of the PHBV Nanocomposites Fabricated by ZnO-2L-95C Particles 110
4.6.1.2 Thermal Stability of the PHBV Nanocomposites Fabricated by ZnO-2L-95C Particles 115
4.6.1.3 Melting and Crystallization Behavior of the PHBV Nanocomposites Fabricated by ZnO-2L-95C Particles 129

4.6.1.4 Mechanical Properties of the PHBV Nanocomposites Fabricated by ZnO-2L-95C Particles 135
4.6.2 PHBV/ZnO Nanocomposites Fabricated by CMI Containing ZnO Particles 139
4.6.2.1 Structural Characterization of the PHBV Nanocomposites Fabricated by CMI Containing ZnO Particles 142
4.6.2.2 Thermal Stability of the PHBV Nanocomposites Fabricated by CMI Containing ZnO Particles 143
4.6.2.3 Melting and Crystallization Behavior of the PHBV Nanocomposites Fabricated by CMI Containing ZnO Particles 146
4.6.2.4 Mechanical Properties of the PHBV Nanocomposites Fabricated by CMI Containing ZnO Particles 152
4.6.3 PHBV Nanocomposites Fabricated by Sonochemically Synthesized ZnO Particles 154
4.6.3.1 XRD Analysis of the PHBV Nanocomposites Fabricated by Sonochemically Synthesized ZnO Particles 155
4.6.3.2 FTIR Analysis of the PHBV Nanocomposites Fabricated by Sonochemically Synthesized ZnO Particles 157
4.6.3.3 Thermal Stability of the PHBV Nanocomposites Fabricated by Sonochemically Synthesized ZnO Particles 158
4.6.3.4 Melting and Crystallization Behavior of PHBV Nanocomposites Fabricated by Sonochemically Synthesized ZnO Particles 163
4.6.3.5 Mechanical Properties of the PHBV Nanocomposites Fabricated by Sonochemically Synthesized ZnO Particles 170

CHAPTER 5

CONCLUSION AND RECOMMENDATIONS 173

REFERENCES 179

CURRICULUM VITAE 193

LIST OF SYMBOLS

a	Lattice constant
A_0	Cross-sectional area
B	Peak width
c	Lattice constant
C	BET constant
d	Lattice spacing
D	Distance between grips
E	Elastic modulus
E_a	Activation energy
El	Elongation
F	Tensile force
G	Gage length
H_c	Crystallization enthalpy
H_m	Melting enthalpy
I	Intensity
K	Numerical constant
L	Crystallite size
L_0	Initial gage length
LO	Overall length
M_v	Molar volume
n	Order of diffraction peak
N_{Av}	Avogadro's constant
P	Pressure
P_0	Atmospheric pressure
R	Radius of fillet
S	Surface area
T	Temperature
T_c	Crystallization temperature
T_{cc}	Cold crystallization temperature
T_g	Glass transition temperature
T_i	Initial temperature
T_m	Melting temperature
T_{max}	Thermal degradation temperature
T_x	Characteristic degradation temperature
w	Weight fraction
W_0	Initial weight
WO	Overall width
W_t	Remaining weight

X_c	Crystallinity
X_m	Monolayer capacity
ε	Strain
θ	Bragg angle
λ	Wavelength
σ	Stress

LIST OF ABBREVIATIONS

APTES	(3-Aminopropyl)triethoxysilane
BET	Brunauer-Emmett-Teller
BN	Boron nitride
CMI	Carboxymethyl inulin
CNC	Cellulose nanocrystals
CNT	Carbon nanotubes
CNW	Cellulose nanowhiskers
DMA	Dynamic mechanical analysis
DSC	Differential scanning calorimery
DTG	Differential thermogravimetry
EDA	Ethylene diamine
FESEM	Field emission scanning electron microscopy
FGS	Functionalized graphene nanosheets
FTIR	Fourier trasform infrared spectroscopy
HAP	Hydroxyapatite
HDPE	High density polyethylene
HMT	Hydroxymethyltetramine
HNT	Halloysite nanotubes
IR	Infrared
JCPDS	Joint Committee on Powder Diffraction Standards
MMT	Montmorillonite
MPS	3-Mehacryloxypropyltrimethoxysilane
OMMT	Organically modified montmorillonite
OP	Oxygen permeability
OTES	Triethoxy(octyl)silane
PA	Polyamide
PAM	Polyaxrylamide
PBAT	Poly(butylene adipate-co-terephthalate
PBS	Poly (butylene succinate)
PCL	Polycaprolactone
PEG	Polyethylene glycol
PET	Polyethylene terephthalate
PHA	Polyhydroxyalkanoate
PHB	Polyhydroxybutyrate
PHBV	Poly(3-hydroxybutyrate-co-3hydroxyvalerate)
PLA	Polylactic acid

POM	Polarized optical microscopy
PP	Polypropylene
PTT	Polytrimethylene terephthlate
PU	Polyurethane
PVA	Poly(vinyl alcohol)
PVP	Polyvinyl pyrrolidone
RH	Relative humidity
SEM	Scanning electron microscopy
STP	Standard temperate and pressure
TEM	Transmission electron microscopy
TGA	Thermogravimetric analysis
UV	Ultraviolet
WAXS	Wide angle X-ray scattering
WVP	Water vapor permeability
XRD	X-ray diffraction

LIST OF FIGURES

Page

Figure 2.1 Global production capacities of bioplastics in 2016 5
Figure 2.2 Transmission electron micrograph of ultrathin section of *Azotobacter chroococcum* cell (PHA is the major constituent of the granules) 6
Figure 2.3 The chemical structure of PHB 6
Figure 2.4 General chemical structure of PHA 6
Figure 2.5 Chemical structure of PHBV 7
Figure 2.6 Worldwide shares of biopolymers production in different market segments in 2016 and projection for 2021 9
Figure 2.7 Unit cell of the wurtzite structure of ZnO 22
Figure 2.8 Hexagonal ZnO crystal 23
Figure 2.9 Molecular structure of HMT 25
Figure 2.10 Chemical structure of CMI 29

Figure 3.1 The batch reactor system used for the synthesis of ZnO particles 33
Figure 3.2 Diffraction of X-rays from the sample in XRD analysis 42
Figure 3.3 Mechanical analysis specimens shape and dimensions 54

Figure 4.1 SEM micrographs of the ZnO-1L-75C particles (a) at 50000x magnification, (b) at 50000x magnification in another area, and (c) at 5000x magnification 58
Figure 4.2 SEM micrographs of the ZnO-1L-95C particles at different zones (a) at 100000x magnification, (b) at 80000x magnification, and (c) at 10000x magnification 61
Figure 4.3 SEM micrographs of the ZnO-2L-95C particles (a) at 15000x magnification, (b) at 7500x magnification, and (c) at 5000x magnification 62
Figure 4.4 X-ray diffractogram of the ZnO-2L-95C particles 70
Figure 4.5 FTIR spectrum of the ZnO-2L-95C particles (a) before and (b) after baseline correction 71
Figure 4.6 SEM micrographs of the ZnO-2L-95C particles after 60 min of ultrasound application (a) at 20000x magnification and (b) at 5000x magnification . 73
Figure 4.7 Size distribution of ZnO-2L-95C particles (a) before and (b) after 60 min of ultrasound application, obtained by light-scattering technique 74
Figure 4.8 Size distribution for (a) particle length and (b) particle width of ZnO-2L-95C-US60 particles obtained from the analysis of SEM micrographs 75
Figure 4.9 Molecular structure of MPS 76
Figure 4.10 BET isotherm obtained for ZnO-2L-95C particles 77
Figure 4.11 Multiple-point BET plot of ZnO-2L-95C particles 78

Figure 4.12 FTIR spectra of ZnO-2L-95C particles before and after surface modification with MPS 79
Figure 4.13 Schematic model of grafting reactions of MPS on ZnO particles 81
Figure 4.14 SEM micrograph of the ZnO-2L-95C particles after surface modification with MPS 81
Figure 4.15 SEM micrographs of the MPS treated ZnO-2L-95C particles after 15 min of ultrasound application (a) at 5000x magnification, (b) at 5000x magnification in another area, (c) at 20000x magnification and (d) at 20000x magnification in another area 82
Figure 4.16 SEM micrographs of the MPS treated ZnO-2L-95C particles after 60 min of ultrasound application (a) at 2000x magnification and (b) at 5000x magnification 83
Figure 4.17 SEM micrographs of the ZnO particles synthesized with different CMI concentrations: (a) without CMI, (b) 50 ppm CMI, (c) 450 ppm CMI, and (d) 750 ppm CMI 84
Figure 4.18 Effect of CMI concentration on the mean dimensions of the rod-shaped ZnO particles 88
Figure 4.19 Schematic illustration of the mechanism how CMI affects particle size and shape 89
Figure 4.20 Size distribution histograms and Gaussian curves of (a) ZnO-2L-95C particles and (b) ZnO-750ppm-2L-95C particles 91
Figure 4.21 XRD diffractogram of ZnO-50-2L-95C particles 92
Figure 4.22 XRD diffractogram of ZnO-450-2L-95C particles 92
Figure 4.23 FTIR spectra of (a) ZnO-2L-95C, (b) ZnO-50-2L-95C, and (c) ZnO-450-2L-95C 96
Figure 4.24 SEM micrographs of ZnO-2L-95C-UB40 particles at (a) 10000x and (b) 5000x magnification 99
Figure 4.25 Size distribution histograms and Gaussian curves of ZnO-2L-95C-UB40 particles 100
Figure 4.26 XRD diffractogram of the ZnO-2L-95C-UB40 particles 102
Figure 4.27 FTIR spectrum of the ZnO-2L-95C-UB40 particles 105
Figure 4.28 Molecular structure of OTES 106
Figure 4.29 SEM micrograph of OTES-treated ZnO-2L-95C-UB40 particles 107
Figure 4.30 FTIR spectra of untreated, OTES-treated ZnO-2L-95C-UB40 particles 107
Figure 4.31 SEM micrographs of the PHBV/ZnO-US nanocomposite at (a) 50000x, (b) 20000x, and (c) 15000x magnification 111
Figure 4.32 SEM micrographs of the PHBV/ZnO-MPS nanocomposite at (a) 50000x, (b) 20000x, and (c) 15000x magnification 112
Figure 4.33 SEM micrographs of the PHBV/ZnO-MPS-US nanocomposite at (a) 50000x, (b) 20000x, and (c) 15000x magnification 113
Figure 4.34 Thermogravimetry curves of the extruded neat PHBV sample: (a) weight loss and (b) derivative weight loss curves 117
Figure 4.35 Thermogravimetry curves of neat PHBV and PHBV/ZnO-US samples: (a) weight loss and (b) derivative weight loss curves 118
Figure 4.36 Thermogravimetry curves of neat PHBV and PHBV/ZnO-MPS samples: (a) weight loss and (b) derivative weight loss curves 119
Figure 4.37 Thermogravimetry curves of neat PHBV and PHBV/ZnO-MPS-US samples: (a) weight loss and (b) derivative weight loss curves 120

Figure 4.38 Thermogravimetry curves of neat PHBV and PHBV/ZnO-2L-95C nanocomposites at a narrower temperature range: (a) weight loss and (b) derivative weight loss curves 121
Figure 4.39 Calculation of the Ea values for neat PHBV and PHBV/ZnO-2L-95C nanocomposites by the Horowitz-Metzger method: (a) neat PHBV, (b) PHBV/ZnO-US, (c) PHBV/ZnO-MPS, and (d) PHBV/ZnO-MPS-US .. 123
Figure 4.40 DSC scans of neat extruded PHBV (a) 1st heating scan, (b) cooling scan, and (c) 2nd heating scan 124
Figure 4.41 DSC scans of the PHBV/ZnO-US nanocomposite shown together with neat PHBV (a) 1st heating scans, (b) cooling scans, and (c) 2nd heating scans 125
Figure 4.42 DSC scans of the PHBV/ZnO-MPS nanocomposite shown together with neat PHBV (a) 1st heating scans, (b) cooling scans, and (c) 2nd heating scans 126
Figure 4.43 DSC scans of the PHBV/ZnO-MPS-US nanocomposite shown together with neat PHBV (a) 1st heating scans, (b) cooling scans, and (c) 2nd heating scans 127
Figure 4.44 DSC scans of the neat PHBV and the PHBV/ZnO-2L-95C nanocomposites shown together at a narrower temperature range (a) 1st heating scans, (b) cooling scans, and (c) 2nd heating scans 128
Figure 4.45 Glass transition temperatures of the (a) neat PHBV, (b) PHBV/ZnO-US, (c) PHBV/ZnO-MPS, and (d) PHBV/ZnO-MPS-US samples from the DSC 1st heating curves 132
Figure 4.46 Stress-strain curves of (a) neat PHBV, (b) PHBV/ZnO-US, (c) PHBV/ZnO-MPS, and (d) PHBV/ZnO-MPS-US nanocomposites obtained from tensile testing 136
Figure 4.47 Mechanical properties of neat PHBV and the PHBV/ZnO-2L-95C nanocomposites: (a) tensile strength and elastic modulus and (b) elongation at break and toughness 137
Figure 4.48 SEM micrographs of the PHBV/ZnO(50) nanocomposite at (a) 50000x, (b) 20000x, and (c) 15000x magnification 140
Figure 4.49 SEM micrographs of the PHBV/ZnO(450) nanocomposite at (a) 50000x, (b) 20000x, and (c) 15000x magnification 141
Figure 4.50 Thermogravimetry curves of neat PHBV and PHBV/ZnO(50) samples: (a) weight loss and (b) derivative weight loss curves 143
Figure 4.51 Thermogravimetry curves of neat PHBV and PHBV/ZnO(450) samples: (a) weight loss and (b) derivative weight loss curves 144
Figure 4.52 Thermogravimetry curves of neat PHBV, PHBV/ZnO(50) and PHBV/ZnO(450) nanocomposites at a narrower temperature range: (a) weight loss and (b) derivative weight loss curves 145
Figure 4.53 Calculation of the Ea values for (a) PHBV/ZnO(50) and (b) PHBV/ZnO(450) nanocomposites by the Horowitz-Metzger method 146
Figure 4.54 DSC scans of the PHBV/ZnO(50) nanocomposite shown together with neat PHBV (a) 1st heating scans, (b) cooling scans, and (c) 2nd heating scans 147
Figure 4.55 DSC scans of the PHBV/ZnO(450) nanocomposite shown together with neat PHBV (a) 1st heating scans, (b) cooling scans, and (c) 2nd heating scans 148

Figure 4.56 DSC scans of neat PHBV, PHBV/ZnO(50), and PHBV/ZnO(450) shown together at a narrower temperature range (a) 1st heating scans, (b) cooling scans, and (c) 2nd heating scans 149
Figure 4.57 Glass transition temperatures of the (a) PHBV/ZnO(50) and (b) PHBV/ZnO(450) nanocomposite samples from the DSC 1st heating curves 151
Figure 4.58 Stress-strain curves of (a) PHBV/ZnO(50) and (b) PHBV/ZnO(450) nanocomposites obtained from tensile testing 153
Figure 4.59 Mechanical properties of PHBV/ZnO(50), PHBV/ZnO(450), and PHBV/ZnO-US nanocomposites: (a) tensile strength and elastic modulus and (b) elongation at break and toughness 154
Figure 4.60 X-ray diffraction patterns of (a) neat PHBV, (b) PHBV/UB(1), and (c) PHBV/UB-OTES(1) samples 156
Figure 4.61 X-ray diffraction patterns of (a) PHBV/UB-OTES(0.5) and (b) PHBV/UB-OTES(3) samples 157
Figure 4.62 FTIR spectra of (a) neat PHBV, (b) PHBV/UB(1), and (c) PHBV/UB-OTES(1) samples 159
Figure 4.63 FTIR spectra of (a) PHBV/UB-OTES(0.5) and (b) PHBV/UB-OTES(3) samples 160
Figure 4.64 TG curves of neat PHBV, PHBV/UB(1), PHBV/UB-OTES(0.5), PHBV/UB-OTES(1) and PHBV/UB-OTES(3) samples together and at a narrow temperature scale 162
Figure 4.65 DTG curves of neat PHBV, PHBV/UB(1), PHBV/UB-OTES(0.5), PHBV/UB-OTES(1) and PHBV/UB-OTES(3) samples together and at a narrow temperature scale 162
Figure 4.66 Calculation of the Ea values for (a) neat PHBV, (b) PHBV/UB(1), (c) PHBV/UB-OTES(0.5), (d) PHBV/UB-OTES(1) and (e)PHBV/UB-OTES(3) by the Horowitz-Metzger method 162
Figure 4.67 DSC 1st heating curves of the (a) PHBV/UB-OTES(0.5), (b) PHBV/UB-OTES(1), and (c) PHBV/UB-OTES(3) samples 164
Figure 4.68 DSC cooling curves of the (a) PHBV/UB-OTES(0.5), (b) PHBV/UB-OTES(1), and (c) PHBV/UB-OTES(3) samples 165
Figure 4.69 DSC 2nd heating curves of the (a) PHBV/UB-OTES(0.5), (b) PHBV/UB-OTES(1), and (c) PHBV/UB-OTES(3) samples 166
Figure 4.70 DSC scans of neat PHBV, PHBV/UB-OTES(0.5), PHBV/UB-OTES(1) and PHBV/UB-OTES(3) shown together at a narrower temperature range (a) 1st heating scans, (b) cooling scans, and (c) 2nd heating scans 167
Figure 4.71 Stress-strain curves of (a) PHBV/UB(1), (b) PHBV/UB-OTES(0.5), (c) PHBV/UB-OTES(1), and (d) PHBV/UB-OTES(3) nanocomposites obtained from tensile testing 171
Figure 4.72 Mechanical properties of PHBV, PHBV/UB(1), PHBV/UB-OTES(0.5), PHBV/UB-OTES(1) and PHBV/UB-OTES(3) nanocomposites: (a) tensile strength and elastic modulus and (b) elongation at break and toughness 172

LIST OF TABLES

Page

Table 2.1 Names and properties of common biopolymers 4
Table 2.2 Common PHA and corresponding *R* groups 7
Table 2.3 Comparison of the physical properties of different PHA, PP, and HDPE (high density polyethylene). 8

Table 3.1 Properties and concentrations of precursor species for the synthesis reaction of ZnO 34
Table 3.2 Different ZnO particles synthesized and their synthesis parameters 36
Table 3.3 Properties of silanes utilized in surface modification of ZnO particles 38
Table 3.4 Physical properties of PHBV purchased from AdMajoris Company (Maj'Eco FN000HA Grade for Injection Molding) 47
Table 3.5 Condition applied during mechanical pressing of PHBV/ZnO nanocomposite pellets 48
Table 3.6 Dimensions of the mechanical analysis specimens 54

Table 4.1 XRD parameters of ZnO-2L-95C particles and the parameters given in standard JCPDS 36-1451 card 68
Table 4.2 Average crystallite sizes of ZnO-2L-95C estimated from XRD spectrum 69
Table 4.3 Effect of CMI concentration on the particle dimensions and aspect ratio. 86
Table 4.4 XRD parameters of ZnO-50-2L-95C and ZnO-450-2L-95C particles 93
Table 4.5 Average crystallite sizes of ZnO-50-2L-95C and ZnO-450-2L-95C particles estimated from XRD spectrums 94
Table 4.6 XRD parameters of ZnO-2L-95C and ZnO-2L-95C-UB40 particles 102
Table 4.7 Average crystallite sizes of ZnO-2L-95C-UB40 estimated from XRD spectrum 103
Table 4.8 Sample codes and formulations of the PHBV/ZnO nanocomposites fabricated from ZnO-2L-95C particles 110
Table 4.9 Average numbers of particles per SEM image of PHBV nanocomposites fabricated by ultrasound-dispersed and/or MPS-modified ZnO-2L-95C particles 114
Table 4.10 Parameters of thermal degradation calculated for the neat extruded PHBV and the PHBV/ZnO-2L-95C nanocomposites 122
Table 4.11 Melting parameters of neat PHBV and PHBV/ZnO-2L-95C nanocomposites calculated from the DSC 1st heating runs 131
Table 4.12 Crystallization parameters of neat PHBV and PHBV/ZnO-2L-95C nanocomposites calculated from the DSC cooling runs 133
Table 4.13 Melting parameters of neat PHBV and PHBV/ZnO-2L-95C nanocomposites calculated from the DSC 2nd heating runs 134

Table 4.14 Mechanical properties of neat PHBV and the PHBV/ZnO-2L-95C nanocomposites 137
Table 4.15 Sample codes and formulations of the PHBV/ZnO nanocomposites fabricated from CMI containing ZnO particles 142
Table 4.16 Average numbers of particles per SEM image of PHBV nanocomposites fabricated by CMI containing ZnO particles 142
Table 4.17 Parameters of thermal degradation calculated for neat PHBV, PHBV/ZnO(50) and PHBV/ZnO(450) samples 146
Table 4.18 Melting parameters of neat PHBV, PHBV/ZnO(50) and PHBV/ZnO(450) calculated from the DSC 1st heating runs 150
Table 4.19 Crystallization parameters of neat PHBV, PHBV/ZnO(50), PHBV/ZnO(450), and PHBV/ZnO-US nanocomposites calculated from the DSC cooling runs 151
Table 4.20 Melting parameters of neat PHBV, PHBV/ZnO(50), PHBV/ZnO(450), and PHBV/ZnO-US samples calculated from the DSC 2nd heating runs 152
Table 4.21 Mechanical properties of neat PHBV, PHBV/ZnO(50), PHBV/ZnO(450), and PHBV/ZnO-US 153
Table 4.22 Sample codes and formulations of the PHBV/ZnO nanocomposites fabricated from Sonochemically synthesized ZnO particles 154
Table 4.23 X-ray diffraction patterns of neat PHBV, PHBV/UB(1), and PHBV/UB-OTES(1) 157
Table 4.24 Transmittance peaks observed in the FTIR spectrum of neat PHBV and the molecular bonds associated with the peaks 161
Table 4.25 Parameters of thermal degradation calculated for neat PHBV, PHBV/UB(1), PHBV/UB-OTES(0.5), PHBV/UB-OTES(1) and PHBV/UB-OTES(3) samples 162
Table 4.26 Melting parameters of neat PHBV, PHBV/UB-OTES(0.5), PHBV/UB-OTES(1), and PHBV/UB-OTES(3) nanocomposites calculated from the DSC 1st heating runs 168
Table 4.27 Crystallization parameters of neat PHBV, PHBV/UB-OTES(0.5), PHBV/UB-OTES(1), and PHBV/UB-OTES(3) nanocomposites calculated from the DSC cooling runs 169
Table 4.28 Melting parameters of neat PHBV, PHBV/UB-OTES(0.5), PHBV/UB-OTES(1), and PHBV/UB-OTES(3) nanocomposites calculated from the DSC 2nd heating runs 170
Table 4.29 Mechanical properties of neat PHBV, PHBV/UB(1), PHBV/UB-OTES(0.5), PHBV/UB-OTES(1) and PHBV/UB-OTES(3) nanocomposites 172

ABSTRACT

WET CHEMICAL SYNTHESIS OF ZnO PARTICLES AND INCORPORATION INTO PHBV MATRIX

Tuğçe BEKAT

Department of Chemical Engineering

PhD. Thesis

Adviser: Prof. Dr. Mualla ÖNER

Biopolymers do not depend on petroleum sources and they are produced by eco-friendly routes. Therefore, they are important alternatives for conventional plastics. Polyhydroxyalkanoates (PHA) are naturally synthesized by many types of bacteria and are biodegradable and biocompatible thermoplastic polymers. One commonly studied type of PHA is polyhydroxybutyrate-co-valerate (PHBV). Despite its advantages of being completely bio-based and biodegradable, it exhibits high crystallinity, narrow processing window, and brittleness. Poor thermal and mechanical properties of PHBV are a disadvantage in packaging applications.

Fabrication of polymer nanocomposites by addition of various nanoparticles into polymers are a common and promising method for improvement of polymer properties. ZnO particles are commonly studied for fabrication of polymer nanocomposites due to their high volume to area ratio, highly crystalline structure, good mechanical properties, low thermal expansion coefficient, high thermal conductivity, and antimicrobial activity.

In this study, various morphologies of ZnO particles were synthesized by wet chemical synthesis method. Reaction parameters such as precursors concentration, reaction temperature, and reactor volume were studied. Effects of carboxymethyl inulin on the morphological properties of ZnO particles were investigated. Sonochemical synthesis combined with wet chemical synthesis was also studied and the effects on particle dispersion were investigated. In order to achieve uniform particle dispersion, surface modification was applied to ZnO particles and untreated and surface-treated particles were compared. Effects of ultrasonic dispersion were also analyzed in terms of particle dispersion. Synthesized ZnO particles with varying conditions were characterized by

measurement of surface area, X-ray diffraction analysis (XRD), scanning electron microscopy (SEM) and Fourier transform infrared spectroscopy (FTIR).

ZnO particles synthesized by varying conditions were incorporated into PHBV matrix by the melt-extrusion method using a twin-screw extruder. Fabricated PHBV/ZnO nanocomposites were characterized for their structural, thermal, and mechanical properties. SEM, XRD, and FTIR analyses were utilized for structural characterization of the nanocomposites. Thermal properties of the nanocomposites were characterized by thermogravimetry analysis (TGA) and differential scanning calorimetry (DSC). Mechanical properties were studied by tensile testing. Effects of different ZnO particles on the properties of PHBV were studied.

Key words: Polymer nanocomposites, zinc oxide, polyhydroxybutyrate-co-valerate

ÖZET

ZnO PARÇACIKLARININ SUDA KİMYASAL SENTEZİ VE PHBV MATRİSİNE İLAVESİ

Tuğçe BEKAT

Kimya Mühendisliği Anabilim Dalı

Doktora Tezi

Tez Danışmanı: Prof. Dr. Mualla ÖNER

Biyopolimerler petrol kaynaklarına bağımlı olmamaları ve çevre dostu yöntemlerle üretilmeleri nedeniyle geleneksel polimerlere önemli bir alternatif oluşturmaktadır. Polihidroksialkanoatlar (PHA) birçok bakteri tarafından doğal olarak sentezlenen biyobozunur ve biyo-uyumlu termoplastik polimerlerdir. PHAların yaygın olarak çalışılan bir çeşidi polihidroksibütirat-co-valerattır (PHBV). Tamamen biyo-bazlı ve biyobozunur bir polimer olması gibi avantajlarına karşın, yüksek kristalinite, işlenebilme aralığının dar olması ve kırılganlık gibi olumsuz özelliklere sahiptir. Bu özellikler ambalaj üretiminde kullanı konusunda dezavantaj oluşturmaktadır.

Çeşitli nanoparçacıkların polimerlere eklenmesiyle polimer nanokompozitlerin üretilmesi, polimer özelliklerinin iyileştirilmesi konusunda yaygın kullanılan ve gelecek vaadeden bir yöntemdir. ZnO parçacıkları; yüksek hacim-alan oranı, yüksek kristalinite, iyi mekaniksel özellikler, düşük termal genleşme katsayısı, yüksek termal iletkenlik ve antimikrobiyal aktivite gibi özellikleri nedeniyle, polimer nanokompozitlerin üretiminde yaygın olarak tercih edilmektedirler.

Bu çalışmada, farklı ZnO parçacık morfolojileri, suda kimyasal sentez yöntemiyle üretilmiştir. Reakstant konsantrasyonu, reaksiyon sıcaklığı ve reaktör hacmi gibi parametrelerin sentez reaksiyonu üzerine etkileri çalışılmıştır. Karboksimetil inülinin ZnO parçacıklarının morfolojileri üzerine etkileri incelenmiştir. Sonokimyasal sentez yönteminin suda kimyasal sentez yöntemiyle kombinasyonyla parçacık sentezi gerçekleştirilmiş ve parçacık dağılımı üzerine etkileri incelenmiştir. Düzgün parçacık dağılımı elde etmek için parçacıklara yüzey modifikasyonu uygulanmış, yüzeyi

kaplanmış ve kaplanmamış olan parçacıklar mukayese edilmiştir. Parçacık dağılımı için ayrıca ultrasonik ayırma yöntemi çalışılmıştır. Farklı koşullarda üretilen ZnO parçacıkları yüzey alanı ölçümü, X-ışını difraktometresi (XRD), taramalı elektron mikroskobu (SEM) ve Fourier dönüşümlü infrared spektroskopi (FTIR) yöntemleriyle karakterize edilmiştir.

Farklı koşullarda sentezlenen ZnO parçacıkları PHBV matrisine eriyik harmanlama yöntemiyle, çift vidalı ekstruder kullanılarak ilave edilmiştir. Üretilen PHBV/ZnO nanokompozitleri yapısal, termal ve mekanik özellikleri bakımından karakterize edilmiştir. Yapısal analiz için SEM, XRD ve FTIR analizleri, termal özellikler için termogravimetrik analiz (TGA) ve diferansiyel taramalı kalorimetri (DSC) analizleri, mekanik özellikler için ise çekme testi uygulanmıştır. Farklı ZnO parçacıklarının PHBV özelliklerine olan etkileri incelenmiştir.

Anahtar Kelimeler: Polimer nanookompozit, çinko oksit, polihidroksibütirat-co-valerat

CHAPTER 1

INTRODUCTION

1.1 Literature Review

Conventional plastics occupy an important role in packaging, medical, domestic and industrial applications due to their low cost, versatileness, strength, and other advantages. However, they mainly depend on petroleum sources and their disposal results in environmental problems. Biopolymers are promising environmental-friendly alternatives for conventional plastics. Polyhydroxybutyrate-co-valerate (PHBV) is a widely studied biopolymer that is both bio-based and biodegradable; however its poor thermal and mechanical properties limit its applications.

1.2 Objective of the Thesis

The objective of the thesis is the wet chemical synthesis of zinc oxide (ZnO) particles of varying properties by the application of different reaction conditions and the incorporation of these particles into PHBV matrix. Improvement in the thermal and mechanical properties of PHBV by the incorporation of ZnO particles is aimed.

1.3 Hypothesis

ZnO particles of varying properties can be synthesized by wet chemical synthesis by changing reaction parameters. If homogeneous particle dispersion and interface compatibility can be achieved, incorporation of these particles into PHBV matrix will provide improvements in the thermal and mechanical properties of PHBV.

CHAPTER 2

GENERAL INFORMATION

In modern life, conventional plastics occupy a very important place due to the comfort and life quality they provide; however, environmental concerns related to accumulation of plastic wastes evolves as a major problem. Conventional plastics are petroleum-based polymers that possess many useful properties such as lightness, low price, versatileness, strength, resistance, and robustness and are utilized in many fields such as packaging, medical, domestic, and industrial applications. Many plastic commodities are disposable and when discarded they are toxic to the environment during their long degradation periods. Furthermore, extensive utilization of conventional plastics has resulted in reduction of crude oil resources [1-3].

Conventional plastic wastes are mainly eliminated by landfill, incineration and recycling. Landfill is not an effective method due to very slow degradation rates of the plastics. Incineration results in air pollution. Recycling is time-consuming and challenging due to the many additives within plastics and vast usage of plastic blends [1].

Bio-based polymers are important alternatives for conventional plastics since they do not depend on petroleum resources and are manufactured by eco-friendly routes. Most of them are also biocompatible. Biodegradable polymers are important due to their short and non-toxic degradation cycles, sustainability and environment-friendly properties. Development of bio-based and biodegradable polymers that reduce the petroleum dependence and enable sustainable materials has been a growing research area in the last decades [1, 3-4].

According to the market research conducted by Nova-Institute GmbH [5] current worldwide production capacity of biopolymers is 6.6 million tons per year, which

corresponds to 2% of the global polymer market. Annual production capacity of biopolymers is expected to increase to 8.5 million tons by the year of 2021.

2.1 Biopolymers

Biopolymer can be defined as "a type of polymeric material partially or fully bio-based and/or biodegradable". A bio-based polymer has some of all of its carbon produced from a renewable source. A biodegradable polymer is, on the other hand, one that degrades into CO_2, methane, H_2O, and biomass through biological action in a defined environment and timescale. Defined environments include composting, anaerobic digestion, marine and soil environments. At least one step of degradation of biodegradable polymers takes place as the metabolism of a natural organism. Biodegradation occurs via fragmentation or disintegration under suitable conditions such as moisture, temperature, and oxygen; without producing any toxic or environmentally harmful residues [3].

In other words, a biopolymer can be only bio-based or only biodegradable; or both bio-based and biodegradable. Therefore, biodegradable polymers can be classified according to their manufacturing resources as biological (natural or microbial) and synthetic.

Natural biodegradable polymers are produced by direct extraction from biomass. Plant carbohydrates such as starch, cellulose, chitosan, alginate, agar, pectin, and carrageenan or plant-origin proteins like soy protein, zein, wheat gluten, gelatin, collagen, whey protein, and casein are natural biodegradable polymers [3, 6].

Synthetic biodegradable polymers are produced by conventional chemical synthesis from renewable or non-renewable monomers. Poly(lactic acid) (PLA), poly(ε-caprolactone) (PCL), poly(butylene succinate) (PBS), and poly(vinyl alcohol) (PVA), and poly(glycolic acid) are common types of synthetic biodegradable polymers. PLA is obtained from biomass and the others from petrochemicals [3, 6].

Third class of biodegradable polymers are obtained from microorganisms or genetically modified bacteria. Polyhydroxyalkanoates (PHA), bacterial cellulose, xanthan, pullulan, and curdlan are microbial biodegradable polymer types [3, 6]. Table 2.1 shows manufacturing resource types and biodegradability properties of common biopolymers.

Table 2.1 Names and properties of common biopolymers [5]

Polymer	**Resource**	**Bio-based Carbon Content**	**Biodegradability**	**Production Capacity by 2014 (ton)**
PHA	Microbial	100 %	Industrial, home, soil, marine, anaerobic	35,000
PLA	Natural	100 %	Industrial	195,000
Starch	Natural	100 %	Industrial, home, soil, marine, anaerobic	395,000
PBS	Natural or petrochemical	Up to 100 % (mostly petrochemical)	Industrial, soil, marine	125,000
PBAT, poly(butylene adipate-*co*-terephthalate)	Partially bio-based	Up to 50% (mostly petrochemical)	Industrial, home, soil	100,000
PET, polyethylene terephthalate	Partially bio-based	20 %	None	1,000,000
PTT, polytrimethylene terephthalate	Partially bio-based	27 %	None	120,000
PA, polyamides	Partially bio-based	40 to 100 %	None	105,000
PU, polyurethanes	Partially bio-based	10 to 100%	None	1,400,000
PE, polyethylene	Bio-based	100 %	None	200,000

Although they are not commercially produced in highest amounts among common biopolymers; starch, PLA, and PHA are the most widely studied groups of biopolymers due to their biodegradability. They also draw attention from a commercial point of view since they can be processed using conventional equipment, produced on large industrial scales, have competitive prices and relatively satisfactory properties [6]. The most

dynamic development is predicted for the PHA; and although their production capacity is still small in 2016 (Figure 2.1), it is projected to almost triple by 2021 [5].

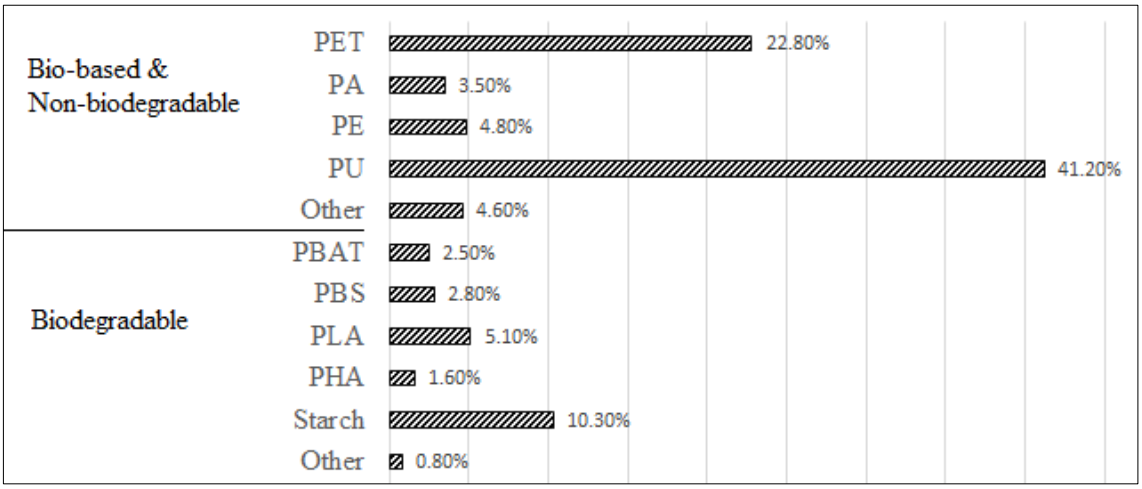

Figure 2.1 Global production capacities of bioplastics in 2016 [5]

2.1.1 Polyhydroxyalkanoates (PHA)

PHA are a big family of biodegradable, environmentally friendly, and biocompatible thermoplastic polyesters [7]. They are naturally synthesized by many types of Gram-positive and Gram-negative bacteria as carbon and energy reserves or reducing power storage materials [1]. Accumulation of PHA within the cell is a natural way of storing carbon and energy for the bacteria and these polyesters are accumulated in case of bacterial growth limitation by nitrogen, phosphorus, and oxygen depletion [6] and when excess amount of carbon source is present. PHA can be accumulated within the intracellular granules of bacteria cells to levels as high as 90 wt.% of the dry cell mass (Figure 2.2). Soluble intermediates within the bacteria cell are polymerized into insoluble PHA molecules, so that alterations in osmotic state are prevented [7].

The first PHA identified by the French bacteriologist Maurice Lemoigne in 1926 was polyhydroxybutyrate (PHB) [8]. It was identified in the bacterium *Bacillus megaterium* and showed intra-cellular granules [1]. PHB can be found in many types of bacteria can be grown in a wide variety of natural environments. Bacteria that have the ability to produce and polymerize the monomer [R]-3-hydroxybutyric acid store PHB as a reserve polymer [8].

The chemical structure of PHB is given in Figure 2.3. As seen from the figure, repeating unit of PHB has a chiral center. All polymers within the family of PHA have the same three-carbon backbone structure, but they differ in the type of alkyl group at the *ß* or 3-

position. All PHA polyesters have the same configuration for the chiral center at the 3-position. This configuration is important in terms of physical and biodegradation properties of PHA [8].

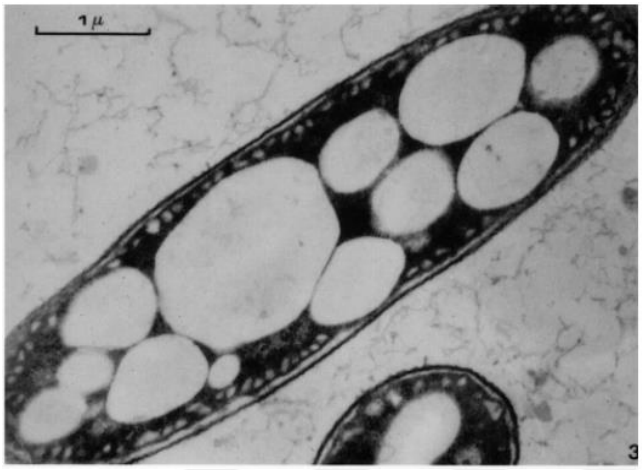

Figure 2.2 Transmission electron micrograph of ultrathin section of *Azotobacter chroococcum* cell (PHA is the major constituent of the granules) [8]

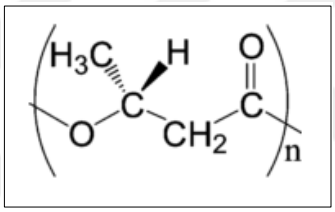

Figure 2.3 The chemical structure of PHB [8]

The general chemical structure of PHA composed of 3-hydroxy fatty acids is given in Figure 2.4. The value of *n* depends on the pendant group and the type of the bacteria and is typically between 100 and 30,000 [1, 7]. The most common polymers, depending on the *R* group shown in Figure 2.4, are given in Table 2.2.

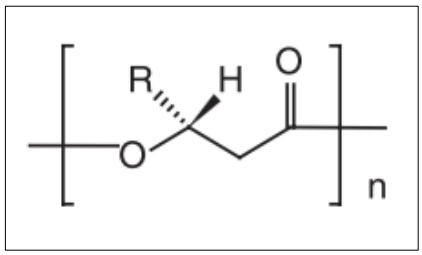

Figure 2.4 General chemical structure of PHA [7]

The family of PHA polyesters can be divided into 3 classes according to their chain length. Short chain length PHA are with carbon number of monomers between C_3 to C_5, medium chain length PHA are with carbon number between C_6 and C_{14}, and long chain

length PHA are with carbon number larger than C_{14}. To date, more than 100 different PHA monomers with straight, branched, saturated, unsaturated, and aromatic structures were reported; however, only few of these types were produced in large quantities. Type of bacterium and growth conditions are effective on the chemical composition and molecular weight (generally between $2*10^5$ and $3*10^6$ Da). Functionalized groups in the side chain such as halogens, carboxyl, hydroxyl, etc. allow chemical modification and are of special interest. Side chain length and type of functional group strongly affect polymer properties such as melting point, crystallinity and stiffness [2].

Table 2.2 Common PHA and corresponding *R* groups [7]

R group	**PHA name**	**Abbreviation**
CH_3	Poly(3-hydroxybutyrate)	PHB
CH_2CH_3	Poly(3-hydroxyvalerate)	PHV
$CH_2CH_2CH_3$	Poly(3-hydroxyhexanoate)	PHHx

Examples of short chain length PHA are poly(3-hydroxybutyrate) (P-3HB), poly(4-hydroxybutyrate) (P-4HB), poly(3-hydroxyvalerate) (P3HV) and its copolymer P(3HB-*co*-3HV) (PHBV, Figure 2.5). Utilization of even numbered *n*-alkanoates produces PHB homopolymer and odd numbered n-alkanoates produce copolymers of 3HB and 3HV [1]. Copolymers of PHB are formed when mixed substrates such as glucose and valerate are used [7].

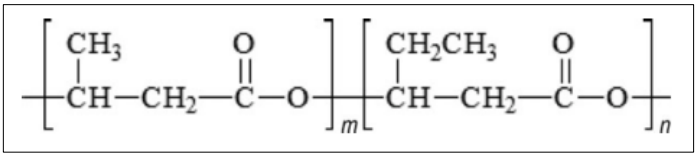

Figure 2.5 Chemical structure of PHBV [9]

Short chain length PHA possess high degree of crystallinity (around 60 to 80%) and therefore they are stiff and brittle in nature. P(3HB) has a stereo regular structure and is highly crystalline. It has low oxygen permeability (OP) and good thermoplastic properties. However, it has poor mechanical properties such as low tensile strength and elasticity modulus, in comparison to conventional thermoplastics. PHB is a highly brittle and stiff polymer [1]. Its thermal degradation temperatures are not far above its melting point; therefore, it has a narrow processing window [10].

P(3HB-*co*-3HV) copolymer is synthesized by the incorporation of 3-hydroxyvalerate monomer into the 3HB polymer chain. Some of the shortcomings of PHB improves by the incorporation of 3HV. PHBV has lower melting temperature, crystallinity, stiffness, and elasticity modulus; and higher elongation at break and impact strength than PHB [1] Due to the decrease in melting point, the processing window of PHBV is slightly broader. However, the decrease in crystallinity decreases stiffness and impairs barrier properties, which could be a disadvantage in packaging applications [10]. The composition of PHBV depends on the 3HV content (up to 30%) and the thermo-mechanical properties vary accordingly [1]. Physical properties of some common PHA and their comparison with the most common conventional thermoplastics are given in Table 2.3.

Biodegradation of PHA takes place within a few months in anaerobic sewage and within years in seawater, by the PHA hydrolase and PHA depolymerase enzymes of microorganisms. UV light accelerates the degradation of PHA. As mentioned before, PHA are both bio-based and biodegradable. Production of PHA is biological and based on renewable resources. Fermentative production of PHA uses agricultural feeds such as sugars and fatty acids as carbon and energy resources.

Table 2.3 Comparison of the physical properties of different PHA, PP, and HDPE (high density polyethylene) (PHB3V contains 3 mol% HV, PHB20V contains 20 mol% HV, and PHB4B is P(3HB-co-4HB with 16 mol% 4HB) [1, 7].

Property	**PHB**	**PHB3V**	**PHB20V**	**PHB4B**	**PP**	**HDPE**
Melting temperature (T_m), °C	177	170	145	130-150	176	122
Glass transition temperature (T_g), °C	2	-	-1	-7	-10	-80
Crystallinity (X_c), %	60	-	56	45	50-70	-
Tensile strength, MPa	40-43	38	20-32	26	29-38	18-33
Elasticity modulus, MPa	3.5-4	2.9	1.2	-	1-1.7	0.4-1
Elongation at break, %	5	-	50	444	400-850	12-700

2.1.1.1 Applications of PHA

Most of the conventional polymers produced are consumed by the packaging industry. Same trend is also observed for the biopolymers. The major part of biopolymers is utilized as rigid (bottles and others) and flexible packaging (films and others). The considerable interest of packaging industry results from the fact that packaging is only needed for short periods but in big quantities, and then discarded and contributes to the waste accumulation. Biodegradability property can also be interesting for agriculture and horticulture applications. Bio-based polymers are also used in many other applications such as high-performance durable applications. Figure 2.6 shows the global production of biopolymers in 2016 by market segments, and the projection for these segments in 2021 [5].

Due to their biodegradability, PHA are important candidates for biomedical applications. *R*-3-hydroxybutyric acid is normally found in blood and cell envelope of eukaryotes. However, due to its high crystallinity, PHB has a rather slow degradation rate within the body [2, 7]. Therefore, medical studies mainly focus on the less crystalline PHBV. Another research area in medical applications of PHA is drug carriers, nevertheless the rates of drug release obtained so far had excessive values. There are also some studies on PHA as scaffolds in tissue engineering [2].

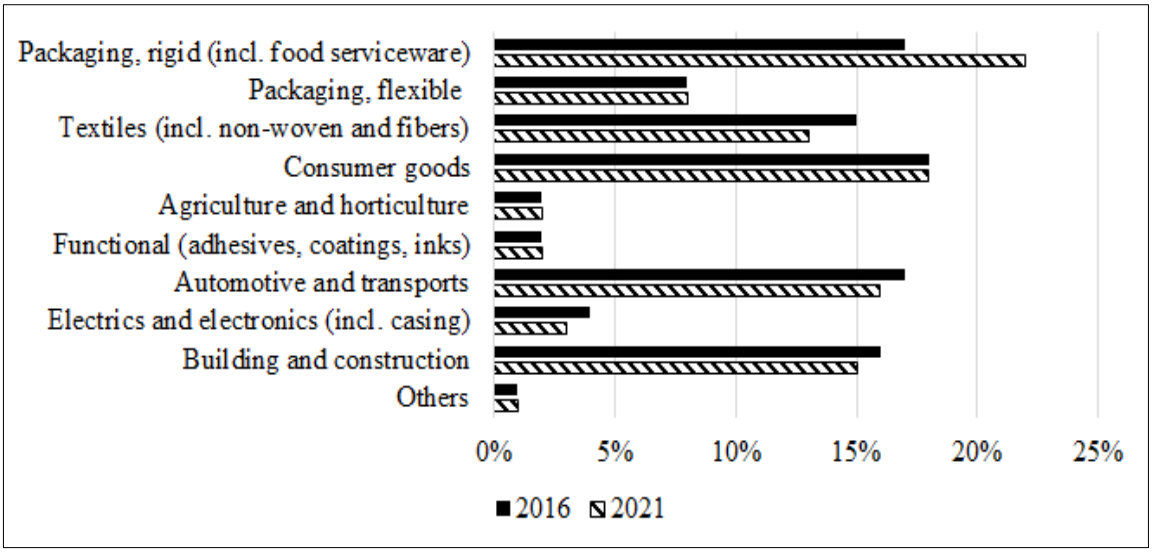

Figure 2.6 Worldwide shares of biopolymers production in different market segments in 2016 and projection for 2021 [5]

Due to environmental concerns and petroleum dependency, main application area of the PHA are as packaging materials. Food packaging applications are one major utilization

area for PHA and other biopolymers. However, as well as biodegradability, physical, thermal, mechanical, and barrier properties of biopolymers should also compensate the properties of conventional packaging materials. Despite many efforts in improvement of the properties of PHA, their properties are still not satisfactory and encounter difficulties in industrial applications [3].

2.1.2 Recent Advances in PHA

One common method for improvement of PHA properties and cost reduction is blending with other biopolymers [1]. The polymer to be blended with PHA should be miscible with PHA and also biodegradable. Blends of PHB with poly(vinyl acetate) [11], poly(vinylidenefluoride) [12], PLA [13, 14], PCL [15], and chitin [16] were reported in the literature.

Studies on the blends of PHBV with PBS [17], poly(2-hydroxyethylmetacrilate) [18], maize starch [19], chitosan [20], polyethylene oxide [21] and PLA [22, 23] were also reported.

Most promising and widely used method in enhancement of the properties of PHA and other polymers is the fabrication of polymer nanocomposites. Nanocomposites are obtained with the incorporation of various nanomaterials into polymer matrices in small amounts (up to 10 wt.%) and significant improvements in polymer properties can be achieved. Nanofillers of different morphologies, such as layered, spherical, rod, and plate, can be utilized and final polymer properties partly depend on the particle dimensions and aspect ratios. Final properties mainly depend on the polymer-nanofiller interactions and good nanofiller dispersion. Nano-biocomposites obtained by the addition of nanofillers into biopolymer matrices are promising materials since they allow properties enhancement maintaining biodegradability and without causing toxicity [4]. Nevertheless, PHBV does not contain strong interactive functional groups; therefore, homogeneous dispersion of inorganic particles within the PHBV matrix is quite difficult [24].

Nanoclays are the most commonly used additives in fabrication of polymer nanocomposites. In 2002, Chen et al. [25] added organically modified montmorillonite (OMMT) into PHBV matrix by using polymer intercalation from solution. X-ray diffraction (XRD) analysis indicated intercalated clay structure within the polymer nanocomposite since d_{100} spacing of the clay increased from 1.8 nm to 2.3 nm. This was

also verified by transmission electron microscopy (TEM). In order to observe the effect of the intercalated clay on the thermomechanical properties of the polymer, dynamic mechanical analysis (DMA) was applied. T_g value of the samples shifted to higher temperatures with increasing clay content. The increase in T_g and dynamic storage modulus of the samples compared to neat PHBV was attributed to maximizing the adhesion between the polymer and layered clay surfaces which restricts segmental motion at the interface. They also measured mechanical properties of the nanocomposites and observed that addition of 3 wt.% clay increased tensile strength of PHBV by 32%. When clay content exceeded 3%, both tensile strength and strain at break values were decreased. These decreases were attributed to the aggregation of the clay.

Wang et al. [26] prepared PHBV/OMMT nanocomposites by solution intercalation method and studied the structure, thermal properties and crystallization behavior of the nanocomposites by XRD, differential scanning calorimetry (DSC), thermogravimetry analysis (TGA), and polarizing optical microscopy (POM). Biodegradability of the nanocomposites were also investigated. XRD analysis revealed intercalated clay distribution. Aggregation was observed when clay content was increased to 10 wt.%. PHBV and its nanocomposites showed two endothermic peaks in DSC analysis, which revealed the existence of two crystalline phases. Low-temperature peak was the main peak for pure PHBV and the intensity of the high-temperature peak increased with increasing clay content. It was inferred that the low-temperature peak was related to homogeneous nucleation of PHBV, while the high-temperature peak was related to heterogeneous nucleation. TG analysis revealed single step weight loss. While T_m value of PHBV was decreased with clay addition, thermal degradation temperature hardly changed. Therefore, the range of processing temperature of PHBV was enlarged by clay addition. Melting enthalpy (ΔH_m) and X_c was decreased with increased clay addition. POM photographs also suggested that OMMT affected crystallization and spherulite size of PHBV. Biodegradability of PHBV in soil suspension was observed to decrease with OMMT addition.

Ublekov et al. [9] also studied addition of MMT into PHBV by solution intercalation method and investigated the nanocomposites by wide angle X-ray scattering (WAXS). They reported a stable pseudohexagonal *ß*-structure of PHBV grown on the layers of

MMT. This new structure was similar to the ß-form of PHBV with chains in planar zigzag conformation with a better three-dimensional crystalline order.

Correa et al. [27] incorporated OMMT clay into PHBV as a nanofiller and acetyl tributyl citrate as plasticizer by using melt-mixing and melt-extrusion methods. Intercalated/exfoliated clay structure was observed for the nanocomposites. In thermal analyses, the transition temperatures were not significantly changed with clay addition. However, crystallization was enhanced due to the nucleating agent effect of the clay. Thermal degradation temperatures of PHBV were not significantly changed by clay addition. Addition of plasticizer resulted in a decrease in tensile strength and elasticity modulus, in tensile tests. Addition of clay alone did not affect these two properties significantly. Clay addition decreased the OP of PHBV when no plasticizer was used and this effect was explained by the increase of tortuosity.

Halloysite nanotubes (HNT), naturally occurring polymorph of kaolinite, was added into PHBV by twin-screw extrusion [28]. Both natural and modified HNT with different functionalized organosilanes were used. Four different types of silanes were used. Two of them were organosilanes containing different amine groups – (3-aminopropyl) triethoxysilane (APTES) and [3-(methylamino)propyl]trimethoxysilane (MAPTMS) – which form H-bonds with the carbonyl group of PHBV. Third one was an organosilane with an ether functional group in its structure – (3-glycidyloxypropyl)trimethoxysilane (GOPTMS) – giving a polar character which can interact with PHBV matrix through secondary interactions. Fourth one was an organosilane with an 8-carbon atom chain – octyltriethoxysilane (OTES) – which can interact with PHBV through Van der Waals forces. In TEM analysis, best particle dispersion was observed for the nanocomposite containing unmodified HNT particles, followed by the composite containing MAPTMS-modified particles. APTES-modified particles showed formation of agglomerates and the poorest dispersion among the samples. The nanocomposite sample prepared by unmodified HNT exhibited the same crystallinity as neat PHBV, while the nanocomposites containing silane-modified HNT had lower crystallinity. Thermal degradation temperature (T_{max}) of PHBV was slightly decreased with the addition of both unmodified and modified HNT. The amine group silanes were reported to react with PHBV, changing its chemical structure and consequently damaging its final properties. The nanocomposites prepared with GOPTMS and OTES-modified HNT

exhibited improved mechanical properties despite poor particle dispersion, due to the prevented secondary interactions.

Another common nanofiller used in polymer nanocomposites is carbon nanotubes (CNTs). Shan et al. [29] studied the effect of multi-walled CNTs on the crystallization behavior of PHBV. In DSC first heating curves, PHBV exhibited double melting peaks with the high-temperature peak being the dominant one. The PHBV/CNT nanocomposites with low CNTs content exhibited double-peak behavior with low-temperature peak being the dominant peak. When CNTs content was higher, only one peak appeared in the melting curves. T_c values also increased remarkably with CNTs addition, indicating the efficient heterogeneous nucleation of CNTs for facilitating PHBV crystallization. POM observation showed that PHBV spherulites were large due to the low nucleation density. Spherulites got smaller with the addition of CNTs. However, the calculated crystallite size of the nanocomposites from XRD analysis did not agree with these results, showing larger crystallite sizes than neat PHBV. Isothermal crystallization kinetics were examined based on Avrami equation, and it was found that the crystallization half-time decreased and the overall crystallization rate increased dramatically with CNTs addition.

Incorporation of hydrophilic fumed silica particles into PHBV by twin-screw extrusion was studied by Khankrua et al. [30]. Scanning electron microscopy (SEM) analysis revealed that addition of silica at low contents between 0.1 and 0.5 wt.% resulted in good dispersion of particles within the polymer matrix. However, for larger silica contents (1 to 5 wt.%), particle agglomeration was observed. Due to the interaction between polar groups on the surface of silica, the particles had a tendency to agglomerate. In TGA curves, degradation of the nanocomposites started at a higher temperature compared to neat PHBV. This was explained by the very high surface area of the particles creating an increased interfacial area and facilitating the transfer of heat from polymer to the particles. Tensile tests showed that the elasticity modulus of PHBV slightly increased at low loadings of silica (0.1-0.2 wt.%), then decreased with 0.5 wt.% loading, and then increased again for the silica loadings of 1 to 5 wt.%. Elongation at break value did not change significantly for low contents of silica, and decreased for higher silica contents.

Ambrosio-Martin et al. [31] studied fabrication of nanocomposites based on PHBV and functionalized graphene nanosheets (FGS) by ball milling. The ball milling method was

reported to be efficient in achieving proper nanofiller dispersion. In DSC analysis, X_c and crystallization temperature (T_c) were observed to increase with FGS addition. TG analysis was carried out both under nitrogen and air atmosphere. There was no change in T_{max} under nitrogen atmosphere, while a decrease in thermal stability was observed with FGS addition under air atmosphere. The decrease in thermal stability with FGS addition was explained by the high thermal conductivity of graphene. Although graphene was considered as a good mass barrier for volatile degradation products, its high thermal conductivity was suggested to create low heat barrier effect.

In another study, Ambrosio-Martin et al. [32] reported mechanical, barrier, and electrical properties of PHBV/FGS nanocomposites. Water sorption isotherms did not show any difference with FGS addition, compared to neat PHBV. OP measured at 80% relative humidity (RH) was observed to decrease with FGS addition, increasing the oxygen barrier property of PHBV. In DMA analysis, FGS nanoparticles increased the storage modulus of PHBV in the whole temperature span studied.

The effects of addition of silver (Ag) nanoparticles on the crystallization and thermal stability of PHBV was studied by Huang et al. [33]. Ag nanoparticles were synthesized by a chemical reduction method, coated with a monolayer of surfactants consisting of oleic acid and *n*-propylamine and were incorporated into PHBV in concentrations between 0.1 and 2 wt.% by melt mixing method. The PHBV/Ag nanocomposite with 1% Ag content showed a rather homogeneous particle dispersion, while the Ag content of 2% resulted in some extent of particle agglomeration. This effect was explained by the decomposition of the coating in the blending process. This result was reported to support the view that higher Ag nanoparticles content would result in larger aggregates due to the strong interaction among the particles. In DSC analysis, the characteristic double melting behavior was observed for neat PHBV and its composites with low Ag loading. For the nanocomposites with higher Ag content, only one melting peak appeared and T_m shifted to higher temperatures. In the cooling curves obtained in DSC analysis, T_c continuously shifted to higher temperatures with increasing Ag content, suggesting efficient nucleation by Ag nanoparticles for facilitating PHBV crystallization. Calculated X_c from DSC first heating curve also increased with increased Ag content. In POM photographs, pure PHBV had radial ring spherulites in polygonal forms. The spherulites were big in size due to the low nucleation density of PHBV. Addition of Ag particles reduced the size of the spherulites and increased their

number. TGA curves showed one-stage degradation for PHBV and its nanocomposites, with T_{max} slightly increasing with increasing Ag content.

In another study carried out with Ag nanoparticles [34], *in situ* stabilized Ag nanoparticles produced into a microbial cultures-based PHB18V (valerate content of 18 mol%) and was melt-mixed into a commercial PHB3V with a valerate content of 3 mol%. Very low content of Ag nanoparticles (0.04 wt.%) unexpectedly decreased OP value dramatically (by 56% compared to neat PHBV). The thermal, mechanical, and optical properties of PHB3V were not significantly changed with Ag nanoparticles addition. Ag nanoparticles exhibited strong antibacterial activity against two common foodborne pathogens.

Tungsten disulphide inorganic nanotubes were incorporated into PHBV by solution blending method by Silverman et al. [35]. Commercial tungsten disulphide nanotubes were used without chemical modification and in the concentrations of between 0.1 and 1 wt.%. All tungsten disulphide particles were well dispersed within the PHBV matrix due to the lubricant character of the particles. TGA curves of neat PHBV and 0.1% tungsten disulphide nanocomposite showed no noticeable difference. For the 0.5% and 1% nanocomposites, initial thermal degradation temperature (T_i) was increased by 10 and 20°C, respectively. T_{max} was also increased for these two samples. T_c shifted to higher temperatures with the addition of nanotubes, even for the smallest content of 0.1%, indicating a remarkable heterogeneous nucleation capacity of the particles for accelerating the crystallization process. Large increments were observed in X_c between the neat PHBV and its nanocomposites.

Hydroxyapatite (HAP), a naturally occurring mineral, was also studied as an additive for PHBV [36]. HAP nanoparticles were synthesized by wet chemical synthesis. The particles were incorporated into PHBV by melt extrusion method. Both untreated and silane treated particles were used. Silane treatment was applied using (trimethoxysilyl)propyl methacrylate (MPS). HAP nanoparticles were successfully dispersed within PHBV matrix for concentrations up to 5 wt.%, according to SEM analysis. However, particle agglomerates and poor dispersion were observed when HAP content was increased to 10 wt.%. Tensile strength and elasticity modulus of PHBV was increased by HAP addition up to 5%. However, elongation at break value was affected negatively. In DSC first heating curves, double peak melting behavior was observed for PHBV and its nanocomposites. The intensity of the low-temperature peak was increased

with increasing HAP content. T_m values did not change significantly, while T_c was slightly decreased with HAP addition. Crystallinity of PHBV was observed to decrease with HAP addition.

In another recent study of Öner et al. [37], commercial boron nitride (BN) nanoparticles were incorporated into PHBV matrix by melt-extrusion method. Thermal stability of PHBV was observed to increase with BN addition due to the higher thermal stability of the fillers. In DSC analysis, T_m was not affected significantly with the addition of BN particles. T_c and X_c values were slightly increased. BN particles were reported to decrease OP of PHBV, enhancing oxygen barrier property.

Other than nanoclays and other inorganic particles, natural materials and fibers were also used as additives for PHBV due to their biodegradability. Javadi et al. [38] prepared PHBV/coir fiber composites by conventional and microcellular injection molding processes. Surface of the coir fibers was modified by alkali and methacrylate silane treatment in order to improve the adhesion of the hydrophilic fibers with PHBV. Morphology, thermal, and mechanical properties of the composites were investigated. Double melting peaks were observed during the first heating cycle of DSC analysis and the peaks were attributed to crystal thickening and recrystallization. X_c of PHBV was increased by addition of both treated and untreated coir fibers. Mechanical properties such as specific toughness and strain at break were improved with the addition of both treated and untreated coir fibers. Silane-treated coir fiber samples showed better improvement than the untreated coir samples.

Cellulose nanowhiskers (CNW) were also used as nanofiller for PHBV [39]. The influence of CNW on the crystallization, thermal, mechanical, and dynamic mechanical properties of PHBV were evaluated by POM, DSC, tensile testing, bulge testing, and DMA. TEM micrographs showed homogeneous dispersion of CNW within PHBV matrix, and the dispersion state was also confirmed by atomic force microscopy. When CNW were added into PHBV by 5 wt. %, the thermal degradation temperature was slightly reduced. This was explained by the increased thermal conductivity of the sample with CNW addition. DSC analysis revealed that T_g of PHBV samples were not changed with CNW addition, while the cold crystallization temperature (T_{cc}) progressively decreased. This behavior was explained by CNW being effective nucleating agents for PHBV, reducing the energy barrier to form PHBV nuclei. All samples of PHBV and its composites revealed double melting peaks, similar to

previously mentioned results, demonstrating a melting-recrystallization-melting process. According to the POM analysis performed, addition of CNW significantly increased the number of PHBV spherulites and consequently dramatically reduced their size. These results suggested strong nucleation effect of CNW on PHBV, in agreement with DSC results. Mechanical properties were examined by both tensile and bulge tests and the results of the two tests were in agreement. Elasticity modulus, tensile strength, and toughness of the PHBV samples were increased significantly by the addition of CNW. DMA test resulted revealed an increase in storage modulus and a shift of Tan δ peak to higher temperatures, due to the restrain of CNW on molecular mobility.

Cellulose nanocrystals (CNCs) were incorporated into PHBV matrix by solvent exchange method in a study of Yu et al. [40]. For the CNCs content of 0 to 10 wt.%, tensile strength and elasticity modulus were improved dramatically. However, elongation at break value was also decreased remarkably. These changes were attributed to the restrained chain movement during the deformation, due to the presence of CNCs. For CNCs contents higher than 10 wt.%, slight decreases in tensile strength and elasticity modulus and an increase in elongation at break were observed. In TG analysis, T_{max} gradually increased about 50°C with the increase of CNCs content, expanding the processing window of PHBV. This result contradicted with the results of the previously mentioned study of Ten et al. PHBV [39] where addition of CNWs decreased T_{max} of PHBV slightly. This contradiction was explained by the dependence of the reinforcing effect on not only the incorporation of the particles in the polymer matrix, but also intermolecular hydrogen bonding interactions between the polymer and the particles. DSC analysis revealed that incorporation of CNCs increased the nucleation and crystallization rate of the nanocomposites, leading to a narrow crystallite size distribution. According to the XRD analysis, the crystallinity of PHBV was increased when CNCs were added by 1 wt.%, and decreased gradually for higher contents of CNCs (up to 20 wt.%). This indicated that CNCs were efficient nucleating agents for crystallization rate, but not for the crystallinity.

Another organic material used as an additive for PHBV was lignosulfonate. Lemes et al. [41] studied the effect of lignosulfonate on PHBV by SEM, DSC, and TGA. Lignosulfonate was added into PHBV by melt-mixing method using an internal mixer. Cryo-fractured surfaces of the samples analyzed by SEM analysis revealed existence of pits that were created by the particles which were loosened from the matrix. This

indicated poor interfacial adhesion between the particles and the polymer matrix. In DSC analysis, T_c increased and X_c, T_m, and T_g decreased with increasing lignosulfonate content. TG analysis revealed that lignosulfonate particles decreased the thermal stability of PHBV.

Lignin powder, another natural material, was also added to PHBV by Shichao et al. [42]. Amorphous alkaline lignin was added into PHBV by melt processing method up to 10 wt.% concentration and the effects on crystallization behavior and thermal properties were investigated. In DSC second melting peaks, PHBV exhibited single melting peak, while PHBV/lignin composites exhibited double melting behavior. T_c decreased and X_c increased with addition of lignin, compared to neat PHBV. The basic crystal structure was not changed by lignin addition, but the average size of the lamellar stacks perpendicular to (020), (110), and (002) lattice planes were observed to decrease in XRD analysis. POM analysis revealed that the spherulites growth rate of PHBV decreased with lignin addition. In TG analysis, T_{max} was decreased by lignin addition, suggesting a decrease in thermal stability of PHBV.

2.1.3 ZnO As Nanofiller For PHA

ZnO nanostructures as promising nanofillers for PHBV due to their high volume to area ratio, highly crystalline structure, good mechanical properties, low thermal expansion coefficient, high thermal conductivity, and antimicrobial activity [43].

Yu et al. [24] prepared PHBV/ZnO composite nanofibers by electrospinning method. ZnO nanoparticles with a diameter of 10-20 nm were synthesized by a sol-gel method and were doped into PHBV fibers without using any dispersing agents. Doping concentration of ZnO particles was chosen as 1 wt.%, since higher concentration were expected to bring aggregation problem. XRD results showed no significant difference between neat PHBV and the PHBV/ZnO nanocomposites, indicated ZnO did not significantly affect the crystalline structure of PHBV or the doping concentration of ZnO was too low to be detected. As calculated from XRD data by Scherrer formula, the crystallite size of PHBV decreased slightly with ZnO addition, implying that ZnO particles might have had a restrictive effect on the crystallite growth of PHBV. In DSC analysis, T_m value of PHBV was not significantly changed with ZnO addition, suggesting ZnO did not influence the basic crystalline structure. X_c slightly decreased with ZnO addition, implying ZnO particles acted as retarding agent for crystallization of

electrospun PHBV fibers. During the cooling scan, both T_c and the crystallization enthalpy (ΔH_c) decreased with ZnO addition, again implying that ZnO nanoparticles retarded PHBV matrix from crystallization and slowed the crystallization rate.

Naphade and Jog [44] also fabricated PHBV/ZnO nanocomposite fibers by electrospinning. Elongated-shaped commercial ZnO particles with length of 40 to 100 nm and dimeter of about 50 nm were used. Concentration of ZnO particles in the electrospun fibers was between 3 and 7 wt.%. Structural and optical properties of the electrospun nanocomposite fibers were studied using SEM, Fourier transform infrared spectroscopy (FTIR), XRD and photoluminescence analyses. The morphology of PHBV fibers did not change significantly with the addition of ZnO particles. ZnO nanoparticles were reported to increase the overall crystallinity of PHBV according to FTIR and XRD analysis results. This result contradicts with the findings of Yu et al. [24], where ZnO particles were suggested to have a restrictive effect on PHBV crystallization. The ratio of UV to visible emission intensity was reported to be increased by 12.8 in the composite fibers compared to bare ZnO particles.

Fabrication of PHBV/ZnO nanocomposites by solution casting technique was studied by Diez-Pascual and Diez-Vicente [10]. Commercial ZnO powder with <100 nm particle size was incorporated into PHBV in different amounts (1 to 8 wt.%) by solution casting without the need of any surfactants or coupling agents. Morphology, crystallization behavior, thermal stability, mechanical, barrier, migration, and antibacterial properties of the nanocomposites were investigated. SEM images of the nanocomposites revealed very uniform nanofiller dispersion at low ZnO loadings (up to 4 wt.%) without any agglomerates. It was suggested that the interactions between the -OH groups of ZnO surface and polar moieties of PHBV prevented particle agglomeration. However, the nanocomposite with 8 wt.% ZnO loading displayed particle agglomerates with somewhat well distribution. In DSC analysis, X_c and T_c were increased remarkably, suggesting heterogeneous nucleating effect of ZnO particles on PHBV matrix. Neat PHBV displayed double melting behavior, in agreement with previously mentioned studies, which was interpreted in terms of melting, recrystallization, and remelting model. In TG analysis, PHBV and its nanocomposites showed one-step degradation with T_{max} increasing as ZnO content increased. ZnO nanoparticles exhibited remarkable thermal stabilization effect on PHBV. This was explained by the good dispersion of ZnO particles within the matrix and strong

interactions by H-bonding that create a barrier effect against the transport of decomposition products from the bulk of the matrix to the gas phase. High thermal conductivity of ZnO was also suggested to facilitate heat dissipation within the composite and result in enhanced thermal stability. Tensile strength and elasticity modulus of PHBV were observed to increase with ZnO addition. This was attributed to very homogeneous particle dispersion, strong interfacial adhesion between the phases via H-bonding, and the increase in the crystallinity of PHBV. The nanocomposite with 8 wt.% ZnO content, however, showed a decrease in tensile strength and modulus, compared to the nanocomposite with 4 wt.% content, due to the agglomeration detected in SEM analysis. Small particle clusters observed in this nanocomposite were reported to limit the stress transfer due to the decrease in the interfacial contact area. Also, the small reduction in the level of crystallinity was reported to be effective in the decrease in tensile properties. Elongation at break value, on the other hand, was reported to decrease with increasing ZnO particles addition. This was explained by the restriction of the ductile flow of the polymer chains by the fillers. DMA analysis revealed that, at temperatures below T_g, storage modulus increased significantly with increasing ZnO concentration, confirming the reinforcing effect of ZnO nanoparticles. Toughness values of the nanocomposites were measured by Charpy notched impact strength measurements and were calculated from the area under the stress-strain curves in tensile tests. The toughness results obtained were consistent with each other. Toughness of PHBV was increased by the addition of ZnO up to 2 wt.%. For higher ZnO contents, the toughness value was about the same as neat PHBV. Barrier properties tests demonstrated that water uptake, water vapor permeability (WVP), and OP of PHBV was decreased for the ZnO contents up to 4 wt.%. PHBV/ZnO nanocomposite films exhibited antibacterial activity against the studied human pathogen bacteria. Overall migration levels of the nanocomposites in polar and nonpolar simulants decreased with increasing ZnO content and the values were well below the allowed limits for food packaging materials.

Incorporation of ZnO particles in PHB was also studied by Diez-Pascual and Diez-Vicente [43]. Same commercial ZnO powder was distributed into PHB matrix by solution casting method in concentrations of 1 to 10 wt.%. ZnO nanoparticles acted as nucleating agents increasing T_c and X_c, similar to the results obtained in their previous research with PHBV. Thermal stability of PHB was also increased. Tensile strength,

elasticity modulus, and impact strength of PHB was enhanced by ZnO nanoparticles addition. However, elongation at break value was decreased. Water uptake, WVP and OP of PHBV were also improved. Antibacterial activity against Gram-positive and Gram-negative bacteria was reported. Migration levels of PHB in polar and non-polar simulants decreased with increasing ZnO content.

Recently, Abdalkarim et al. [45] used CNC-ZnO nanohybrids as reinforcing materials for PHBV. CNC-ZnO nanohybrids were prepared with a reaction of CNCs, zinc nitrate and NaOH. Nanohybrids were then incorporated into PHBV in concentrations up to 15 wt.% by electrospinning method and PHBV/CNC-ZnO nanocomposite fibers were obtained. CNC-ZnO nanohybrids were reported to act as nucleating agents, accelerating the crystallization rate of PHBV through heterogeneous nucleation. However, X_c of PHBV was decreased with CNC-ZnO addition due to the confined crystalline structure of PHBV induced by the interaction between the polymer and the fillers. T_{max} was improved by CNC-ZnO addition, indicating enhanced thermal stability. Tensile strength and elasticity modulus of PHBV was increased dramatically with particles addition, whereas elongation at break value was decreased. CNC-ZnO addition into PHBV matrix also affected WVP and antibacterial properties positively.

In another recent work by Castro-Mayorga et al. [46], hexagonal-pyramid, star, rod, and porous ball shaped ZnO particles were synthesized by an aqueous precipitation method using zinc nitrate hexahydrate, zinc acetate dihydrate, and NaOH. PHBV3 (3 mol% valerate content) was purchased and PHBV18 (18 mol% valerate content) was synthesized from mixed microbial cultures. They used different methods for the fabrication of PHBV/ZnO nanocomposites, including melt-mixing and electrospinning. Incorporation of ZnO nanoparticles into PHBV by melt-mixing was reported to hinder recrystallization during heating. Incorporation of ZnO particles as a coating resulted in a drop in the melting enthalpy and crystallinity. T_{max} value of PHBV was decreased by ZnO particles addition, decreasing the thermal stability. This effect was attributed to the high thermal conductivity and catalytic properties of ZnO. Water vapor and oxygen barrier properties of PHBV were reported to be affected negatively, in contradiction to previously reported literature [43]. The mechanical properties of the nanocomposites were affected by the fabrication method, as well as the presence of ZnO particles. Addition of ZnO particles by melt mixing method and in a coating form decreased the

toughness of PHBV. Electrospinning method, on the other hand, did not affect the elongation and stiffness.

2.2 Synthesis and Properties of ZnO Particles

ZnO is an inorganic material with a wurtzite crystalline structure (Figure 2.7). ZnO is a versatile material with unique physical and chemical properties, such as high chemical stability, high electrochemical coupling coefficient, broad range of radiation absorption, high photostability, broad energy band, high bond energy, high thermal and mechanical stability, hardness, rigidity, low toxicity, biocompatibility, and biodegradability. Its multifunctional properties make it an attractive material for electronics, optoelectronics, laser technology, sensors, convertors, energy generators, and photocatalysts, as well as polymer nanocomposites [47, 48].

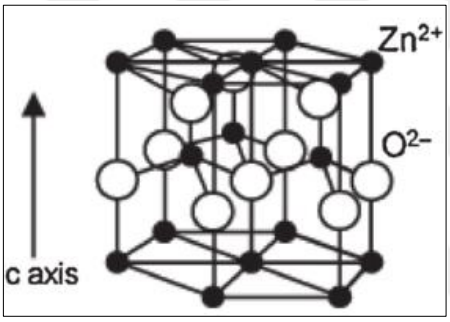

Figure 2.7 Unit cell of the wurtzite structure of ZnO [49]

ZnO is a polar non-transition metal oxide and its thermodynamically stable crystallographic phase is wurtzite. It occurs in the nature as the mineral zincite, however it rarely occurs as a natural single crystal. Hexagonal packing of O^{2-} and Zn^{2+} atoms in the crystallographic point group *3m* and Zn atoms in crystallographic space group $P6_3mc$ describes its ionic and polar structure. There are eight tetrahedral sites of hexagonal close packing and the occupancy of the four of these arrays controls the structure. The crystal habit of ZnO exhibits a basal polar plane $(00\bar{1})$ and two types of low-index faces – a nonpolar $(\bar{1}00)$ face (and symmetric ones) and a tetrahedron corner-exposed polar (001) face – (Figure 2.8). Most stable faces are the low-symmetry nonpolar faces with 3-fold coordinated atoms. Since there is no center of inversion in the wurtzite structure, there is an inherent asymmetry along the *c*-axis. This allows the growth of anisotropic crystalline [50].

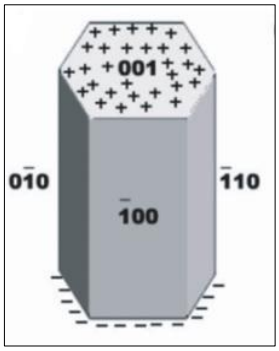

Figure 2.8 Hexagonal ZnO crystal [51]

ZnO particles can be synthesized by various methods, such as vapor deposition, chemical precipitation, hydrothermal synthesis, sol-gel process, precipitation from microemulsions, etc. [48]. As a result of wide variety of synthesis methods, ZnO particles with different shapes, sizes and structures can be obtained. ZnO particles can occur in one-dimensional (rods, needles, helixes, springs, rings, ribbons, tubes, belts, wires, and combs), two-dimensional (plates, sheets, pellets), and three-dimensional structures (flowers, dandelions, snowflakes, etc.) [47, 48]. Since the properties of ZnO structures strongly depend on the shape and size of the particles, precise control of the particle morphology is of crucial importance [49].

The aforementioned synthesis methods for various ZnO nanostructures can be grouped under two broad categories as solution phase synthesis and gas phase synthesis. The crystal growth process is carried out in a liquid in solution phase synthesis. When an aqueous solution is used, the process is called a hydrothermal growth process. Synthesis in alcoholic solutions, sol-gel process, spray pyrolysis and electrophoresis are other examples of solution phase synthesis. In gas phase synthesis, gaseous environment in closed chambers are used and the synthesis is carried out at high temperature (500 to 1500 °C). Vapor phase transport, physical vapor deposition, metal-organic chemical vapor deposition, microwave assisted thermal decomposition are examples to gas phase synthesis methods [51].

Physical vapor deposition methods require high temperature and may result in the incorporation of impurities into ZnO structures. Metal-organic vapor deposition method is a very high-cost method and generally results in poor deposition uniformity and low product yield. Wet chemical synthesis methods, on the other hand, are low cost, less hazardous, easy to scale up, carried out at low temperatures, compatible with organic

substrates, do not need the usage of metal catalysts, and possess a variety of tunable parameters for effective control of particle morphology and properties [52].

2.2.1 Chemical Precipitation Method for ZnO Synthesis

Controlled chemical precipitation is a widely used method for ZnO synthesis, since it allows low-temperature, cost-effective, and scalable synthesis of wide variety of particles with repeatable properties [48, 53]. The method basically involves fast and spontaneous reduction of a zinc salt solution by a reducing agent. Growth of particles is restricted in specific dimensions. Precursor of ZnO is then precipitated from the solution and undergoes thermal treatment. The precipitation process is controlled by the parameters like pH, temperature and reaction time. The particles synthesized with chemical precipitation generally exhibit high level of agglomeration and the agglomerates that form are difficult to break [48].

In chemical precipitation of ZnO from aqueous solution, a zinc salt is used as the zinc source together with hexamethylenetetramine (HMT) or an alkaline (NH_3 or NaOH). The driving force of crystallization is associated with the degree is supersaturation which is controlled by varying the pH of the solution. The orientation of ZnO particles can be controlled under specific conditions. Addition of particular organic molecules effect crystal morphology [49].

The modification of growth rate, site, and direction of the crystals in chemical precipitation method can be used to control the architecture of the crystals. Nucleation rate and growth rate affect the size and shape of the crystals depending on the degree of supersaturation. Fine grains occur by a high nucleation rate when the degree of supersaturation is high. In this case, nucleation is predominant rather than crystal growth. When the degree of supersaturation is low, rod-shaped particles elongated in the *c*-direction are produced with a low nucleation rate. ZnO grains have tendency to form rod-shaped crystals due to the anisotropic nature of the unit cell [49].

Solubility of ionic Zn species change with pH of the solution; therefore, the degree of supersaturation can be controlled by changing pH. Direct deposition of ZnO crystals is possible between the pH values of 9 to 13. Degree of supersaturation can be increased by the addition of NaOH. When HMT is used instead of NaOH, the degree of supersaturation can be kept at a low level. HMT produces OH^- ions with NH_4^+ ions, gradually increasing the pH of the medium [49].

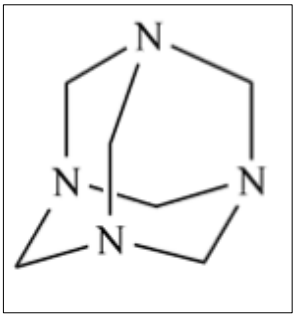

Figure 2.9 Molecular structure of HMT [52]

HMT ($(CH_2)_6N_4$, also known as methenamine or hexamine, Figure 2.9) is a non-ionic tetradentate cyclic tertiary amine and it is highly soluble in water. Thermal degradation of HMT releases OH^- ions which react with Zn^{2+} ions to create ZnO through following reactions [51]:

$$(CH_2)_6N_4 + 6\,H_2O \rightarrow 6\,CH_2O + 4\,NH_3 \quad (2.1)$$

$$NH_3 + H_2O \rightarrow NH_4^+ + OH^- \quad (2.2)$$

$$2\,OH^- + Zn^{2+} \rightarrow ZnO(s) + H_2O \quad (2.3)$$

The role of HMT in the synthesis of ZnO is generally accepted as supplying OH^- ions to drive the precipitation reaction. Another opinion suggests that HMT acts as a kinetic buffer since its hydrolysis decreases with increasing pH. During the formation of ZnO, the phase that is less thermodynamically stable precipitates faster. At the initial growth stage, the growth of ZnO is through $Zn(OH)_2$ due to the pH and Zn^{2+} concentration. As the pH increases gradually and Zn^{2+} concentration decreases, $Zn(OH)_2$ becomes thermodynamically unstable and starts dissolving. Further growth would be through direct ZnO deposition. Another opinion on the contribution of HMT on the growth of ZnO suggests that; since HMT is a long-chain polymer and a nonpolar chelating agent, it preferentially attaches to the nonpolar faces of the zincite, cuts off the access of Zn^{2+} ions to these faces, and leaving only the polar (001) face for epitaxial growth [51].

Fujita et al. [54] performed synthesis of ZnO by chemical precipitation using HMT together with zinc nitrate hexahydrate ($Zn(NO_3)_2{\cdot}6H_2O$) and zinc chloride ($ZnCl_2$). It was reported that when HMT and a zinc salt were used to synthesize ZnO by homogeneous precipitation method, the phase obtained depended on the synthesis conditions such as precursors, concentration of precipitants, zinc salt, and pH of the solvent. When zinc nitrate or zinc chloride were used as starting materials, ZnO could be obtained from the aqueous solution. They studied the synthesis of ZnO from aqueous

solutions of zinc nitrate/HMT and zinc chloride/HMT. When zinc nitrate was used, globular or rod-shaped particles were obtained, and when zinc chloride was used, globular and needle-shaped particles were obtained; depending on the precursor concentrations and pH of the solution.

Zhou and Deng [55] reported synthesis of ZnO nanorods by solution synthesis method using zinc nitrate hexahydrate and HMT. The reaction temperatures were ranging from 55 to 85 °C and the reaction time was above 3 hours. The ZnO nanorods obtained had a hexagonal cross section with a width of 200 to 300 nm. The lengths of the rods were about 3 to 5 μm. Zn^{2+} concentration was described with a first-order reaction mechanism. The length of the ZnO nanorods were analyzed and it was reported that lower temperature was beneficial to nanorod growth whereas high temperature resulted in a competition between nucleation and nanorod growth. The kinetics model suggested in the study agreed with the low-temperature experimental results while they deviated from high-temperature experimental results.

Utilization of organic additives in chemical precipitation is a common method in controlling crystal growth. Adsorption of these species on specific surfaces like (001), suppresses the growth along the *c*-direction. Relative growth rates of each crystal face can be altered by utilization of organic additives and crystal morphology can be changed. Organic additives, such as citric acid, surfactants, and water-soluble polymers affect nucleation and particle growth, as well as coagulation and flocculation of particles [48, 49].

Liu and Zeng [56] synthesized highly regulated, monodispersed ZnO nanorods using wet-chemical approach at room temperature. When zinc nitrate hexahydrate and NaOH were used in the synthesis reaction, the size of the ZnO nanorods synthesized were reported to get smaller with increasing OH^- concentration. Ethylenediamine (EDA) was used as an additive in the synthesis reactions. EDA chelating molecules were reported to act as surface modifiers, inhibiting radial growth of the nanorods. EDA was also reported to work as a transport carrier in Ostwald ripening. Different types of zinc salts were used as precursors in the formation of ZnO nanorods, such as zinc nitrate, zinc chloride, zinc acetate, and zinc sulfate. All the zinc salts produced similar ZnO nanorods having almost the same morphology.

Garcia and Semancik [57] synthesized ZnO nanorods using zinc nitrate hexahydrate and HMT by chemical precipitation method using seed crystals obtained from NaOH and zinc nitrate hexahydrate. Hexagonally prismatic ZnO crystals were obtained. The effects of three different growth modifiers (poly(diallyldimethylammonium chloride), sodium poly(styrene sulfonate), and trisodium citrate) on the median aspect ratio (ratio of rod length to width, L/W) of the rod-shaped ZnO particles were investigated. The L/W of ZnO crystals without addition of the growth modifiers was 5.2. The L/W ratio was reduced by the addition of the modifiers and the lowest aspect ratio was obtained by trisodium citrate.

Jitianu and Goia [58] synthesized ZnO particles using zinc nitrate and NaOH at 60 °C by a simple precipitation method. Non-uniform agglomerated ZnO particles were obtained as an unstable dispersion when these reaction conditions were used. When a commercial dispersant (Daxad 11G) was added into the reaction solution, the shape of the ZnO particles obtained were changed, but the stability of the dispersion was not affected. When arabic gum was used as a dispersant, uniform ZnO particles with an average size of 260 nm were obtained in a very stable dispersion. The calculated crystallite size also increased from 21 nm for the particles synthesized in absence of any dispersant, to 44 nm for the particles synthesized with arabic gum. When the synthesis reaction with arabic gum addition was carried out at 20 °C instead of 60 °C, spherical aggregates of very small nanoparticles were obtained instead of the hexagonal prism like particles obtained at 60 °C. The crystallite size calculated from XRD analysis also decreased to 10 nm. When zinc sulfate was used as the zinc salt, instead of zinc nitrate, particle shape and crystallite size were preserved, but the aspect ratio of the particles was changed. This was explained by the divalent sulfate ions favoring the formation of hexagonal prisms. When zinc acetate was used as the zinc salt, ZnO particles of irregular shape and broad size distribution were obtained. It was reported that the acetate ions prevented the formation of uniform particles due to their larger size preventing the effect of attracting forces between primary nanoparticles.

Preda et al. [59] synthesized ZnO micro and nanostructures with varying morphologies by chemical reaction of zinc nitrate and HMT and in presence of polysaccharides as growth modifiers. The polysaccharides used were sodium alginate, gum arabic, and chitosan. The ZnO particles synthesized in the absence of polysaccharides were star-shaped structures formed by hexagonal prismatic rods. The morphology of the ZnO

particles were changed to double-jellyfish, double-raspberry, and edelweiss-flower structures with the addition of different polysaccharides.

Panigrahy et al. [60] studied the effects of two polymers, polyvinyl pyrrolidone (PVP) and polyethylene glycol (PEG), as growth modifiers for the synthesis ZnO particles by aqueous chemical synthesis. Zinc chloride and HMT were used as reaction precursors and a copper substrate was used. In the absence of polymers, by changing the concentrations of zinc chloride and HMT, nanoneedles, flowerlike structures, and nanosquare disks were obtained. Applying the same conditions used at the synthesis of nanoneedles, by prolonging the reaction time from 80 min to 100 min, nanorods of ZnO were obtained. Addition of PVP to the synthesis reaction of ZnO resulted in hexagonal rod morphology. As the concentration of PVP was increased, the diameter of the rods increased and the length and aspect ratio was increased. PVP favored growth along the lateral direction while suppressing the growth along the longitudinal direction. Addition of PEG into the reaction mixture, on the other and, resulted in the production of thin and long, round-shaped highly dense ZnO nanowires. PEG addition decreased the diameter of the ZnO particles to 70 – 80 nm, and increased the length of the particles to around 5 μm. The aspect ratio of the particles was increased to 65 – 70.

Gao et al. [61] added two types of water soluble polymers in the synthesis reaction of ZnO particles from zinc chloride, HMT and ammonia. The two water soluble polymers, poly(acrylamide-co-acrylic acid) partial sodium salt (PAM-PAA) and polyacrylamide (PAM) were used as crystal growth modifiers. ZnO rods consisting of stacked cones were synthesized with the addition of PAM-PAA and irregular rod-like particles were obtained with the addition of PAM, when no ammonia was added into the reaction. Addition of ammonia in different concentrations also resulted in different irregular ZnO morphologies. The polymers were suggested to have two different roles in ZnO particles synthesis. Random adsorption of Zn^{2+} ions on the polymer surfaces were suggested to lead site-specific supersaturation in respect to the nucleation of ZnO. Morphological development was also suggested to be affected by interactions of ZnO species with polymers and their hydrolyzed products.

Akin and Öner [62] used zinc nitrate hexahydrate and HMT as reaction precursors and a water-soluble biopolymer carboxymethyl inulin (CMI) as crystal growth inhibitor for the synthesis of ZnO particles by chemical precipitation method. In the absence of CMI, rod-shaped ZnO particles were synthesized at a reaction temperature of 60 °C. Using the

same conditions, reaction temperature was increased to 75 and 95 °C. The length and the diameter of the rod-shaped particles obtained, increased with increasing temperature. The mean aspect ratio of the particles also increased from L/W = 2.9 to 9.1 for the reaction temperature of 95 °C. With the addition of CMI, crystal growth along the *c*-axis was suppressed. As the concentration of CMI was increased, the rods increased in width and decreased in length, decreasing the aspect ratio. When CMI concentration was increased to 150 ppm, the particle morphology changed from rods to hexagonal bipyramids. However, the particles showed bimodal distribution composing of bipyramids together with a small amount of spherical nanocrystal agglomerates. Further increase in CMI concentration to 450 ppm resulted in bimodal distribution composing of smaller nanoparticle agglomerates and bipyramids.

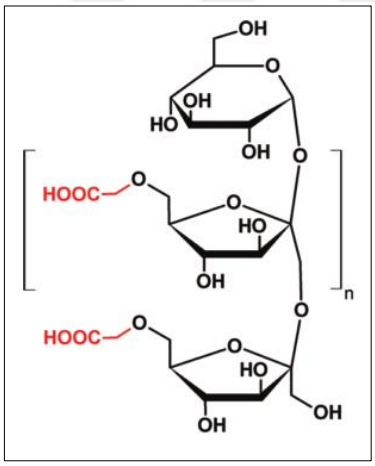

Figure 2.10 Chemical structure of CMI [63]

CMI is a non-toxic and biodegradable biopolymer produced by the carboxymethylation of inulin that is extracted from the roots of chicory plants (Figure 2.10). Inulin is a linear polydisperse polysaccharide of fructose, consisting of fructose molecules linked by *ß*-bonds. Typically, a glucose molecule resides at the end of fructose chain linked by an α-bond. The chain length of this molecule ranges from 2 to 60 units [63]. CMI was previously reported as a crystal growth modifier for the syntheses of calcium carbonate [64, 65], calcium oxalate [66], HAP [67, 68].

2.2.2 Surface modification of ZnO Particles

Fabrication of polymer nanocomposites by the addition or inorganic nanoparticles into organic polymer matrices provides improvements in many polymer properties. However, improvements mainly depend on the homogeneous dispersion of these small

size particles [69, 70]. Due to their high surface energy and their incompatibility with the organic matrix, nanoparticles tend to agglomerate when distributed into polymers. Therefore, it is difficult to achieve homogeneous particle dispersion within polymer matrices. Surface modification of inorganic particles is an effective method in achieving homogeneous particle dispersion and improvement of compatibility with the polymer matrix [69].

Organosilanes are functional molecules that can form stable chemical bonds both with inorganic particles and organic polymers [71]. Two types of reactive moieties are present in functional trialkoxysilanes ($R'Si(OR)_3$). Alkoxy groups (OR) can connect to the surfaces carrying hydroxyl groups and organic functionality (R'; amine, methacrylate, vinyl, phenyl etc.) can connect to organic matrices [72]. Silane coupling agents have a unique ability to bond inorganic particles and polymer matrices; thus, have a wide range of applications. Silanes are compatible with almost every organic polymer [73]. Silane modified particles were reported to behave differently and show better distribution in organic polymer matrices compared to untreated particles [74].

CHAPTER 3

EXPERIMENTAL

ZnO particles of various morphologies were synthesized by varying reaction parameters of wet chemical synthesis method. The ZnO crystals obtained in suitable morphologies for nanocomposites fabrication were incorporated into PHBV matrix by melt extrusion. Some of the ZnO particles were surface modified by a silane agent prior to melt extrusion. Surface-treated and untreated ZnO particles were incorporated into PHBV in varying concentrations. The structural, thermal, and mechanical properties of the fabricated PHBV/ZnO nanocomposites were investigated.

3.1 Synthesis of ZnO Particles

Wet chemical synthesis of ZnO particles in aqueous solution was carried out according to the method described by Akin and Öner [62]. Parameters of synthesis reaction were varied in order to obtain ZnO particles of different sizes and shapes.

The precursors used in the synthesis reaction of ZnO were zinc nitrate hexahydrate ($Zn(NO_3)_2{\cdot}6H_2O$) and HMT ($(CH_2)_6N_4$, hexamethylenetetramine). Utilization of zinc nitrate and HMT is very common in the wet synthesis of ZnO [48, 49, 52, 55, 75]. Zinc nitrate hexahydrate acts as a zinc salt that provides Zn^{2+} ions required for the formation of ZnO crystals [52]. Hydrolysis of a zinc salt, such as zinc nitrate hexahydrate, in a basic solution is known to result in crystallization of ZnO [52]. HMT is generally accepted to serve as a buffer, gradually increasing the pH of the reaction solution [49]. HMT first hydrolyzes in water to form formaldehyde and ammonia; and then further hydrolyzes to OH^- and NH_4^+ ions as follows [55]:

$$(CH_2)_6N_4 + 6\,H_2O \rightarrow 6\,CH_2O + 4\,NH_3 \quad (3.1)$$

$$NH_3 + H_2O \rightarrow NH_4^+ + OH^- \quad (3.2)$$

The OH^- ions then form a complex with Zn^{2+} ions [55] produced by zinc nitrate hexahydrate. Ammonia (NH_3) produced by HMT provides the basic environment required for the formation of ZnO [52]. As the pH increases gradually, and the solution is mildly basic; the degree of supersaturation is kept at a low level [Kawano and Imai; 2010]. When HMT is used as a precursor for ZnO synthesis reaction, the O^{2-} ions required to form ZnO are provided by H_2O in the reaction medium; unlike strong alkali-mediated methods where O^{2-} comes from the alkali [52]. Therefore, the synthesis reaction utilizing HMT requires to be carried out in an aqueous medium and cannot be carried out in organic solvents.

The concentrations of the precursors zinc nitrate and HMT were 0.03 M in the work of Akin and Öner [62]. Instead, the concentrations of the precursors were selected as 0.06 M in this work. The concentrations of zinc nitrate and HMT reported in the literature are typically below 0.1 M [60, 61]. Low concentrations of reactants are known to yield more uniform dispersions [76]. Equimolar concentrations of the precursors were used according to the stoichiometric ratios of the crystallization reaction. The properties and the used concentrations of the precursor species are given in Table 3.1. Solutions of precursors in water were prepared according to the required concentrations in 2 L volumetric flasks and mixed vigorously prior to use in synthesis reactions.

Synthesis reaction was carried out in a double-jacketed glass reactor connected to a circulating oil bath (PolyScience, USA) with 10 L capacity (Figure 3.1). The jacketed reactor is connected to the bath by 3/8” plastic tubing in which a synthetic thermal liquid (Haake Synth 260 bath liquid) circulates. The oil bath is set to desired temperature and by the circulation of the thermal liquid at the jacket of the reactor, the reaction temperature is kept constant at the desired value. Mixing of the reaction mixture is applied by magnetic stirring.

As the concentrations of the precursor species were doubled, the volume of the reactor was also doubled. A double-jacketed glass reactor of 2 L capacity was used. Some trials were also carried out in a 1 L capacity reactor. For the synthesis reaction of ZnO, the reactor was connected to the oil bath and was placed on a magnetic stirrer plate. Equal volumes of precursors were added into the reactor. A condenser was connected to the lid of the reactor in order to prevent evaporation of the reaction mixture. Circulating oil bath temperature was set to the desired value. Magnetic stirring was applied at 400 rpm throughout the synthesis reaction.

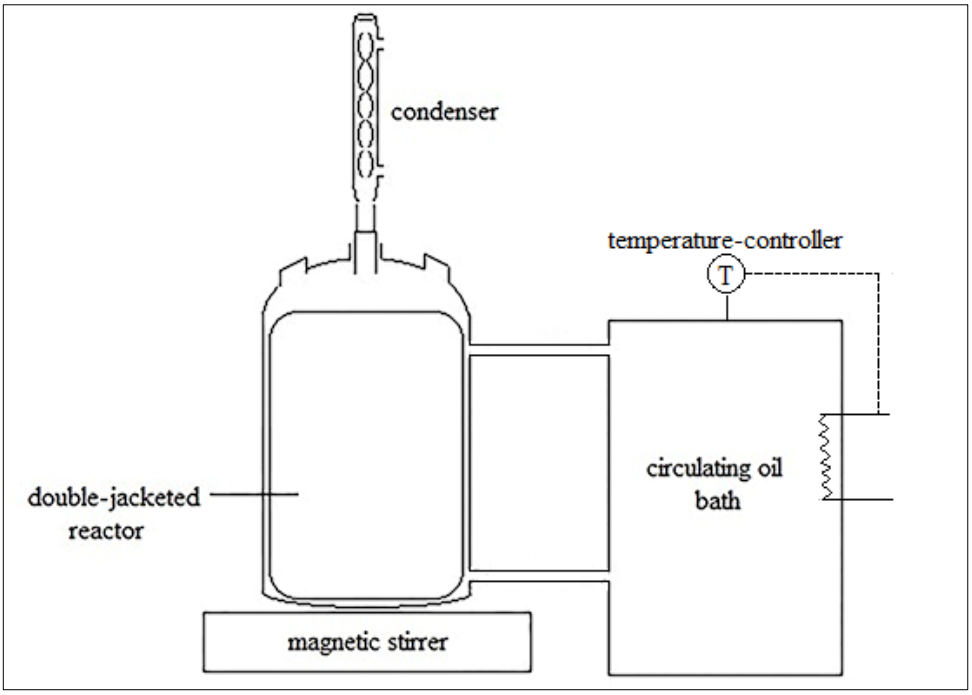

Figure 3.1 The batch reactor system used for the synthesis of ZnO particles

Other than precursors concentration, reaction temperature is an important parameter in the synthesis reaction of ZnO. Precursor concentration was reported to the affective on the crystal density and aspect ratio [75], while reaction temperature and time were reported to affect morphology and aspect ratio [52]. Aspect ratio of one-dimensional ZnO particles (ratio of crystal length to width, L/W) depends on the relative growth rates of polar and non-polar surfaces and the ratio is smaller at lower temperatures [77]. Akin and Öner studied the effect of reaction temperature on the formation of ZnO rods at three different reaction temperatures (60, 75, and 95 °C) and the highest aspect ratio was obtained at 95 °C [62]. Since aspect ratio of inorganic particles is an important parameter in polymer nanocomposites properties [4], reaction temperature was selected as 95 °C in this study. Considering the heat losses within the system, the circulating oil bath was set to 106 °C. The reaction was assumed to start as the circulator bath temperature reached at 95 °C. The reaction was carried out for 90 minutes.

As ZnO particles form throughout the reaction, they precipitated as white solids. At the end of the reaction time, the reactor was disconnected from the oil bath and was left to cool to room temperature. After the ZnO suspension was cooled, the ZnO particles were separated from the reaction solution by filtration method. A filtration apparatus and a membrane with 0.22 μm pore size was used for this purpose. The filtrate consisting of

ZnO particles was then washed with deionized water and dried in a vacuum oven (Binder VD53 Vacuum Drying Chamber) at 60 °C for 24 h.

Table 3.1 Properties and concentrations of precursor species for the synthesis reaction of ZnO

Precursor	**Formula**	**Purchased brand**	**Purity, %**	**Molecular weight, g/mol**	**Concentration used, M**
Zinc nitrate hexahyd-rate	$Zn(NO_3)_2{\cdot}6H_2O$	Sigma Aldrich (purum p.a., crystallized)	≥ 99	297.49	0.06
Hexamet-hylene tetramine (HMT)	$(CH_2)_6N_4$	Merck (for synthesis)	≥ 99	140.19	0.06

3.1.1 Addition of CMI as Growth Modifier

Polymers are known to affect nucleation, growth and aggregation processes during ZnO formation and they are utilized as modifiers for crystal growth [61]. The morphology of crystals synthesized by chemical precipitation method is known to be very sensitive to reaction parameters such as temperature, pH, reaction time, usage of seed crystals, and existence of impurities. Utilization of growth modifiers help to overcome these sensitivities by allowing chemical control on crystal morphology [57].

Modification of crystal growth occurs via face-specific growth kinetics. Since different crystal faces are chemically different, they have different growth rates and this determines the morphology of the crystal. Growth modifiers interact through face-specific reactions with the crystals as they grow, and therefore affect crystal morphology by altering the relative growth rates of crystal faces [57, 61 62, 67, 68].

Carboxymethyl inulin (CMI) is a polysaccharide-derived polycarboxylate, synthesized from inulin. Carboxylate groups are introduced to the polysaccharide by carboxymethylation [64]. CMI is a water-soluble polymer that is known to be nontoxic and naturally biodegradable [63]. CMI was used as a growth modifier for ZnO in the work of Akin and Öner and different concentrations of CMI were reported to change the

morphology of ZnO rods into hexagonal prismatic bipyramids and into smaller nanoparticles [62].

In this study, CMI was added into the synthesis reaction of ZnO in varying concentrations in order to investigate the effect on the morphology of ZnO particles. Precursor concentrations and reactor volume was doubled, compared to the work of Akin and Öner [62] and the effect of reaction parameters were investigated. For this purpose, required amount of CMI (Italmatch Chemicals, Dequest PB11625, Industrial grade) was weighed in a beaker. At the stage of addition of reaction precursors into the reactor, first HMT solution was added. Then, CMI was mixed with zinc nitrate hexahydrate solution and added into the reactor. The synthesis reaction of ZnO was carried out as it was described in the previous section. Varying concentrations of CMI used were 50, 450, 750, and 3000 ppm.

3.1.2 Ultrasound Assisted Synthesis

Utilization of ultrasound during synthesis of inorganic materials often create high energy physical effects, such as improvement of mass transport due to turbulent mixing and acoustic streaming, generation of high velocity interparticle collisions, and fragmentation of solids leading to increase in the surface area [78]. Ultrasound pretreatment prior to ZnO synthesis was previously reported in the literature [56, 79]. Liu and Zeng reported that pretreatment of hydrothermal reaction solution in an ultrasonic bath for 20 to 40 minutes resulted in a significant decrease in the diameters of ZnO particles and increased aspect ratio dramatically [56]. Wang et al. reported that ultrasonic pretreatment of the reaction solution for 35 min changed the morphology of tower-like ZnO arrays into tube-like ZnO nanostructures.

In this study, the effect of ultrasonic pretreatment on the morphology of ZnO particles synthesized by wet chemical method were investigated. For this purpose, 1 L of HMT solution and 1 L of zinc nitrate hexahydrate solution were added into a 2 L beaker and mixed vigorously. Then the mixed reaction solution was divided into two 1 L beakers and placed into an ultrasonic bath. The ultrasonic bath (Isolab Laborgerate GmbH, Germany) had 10 L capacity and applied an ultrasonic power of 240 W at a frequency of 40 kHz. Ultrasonic mixing was applied to the reaction solution for 40 min. By the end of this time, the temperature of the solution was increased to 40 °C and the formation of particles could be observed as white colloids. After ultrasonic

pretreatment, the reaction solution was taken to the double-jacketed reactor and the reaction was carried out with the same procedure described in previous sections.

Table 3.2 Different ZnO particles synthesized and their synthesis parameters

Sample code	**CMI concentration, ppm**	**Reactor volume, L**	**Reaction temperature, °C**	**Ultrasound application, min**
ZnO-2L-95C	-	2	95	-
ZnO-1L-95C	-	1	95	-
ZnO-1L-75C	-	1	75	-
ZnO-50-2L-95C	50	2	95	-
ZnO-450-2L-95C	450	2	95	-
ZnO-750-2L-95C	750	2	95	-
ZnO-2L-95C-UB40	-	2	95	40

In summary, ZnO particles were synthesized by wet chemical synthesis using zinc nitrate hexahydrate and HMT as precursors. ZnO particles were synthesized without any additives at two different reactor volumes and two different reaction temperatures. Also, addition of CMI as growth modifier at different concentrations was studied. Other than these particles, ZnO particles were synthesized applying ultrasound pretreatment, without addition of any additives. ZnO particles synthesized in this study and their synthesis parameters are given in Table 3.2. The concentrations of the precursors zinc nitrate hexahydrate and HMT were 0.06 M for all ZnO particles synthesized.

3.2 Surface Modification of Synthesized ZnO Particles

Improvement of properties of polymer nanocomposites, especially mechanical properties [80], depend on the homogeneous distribution of the inorganic particles within the polymer matrix [81]. Surface treatment of inorganic particles is known to an effective method to achieve good interfacial compatibility between the particles and the polymer matrix, and achieve homogeneous distribution of the particles [70].

Organosilanes are hydrolysable in presence of water and the resulting silanols can form hydrogen and covalent bonds with hydroxyl groups of inorganic particles [82]. Homogenizing agents such as alcohols and acetone are known to facilitate hydrolysis

[83]. Ethanol was also reported to increase the hydroxyl surface of ZnO [84]. Accordingly, the surface modification reaction of ZnO particles in this study was carried out in an ethanol-water solution.

The reactive silanol group that forms stable bonds with oxides can also undergo homocondensation reactions that creates homocondensates [84]. If the rate of the homocondensation reaction is faster than the reactions between silanols and the particles, the silane used may not be available for interaction with the particle surface [71]. Working under anhydrous conditions or at acidic pH values [84] suppress homocondensation reactions to negligible levels [71]. Hence, the water content of the ethanol-water solution used in this study was kept low and the pH of the solution was set to an acidic value.

There are various types of silanes according to their reactive functionalities such as amino, vinyl, styrenic, epoxy, acryloxy, and mercapto [80]. Selection of the appropriate type of silane for a given system is extremely difficult and is affected by many factors such as surface energy, absorption, adsorption, acid-base interaction, network formation with polymer and covalent reaction [85]. Selection of the silane type can be based on empirical evaluation and mainly the compatibility of the polymer with the silane should be taken into consideration [85].

3-methacryloxypropyltrimethoxysilane (MPS) is a type of silane that contains three methoxy groups and previously was reported to an effective surface modifier for ZnO particles [69, 84]. Octyltriethoxysilane (OTES) is an 8-carbon atom chain silane which can interact with PHBV matrix through Van der Waals forces, and it was previously reported to improve the mechanical performance of PHBV [28]. Therefore, MPS and OTES were utilized for the surface modification of the ZnO particles in this study, prior to incorporation into PHBV matrix. OTES is a kind of silane that is known to undergo hydrolysis very slowly and therefore the time required for the hydrolysis reaction is considerably long (around 18 h) [72]. Complete hydrolysis of MPS takes around 6 h [72].

For the surface modification of the ZnO particles with MPS or OTES, an ethanol-water (9:1, v/v) solution of 100 mL was prepared in a beaker. Ethanol was purchased from Merck, USA (absolute for analysis). pH of the solution was 7.4 as prepared and was adjusted to an acidic value using acetic acid. Acetic acid used was purchased from

Merck, USA (absolute for analysis). The pH value of the solution was adjusted to the value of 4.9 – 5.0 using Mettler Toledo (USA) S220 pH meter.

The solution of ethanol and water with adjusted pH was then taken on a magnetic stirrer plate and rigorous mixing was applied at 1000 rpm. Meanwhile, required amount of silane was taken by a syringe and added into the stirred solution dropwise. Required silane amount for minimum monolayer coverage can be calculated as follows, by taking surface coverage of the silane and the surface area of the particles into consideration [86]:

$$Required\ amount\ of\ silane = \frac{(amount\ of\ filler)*(surface\ area\ of\ filler)}{wetting\ surface} \quad (3.3)$$

The minimum surface coverage area of MPS is given as 314 m^2/g and for OTES it is given as 282 m^2/g [87]. The properties of the MPS and OTES used are given in Table 3.3.

Table 3.3 Properties of the silanes utilized in surface modification of ZnO particles

Property	**MPS**	**OTES**
Chemical name	3-(Trimethoxysilyl)propyl methacrylate	Triethoxy(octyl)silane
Synonym	3-methacryloxypropyltrimethoxy silane	Octyltriethoxysilane
Chemical formula	$CH_2=C(CH_3)CO_2(CH_2)_3Si(OCH_3)_3$	$(C_2H_5O)_3Si(CH_2)_7CH_3$
Brand, catalog no. and purity	Sigma Aldrich, 440159, 98%	Sigma Aldrich, 440213, ≥97.5 %
Molecular weight	248.35 g/mol	276.49 g/mol
Boiling point	190 °C	84 – 85 °C
Density	1.045 g/mL at 25 °C	0.88 g/mL at 25 °C
Minimum covering area	314 m^2/g [87]	282 m^2/g [87]

It was previously reported that, if the amount of silane to be used was appropriate for monolayer or moderate layer coverage of inorganic particles, the results of surface modification was satisfactory [84]. However, if higher amounts of silane was used, formation of homocondensates was observed [71]. The amount of silane required for the

surface modification of ZnO particles used in this study was calculated from the surface coverage capacity of MPS and OTES and the surface area of the ZnO particles. The surface area of the ZnO particles synthesized was measured by BET (Brunauer, Emmett, Teller) analysis, described in the following section. An excess of the silane compared to the calculated value of monolayer coverage was used, however, excessive usage of silane was avoided.

After the addition of required amount of silane into the pH-adjusted ethanol-water solution, the silane solution was left for 1h for the hydrolysis reaction of silane. Magnetic stirring was applied at 400 rpm during the hydrolysis reaction. In the meantime, ZnO particles were also added into an ethanol-water solution (9:1, v/v) in a beaker and the beaker was placed inside an ultrasonic bath (Isolab Laborgerate GmbH, Germany) and kept for 30 min for the purpose of particle dispersion. At the end of the hydrolysis time for silane, the ZnO solution was added into the silane solution for the reaction of ZnO particles with silane molecules. In case of surface modification with MPS, the reaction mixture was kept in a shaker bath at 70 °C for 2 h. For surface modification with OTES, the reaction mixture was kept on a hot plate at 75 °C for 20 h and magnetic stirring at 750 was applied. At the end of the reaction time, the modified ZnO particles were removed from the mixture by centrifugation at 4200 rpm for 20 min (Sigma 3-16P, Sigma Centrifuges, UK). The separated particles were washed with ethanol two times, in order to remove any remaining silanes that were not bonded on the particles. Particles were again separated by centrifugation. Then the ZnO particles were dried in a vacuum oven (Binder VD53 Vacuum Drying Chamber, Binder, Germany) at 60 °C for 24 h for curing.

3.3 Ultrasonic Dispersion of ZnO Particles

Nano and sub-micron inorganic particles are known to form agglomerates due to their high surface energies [88]. Agglomeration occurs during synthesis as well as following processing steps and strongly bonded compact agglomerates can be formed even in microscale sizes [89]. In order to achieve successful dispersion of inorganic particles, the particle agglomerates should be fragmented into primary particles while avoiding re-agglomeration [89]. Utilization of ultrasound is one of the two main methods for achieving particle dispersion, the other being surface modification [70]. Ultrasonic dispersion is an effective method for the dispersion of particles in a liquid medium [90].

Ultrasound can be applied either in an ultrasonic bath indirectly, or directly by using an ultrasonic horn submerged in the liquid. The use of an ultrasonic horn was reported to be much more effective than an ultrasonic bath [89]. In this study, an ultrasonic horn was used for the dispersion of synthesized ZnO particles in a liquid medium.

The synthesized ZnO particles were added into an ethanol-water (9:1, v/v) solution and the pH of the solution was adjusted to 5.0 by the addition of acetic acid. The conditions used were the same as the silanization conditions mentioned in the previous section, since ultrasonic dispersion procedure was combined with silanization procedure. Ultrasonic dispersion of the particles in ethanol-water solution was performed using Sonics & Materials, Inc. (USA) Vibra Cell ultrasonic processor supplying ultrasound energy at 20 kHz frequency with a maximum power input of 750 W. An ultrasonic probe of 13 mm-diameter was used and ultrasound was applied at 40 % amplitude. Ultrasonication time was varied as 15 and 60 min. After the completion of ultrasonication time, the particles were removed from the liquid solution by filtration and drying. A filtration apparatus and a membrane with 0.22 μm pore size was used for the filtration of particles and the drying process was carried out in a vacuum oven (Binder VD53 Vacuum Drying Chamber) at 60 °C for 24 h.

3.4 Characterization of ZnO Particles

The specific surface area, crystalline structure and lattice parameters, morphology and molecular environment of the synthesized ZnO particles were investigated by various analyses as described in the following sections.

3.4.1 Measurement of the Surface Area by BET Method

Surface area of the synthesized particles were measured by BET analysis based on the BET theory. BET theory was developed by S. Brunauer, P. Emmett, and E. Teller as an extension of the Langmuir theory and the name of the method comes from the initials of the developers [91, 92].

In Langmuir theory, monolayer adsorption of gas molecules onto a solid surface is related to the gas pressure of the medium at a constant temperature. The Langmuir theory is extended to multilayer adsorption by the BET theory, assuming that gas molecules physically adsorb on solids in infinite layers, these adsorption layer do not interact, and that the theory can be applied to each layer [91]. The volume of a gas

required to form a unimolecular layer on the solid is estimated by BET theory and from the information of surface occupied by one molecule, the specific surface area of the solid is predicted [93]. BET equations express the relation between the total volume of the gas adsorbed on the solid and the relative vapor pressure, which is an adsorption isotherm [93].

In BET surface area analysis, nitrogen gas is usually utilized due to its strong interaction with most solids and its availability. A known amount of nitrogen gas is sent to the sample chamber. Adsorption of nitrogen gas occurs until the saturation pressure and the adsorption layers are formed. Then the solid is removed and heated for the release of nitrogen gas adsorbed. The released nitrogen gas is quantified and the BET isotherm is obtained for the material, which is a plot of the volume of the gas adsorbed as a function of relative pressure. The solid sample must be degassed under vacuum at high temperatures prior to the BET analysis in order to remove any water or other contaminants on the solid surface [91].

In the multiple-point BET method, a minimum of three data points (ideally five data points), in the relative pressure range of 0.025 to 0.30 is used to determine the surface area of the solid. When relative pressure value is greater than 0.5, it corresponds to the capillary condensation section of the BET isotherm. When the relative pressure value is very small, then is corresponds to only monolayer formation. Therefore, relative pressure values in the mentioned interval are used. When these values are plotted, a linear graph with a positive slope should be obtained. The information obtained from this graph is then used for the calculation of the surface area of particles [91].

The specific surface area of the synthesized ZnO particles were measured by nitrogen sorption isotherms according to multiple point BET method using Quantachrome Quadrasorb SI (Quantachrome Instruments, USA) Gas Sorption Analyzer. Outgassing was applied to the ZnO particles prior to the analysis at 300 °C for 16 h in order to remove water and other contaminants.

3.4.2 X-Ray Diffraction Analysis of ZnO Particles

X-ray diffraction (XRD) is an analytical method that is used to obtain information about the structures of crystalline materials and unit cell dimensions [94]. X-rays have wavelength in the A° (10^{-10} m) range and they can be scattered by the electrons of a comparable sized atom [95]. X-rays can penetrate into materials and hence provide

information about the structural arrangement of atoms and molecules [96]. XRD analysis is applied by generating X-rays in a cathode ray tube and directing these rays towards the sample [94, 96].

Crystalline materials have well-defined smooth faces and the angles between these faces are fixed. A crystal consists of infinite number of identical unit cells that are stacked together in a three-dimensional lattice (Figure 3.2). The atoms shown by small spheres in the figure, form different sets of planes referred as lattice planes and the interplanar spacing between these planes are shown with d [96, 97]. When X-rays are directed to the sample, they strike the planes at an angle θ and assumed to be reflected with the same angle. The interaction between the rays and the sample produces a diffraction peak only when the conditions of Bragg's law are satisfied [94, 96, 97]. Bragg's law is given by the equation:

$$2.d.sin\theta = n.\lambda \tag{3.4}$$

where λ is the wavelength of the X-ray and n is an integer that shows the order of the diffraction peak (which is equal to 1 for a single crystal [97]). Bragg's law shows the relation between the wavelength of the X-ray radiation, diffraction angle and the lattice spacing of the crystal sample [94].

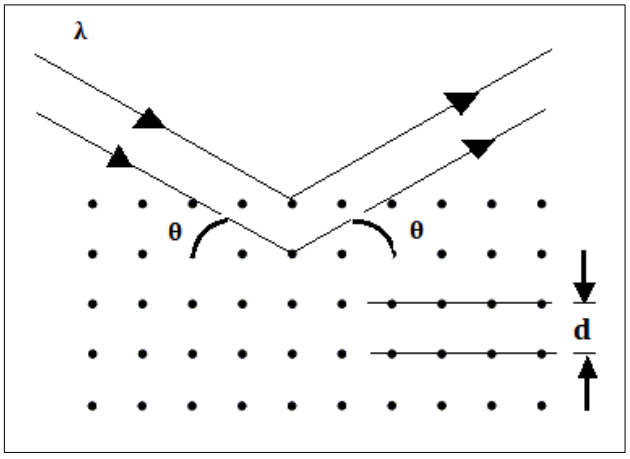

Figure 3.2 Diffraction of X-rays from the sample in XRD analysis [97]

All possible diffraction directions of a sample lattice are scanned through a range of 2θ angles during XRD analysis. Therefore, θ is a variable obtained by rotating the crystal relative to the X-ray beam. [97]. The wavelength λ has a fixed value and depends on the target material. Copper is the most common target material and has a CuK_{α} radiation wavelength of 1.5418 A° [94, 97]. The lattice spacing d is also a constant value

determined by the size of the unit cell. The diffraction peaks obtained during analysis are converted to d-spacings. The intensity of a reflected beam is directly proportional to the electron density of a plane [94]. Since all crystalline materials have characteristic reflection intensities and d-spacings, these values can be used in the identification of materials [97]. For the qualitative analysis of the sample, d-spacings and relative intensities of the 10 strongest lines are compared with the patterns of known compounds [97]. The 2θ positions of the diffraction peaks are measured as the center of the peak at 80% height. The results of XRD analysis are commonly represented as a plot of 2θ against X-ray counts (intensity, I). Intensity can be given as peak height intensity or as relative intensity which is the ratio of the peak intensity to that of the most intense peak [94].

XRD analysis can also be used in determination of particle size since the angular spread of the reflection from a crystal plane is affected by crystal size. The angular spread of reflection from a sample increases when the average size of crystallites decreases. The half-height width of a peak (full width at half maximum, FWHM) in the diffractogram can be used as a measure of the mean particle size [97], since the diffracted beam is broadened when crystallite size is smaller [98]. The relation between the peak width (B) and the crystallite size (B) is given by Scherrer equation as:

$$B = \frac{K.\lambda}{L.cos\theta} \tag{3.5}$$

where K is a numerical constant taken as 0.93 [98]. The peak width B is equal to FWHM and its units are radians.

The crystalline phase of the synthesized ZnO particles in this study was identified by XRD analysis using PANalytical X'Pert Pro PW 3040/60 (PANalytical, The Netherlands) powder diffractometer with CuK_{α} radiation. The radiation source was operated at 45 kV and 40 mA. The 2θ range was from 5 to 90° at a scan rate of 0.026°/step.

3.4.3 Scanning Electron Microscopy of ZnO Particles

Scanning Electron Microscopy (SEM) is a method based on focusing a beam of high-energy electrons on the surface of solid specimens and generating a variety of signals [99]. The generated signals from electron-sample interactions are used to obtain information related to exterior morphology, chemical composition, crystalline structure

and orientation of materials [99, 100]. By the application of SEM over a selected area of the sample surface, a two-dimensional image is generated where information on the mentioned properties of the samples can be obtained [99]. Thermionic emitters, that use electrical current to heat up a filament, and field emitters, that draw electrons from field emission gun by placing the filament at a large electrical potential gradient, are the two main electron emission sources utilized in SEM [100]. When a field emission gun is utilized, the instrument is referred to as FESEM.

The resolution of a SEM image obtained is defined as the ability to resolve different points very close to each other as separate entities. The resolution of a SEM is determined by the accelerating voltage and initial crossover diameter [100].

If the specimen to be analyzed is not conductive, surface coating of the specimen is necessary. Metallic coatings such as aluminum, gold, and platinum are commonly used for specimen coating and the preferred method to coat the specimens is sputter coating [100].

In this study, SEM analysis was applied in order to examine the external morphologies of the ZnO particles synthesized. SEM analysis was performed using Zeiss Evo LS 10 (Zeiss, Germany) SEM at an acceleration voltage of 10 kV. Samples were coated with a thin layer of gold prior to examination.

Size distribution of the ZnO particles synthesized were calculated by inspection of SEM images obtained. The dimensions of the particles from at least three different SEM figures were measured manually utilizing Visio (Microsoft, USA) software and mean dimensions and size distribution curves were obtained using OriginPro (OriginLab, USA) software. Only the particles which both ends are visible and are aligned parallel to the plane of the screen were measured. In order to obtain a reliable size distribution, particles as many as possible, preferably a minimum of 100 unaggregated particles were measured. A Gaussian distribution function was fitted to each distribution curve using OriginPro software. Particle size distributions were also analyzed by a laser particle sizer Analysette 22 (Fritsch, Germany).

3.4.4 Fourier Transform Infrared Spectroscopy of ZnO Particles

Infrared (IR) spectroscopy is an analytical method utilized to monitor the vibrations of functional groups in the molecular structures and it is based on IR radiation passed

through a sample [101, 102]. Electro-magnetic radiation in the region from 0.7 μm to 1000 μm is referred as IR radiation [101]. For IR spectroscopy, the mid-IR region between 2.5 μm to 25 μm (wavenumbers of 400 cm^{-1} to 4000 cm^{-1}) is the common region utilized [101, 103]. The energies of IR photons are similar to the vibration energies of molecular bonds [103]. Mid-IR region includes all the frequencies that are related to the vibrations of all functional groups of organic molecules [101]. An IR photon with a frequency equal to the vibrational frequency of a molecular bond can be absorbed by the bond and this phenomenon is the basis for IR spectroscopy [103].

IR radiation passed through a sample is partially absorbed and partially transmitted by the sample. The resulting IR spectrum represents molecular absorption and transmission; and the peaks correspond to the vibration frequencies between the bonds of the atoms in the sample [102]. The IR spectrum obtained is unique for each material, since different materials are different combinations of atoms. Therefore, IR spectroscopy can be used for qualitative identification of the samples. Typical spectral peaks are narrow and distinct, allowing identification of a band corresponding to a specific structure [101]. Furthermore, the size of the peaks provides direct information about the amount of the present materials [102]. Peak intensity can be measured as percent transmittance or in absorbance units [103].

The resulting signal of an IR spectrometer is called an interferogram and since it cannot be interpreted directly, it is transformed into frequencies. This operation is performed by a mathematical function called Fourier Transform and it allows the analysis of the entire IR spectrum. Then the frequency spectrum, which is a plot of individual frequencies versus their intensities, is obtained and the method is referred to as Fourier Transform Infrared (FTIR) spectroscopy. FTIR is the preferred method of IR spectroscopy [102, 103].

The chemical bonds within a molecule can undergo different types of motion and stretching and bending motions of the bonds can absorb IR radiation. Stretching type motions are symmetric and asymmetric stretching, whereas bending type motions are scissoring, twisting, rocking, and wagging [103]. When the electric component of the IR radiation interacts with a polar bond and creates a change in the dipole moment of the bond as a result of vibration, a molecule can absorb IR radiation. Alternative stretching and compressing of the polar bond occurs due to the oscillating electric field of the radiation and the bond vibrates. When the natural vibration of the bond is equal to the

vibration resulting from oscillating electric field, the bond can absorb the energy [103]. IR bands are obtained only when molecular vibrations cause a change in the dipole moment of the molecule. For this reason, nonpolar O_2 and N_2 in the atmosphere do not show any IR bands, whereas polar CO_2 produces a band at 2300 cm^{-1} due to the movement of O atoms [104].

FTIR spectra is represented with wavenumber (cm^{-1}) for convenience, instead of wavelength of the electromagnetic radiation. The region of the FTIR spectrum between 4000 – 1500 cm^{-1} is the functional group region that can be used to identify is a specific functional group is present in the sample. The region between 1500 – 400 cm^{-1} is the fingerprint region and the peaks in this region are produced as a result of complex deformations of the molecules [104]. The fingerprint region allows differentiation between the spectra of different molecules, since the bands in the functional group region can be contained by different molecules [103].

Molecular environment of the ZnO particles synthesized in this study were investigated by (FTIR) spectroscopy using Bruker Alpha-P FTIR Spectrometer (Bruker, USA). The spectra were obtained by average signaling 20 scans at a resolution of 4 cm^{-1} in the wave number range of 4000 – 400 cm^{-1}.

3.5 Incorporation of ZnO Particles into PHBV Matrix

There are several methods for the incorporation of inorganic particles into polymer matrices such as *in situ* polymerization, solution intercalation, melt blending, and melt extrusion. Melt extrusion method involves the usage of an equipment called extruder and the particles are mixed into the polymer by heating the mixture above the melting point of the polymer under shear. Melt extrusion method is environmentally benign since it does not utilize organic solvents and is also compatible with current industrial applications.

For the incorporation of ZnO particles into PHBV matrix, Twin Screw Extruder Microlab (Rondol, France) with a screw diameter of 10 mm was utilized. The extruder is equipped with two identical screws with a length to diameter ratio of 20, which create the shear and achieves the blending of particles into polymer matrix. There are five temperature zones throughout the twin screws, that can be set to desired temperature values. The middle temperature zone is set to a temperature higher than the melting temperatures of the polymer and mixing of the particles occurs in this zone with the

help of mixing paddles on the screws. When setting the temperatures of the zones, the effect of high shear is taken into consideration, as well as the melting temperature of the polymer.

Table 3.4 Physical properties of PHBV purchased from AdMajoris Company (Maj'Eco FN000HA Grade for Injection Molding)

Property, (analysis and conditions)	**Value**
Density (ISO 1183)	1.25 g/cm^3
Melt flow rate (ISO 1133, 190 °C/2.16 kg)	15 – 30 g/10min
Optical property	Opaque
Melting temperature (ISO 3146)	150 °C
Glass transition temperature	5 °C
Degradation temperature	200 °C
Tensile stress at break (ISO 527, 50 mm/min)	35 MPa
Tensile modulus (ISO 527, 1 mm/min)	2950 MPa
Tensile strain at break (ISO 527, 50 mm/min)	2 %
Charpy impact, un-notched (ISO 179)	4.8 kJ/m^2
Heat deflection temperature (ISO 75-2, 1.8 MPa)	72.5 °C

For the incorporation of the ZnO particles into PHBV matrix, temperature profile was applied as 90 – 135 – 160 – 160 – 150 °C from feed to die and the screw speed was 80 rpm. The ZnO particles and the PHBV to be extruded were dried at 60 °C for 18 h, prior to extrusion. PHBV with a valerate content of 8 mol% was supplied from AdMajoris Company (France) with the trade name of Maj'Eco FN000HA. Physical properties of the PHBV used are given in Table 3.4. At the end of the extrusion, PHBV/ZnO nanocomposites were obtained from the die of the twin-screw extruder. Then these nanocomposites were cut into pellets using the pelletizer accessory of the extruder and PHBV/ZnO nanocomposite pellets were obtained. The pellets were dried in a vacuum oven (Binder VD53 Vacuum Drying Chamber) at 60 °C for 18 h.

For the production of specimens required for SEM, XRD, FTIR, and mechanical analyses, the PHBV/ZnO pellets were compression molded into nanocomposite sheets

of about 0.8 mm thickness, using a mechanical press (Gulnar Makine, Turkey). The mechanical press was a double-stage press consisting of hot and cold cycles. The press operated at a maximum pressure of 120 bar with a total power of 11 kW.

The mass of the required pellets was 15 g for mechanical analysis. Required amounts of pellets were weighed and placed in between to stainless steel plates of 1 mm thickness. A circular shaped mold of 0.5 mm thickness was placed in between the stainless-steel plates and the pellets were placed in this mold neatly. The plates were then placed in the hot cycle section of the mechanical press and 3 consecutive pressures were applied at 155 °C as described in Table 3.5. After the completion of hot cycle, the plates are removed and placed into the cold cycle section of the press. The pressure and pressing time applied in the cold cycle are also given in Table 3.5.

Table 3.5 Condition applied during mechanical pressing of PHBV/ZnO nanocomposite pellets

Pressing cycle		**Applied Pressure, bar**	**Applied Time, s**
Hot cycle (155 °C)	Degassing	40	60
	Melting	60	30
	Melting and molding	80	90
Cold cycle (25 °C)	Cooling and molding	120	60

The thicknesses of the fabricated PHBV/ZnO nanocomposite sheets were measured with a digital micrometer (Mitutoyo, Digimatic Micrometer 293 MDC-MX Lite, Japan). At least five measurements from random sections of the films were taken and the average values were reported.

3.6 Characterization of PHBV/ZnO Nanocomposites

The structural, thermal, and mechanical properties of the fabricated PHBV/ZnO composites were evaluated. Properties of neat PHBV pellets and sheets fabricated using the same conditions as the composites were also measured and any possible enhancements in PHBV properties were investigated.

3.6.1 Structural Characterization of PHBV/ZnO Nanocomposites

Structural characterization of the fabricated PHBV/ZnO nanocomposites was performed by SEM, XRD, and FTIR analyses.

Uniform distribution of particles within a polymer nanocomposite is the primary challenge in enhancement of polymer nanocomposite properties [105]. Morphological evaluation of the fabricated nanocomposites by SEM analysis provides a qualitative characterization of nanoparticle distribution. Two-dimensional image of the nanocomposite sample is obtained by the SEM technique that represents the filler and polymer matrix phases in the real nanocomposite [106].

SEM images are obtained by focusing a beam of high-energy electrons on the nanocomposite sample surface and when a field emission gun is used as the electron source, the SEM equipment is referred to as FESEM, as described in section 3.4.3. The morphology of the PHBV/ZnO nanocomposite sheets was investigated by a Philips XL30 ESEM-FEG microscope at an accelerating voltage of 5 kV. The nanocomposite sheets were immersed in liquid nitrogen and cryo-fractured; then, sputtered with a gold-palladium mixture under vacuum prior to examination.

The nanocomposite structure, crystallinity and crystal parameters of the PHBV/ZnO sheets were evaluated by XRD analysis using PANalytical X'Pert Pro PW diffractometer with Cu Kα radiation (λ = 0.154 nm). The radiation source was operated at 45 kV and 40 mA. The samples were examined over the angular range of 2° to 40°.

Chemical structure of the PHBV/ZnO nanocomposite sheets were investigated by FTIR spectroscopy using Bruker Alpha-P FTIR Spectrometer (Bruker, USA). The spectra were obtained by average signaling 20 scans at a resolution of 4 cm^{-1} in the wave number range of 4000 – 400 cm^{-1}.

3.6.2 Thermal Characterization of PHBV/ZnO Nanocomposites

Thermal characterization of the PHBV/ZnO nanocomposites can be divided into two categories as characterization of thermal stability and characterization of melting and crystallinity properties. Thermal stability of PHBV and its nanocomposites was evaluated by TGA (Thermogravimetry Analysis). Melting and crystallization behavior was investigated by DSC (Differential Scanning Calorimetry).

3.6.2.1 Thermal Stability of the PHBV/ZnO Nanocomposites

Thermogravimetric analysis (TGA) was used to evaluate the thermal stability of the PHBV polymer and to analyze the effect of introduction of ZnO nanoparticles into PHBV matrix on the thermal stability. TGA is a method which monitors the change in the mass of a sample as a function of temperature or time [107, 108]. The sample can be heated at a constant rate up to a determined temperature and the method is called dynamic measurement. Alternatively, the sample can be kept at a constant temperature and the method is called isothermal measurement [107]. The micro-thermobalance within the instrument measures the changes in the sample mass. The changes in the sample mass can be due to adsorption or desorption of volatiles, thermal degradation, oxidation, reduction, or other chemical reactions [108]. TG analysis can be carried out under a reactive, oxidizing, or an inert atmosphere [107].

The results obtained from TG analysis are represented as percent mass against temperature or time. An alternative presentation of the data is by taking the first derivative of the TGA curve obtained and presenting with respect to temperature or time. In this case, the curve obtained is called as DTG (differential thermogravimetry) curve. DTG curve shows the rate of the mass change. The change in the sample mass during the analysis produces steps in the TGA curve and peaks in the DTG curve [107].

Thermal stability of the PHBV and PHBV/ZnO nanocomposite pellets were analyzed by thermogravimetry analysis (TGA) using SII Nanotechnology TG/DTA 6300 (Hitachi Corporation, Japan) thermal analysis instrument. Dynamic measurement was applied with a constant heating rate of 10 °C/min. The analysis was carried out under inert atmosphere, using nitrogen gas as purge gas. The samples of 10 mg mass were heated from 25 °C to 560 °C. Decomposition peak temperatures (T_{max}) of the samples were determined from the DTG curves as the temperatures corresponding to the highest rate of weight loss. The characteristic degradation temperatures $T_{x\%}$ were determined as the temperatures at which the sample weight equals to the (100-x) % of the sample.

3.6.2.2 Melting and Crystallization Behavior of the PHBV/ZnO Nanocomposites

Thermal transitions of a polymer are the changes that take place with heat and they are important in terms of defining the temperature limits of industrial applications. Melting, crystallization, and glass transition are the examples of thermal transitions of a polymer. Melting of a polymer is a first order thermal transition that occurs only in the crystalline

region of a polymer, and it is the falling apart of the polymer crystals from their ordered arrangements and starting to move freely [109, 110]. Glass transition is a second order thermal transition which is the reversible transition of the amorphous sections of the polymer from a hard and brittle state into a rubber like molten state [109, 110]. Crystallization of a polymer is giving off energy to move into ordered crystal arrangements [110].

Differential Scanning Calorimetry (DSC) is an analysis technique that can be used for studying the thermal transitions of a polymer. Measurement of thermal properties of a material in order to establish the relation between specific properties of the material and temperature is referred to as calorimetry [111]. DSC is a calorimetry technique that heats the sample with a linear temperature profile and measures heat relative to a reference [110]. A DSC device consists of a sample pan and an identical reference pan, both connected to a heater. Both pans are heated at a specific heating rate. Since the sample pan includes the polymer sample, it requires extra heat in order to be kept at the same heating rate with the reference pan. At the end of the analysis, a plot of this extra heat against temperature is obtained [109, 111]. Only a few mg of sample is sufficient for the analysis and the method is used for quantitative analysis [110].

In case of a thermal transition, the amount of heat required to keep the heating rate constant would increase or decrease, depending on the transition being endothermic or exothermic. Crystallization of a polymer is an exothermic transition and therefore it produces an exothermic peak on the DSC plot. Melting is endothermic and produces an endothermic peak. Glass transition results in a sudden shift of the plot in the endothermic direction [110]. Crystallization temperature (T_c) and melting temperature (T_m) of the polymer are determined as the highest point of the peaks produced on the graph. Glass transition temperature (T_g) is determined as the middle point of the observed shift on the graph. The latent heats of melting (ΔH_m) and crystallization (ΔH_c) are calculated from the areas under the peaks [110].

PHBV is composed of amorphous and crystalline regions, like many other polymers [109] and has relatively high crystallinity [112]. The crystalline sections of polymer increase its strength but also makes it brittle, whereas amorphous sections increase the toughness of the polymer [109]. Therefore, crystallinity of a polymer is important in terms of mechanical properties and processability. Degree of crystallinity can be calculated from the ΔH_c value obtained from DSC analysis, using following equation:

$$X_c, \% = \frac{\Delta H_m}{\Delta H^0 * w} * 100 \quad (3.6)$$

where ΔH^0 is the melting enthalpy of 100 % crystalline PHBV and w is the weight fraction of PHBV in the blend. The value of ΔH^0 was taken as 146.6 J/g due to the low valerate content of PHBV [42, 113].

Melting and crystallization behavior of PHBV and its composites were evaluated by DSC analysis using TA Insturments (USA) Q20 DSC under nitrogen atmosphere. Samples of 10 mg mass were heated from -2 °C to 190 °C (1st heating run) at a rate of 10 °C/min and kept at this temperature for 2 min to erase thermal history. Then the samples were cooled from 190 °C to 0 °C at a cooling rate of 10 °C/min (cooling run) and kept at this temperature for 2 min. Finally, the samples were heated from 0 °C to 190 °C again for the 2nd heating run, at a heating rate of 10 °C/min. T_m, T_g, and ΔH_m values were calculated from the heating curves and T_c and ΔH_c values were calculated from the cooling curves.

3.6.3 Mechanical Properties of PHBV/ZnO Nanocomposites

Mechanical properties are important in terms of processability of a material and selection of materials for various engineering applications. The strength of a material is often the primary concern and it is the maximum stress that the material can withstand [114]. Another mechanical property of concern is ductility, which shows how much the material can be deformed before it fractures [114]. The method that provides information about the strength and ductility or the mechanical behavior of a material is called the tensile test [115]. The most common machines used for tensile testing are universal testing machines [114].

For uniaxial tensile testing of a material, the sample is placed in between two grips that clamp the material and tension is applied to the material. The change in the length of sample under the tensile force is recorded. The test is carried out until the sample stretches and finally breaks [115]. The specimens measured by tensile testing are flat bars composed of enlarged ends for gripping and a narrower gage section (Figure 3.3). The gage length of the specimen is the region where the measurements are made and is at the center of the reduced section [114].

During the tensile testing of a material, tensile force applied is recorded as a function of increase in the gage length [114]. The tensile force applied to the material must be

divided to the cross-sectional area of the specimen, since the force required to stretch the material depends on the dimensions of the material [115]. Displacement of the material is also divided by the initial length of the material. A plot of stress (force divided by area) versus strain (displacement divided by initial length) is obtained [115]. Stress (σ) is defined as:

$$\sigma = F/A_0 \tag{3.7}$$

where F is the tensile force and A_0 is the cross-sectional area of the gage section [114]. Strain (ε) is defined as:

$$\varepsilon = \Delta L/L_0 \tag{3.8}$$

where ΔL is the change in gage length and L_0 is the initial gage length [114].

The first portion of the stress-strain curve obtained is linear and called as the elastic region of the curve. In this region, the bonds between the atoms of the material are stretched due to the tensile load applied. The bonds relax and the material returns to its original dimensions as the load in removed. At higher loads, planes of the atoms of the material start to slide over one another. This region of the stress-strain curve is called the plastic deformation and it is no longer linear. At this point, the material cannot turn back to its original dimensions when the load is removed [114, 115].

The slope of the linear elastic deformation region is referred to as Young's modulus or elastic modulus. Tensile modulus of elasticity is a measure of the stiffness of a material [116]. Elastic modulus (E) is defined as:

$$E = \sigma / \varepsilon \tag{3.9}$$

As the tensile load is further increased, the stress-strain cure begins to curve downward. In this region, reduction in gage width or necking of the specimen is observed. After this region, the material will eventually fracture [115]. The tensile strength of a material is defined as the highest value of stress in the stress-strain curve. For less ductile (brittle) materials, necking of the specimen is not observed. In this case, tensile strength is taken as the fracture strength [114].

Toughness (or tensile energy to break) of a material is the amount of the total energy absorbed by the unit volume of the material until fracture [116]. It can be calculated as the area under the stress-strain curve. Ductility is the measure of the ability of the

material to undergo plastic deformation before fracture. There are two common measures of ductility. One of them is the percent elongation (%El) defined as [114]:

$$\%El = \left(\frac{\Delta L}{L_0}\right) * 100 \quad (3.10)$$

The other common measure is the percent reduction of area (%RA). For brittle materials that fracture without necking, the both measures can be calculated from one another from the equation [114]:

$$\%El = \%RA\ /(100 - \%RA) \quad (3.11)$$

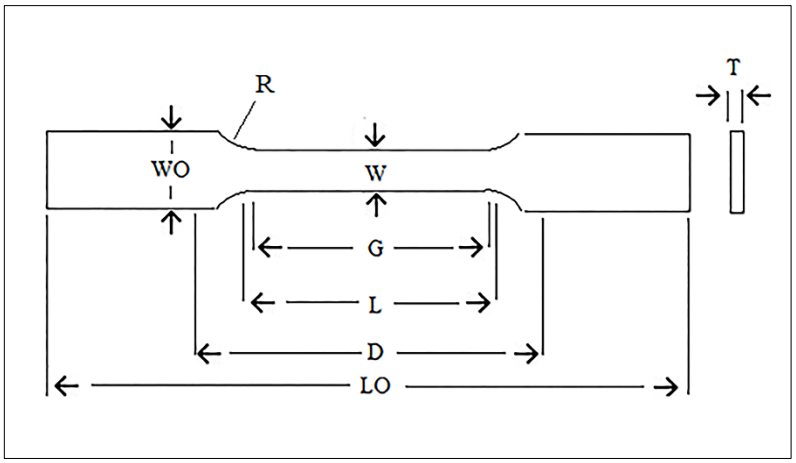

Figure 3.3 Mechanical analysis specimens shape and dimensions [116]

Table 3.6 Dimensions of the mechanical analysis specimens

Dimension symbol	**Name**	**Value, mm**
W	Width of narrow section	5
L	Length of narrow section	40
WO	Overall width	10
LO	Overall length	100
G	Gage length	40
D	Distance between grips	60
R	Radius of fillet	76
T	Thickness	0.8

The specimens required for uniaxial tensile testing were prepared by cutting PHBV/ZnO sample sheets using a special mold (Figure 3.3) and its dimensions are

given in Table 3.6. The mold was placed on the sample sheets and the sheets were placed in between stainless-steel plates. The plates were placed in the mechanical press (Gulnar Makine, Turkey) and were cut by the application of 120 bar pressure for 5 s. The specimens were conditioned after the cutting procedure at 23 °C and 50 % RH for 40 h. Tensile testing was applied at the end of the time for conditioning of the specimens.

Uniaxial tensile properties of the samples were evaluated according to ASTM D882-12 standard [116] using Instron (USA) 5982 Universal testing machine with 100 kN capacity and Devotrans DVT GP (Turkey) universal testing machine with 2 kN capacity, at 23 °C and 50 % RH. An initial load of 1 N was applied and the cross-head speed was 5 mm/min. At least 5 specimens were tested for each sample and the mean values were reported.

CHAPTER 4

RESULTS AND DISCUSSION

4.1 Synthesis of ZnO Particles

The aim of this part of the work was to produce high quality, monodisperse and rod-shaped ZnO particles to be used in the fabrication of PHBV composites. Trials were performed changing several parameters of the synthesis reaction, such as precursors concentration, reaction temperature, and reactor volume.

ZnO particles were synthesized from aqueous solution using wet chemical synthesis method. The precursors of the synthesis reaction were selected as zinc nitrate hexahydrate ($Zn(NO_3)_2{\cdot}6H_2O$) and hexamethylenetetramine ($C_6H_{12}N_4$, HMT) since they were widely reported in the literature for the synthesis of high -quality ZnO nanorods [50, 52, 55]. Zinc nitrate is known to provide the Zn^{2+} ions and the water molecules in the solution are known to provide the O^{2-} ions in the building up of ZnO particles [77]. HMT is accepted to act as a weak base, hydrolyzing gradually to produce hydroxyl (OH^-) ions that drive the precipitation reaction and keeping the supersaturation level low for ZnO growth [51, 55, 77].

As HMT slowly hydrolyzes in water, first formaldehyde (CH_2O) and ammonia (NH_3) are produced. Then ammonia hydrolyzes further and produces OH^- and NH_4^+. The OH^- ion can form a complex with Zn^{2+} [55]. At the initial stage of the synthesis reaction, the formation of ZnO occurs through $Zn(OH)_2$ formation. As the pH increases gradually and the concentration of the Zn^{2+} ions decrease, $Zn(OH)_2$ becomes thermodynamically unstable. Since the thermodynamically less-stable phase would precipitate faster, $Zn(OH)_2$ would start dissolving [51]. The zinc compound $Zn(OH)_2$ then decomposes into ZnO [55]. These steps proceed according to the following reactions [52, 55]:

$$C_6H_{12}N_4 + 6\,H_2O \leftrightarrow 4\,NH_3 + 6\,CH_2O \qquad (4.1)$$

$$NH_3 + H_2O \leftrightarrow NH_3.H_2O \quad (4.2)$$

$$NH_3.H_2O \leftrightarrow NH_4^+ + OH^- \quad (4.3)$$

$$Zn^{2+} + 4\,OH^- \leftrightarrow Zn(OH)_4^{2-} \quad (4.4)$$

$$Zn(OH)_4^{2-} \leftrightarrow Zn(OH)_2 + 2\,OH^- \quad (4.5)$$

$$Zn(OH)_2 \rightarrow ZnO(s) + H_2O \quad (4.6)$$

The reaction steps listed above are all in equilibrium and can be controlled by adjustment of the reaction parameters [52, 77]. Crystallization reactions are known to be sensitive to the parameters such as temperature, pH, reaction time, mixing, type of solvent, and precursor concentrations [57, 58, 77]. The reaction equilibrium could be moved forward or backward by manipulation of these parameters.

4.1.1 Effect of Precursors Concentration

Akin and Öner [62] previously reported the synthesis of ZnO rods in a 1 L volume capacity reactor, with 0.03 M precursors concentration, and at 75 °C and 95 °C reaction temperatures. The ZnO rods obtained at 75 °C had a mean length of 1144 ± 375 nm and a mean width of 165 ± 47 nm; and the rods obtained had a mean length of 1812 ± 467 nm and a mean width of 199 ± 69 nm. Following the synthesis method of Akin and Öner [Akin and Öner; 2012], the precursors concentration was increased to 0.06 M in this study. Since the ZnO particles to be synthesized would be used in fabrication of polymer composites, synthesis of particles in higher amounts would be required. Increased precursors concentration would increase the number of particles obtained in one batch. However, it is also known that, in order to obtain uniform dispersions of particles, low concentrations of reactants are required [76]. Therefore, a considerably low concentration value was selected, although the value in Akin and Öner's work [62] was doubled. Since equimolar concentrations of precursors were recommended for obtaining anisotropic rod particles [50], the ratio of the concentration of zinc nitrate to the concentration of HMT was kept as 1:1.

In a first trial, only the precursors concentration was changed to 0.06 M, and the parameters were kept the same as in Akin and Öner's work [62]. The reactor volume was 1 L and the reaction temperature was 75 °C. The sample code used for the particles was ZnO-1L-75C and the scanning electron microscope (SEM) images of the particles obtained at the end of the reaction are given in Figure 4.1.

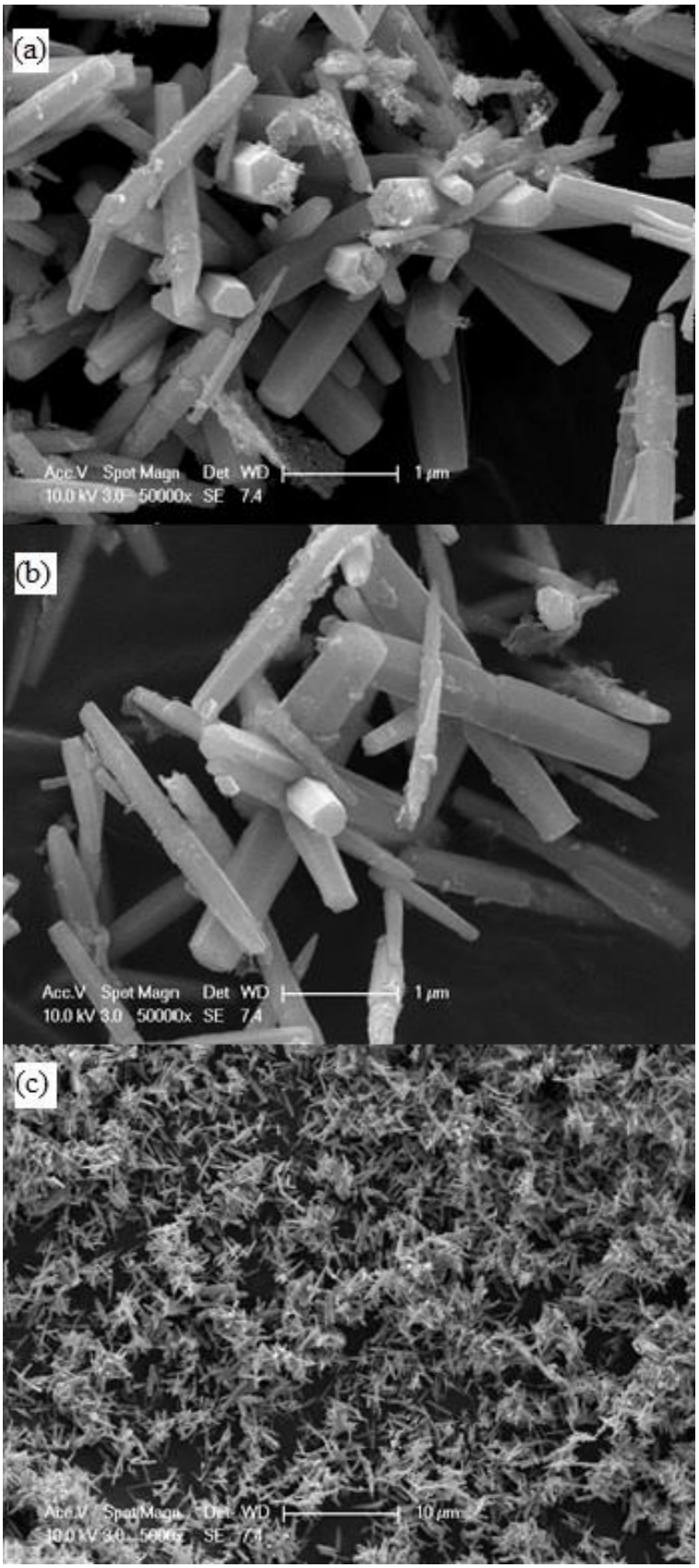

Figure 4.1 SEM micrographs of the ZnO-1L-75C particles (a) at 50000x magnification, (b) at 50000x magnification in another area, and (c) at 5000x magnification

Precursor concentration in ZnO synthesis was reported in the literature to affect particle density [52, 75, 77]. The change in the precursor concentration affected the number of the ZnO particles synthesized in this study. As the concentration of the zinc nitrate was increased, the zinc chemical potential in the solution was also increased. Thus, more nucleation sites were produced in order to balance the increased chemical potential. The number of the ZnO particles growing on these nucleation sites were therefore increased. By doubling the precursors concentration, the mass of the ZnO particles synthesized in one batch was increased.

Xu et al. [77] reported that the particle density was increased by the increase in precursors concentration to a certain degree. Up on further increase in the precursors concentration, the particle density remained almost constant. This was explained by the assumption that, formation of higher amounts of ions did not result in the formation of new nuclei after a certain point. The newly formed ions had a higher probability of reaching to the already formed rod particles than reaching to the newly formed nuclei. Since a critical size of nuclei is required for turning into a crystal, the size of the new nuclei would not exceed the critical size and they would eventually dissolve into the solution body. In this case, the increase in the precursors concentration would not result in an increase in the particle density.

In this study, the increase in the precursors concentration was below the critical range, so that an increase in the number of particles synthesized could be obtained. Since the mass of the synthesized particles were satisfactory for further processing in polymer composites fabrication, further increase in precursors concentration was omitted.

The formation of a rod-shaped morphology in aqueous ZnO growth is known to be more common, since the polar plane of ZnO has a higher surface energy than the nonpolar planes, and crystal growth along the *c*-axis is energetically more favorable [57]. ZnO-1L-75C particles synthesized were observed to have a hexagonal rod-shaped morphology (Figure 4.1). Nevertheless, smaller-size needle-shaped particles were also observed.

The effect of precursors concentration on particle morphology was also reported in the literature [60]. ZnO particles with varying morphologies such as needles, rods, flowers, and cubes were obtained by altering the concentrations of zinc chloride and HMT. When equimolar concentrations of zinc chloride and HMT (0.01 M) were used, ZnO

nanoneedles were obtained in an aqueous solution using a copper substrate. When the concentrations of the precursors were increased to 0.1 M, flower-like structures were obtained. When zinc chloride and HMT concentrations were changed as 0.1 M and 0.05 M, respectively, nanosquare disks were obtained. The effect of precursors concentration on the particle morphology was explained by the change in the rate of supersaturation and in the growth direction of the $Zn(OH)_2$ precursor [60].

Panigrahy et al. [60] reported that, when the concentration of HMT was low, the hydrolysis of HMT and the formation of the OH^- ions were slow and controlled. Therefore, uniform transformation of Zn^{2+} ions into $Zn(OH)_2$ complex could be attained. This resulted particle growth along the *c*-axis, producing nano-needles. When the reaction time was increased from 80 min to 100 min, using the same reaction conditions, the particle morphology changed to nanorods, without change in particle dimensions. They suggested that, when reaction time was shorter, the nuclei growth at the tips of the particles was insufficient and needle geometry was formed. When the reaction time was increased, nucleation at the tip was increased with sufficient growth along the c-axis, resulting in the formation of rod-shaped particles.

In this study, the concentration of HMT was sufficiently low to allow uniform transformation of Zn^{2+} into $Zn(OH)_2$ and facilitating growth along the *c*-axis. The resulting particle morphology was nanorods. The smaller needle-shaped particles observed in SEM figures of ZnO-1L-75C samples (Figure 4.1b) were due to the insufficient nucleation at the tips of the particles, possibly resulting from inhomogeneities in the reaction mixture.

When compared to the particles obtained in the work of Akin and Öner [62], synthesized by lower precursors concentration, the particles in this study did not show a significant change in particle size and morphology. However, doubled precursors concentration resulted in increased particle density (defined as the mass of particles obtained per unit volume). The ZnO-1L-75C particles did not show a very uniform, monodisperse dispersion. Particles rather appeared to have a wide range of dimensions and some crystal defects. Some nuclei which could not complete their transformation into crystals were observed (Figure 4.1a) as attached on the rods.

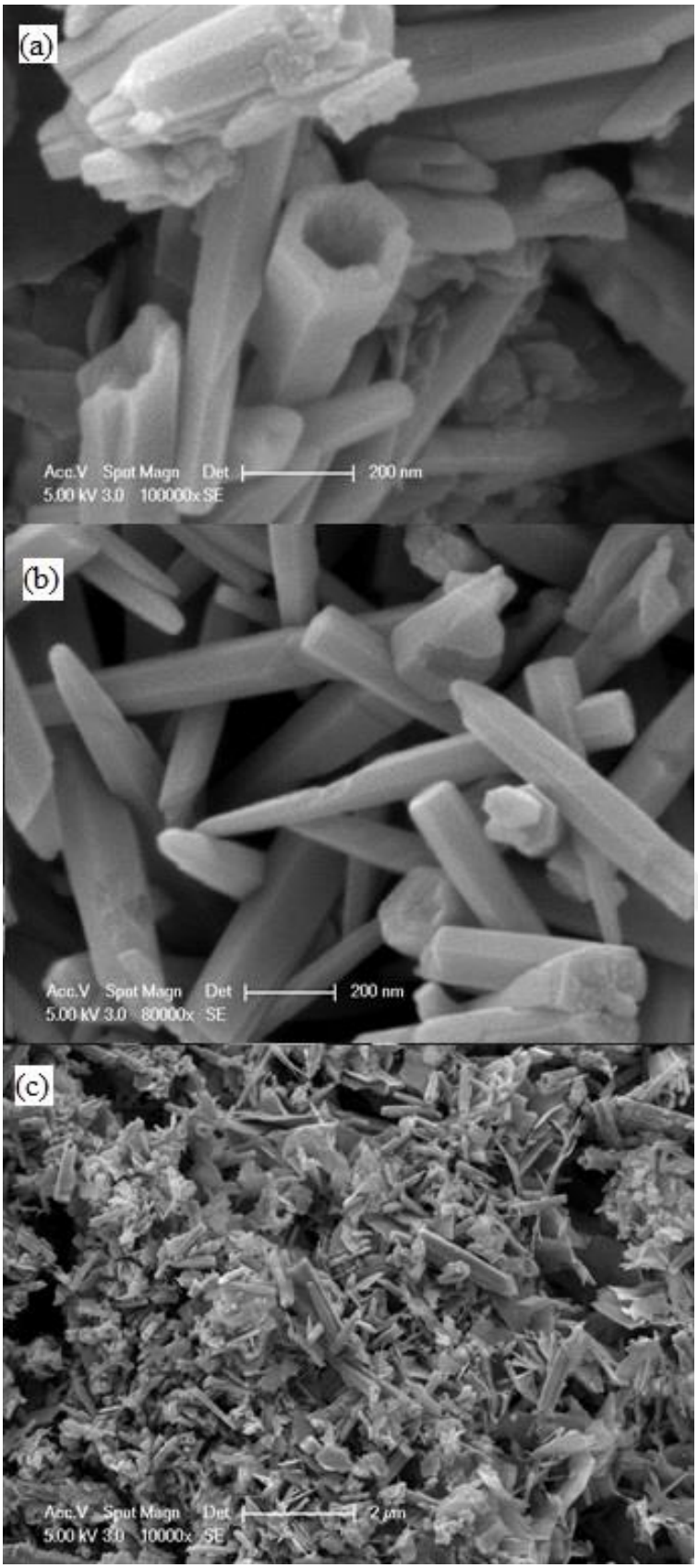

Figure 4.2 SEM micrographs of the ZnO-1L-95C particles at different zones (a) at 100000x magnification, (b) at 80000x magnification, and (c) at 10000x magnification

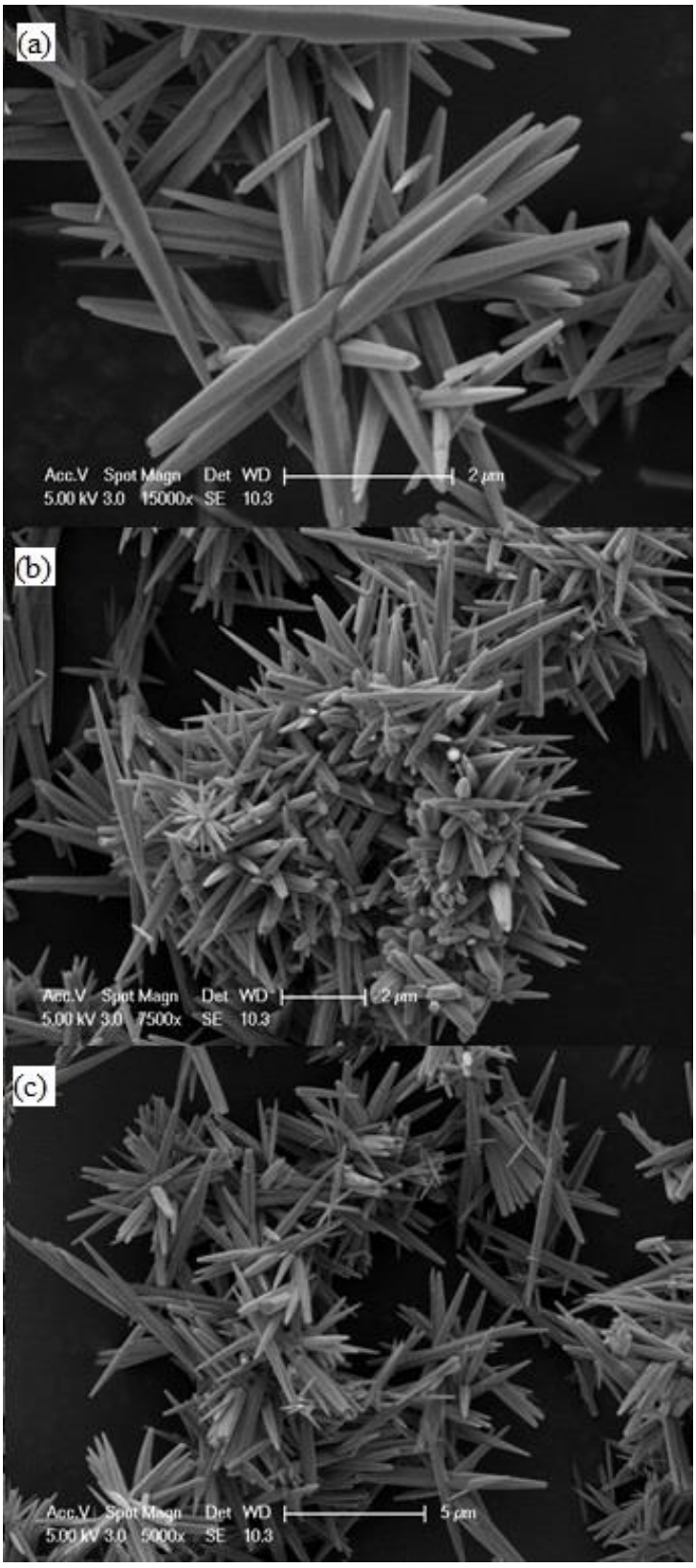

Figure 4.3 SEM micrographs of the ZnO-2L-95C particles (a) at 15000x magnification, (b) at 7500x magnification, and (c) at 5000x magnification

4.1.2 Effect of Reaction Temperature

Reaction temperature was reported to be effective on the aspect ratio of rod-shaped ZnO particles [52, 62, 77] and on particle morphology [52]. Aspect ratio of a rod-shaped particle is defined as the ratio of particle length to particle width (L/W). The width of a hexagonal rod is the longest distance between the opposite corners of the hexagonal face, and the length is defined as the longest distance normal to the hexagonal face.

Akin and Öner [62] reported formation of ZnO rods at three different reaction temperatures (60, 75, and 90 °C). As the reaction temperature was increased, both the width and the length of the particles increased. However, the increase in particle length was greater than the increase in the particle width, which resulted in an increase in the aspect ratio.

Xu et al. [77] also reported the effect of temperature on the aspect ratio of ZnO rods. When ZnO particles were synthesized on a substrate at 70 °C, the aspect ratio of the rods was greater than those obtained at 60 °C. However, when the reaction temperature was increased to 95 °C, the particle morphology changed to pyramid-shaped particles and the aspect ratio was decreased. Therefore, reaction temperature could affect both aspect ratio and morphology.

Since the aspect ratio is related to particle length and width, it depends on the axial and lateral growth rates of the crystals during the synthesis reaction. Xu et al. [77] reported that the ratio of the growth rate of polar faces to the growth rate of nonpolar faces is higher at higher temperatures, resulting in higher aspect ratios. According to the basic theory of crystal nucleation and growth; lower temperature results in lower mobility of the ions, limiting their diffusion within the reaction solution. Therefore, larger size nuclei are formed, decreasing the particle density and aspect ratio. At high temperatures, the ion mobility and diffusion increases and due to their affinity to already formed crystal seeds, growth along the *c*-axis is more pronounced than the formation of new seeds [77].

In this study, using the same reaction parameters as in the previous section, reaction temperature was increased to 95 °C. The particles synthesized were sample coded as ZnO-1L-95C and the SEM micrographs of the particles are given in Figure 4.2. Rather than an increase in the aspect ratio, a change in the morphology of the particles was observed. Among with hexagonal rod-shaped particles, the formation of hexagonal

nanotubes was also observed. Furthermore, zones of irregular shaped particles existed, probably due to the formation of nuclei that could not turn into proper shaped crystals due to the inhomogeneity of the solution mixture. The ZnO nanorods formed had a mean length of 912.2 ± 229.3 nm and a mean width of 124.1 ± 29.6 nm. The mean aspect ratio of the rod-shaped particles was 7.4. The hollow tubes observed had a mean diameter of about 228 nm and a wall thickness of about 50 nm.

Liu et al. [56] previously reported the transformation of ZnO nanorods into nanotubes by treatment in alkaline solution. Etching of the metastable polar planes with alkaline was faster than the etching of the stable nonpolar faces parallel to the *c*-axis, therefore etching took place in the center of the nanorods, resulting in the formation of nanotubes.

Zhang et al. [84] reported formation of ZnO nanotubes from a mixture of ethanol and $Zn(NH_3)_4^{2+}$ aqueous solution obtained by adjusting the pH of zinc acetate solution with ammonia. They suggested that, the role of NH_3 as a reaction product was predominant in the formation of tubular structure. Furthermore, the formation of nanotubes was not observed when the reaction temperature was below 180 °C.

Wei et al. [117] reported synthesis of ZnO nanorods by adding ammonia into zinc chloride solution and adjusting the pH to 10.0. They investigated the development of the particle morphology at different reaction times. After 90 min of reaction, flat-end rod-shaped ZnO particles were obtained. After 1.5 h, small craterlets were formed at the end of the rods. Craterlets grew as the time progressed, finally turning the ZnO particles into hollow tubes. Formation of craterlets and the tubular structure was due to the dissolution of the formed ZnO from the rods. Following reaction was reported to result in the formation and dissolution of ZnO:

$$Zn^{2+} + NH_3.H_2O \leftrightarrow Zn(NH_3)_4^{2+} + OH^- \leftrightarrow ZnO + NH_3 + H_2O \qquad (4.7)$$

They reported that the reaction of $Zn(NH_3)_4^{2+}$ with OH^- that resulted in the deposition of ZnO only took place at temperatures higher than 75 °C. At the beginning of the synthesis reaction, when the $Zn(NH_3)_4^{2+}$ concentration was high, the rate of deposition of ZnO was higher than the rate of dissolution. As the time and the reaction progressed, dissolution became more dominant, resulting in the flat-end rod-shaped particles. During the ageing process, where the reaction mixture was left to cooling, the dissolution effect became much more dominant, since the deposition was very low below 75 °C. Therefore, the fast dissolution rate resulted in the formation of hollow

structures. Since the polar faces were less stable than the nonpolar faces parallel to the *c*-axis, dissolution of these faces was much faster, resulting in the formation of tubular structure. When the reaction time was prolonged, the wall thickness of the tubular structures became thinner. They suggested that, if the reaction time was prolonged enough (about several days) the shortening and even disappearing of the tubular structures could also be observed.

Considering the following hydrolysis reaction of HMT, 7 moles of reactants produced 10 moles of products. Therefore, when the reaction temperature increased, the reaction would shift towards right for the increase of entropy. Thus, hydrolysis of HMT would be faster at higher temperatures [77].

$$C_6H_{12}N_4 + 6\,H_2O \leftrightarrow 4\,NH_3 + 6\,CH_2O \quad (4.8)$$

During the synthesis of ZnO-1L-95C particles, as the HMT hydrolyzed faster, more ammonia was produced increasing the pH of the medium faster than the case of lower temperature. At the beginning of the reaction, higher concentration of OH^- was produced to react with Zn^{2+} ions. At this stage formation of ZnO nanorods occurred. As the reaction continued and the number of Zn^{2+} ions were decreased, dissolution of ZnO from the polar faces of the nanorods started to become more dominant. Therefore, some portion of the nanorods started to transform into hollow tubes. Existence of ZnO nuclei that could not transform into one dimensional crystals also suggests the early depletion of Zn^{2+} ions. Higher decomposition of HMT into OH^- ions increases the degree of supersaturation resulting in higher nucleation [49]. Increasing the reaction temperature was reported to result in a competition between nucleation and nanorod growth [55].

The existence of three different morphologies of the synthesized particles, i.e. nanorods, hollow nanotubes, and irregular seeds, suggested an inhomogeneity of the solution throughout the reaction. For this reason and in order to upscale the production, the reactor volume was doubled. The magnetic stirring applied within the reactor was also increased.

4.1.3 Effect of Reactor Volume

ZnO particles were synthesized in a 2 L volume capacity reactor using the same conditions as in the previous section. Reaction temperature was again selected as 95 °C. As the reactor volume was increased, a bigger size magnetic stirrer was used in order to

achieve better homogeneity. The particles synthesized with these conditions were sample coded as ZnO-2L-95C. The SEM micrographs of the particles are given in Figure 4.3. The ZnO particles synthesized were well-developed hexagonal, one-dimensional rod-shaped crystals. The inhomogeneity, polydispersity and multiple phases observed in the particles reported in the previous sections were not observed for the ZnO-2L-95C particles. Irregular-shaped smaller particles that could not develop into one-dimensional structures were not observed. Formation of hollow structures through dissolution of formed ZnO was also inhibited.

The particles appeared to be considerably monodisperse. The mean length of particles was 6183.0 ± 895.2 nm and the mean width was 395.3 ± 75.2 nm. The mean aspect ratio was calculated as L/W = 15.6. Both the dimensions and the aspect ratio of the particles were considerably higher than the particles obtained in the previous sections.

Increased reaction temperature is known to affect the size and the aspect ratio of the synthesized particles. Both axial and lateral growth rates were reported to increase with increased temperature; nonetheless growth rate of polar surface was affected more than the growth rate of nonpolar surface [62, 77].

When the reactor volume was smaller and mixing was inefficient, i.e. in the synthesis process of ZnO-1L-95C, the effect of reaction temperature could not be observed due to the local zones that Zn^{2+} ions were depleted relatively quickly. Multiple phases of particle morphologies were observed at different zones. However, when the reactor size was doubled and better stirring was applied, homogeneity within the reaction solution could be achieved. Particles of a single morphological phase were obtained with considerably uniform dimensions. The effect of temperature on the dimensions and aspect ratio of the particles could be observed.

Crystal morphologies are known to be very sensitive to synthesis reaction conditions [57, 58]. The results obtained in this study by varying reaction parameters suggests that, the morphology and uniformity of the ZnO particles strongly depend on precursors concentration and reaction temperature, as well as reactor volume and efficient mixing. The effect of reactor volume in this study probably resulted from the slower transfer of heat from the oil bath to the interior parts of the reactor, compared to the heat transfer in smaller volume reactor.

The ZnO-2L-95C particles were observed to have well-developed rod-shaped morphology (Figure 4.3). Anisotropic crystal growth due to the varying free surface energies of different crystallographic faces is known to result in one-dimensional growth of rod-shaped particles [49, 118]. The rod particles formed did not have uniform hexagonal width but they were tapered from the center to the ends. The morphology of rod-shaped crystals often deviates from a perfect hexagonal prism and show tapering along the *c*-axis [57]. Due to tapering along the *c*-axis, the ends of the rods did not have flat polar plane surfaces and the rods had needle-like pointy ends. Since the plane that had the more rapid growth rate disappeared more quickly, tapering was observed along the c-axis [119].

The elongated rod structures of ZnO were observed to form rod arrays that resemble an asterisk shape. Growth mechanism for the formation of regular rod array structures by self-aggregation process was previously proposed by Sepulveda-Guzman and co-workers [53]. Self-aggregation of highly-ordered ZnO nuclei was suggested to result in the formation of rod arrays. They reported that in case of randomly-oriented primary particles, formation of flake arrays instead of rod arrays were observed. Pacholski et al. [118] also demonstrated the oriented attachment of primary particles was a major path for the formation of nanorods.

Zhang et al. [119] also reported the formation of similar flower-like ZnO structures composed of sword-like nanorods. However, they reported that aggregation was not the possible mechanism for the formation of flower-like structures, since the structures could not be disintegrated into primary rod particles with long time ultrasonic treatment. In this study, on the other hand, primary ZnO rods could be obtained by the application of ultrasound, as it will be described in the following sections. Therefore, it was deduced that aggregation of ZnO nuclei was the possible mechanism in the formation of rod arrays.

The ZnO-2L-95C particles synthesized in this section had sufficiently high quality for incorporation into PHBV matrix, due to their well-developed morphology, uniformity and high aspect ratio. Therefore, these particles were utilized in the fabrication of PHBV biocomposites in the following sections, while ZnO-1L-75C and ZnO-1L-95C particles were omitted.

4.1.4 Structural Analysis of ZnO-2L-95C Particles by XRD Analysis

The crystalline structure of the ZnO-2L-95C particles synthesized was evaluated by analysis and the diffractogram obtained is given in Figure 4.4. The diffraction peaks observed agree with the hexagonal phase of ZnO given in the standard card JCPDS 36-1451 by the International Centre for Diffraction Data (formerly Joint Committee on Powder Diffraction Standards, JCPDS). Sharp, strong and clear peaks indicate that the ZnO particles synthesized were well crystallized. The extra peaks observed at 43.76° and 51.17° were associated with $Zn(OH)_2$ according to JCPDS card no. 38-0385 [120].

Table 4.1 the XRD data obtained from the analysis and comparison with the JCPDS card. The 2θ peak positions, relative intensities of the peaks (the ratio of the peak intensity to that of the most intense peak, I), lattice spacings (d) and hkl indices that the peaks were indexed are given in the table. The values of d-spacings was calculated for each peak according to Bragg's law ($\lambda=2d\sin\theta$), where λ is the wavelength of X-rays (1.5418 A°) and θ is the Bragg angle [121].

Table 4.1 XRD parameters of ZnO-2L-95C particles and the parameters given in standard JCPDS 36-1451 card

ZnO-2L-95C particles			**JCPDS 36-1451 card**			
2θ°	**I, %**	**d, A°**	**2θ°**	**I, %**	**d, A°**	**hkl**
31.86	52.14	2.81	31.76	57	2.81	(100)
34.55	36.56	2.60	34.42	44	2.60	(002)
36.29	100	2.48	36.25	100	2.48	(101)
47.60	21.84	1.91	47.53	23	1.91	(102)
56.61	35.05	1.63	56.60	32	1.62	(110)
62.96	39.4	1.48	62.86	29	1.48	(103)
66.42	5.05	1.41	66.37	4	1.41	(200)
67.93	21.65	1.38	67.96	23	1.38	(112)
69.19	13.56	1.36	69.09	11	1.36	(201)
72.68	23.87	1.30	72.50	2	1.30	(004)
76.87	4.14	1.24	79.90	4	1.24	(202)

The values of the unit cell lattice constants a and of c wurtzite-structure ZnO are given as 3.24982 and 5.20661 A°, respectively in JCPDS 36-1451 standard card. The lattice constants of the ZnO-2L-95C particles were calculated using Bragg's law and lattice geometry equation [122, 123]:

$$a = \sqrt{1/3}\frac{\lambda}{sin\theta}, \qquad c = \frac{\lambda}{sin\theta} \tag{4.9}$$

Using the peaks indexed at (100) and (002) [122], the lattice constants of ZnO-2L-95C particles were calculated as $a(100)$= 3.243 A° and $c(002)$ = 5.190 A° (c/a = 1.60). The calculated values were very close to the values given in the standard card.

Table 4.2 Average crystallite sizes of ZnO-2L-95C estimated from XRD spectrum

2θ°	**hkl**	**B, radians**	**L, nm**
31.86	(100)	0.2952	50.51
34.55	(002)	0.3936	38.15
36.29	(101)	0.3444	43.81
47.60	(102)	0.3936	39.82
56.61	(110)	0.246	66.20
62.96	(103)	0.3444	48.82
66.42	(200)	0.6888	24.88
67.93	(112)	0.2952	58.57
69.19	(201)	0.492	35.40
72.68	(004)	0.1968	90.45
76.87	(202)	0.72	25.42

In addition to identification of crystalline phase and lattice parameters, XRD analysis results can also be used for the estimation of constituent crystallite sizes by the X-ray line broadening method using the Scherrer equation [121, 124]:

$$B = \frac{K.\lambda}{L.cos\theta} \tag{4.10}$$

where K is a numerical constant dependent on the crystallite shape (taken as 0.9 [122], B is the full width at half maximum of the peak, and L is the average crystallite size [98]. The L values calculated for each peak obtained for ZnO-2L-95C particles are

given in Table 4.2. Any plane could be chosen for the calculation of average crystallite size [121]; however, since (101) plane was the highest intensity peak, the average crystallite size of the ZnO-2L-95C particles was reported as the L value calculated as this plane which was equal to 43.81 nm. This value was close to the values in several works reported in the literature [123-125].

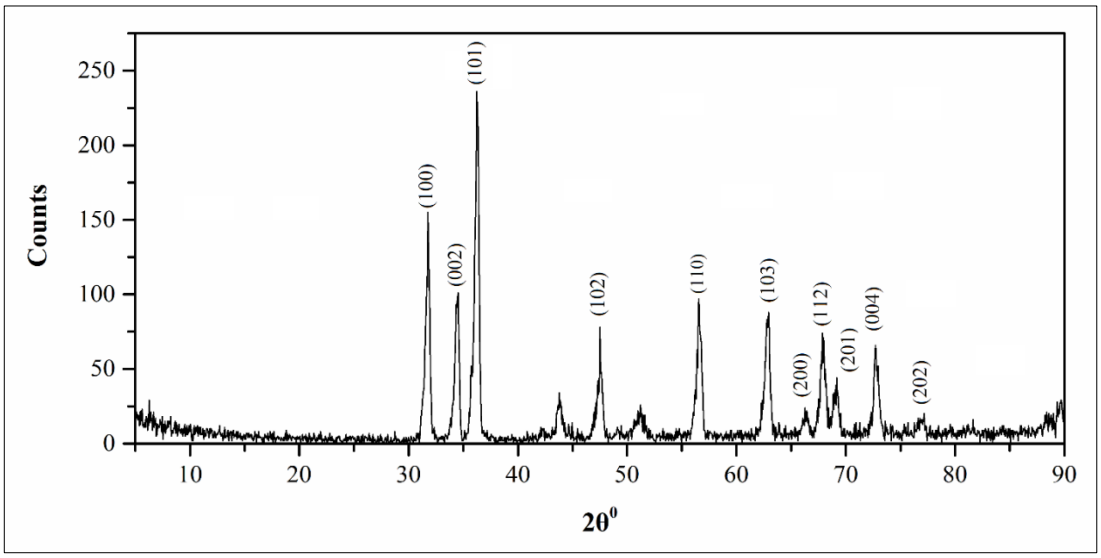

Figure 4.4 X-ray diffractogram of the ZnO-2L-95C particles

4.1.5 FTIR Study of ZnO-2L-95C Particles

The molecular environment of the ZnO particles synthesized was investigated by FTIR spectroscopy. The raw spectrum obtained for the particles and baseline corrected spectrum are given in Figure 4.5. Baseline correction is a spectral manipulation technique used to correct spectra [126].

The peaks in the range of 800 to 400 cm^{-1} generally result from the bonds of inorganic molecules [127]. The peaks at 514 and 708 cm^{-1} observed in the spectrum of ZnO-2L-95C particles (Figure 4.5b) were assigned to Zn-O stretching vibrations. In previous works, Zn–O bond vibrations were reported to result peaks in the region of 400 to 680 cm^{-1}; depending on chemical composition, crystal structure, and morphology. [127-131]. When the particle morphology was rod-shaped, the peak related to Zn–O vibration was reported to broaden and split into two maxima due to the increased polarity of the Zn–O bonds [128].

Sharma and Jha [127] observed prominent bands of Zn-O stretching at around 424 – 428 cm^{-1} and reported that these bands resulted from the stretching vibrations of Zn-O

bonds in tetrahedral coordination. They also observed weaker bands at around 671 – 672 cm^{-1} resulting from the stretching vibrations of Zn-O bonds in octahedral arrangements. In the wurtzite structure of ZnO, oxygen atoms can be located in tetrahedrally-coordinated and octahedrally-coordinated interstitial sites [132, 133].

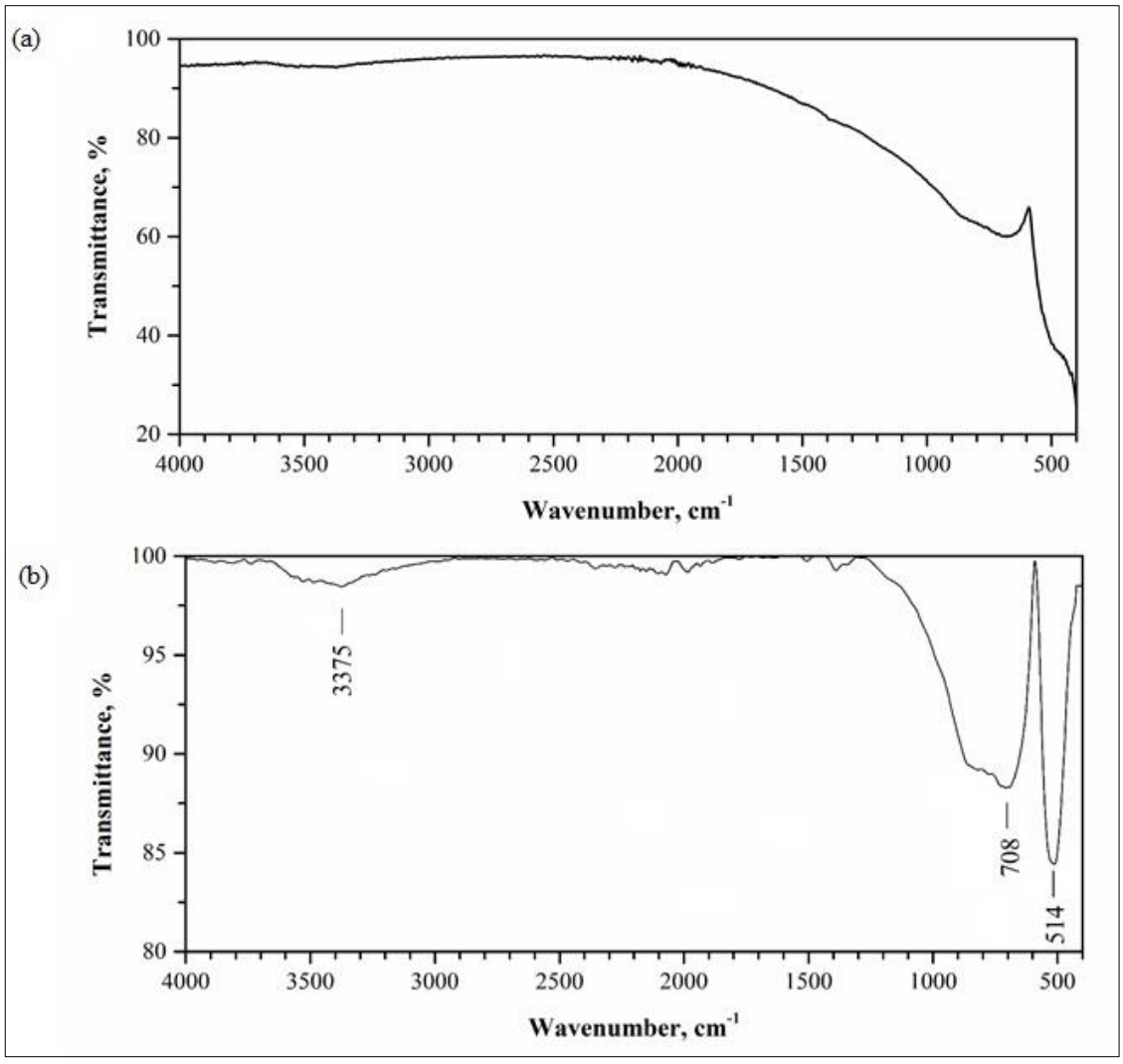

Figure 4.5 FTIR spectrum of the ZnO-2L-95C particles (a) before and (b) after baseline correction

In this study, the FTIR spectra obtained for ZnO-2L-95C particles before baseline correction (Figure 4.5a) exhibited a peak at around 400 – 500 cm^{-1} resulting from the Zn-O stretching vibration. This peak belonged to the Zn-O vibrations in tetrahedral arrangement. When baseline correction was applied, the peak resulting from vibrations in octahedral arrangement also became visible. The appearance of this peak only in baseline corrected spectrum and its lower intensity than the peak of bonds in tetrahedral sites confirms with the wurtzite structure of ZnO, in which the tetrahedral co-ordinations are much stronger than the octahedral co-ordinations [127].

In previous research [69, 134, 135], a broad band at about 3400 cm^{-1} was observed in the spectrum of unmodified ZnO particles and was associated with the OH^- group. In this study, this band was not clearly observed in the raw spectrum of the ZnO particles. ZnO particles were reported to generally have limited hydroxyl group on the surface [84]. Since the ZnO particles were thoroughly washed and then completely dried before the FTIR analysis, the amount of OH^- ions at the particle surface was limited. The band at 3375 cm^{-1} assigned to surface OH^- groups appeared in the baseline-corrected spectrum.

4.2 Ultrasonic Dispersion of ZnO Particles

The ZnO-2L-95C particles were obtained as regular rod array structures that resemble an asterisk shape. Self-aggregation of particles was considered to be the mechanism in the formation of arrays. Since the incorporation of ZnO particles into PHBV matrix requires a homogeneous distribution of the particles within the polymer matrix, disaggregation of the rod array into singular rod particles was necessary. Aggregation of the particles would decrease the surface area at the polymer-particle interface [136].

Sub-micron particles within a suspension are in Brownian motion and as they get close to each other they tend to form agglomerates due to their high surface energies. The ratio of Van der Waals forces to the other forces acting on the particles increases as the particle size decreases. Agglomeration of particles can be broken down by mechanical or ultrasonic mixing. Ultrasonic agitation is the most common and effective method for deagglomeration of particles within a suspension [88, 137]. Acoustic streaming and acoustic cavitation through the formation, growth and implosion of bubbles are the mechanisms of deagglomeration with ultrasound [90]. Ilyas et al. [138] reported that application of ultrasonic agitation significantly increased the dispersion stability of ZnO particles in ethanol-water mixtures of varying concentrations.

In order to break the aggregated rod arrays of ZnO-2L-95C particles, the particles were added in an ethanol-water solution and direct ultrasound was applied using an ultrasonic horn. Ultrasonic agitation was applied for 60 min. SEM micrographs of the particles after ultrasound application is given in Figure 4.6. Complete deagglomeration of the ZnO array structures was achieved by ultrasonic agitation and singular ZnO rod particles were obtained. The particles were sample coded as ZnO-2L-95C-US60.

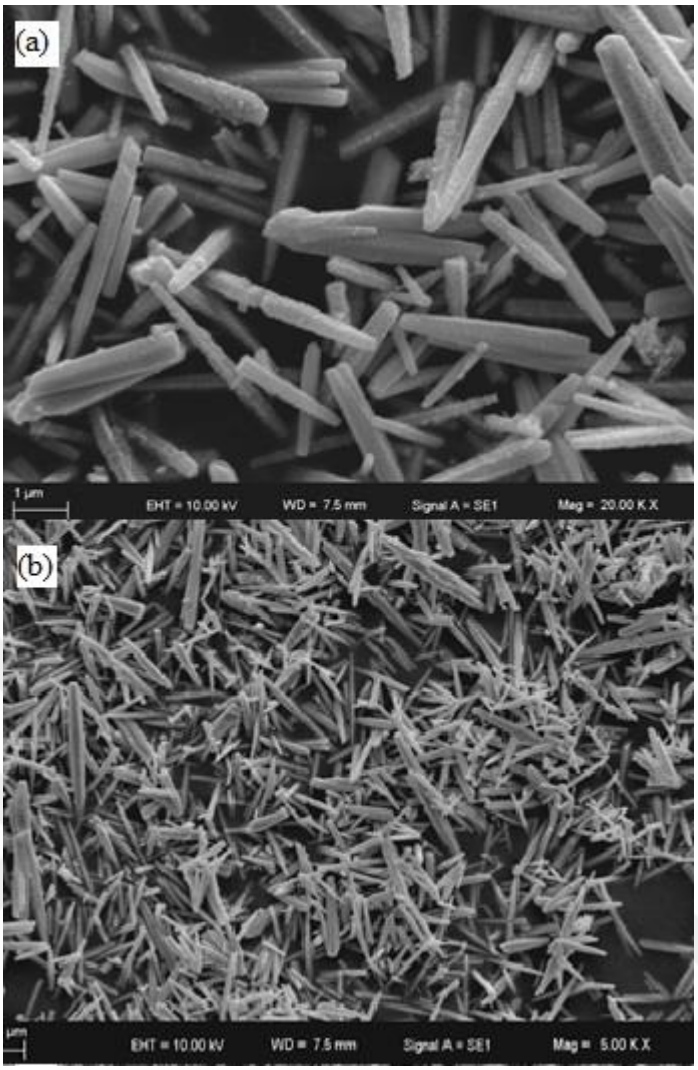

Figure 4.6 SEM micrographs of the ZnO-2L-95C particles after 60 min of ultrasound application (a) at 20000x magnification and (b) at 5000x magnification

Particle size analysis was applied by light-scattering technique in order to evaluate the effect of ultrasonic agitation on reduction of particle size by deagglomeration. The histograms obtained for particle size distribution before and after 60 min of ultrasound application are given in Figure 4.7. Significant reduction in particle size can be observed from the graphs. The median particle size was calculated as 33.7 μm before ultrasound application and as 5.5 μm after 60 min of ultrasonic agitation. Nevertheless, light-scattering method assumes a spherical particle shape and in fact is not appropriate for size measurement of one-dimensional particles. This analysis was only performed to have an idea of the size reduction, not for achieving an accurate value of average size. Accurate measurement of the sizes of one-dimensional particles can be achieved from SEM images.

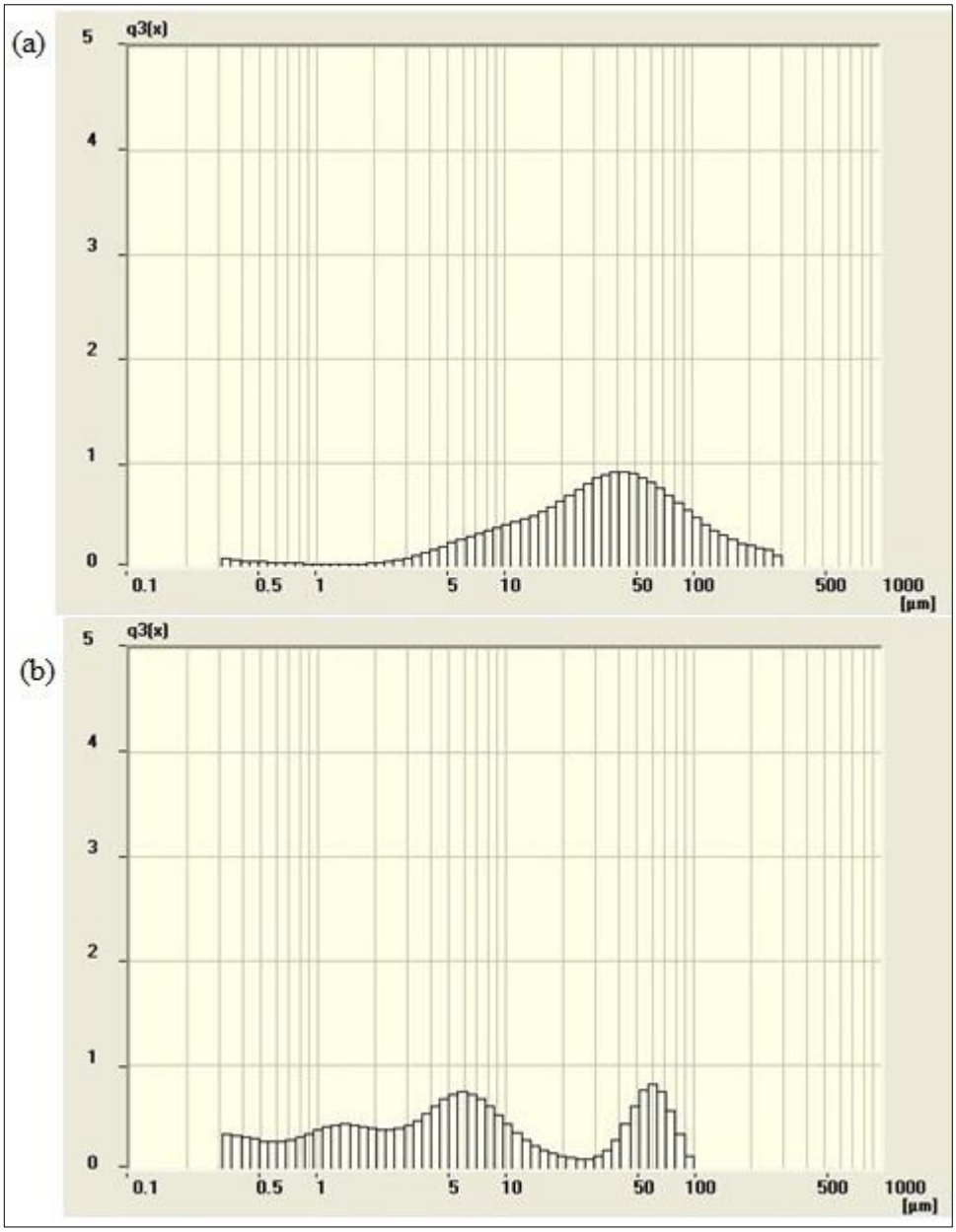

Figure 4.7 Size distribution of ZnO-2L-95C particles (a) before and (b) after 60 min of ultrasound application, obtained by light-scattering technique

Size distribution analysis was applied to the ZnO-2L-95C-US60 particles based on measurement of the sizes of the particles seen on SEM micrographs (Figure 4.6). The size distribution charts of the particles are given in Figure 4.8. The mean length of the particles was calculated as 3590.1 ± 1882.4 nm and the mean width was calculated as 393.6 ± 124.4 nm. Compared to the dimensions of the particles before ultrasound application, it was observed that the mean width of the particles remained almost at the same value, while the mean length was decreased by about 40 %. Most particles were broken into two from the center points where aggregation of the particles occurred. Standard deviations calculated for the dimensions were also increased after ultrasound

application, indicating breakage of the particles. As a result of particle breakage, the aspect ratio of the particles was also decreased from 15.6 to 9.1.

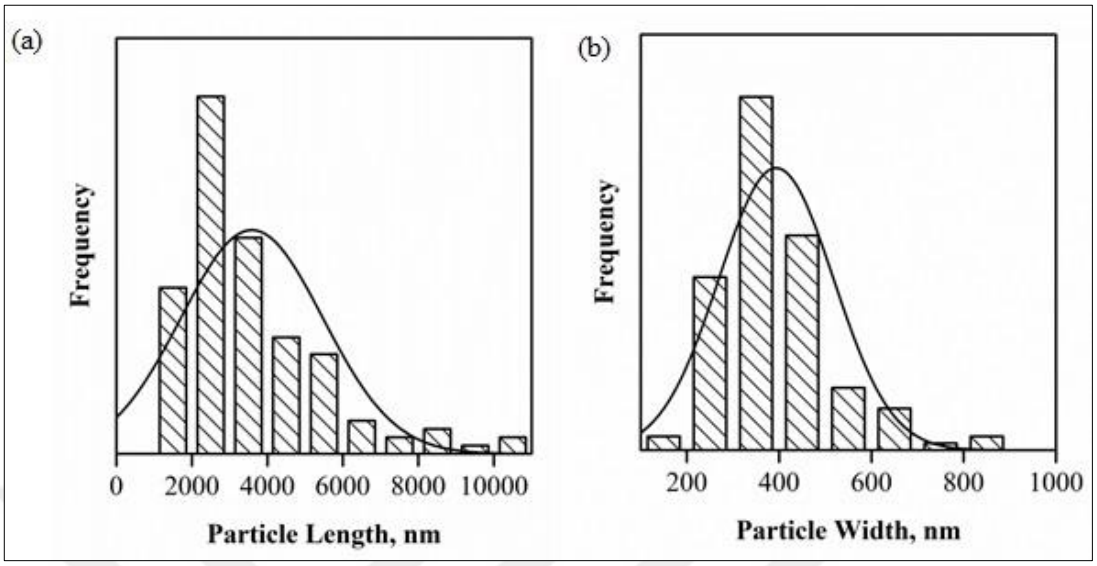

Figure 4.8 Size distribution for (a) particle length and (b) particle width of ZnO-2L-95C-US60 particles obtained from the analysis of SEM micrographs

Despite the decrease in aspect ratio and loss of uniformity in size, ultrasound-dispersed particles were selected to be used in fabrication of PHBV composites, due to the importance of homogeneous distribution of particles within the polymer matrix and surface area between the polymer-particle interface.

4.3 Surface Modification of ZnO-2L-95C Particles

Other than ultrasonic dispersion, another method in dispersion of inorganic particles within suspensions is utilization of functional silanes [70, 139]. As mentioned before, particle agglomeration is an important problem in homogeneous distribution of inorganic particles in polymer matrices. Surface modification of particles with silane coupling agents is an effective method for restraining the aggregation of particles during incorporation into polymers due to their high surface energies [69, 70, 74]. Surface modification also enhances the interfacial interaction between the particles and the polymer [69, 70, 74]. The hydrophilic surfaces of ZnO [134] particles should be turned to hydrophobic by silane modification, in order to have compatibility with the polymer matrix [48, 69].

3-(Trimethoxysilyl)propyl methacrylate silane, also known as (3-(methacryloxy)propyl) trimethoxy silane (MPS), is an organosilane with a methacrylate functional group and it

was reported to successfully produce hydrophobic surface of ZnO [84, 134]. MPS was utilized for the surface modification of the ZnO-2L-95C particles synthesized in order to break particle agglomerates and increase the compatibility of the particles with PHBV matrix. The chemical structure of a MPS molecule is given in Figure 4.9. The methoxy groups on the MPS molecule can bond with the OH^- groups on the ZnO surface [84, 85].

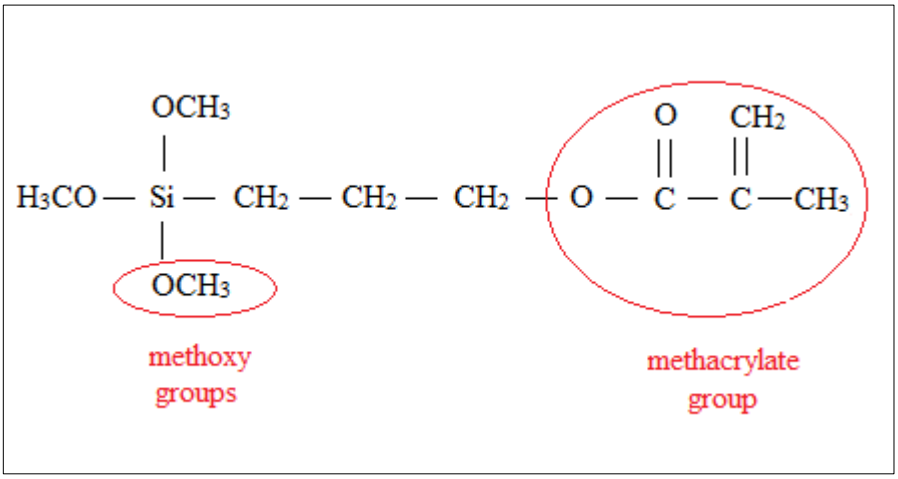

Figure 4.9 Molecular structure of MPS

4.3.1 Determination of the Surface Area of ZnO-2L-95C Particles by BET Analysis

In order to determine the required amount of MPS for monolayer coverage around the ZnO particles, the surface area of the ZnO-2L-95C particles were measured by BET method. The BET isotherm, that relates the total volume of the N_2 gas on the surface of ZnO particles to the relative pressure, was obtained for the particles (Figure 4.10). The volume of the N_2 gas at STP (standard temperature and pressure, i.e. 273 K and 1 atm) was calculated as the cm^3 of gas per gram of ZnO, and the relative pressure was calculated as P/P_0, where P is the pressure and P_0 is the atmospheric pressure (768.80 mmHg).

There are five different types of isotherms that can be obtained in BET analysis, and Type II isotherm is obtained when BET constant (C) is greater than 1 in the BET equation [91]. This is the most common type of isotherm obtained in BET analysis, and the isotherm obtained for ZnO-2L-95C particles was observed to be Type II isotherm. At very low relative pressure values observed on the graph (Figure 4.10), the micropores on the solid particles filled with N_2 gas, and an increasing curve was

obtained on the isotherm graph. Then the graph showed a knee at medium pressures, where monolayer formation occurred. At higher pressure values, capillary condensation occurred and an increasing curve was again observed in the isotherm [91].

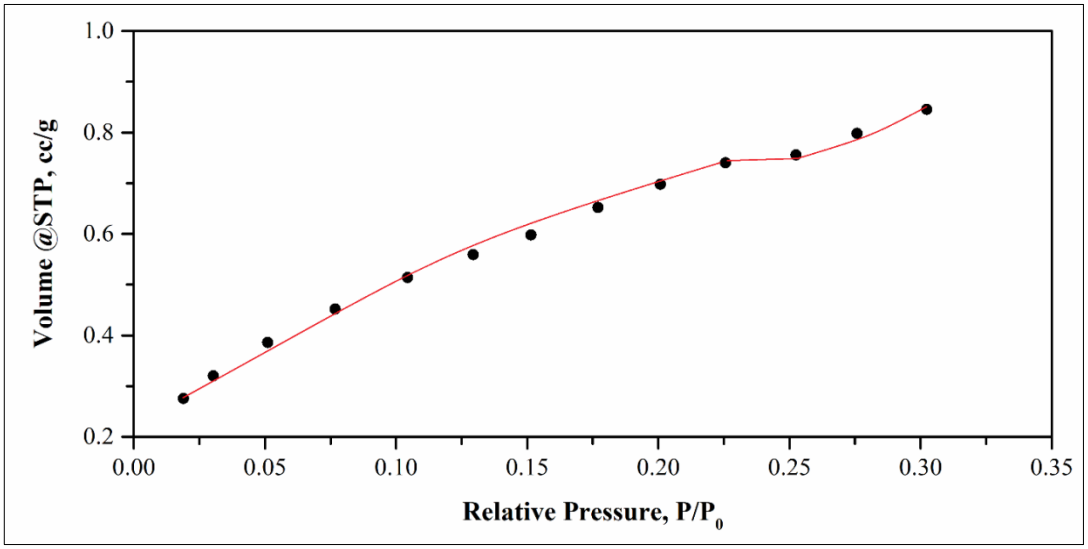

Figure 4.10 BET isotherm obtained for ZnO-2L-95C particles

The surface area of the particles was determined using the information obtained from the isotherm according to the BET equation:

$$\frac{1}{X[(P_0/P)-1]} = \frac{1}{X_m C} + \frac{C-1}{X_m C}\left(\frac{P}{P_0}\right) \qquad (4.11)$$

where X is the weight of N_2 gas adsorbed on the particles at a given relative pressure P/P_0, X_m is the monolayer capacity, defined as the volume of gas adsorbed at STP, and C is the BET constant.

Using multiple-point BET method, various data points were obtained in the P/P_0 range of 0.025 to 0.30. Using the data obtained, a plot of $X[(P_0/P)-1]$ against relative pressure values was obtained as a linear plot (Figure 4.11). The intercept and slope values of the linear plot were calculated using OriginPro software. Using the BET equation given above, and the slope and intercept values; the values of X_m and C are calculated as $8.21*10^{-4}$ and 20.375, respectively.

After the calculation of X_m value, the total surface area S can be calculated from following equation [91]:

$$S = \frac{X_m N_{Av} A_m}{M_v} \qquad (4.12)$$

where N_{Av} is Avogadro's number, A_m is the cross-sectional area of one adsorbed N_2 molecule (0.162 nm^2), and M_v is the molar volume (22.414 L). The total surface area of the ZnO-2L-95C particles were calculated as 2.86 m^2/g.

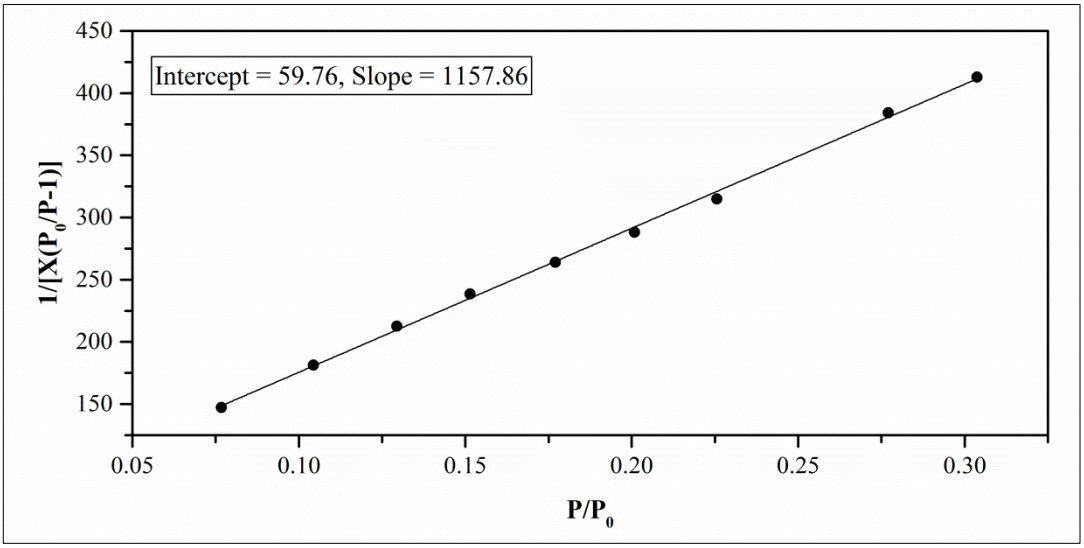

Figure 4.11 Multiple-point BET plot of ZnO-2L-95C particles

4.3.2 Calculation of the Required Amount of MPS for Monolayer Coverage

The theoretical amount of MPS required for the complete monolayer coverage of a rod-shaped particle was reported as 6.9 μmol/m^2 if the orientation of the silane is perpendicular to the particle surface, and as 3.0 μmol/m^2 if the orientation is parallel [71]. The minimum surface coverage area of MPS was reported as 314 m^2/g [87]. Since the values reported were theoretical, the real amount could deviate from the given values in case of incomplete or multilayer coverage.

For the theoretical monolayer coverage of MPS molecules, the minimum required amount of MPS per gram of ZnO was calculated from:

$$\text{Required amount of silane} = \frac{(1\ \text{g ZnO}) * (2.86\ \text{m}^2/\text{g})}{314\ \text{m}^2/\text{g}} \qquad (4.13)$$

The calculated minimum amount of MPS for monolayer coverage of ZnO-2L-95C particles was calculated approximately as 0.01 g MPS per gram of ZnO. Due to the very large wetting capacity of the silane molecule, the calculated value was quite small. Considering the deviation from theory and multilayer coverage, the amount of MPS used for surface treatment was selected as 1 g MPS per gram of ZnO.

4.3.3 FTIR Study of the MPS-Treated ZnO-2L-95C Particles

In order to verify the effectiveness of surface modification by the end of silanization reaction of ZnO with MPS, FTIR spectra of the ZnO particles before and after silane modification were taken and compared (Figure 4.12).

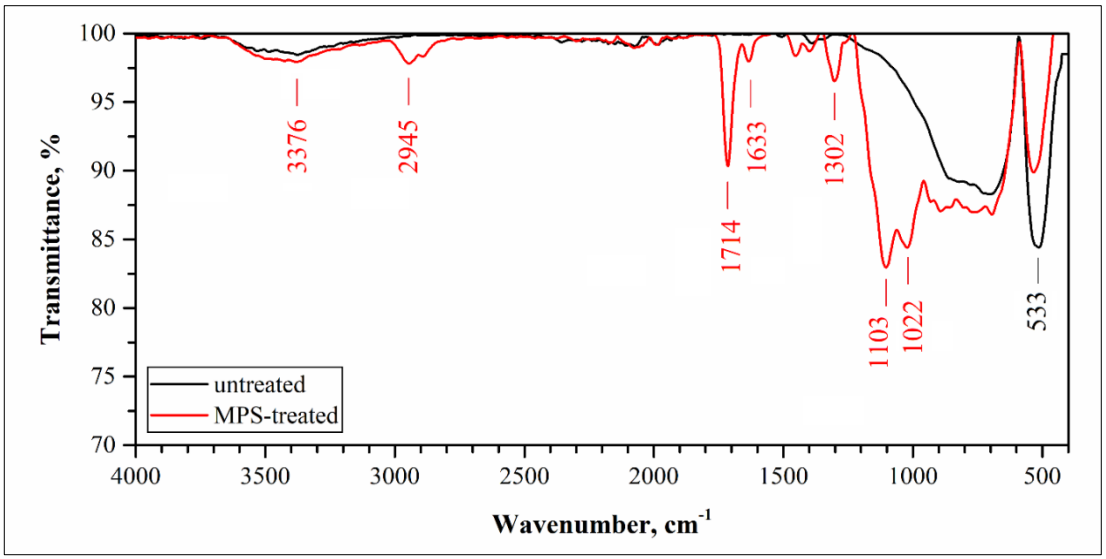

Figure 4.12 FTIR spectra of ZnO-2L-95C particles before and after surface modification with MPS

In the FTIR spectra of the MPS modified particles, a broad and low band was observed between 3000 and 3600 cm^{-1}, with a peak point around 3376 cm^{-1}. Hydrogen bonded OH^- group is known to produce a broad band between 3570 – 3200 cm^{-1}. Nonbonded OH^- group, on the other hand, would produce a narrow band between 3645 – 3600 cm^{-1}. Formation of hydrogen bonding results in the broadening of the band and lowering of the absorption frequency [140]. Therefore, the broad band observed around 3376 cm^{-1} in this study was attributed to the OH^- groups around ZnO particles that were hydrogen bonded with the MPS molecules.

The two small peaks observed at around 2945 cm^{-1} were associated with C-H asymmetric stretching of methyl group and C-H stretching of methoxy group of MPS [140]. Previous work carried out for MPS modification of ZnO [69, 134, 135] similarly reported that the peaks between 2800 and 3000 cm^{-1} were related to the CH_2 and CH_3 groups of MPS.

A peak between 1700 and 1750 is produced by carbonyl groups [140]. The peak observed at 1714 cm^{-1} in the FTIR spectra of the modified particles was assigned to the C=O bond on the methacrylate group of silane, similar to the previously reported work

[69, 134,135]. The smaller peak observed at 1633 cm^{-1} was assigned to the C=C bond on the methacrylate group of MPS [69, 135, 140].

The peak observed at 1302 cm^{-1} and the broad peak observed around 700 cm^{-1} result from vinylidene C-H in-plane bending and *cis*-C-H out-of-plane bending, respectively [140]. These peaks result from the MPS molecules. Si-O-C group in the MPS molecule was reported to have characteristic band at 1170 - 1190 cm^{-1} [134, 135]. Absence of this peak on the spectrum of the surface modified ZnO particles suggests that the methoxy groups (CH_3O) on the MPS molecule were hydrolyzed and the Si-O-C bond no longer existed. The peaks observed at 1103 and 1022 cm^{-1} were assigned to Si-O-Si bonds [140], suggesting the bonds formed between MPS molecules. The peak at 533 cm^{-1} observed in the spectra of both treated and untreated particles was attributed to the Zn-O stretching.

The comparison of the FTIR spectra of the untreated and treated particles indicated that chemical bonding of MPS molecules on the ZnO particles surface was successful. The reaction sequence given in Figure 4.13 was the proposed mechanism of surface modification [71, 74, 84]. The first reaction step given shows the hydrolysis of the silane molecule in the water, producing three moles of methanol per mole of silane. Absence of the peak at 1180 cm^{-1} band of the FTIR spectra obtained for surface modified particle implied that this reaction step took place during the silanization process. The second reaction step shown in the figure was the condensation reaction of silane molecules with each other and the resulting molecules were homocondensates. Formation of the Si-O-Si bond demonstrated by FTIR analysis indicated that occurrence of this step. The final reaction step shows the bonding of silane to the OH^- ions on the ZnO surface.

At the end of silanization procedure, the surface of ZnO was considered to transform from hydrophilic to hydrophobic, gaining compatibility with the PHBV polymer. SEM micrograph of the ZnO particles taken after surface modification is given in Figure 4.14.

The difference in brightness observed in the SEM image, compared to untreated particles images, indicated surface coverage of silane. Transformation of ZnO particles from hydrophilic to hydrophobic was considered to be successful.

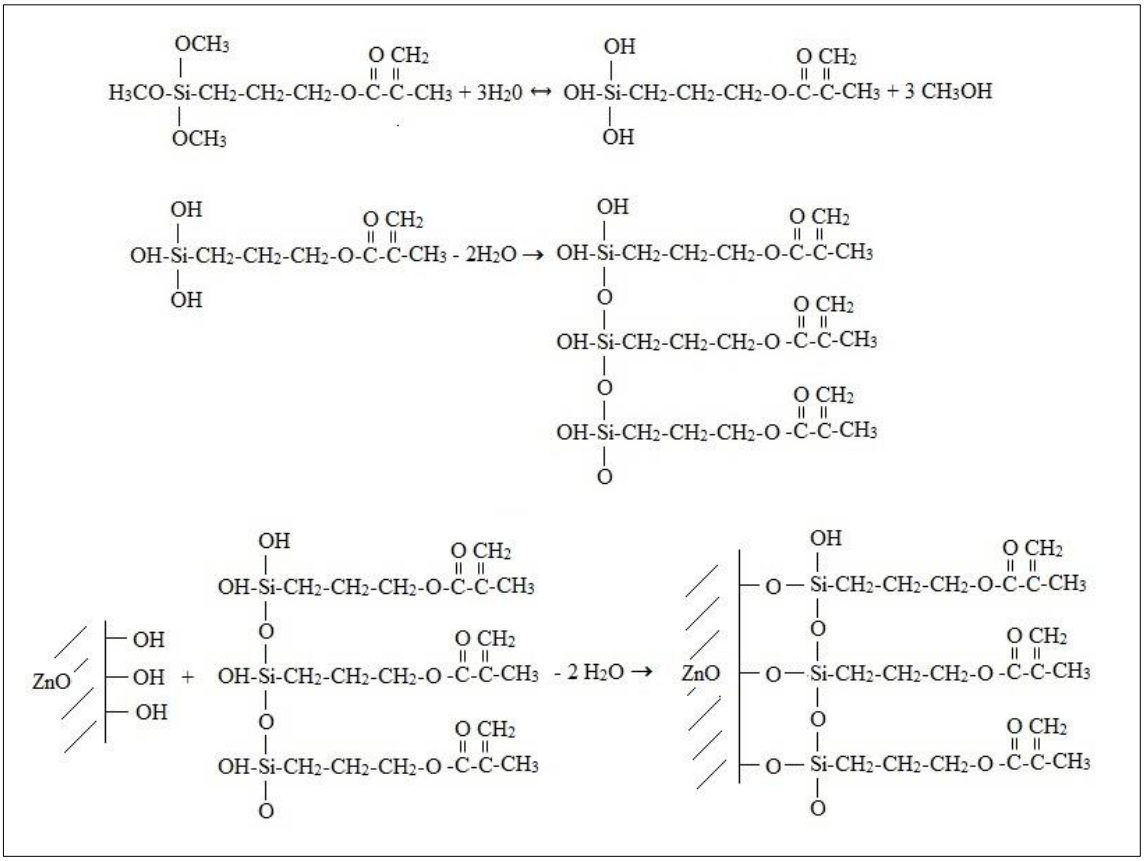

Figure 4.13 Schematic model of grafting reactions of MPS on ZnO particles

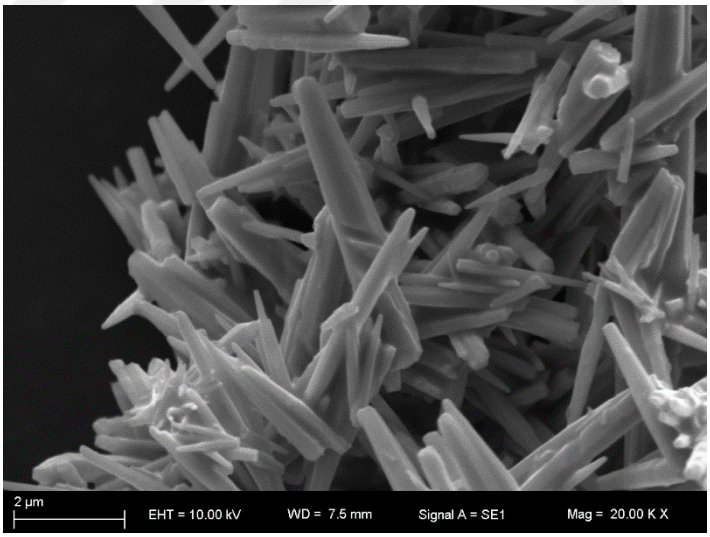

Figure 4.14 SEM micrograph of the ZnO-2L-95C particles after surface modification with MPS

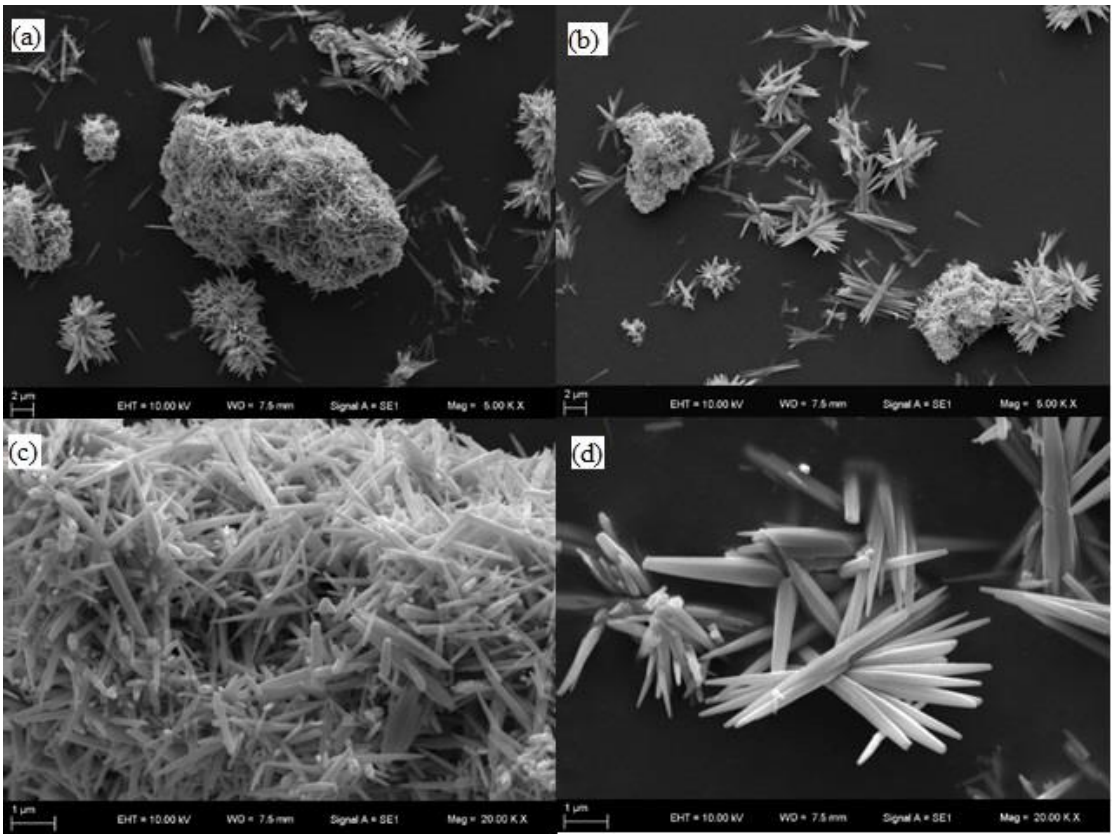

Figure 4.15 SEM micrographs of the MPS treated ZnO-2L-95C particles after 15 min of ultrasound application (a) at 5000x magnification, (b) at 5000x magnification in another area, (c) at 20000x magnification and (d) at 20000x magnification in another area

4.3.4 Ultrasonic Dispersion of the MPS-Treated ZnO-2L-95C Particles

Surface modification using silane was applied for two purposes. One of them was increasing the compatibility of the particles with the polymer by hydrophobicity. The other purpose was inhibition of particle agglomeration. The SEM image of the surface treated particles showed severe agglomeration, indicating that surface modification was ineffective in deagglomeration of the particles. Therefore, ultrasonic dispersion was applied to the surface treated particles.

Procedure for the application of ultrasonic dispersion was the same as described in Section 4.2. Since 60 min of ultrasound application was found to be very effective on untreated particles, ultrasonication time was shortened to 15 min in this case in order to see if shorter time could be effective as well. SEM micrographs of silane treated particles after 15 min of ultrasonic agitation are given in Figure 4.15. Ultrasonic agitation was partially effective in deagglomeration of the particles.

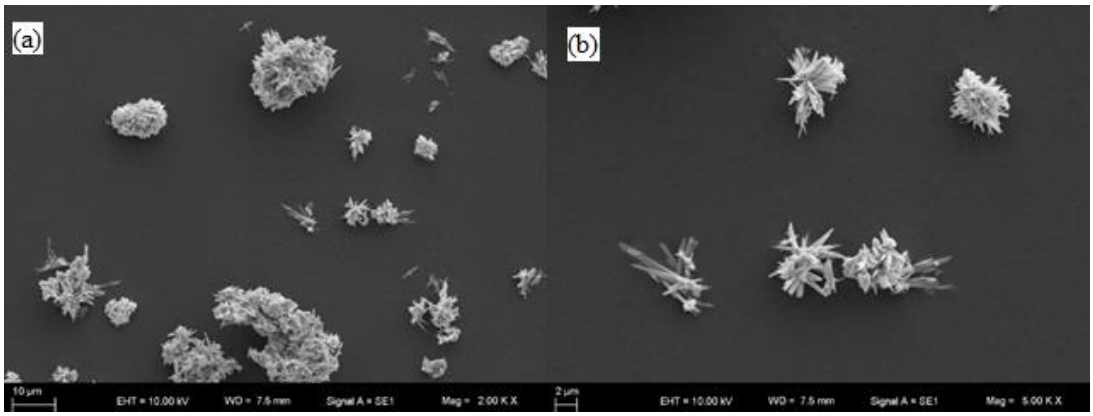

Figure 4.16 SEM micrographs of the MPS treated ZnO-2L-95C particles after 60 min of ultrasound application (a) at 2000x magnification and (b) at 5000x magnification

Ultrasonication time was increased to 60 min in order to increase the effectiveness in particle deagglomeration. SEM micrographs of the surface treated ZnO-2L-95C particles after 60 min of ultrasound application are given in Figure 4.16. Although increased ultrasonication time was more effective than shorter ultrasound application, it was not sufficient for complete deagglomeration of the particles. Asterisk-shaped rod arrays observed in the as-synthesized particles were still observed after 60 min of ultrasonic agitation. The bonds between the silane molecules covering the ZnO particles were thought to be responsible in inhibition of deagglomeration.

4.4 Effect of CMI as a Growth Inhibitor

Control of size and morphology of micro- and nano-sized crystal particles during synthesis is an important challenge since size and morphology are strongly affected by synthesis reaction parameters. Utilization of crystal growth modifiers can help to overcome the sensitivity to these parameters [57]. Growth modifiers are soluble additives to the synthesis reaction that influence the growth and morphology of crystals, usually by adsorbing or binding to the crystal surfaces [141]. There are various types of crystal growth modifiers such as multivalent cations, surface active agents, soluble polymers, biologically active macromolecules, and soluble salts [141].

Carboxymethyl inulin (CMI) is a water-soluble biopolymer used in controlling the crystallization of calcium carbonate [63-65, 142], calcium oxalate [66], and hydroxyapatite [67, 68]. CMI was reported to inhibit $CaCO_3$ precipitation by affecting growth rate and morphology of crystals and length of the inhibition period [63, 64],

increase the induction period (or time lag) in CaOx synthesis [66], and affect the growth rate [67], morphology, surface area and size of hydroxyapatite crystals [68].

The effect of CMI on growth and precipitation of ZnO crystals was studied by Akin and Öner [62]. The size and the morphology of the ZnO particles were affected by the presence of CMI. The effects depended on the concentration of the CMI used, and even very small concentrations were effective. For the concentrations of CMI between 1 and 50 ppm; as the concentration of CMI was increased, the dimensions of the rod-shaped ZnO particles were affected. Longer and thicker ZnO particles were obtained with increasing CMI concentration. However, at the CMI concentration of 150 ppm, a change in the morphology of the particles was observed and hexagonal bipyramid crystals were obtained. When CMI concentration was further increased to 450 ppm, a mixture of small spherical nanoparticles and bipyramids were obtained.

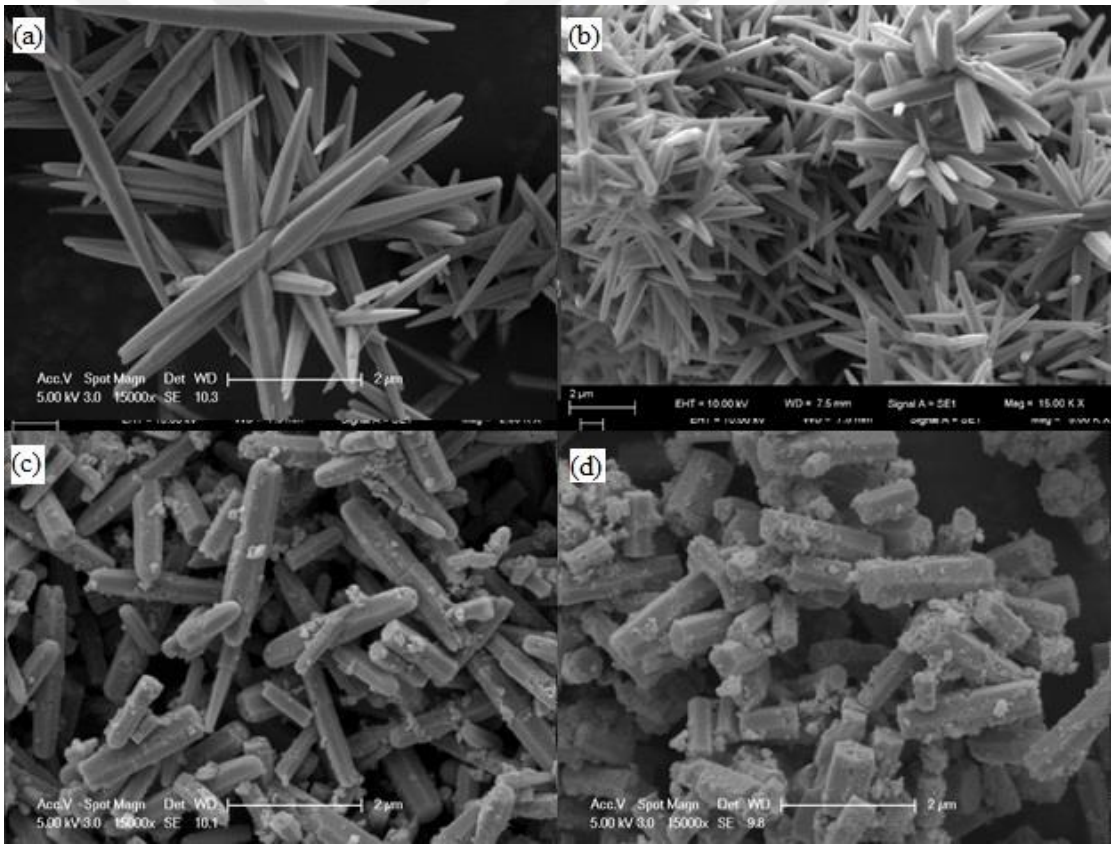

Figure 4.17 SEM micrographs of the ZnO particles synthesized with different CMI concentrations: (a) without CMI, (b) 50 ppm CMI, (c) 450 ppm CMI, and (d) 750 ppm CMI

In this study, the effect of CMI on the growth of ZnO-2L-95C particles was investigated for new reaction parameters used in this study, i.e. precursors concentration and reactor volume. Three different concentrations of CMI (50, 450, and 750 ppm) were studied.

The ZnO particles were synthesized with the same method and parameters as ZnO-2L-95C particles, but varying concentrations of CMI were added together with the reaction precursors. The SEM micrographs of the particles synthesized in presence of different concentrations of CMI are given in Figure 4.17. When 50 ppm of CMI was added to the synthesis reaction, the morphology of the ZnO particles did not show any difference from the particles synthesized without CMI. Rod-shaped ZnO particles were obtained and these particles were formed in regular arrays resembling an asterisk shape, just like the ZnO rods synthesized without CMI addition. Presence of CMI in the reaction mixture affected the dimensions of the rod particles obtained. While the ZnO-2L-95C particles synthesized without CMI had a mean length value of 6381 ± 895.2 nm, the particles synthesized with 50 ppm CMI addition (ZnO-50-2L-95C) had a mean length of 4800.7 ± 638.0 nm. The mean length of the rod particles was decreased by 25 % by the addition of 50 ppm CMI. The mean length of the particles, on the other hand, was increased from 395.3 ± 75.2 nm for the particles synthesized without CMI to 428.1 ± 70.7 nm for the particles synthesized with 50 ppm CMI. The mean width of the particles was increased by 8 %. The aspect ratio of the particles was decreased from 15.6 to 11.2 with 50 ppm CMI addition, corresponding to a 28 % decrease.

When the concentration of CMI added into the synthesis reaction of ZnO particles was increased to 450 ppm, the particles obtained were again rod-shaped. However, some differences were observed in their structure compared to the particles synthesized without CMI or with 50 ppm CMI addition. The regular rod arrays connected the particles from the centers of the rods disappeared and deagglomerated, singular rod-shaped particles were obtained. The hexagonal structure of the rods was still apparent, nevertheless the tips of the hexagonal rods turned from needle-like shape to more rounded tips. The mean length of the ZnO-450-2L-95C particles was 2315.9 ± 449.2 nm and the mean width of the particles was 510.2 ± 82.35 nm. When compared to the particles synthesized without CMI addition, the mean length was decreased by 62.5 % and the mean width was increased by 29 %. The aspect ratio of the ZnO-450-2L-95C particles were calculated as 4.5 and this value was 71 % lower than that of ZnO-2L-95C particles.

Upon further increasing the CMI concentration to 750 ppm, even shorter and thicker rods were obtained. The mean length was 2020.4 ± 233.9 nm in this case and the mean width was 557.3 ± 113.1 nm. This accounts for a decrease in length by 67 % and an

increased in width by 41 %, compared to the ZnO-2L-95c particles. The aspect ratio of ZnO-750-2L-95C particles was calculated as 3.6, which is 94% lower than the aspect ratio of ZnO-2L-95C particles. The rod-shaped particles synthesized by 750 ppm of CMI addition were again observed to be hexagonal shaped. The polar planes of the rods (tips of the hexagonal rod structures) in this case, were observed to be completely flat. The changes in the particle dimensions and aspect ratio with changing CMI concentration is summarized in Table 4.3.

The morphology of a crystal is defined by the relative growth rates of different crystallographic faces. The faces of a crystal with slower growth rates are more effective than the fast-growing faces on the final morphology of the crystal particle. The growth rates of the faces both depend on the structure of the crystal and environmental effects [141].

Table 4.3 Effect of CMI concentration on the particle dimensions and aspect ratio

Sample Code	**CMI concentration, ppm**	**Mean Length, nm**	**Mean Width, nm**	**Aspect Ratio, L/W**
ZnO-2L-95C	0	6381 ± 895.2	395.3 ± 75.2	15.6
ZnO-50-2L-95C	50	4800.7 ± 638.0	428.1 ± 70.7	11.2
ZnO-450-2L-95C	450	2315.9 ± 449.2	510.2 ± 82.35	4.5
ZnO-750-2L-95C	750	2020.4 ± 233.9	557.3 ± 113.1	3.6

The hexagonal wurtzite structure of ZnO crystals is composed of closely packed Zn and O atoms in a hexagonal prism shape. The structure has well defined crystal faces, composing of two polar facets perpendicular to the *c*-axis and the nonpolar side facets parallel to the *c*-axis [143]. One of the polar basal planes (0001) is the Zn-terminated face and it is occupied by Zn^{2+} ions, while the other polar basal plane $(000\bar{1})$ is the O-terminated face composed of O^{2-} ions. The nonpolar side faces of the hexagonal rod particle $\{hkl0\}$ are composed of equal numbers of zinc and oxygen atoms and therefore electrically neutral [144]. The nonpolar faces have a low surface energy, while the polar surfaces have a high surface energy [60]. Therefore, the growth rate of the (0001) plane is higher than the nonpolar $(10\bar{1}0)$ plane, resulting in the anisotropic rod-shaped growth

along the *c*-axis [Biswas, Das et al., 2008]. If the surface of the hexagonal prism structure is considered on a two-dimensional scale, the area occupied by one Zn^{2+} ion is 9.16 A°^{2} on the polar face, while it is 16.94 A°^{2} on the nonpolar faces [145]. Hence, the density of the Zn^{2+} ions is higher on the polar face than the nonpolar faces.

In previous studies related to the utilization of various organic additives as growth modifier for ZnO, it was reported that organic molecules can interact with specific surfaces of the growing ZnO crystals, modifying the growth rates of these faces, therefore altering the final size, shape or morphology of the grown crystals [60, 61, 143-145]. These organic additives, such as water-soluble polymers, are commonly considered to adsorb on the growing particles on specific crystallographic directions changing the growth habit.

Garcia and Semancik [57] studied the effect of three different growth modifiers (poly(diallyldimethylammonium chloride), sodium poly(styrene sulfonate), and trisodium citrate) on the morphology of ZnO nanorods and reported that the modifiers resulted in a decrease in the aspect ratio of the ZnO rods at different extents. The reduction in the aspect ratio implied that the modifiers altered the growth anisotropy by face-specific adsorption to crystal surfaces. They suggested that, adsorbed species could have suppressed the growth of a surface by hindering the attachment of growth units, or alternatively enhanced the growth by reducing the electrostatic repulsion between the surface and the growth units. Among the modifiers they used, citrate is a molecule with three carboxylate groups and at the pH of their system, citrate was completely protonated and had three negatively charged sites. Similar to CMI used in this study, which also has carboxylate groups on its structure, the addition of citrate resulted in an increase in the width of the ZnO crystals, together with a decrease in the length. They hypothesized that citrate bound strongly on the polar (0001) face and weakly on the nonpolar $(10\bar{1}0)$ face and therefore drastically suppressed the axial growth compared to the equatorial growth. They also suggested that, other than adsorbing on specific crystals planes, citrate also bound Zn^{2+} ions as a chelating ligand and reduced their deposition on crystal surfaces.

Golovko and co-workers [144] studied the forces between latex particles functionalized at the surface with carboxylic groups and differently terminated ZnO surfaces by atomic force microscopy. They suggested preferential adsorption of the latex particles on polar (0001) faces of ZnO, reducing the growth rate along this direction. Due to the

electronic structure of ZnO crystal surfaces (i.e. Zn^{2+} and O^{2-}-terminated polar faces and electrically neutral nonpolar faces), preferential adsorption of hydrophilic polymers on certain surfaces would be reasonable to assume. The force-distance measurements they performed confirmed that carboxylic-functionalized particles preferentially adsorbed on the Zn-terminated polar (0001) faces of ZnO crystals, explaining the morphological change in the crystals in presence of hydrophilic polymers.

Considering the ZnO crystals synthesized in this study with varying concentrations of CMI, it can be deduced that, the carboxylate moieties of the hydrophilic CMI polymer was adsorbed on the Zn-terminated polar surfaces of the growing ZnO rods, binding Zn^{2+} ions on this surface. Therefore, deposition of the new growing units on this crystal plane was hindered. This resulted in the decrease in the axial growth of the rods, while the equatorial growth became more pronounced. As the concentration of CMI was increased, the ZnO crystals got shorter in axial length and thicker in equatorial width. The effect of different CMI concentrations added to the synthesis reaction on the length and the width of the ZnO rod-shaped particles is shown in Figure 4.18. The effect of CMI concentration on the dimensions of the particles seemed to be changing exponentially, rather than linearly, suggesting the effect on the dimensions would get smaller as the CMI concentration increases.

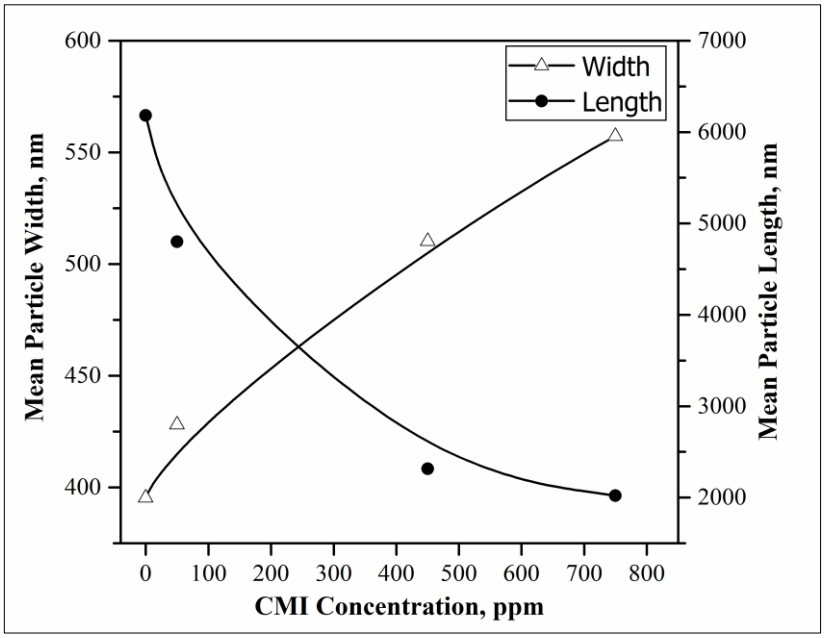

Figure 4.18 Effect of CMI concentration on the mean dimensions of the rod-shaped ZnO particles

The ZnO-2L-95C particles synthesized previously without the addition of CMI (Figure 4.17a), were observed to be tapered along the *c*-axis, deviating from a perfect hexagonal prism. The tips of the rods were observed to have a needle-like shape. This was explained by the rapid growth rate of the polar planes. When CMI was added to the reaction as a growth inhibitor, the tapering along the *c*-axis and the shape of the tips were affected. When the concentration of CMI was 50 ppm, the rods were still tapered in shape but rods with relatively flatter ends were observed together with needle-type ends. When the concentration of CMI was increased to 450 ppm, much less tapering was observed and the ends of the rods were more rounded rather than having needle-shape. When the concentration was further increased to 750 ppm, tapering completely disappeared and the particles had perfect hexagonal cross-sections. The tips of the rods were also completely flat and had well-defined hexagonal shape. The decrease in the axial growth rate was considered to be responsible for this effect. As CMI concentration was increased and the rate of the polar faces decreased, there was sufficient time for the new growing units form a uniform hexagonal surface; rather than fast depositing and nonuniform growth. The suggested mechanism affecting the dimensions, tapering and tip shapes of the ZnO rods was shown schematically in Figure 4.19.

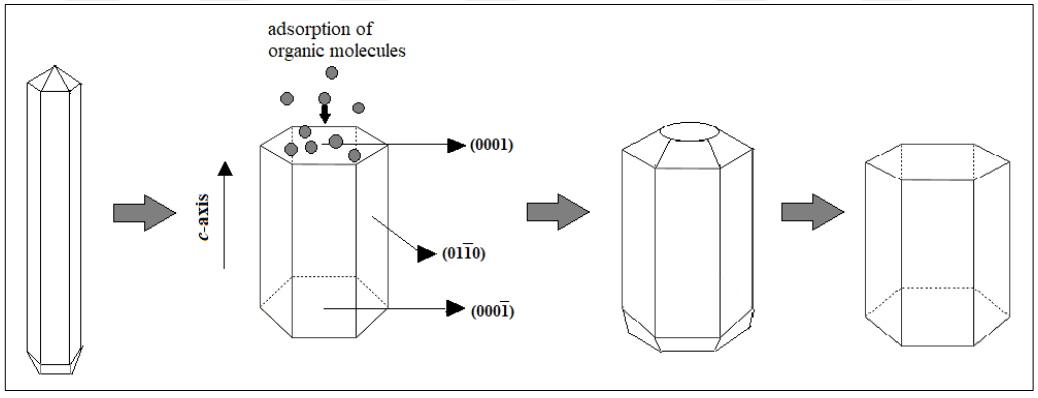

Figure 4.19 Schematic illustration of the mechanism how CMI affects particle size and shape

Another important observation from Figure 4.17 is that the asterisk-shaped rod arrays were formed when no or low concentration of CMI was added, whereas singular rod particles were obtained for higher concentrations of CMI. Other than affecting particle size, shape and morphology, polymers were reported to affect particle agglomeration as well [61, 65]. The polymers were suggested to isolate salt solutions by adsorbing on surfaces immediately after nucleation has started, and to force them to grow as

individual particles [141]. This effect was assumed to be dominant only after a critical concentration of CMI used in this study.

For the concentrations of CMI higher than 50 ppm, twinning of the crystals became apparent. The particles were formed by two adjacent symmetrical rods adhered to each other at the center part of the particles. Twinning phenomenon is explained as growing of twinned crystals along the (0001) direction (Zn-terminated polar face) from the common basal ($000\bar{1}$) plane (O-terminated polar face) [146]. Occurrence of twinning in presence of carboxylate containing growth modifiers such as CMI [62, 63, 66] and citrate [146]. However, study twinning was believed to be the growth mechanism of all crystals synthesized with or without CMI addition in this study. Since the particles synthesized with 0 ppm and 50 ppm CMI were attached to each other from their central points, forming rod arrays, twinning could not be observed in the SEM images of these particles. Twinning of ZnO particles was observed in a variety of synthesis conditions, with or without the addition of growth modifiers [57].

Biswas and his co-workers [143] studied the growth kinetics of ZnO rods with and without the addition of poly(vinyl pyrollidone) (PVP) as a growth modifier. Unlike CMI, presence of PVP resulted in longer and narrower ZnO rods. They investigated the size distributions of the rods obtained with and without PVP. In the absence of PVP, the length and width distribution of the particles were somewhat asymmetric; whereas in case of added PVP, they showed a distribution that can be represented by a Gaussian distribution function. Since the asymmetric distributions of length and width showed a diffusion-limited Ostwald ripening growth mechanism; they suggested that Ostwald mechanism alone does not explain the growth mechanism of the particle in presence of PVP. They reported that the length data of the PVP-capped particles did not fit the diffusion limited growth model or the surface-limited reaction model, but showed good fit to a model that combines both diffusion-limited and surface-limited growth.

Viswanatha and Sarma [147] also studied the growth of ZnO crystals in presence of PVP and used an approach to estimate the size distribution of ZnO particles using UV-absorption spectrum. They tried to fit the data obtained for average particle diameter as a function of time in presence of PVP, to the Ostwald ripening theory. Nevertheless, they could not fit the data in any case. Therefore, they suggested that the growth mechanism deviated from Ostwald ripening.

The length and width distributions of the particles synthesized in this study in absence and presence of CMI were compared (Figure 4.20). For this purpose, the particles synthesized in the highest concentration of CMI (750 ppm) were selected. The histograms were obtained according to the frequency of the given size ranges observed. A Gaussian distribution curve was fitted to each histogram obtained. It can be observed from the graphs that, the length and width distribution obtained for the particles synthesized in presence of CMI fit quite well to the normal distribution curves. The length and width histograms obtained for the particles synthesized in absence of CMI, on the other hand, show asymmetrical distributions. Similar to the findings of the previous studied carried out with PVP, the growth mechanism of the crystals synthesized in presence of CMI seemed to deviate from the Ostwald mechanism.

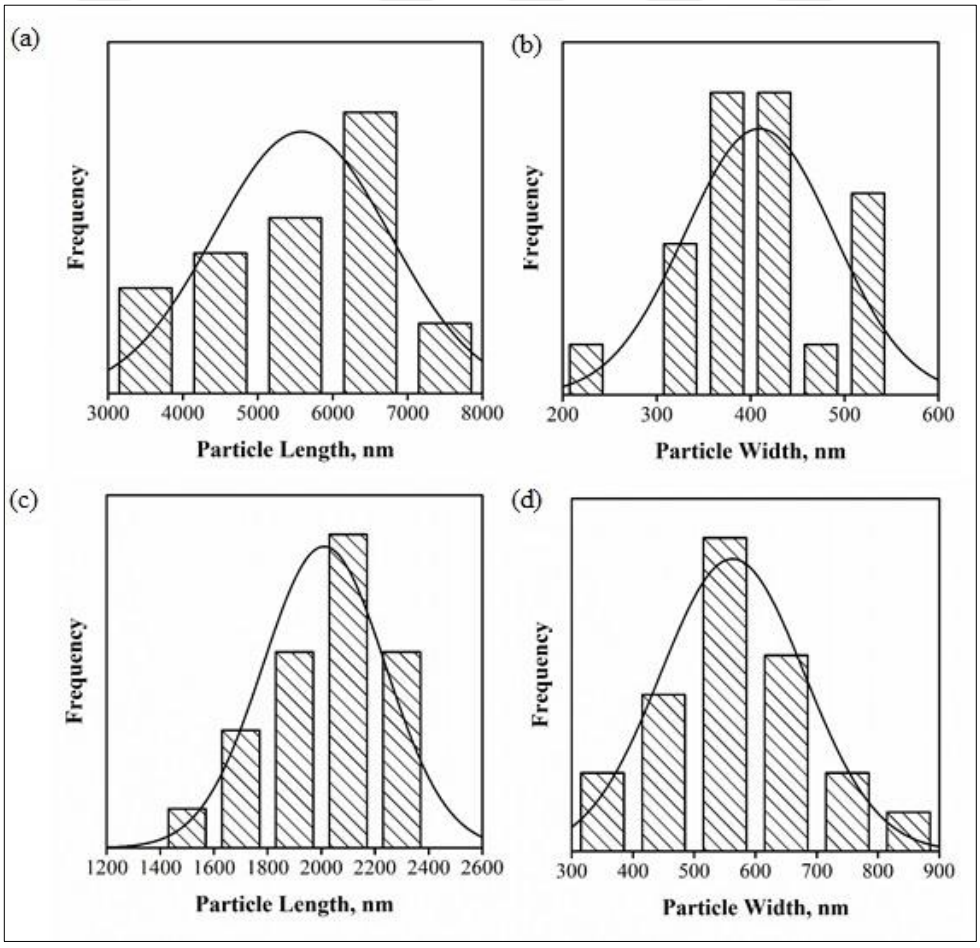

Figure 4.20 Size distribution histograms and Gaussian curves of (a) ZnO-2L-95C particles and (b) ZnO-750ppm-2L-95C particles

4.4.1 XRD Analysis of ZnO Particles Synthesized in Presence of CMI

The effect of CMI addition to the ZnO synthesis reaction on the crystalline structure of the particles was investigated by XRD analysis. XRD analysis was carried out for ZnO particles synthesized in presence of 50 and 450 ppm CMI, since these particles were used in the fabrication of PHBV nanocomposites, as will be described in following sections. The particles synthesized in presence of 750 ppm CMI were not used in nanocomposites fabrication due to their low aspect ratio. Therefore, further characterization was not applied to these particles.

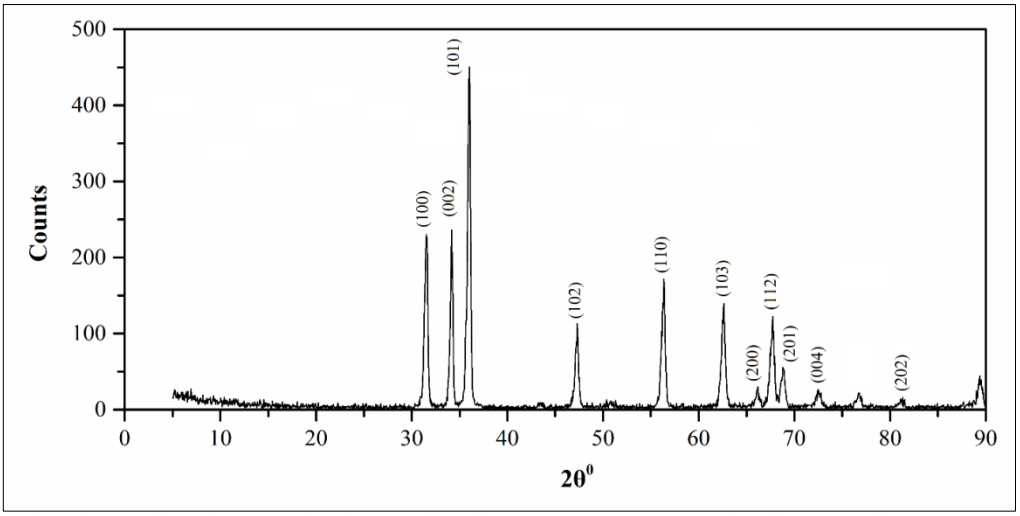

Figure 4.21 XRD diffractogram of ZnO-50-2L-95C particles

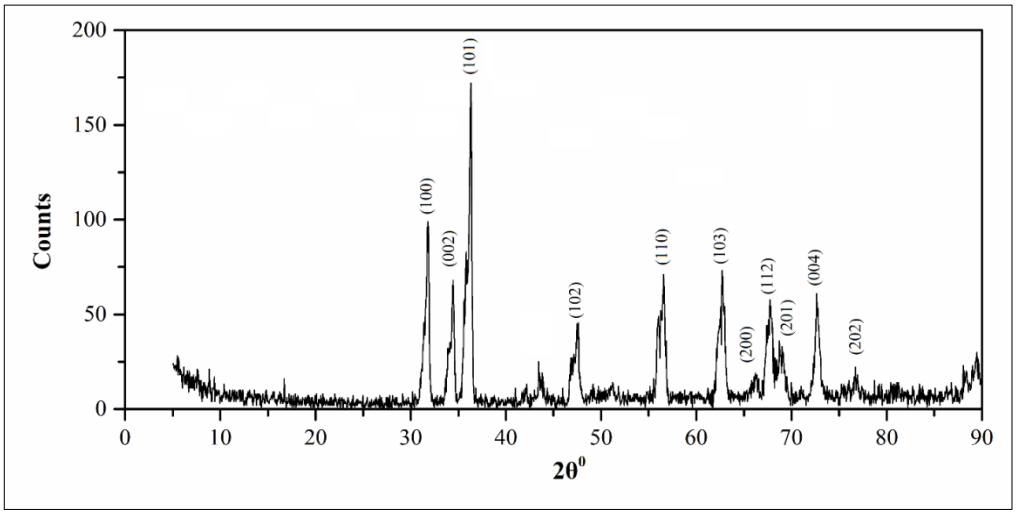

Figure 4.22 XRD diffractogram of ZnO-450-2L-95C particles

The XRD diffractograms obtained for ZnO-50-2L-95C and ZnO-450-2L-95C particles are given in Figure 4.21 and 4.22, respectively. The diffraction peaks obtained for both particles agree well with the standard card JCPDS 36-1451 of hexagonal phase ZnO,

similar to ZnO-2L-95C particles. The sharp and clear peaks indicate well-crystallized structure. The peaks observed at 43.72° and 76.79° for ZnO-50-2L-95C particles and at 35.68°, 42.11°, 43.65°, 55.93°, 76.80° and 88.25° for ZnO-450-2L-95C particles were assigned to impurities in the crystalline structure. These impurities might be due to the existence of CMI within the crystal structure.

Table 4.4 XRD parameters of ZnO-50-2L-95C and ZnO-450-2L-95C particles

ZnO-50-2L-95C particles				**ZnO-450-2L-95C particles**			
2θ°	**I, %**	**d, A°**	**hkl**	**2θ°**	**I, %**	**d, A°**	**hkl**
31.56	50.22	2.84	(100)	31.83	56.30	2.81	(100)
34.22	44.74	2.62	(002)	34.45	36.51	2.60	(002)
36.03	100.00	2.49	(101)	36.29	100.00	2.48	(101)
47.33	24.90	1.92	(102)	47.58	21.26	1.91	(102)
56.41	36.24	1.63	(110)	56.59	38.95	1.63	(110)
62.57	29.28	1.48	(103)	62.83	31.25	1.48	(103)
66.12	5.45	1.41	(200)				
67.73	26.96	1.38	(112)	67.83	28.24	1.38	(112)
68.86	11.20	1.36	(201)	69.11	13.85	1.36	(201)
72.61	3.55	1.30	(004)	72.72	28.92	1.30	(004)
81.15	1.93	1.18	(202)				

Table 4.4 gives the data obtained from XRD analysis for ZnO-50-2l-95C and ZnO-450-2L-95C particles. The 2θ peak positions, relative intensities of the peaks (the ratio of the peak intensity to that of the most intense peak, I), lattice spacings (d) and hkl indices that the peaks were indexed are given in the table. The values of d-spacings were calculated for each peak according to Bragg's law, as described in the section 4.1.4.

The (100) plane shows the equatorial face of the ZnO rods and the relative intensity of the peak associated with this plane was higher for the ZnO-450-2L-95C particles, compared to the ZnO-50-2L-95C particles. Since peak intensity are related to the electron density at that direction [94], and ZnO-450-2L-95C particles had higher width, an increase in (100) peak density was observed. Similarly, the relative peak density of

(002) that represents the polar face was lower for ZnO-450-2L-95C particles since they had lower length compared to ZnO-50-2L-95C particles. Therefore, it can be said that the XRD results were in agreement with the SEM results.

Table 4.5 Average crystallite sizes of ZnO-50-2L-95C and ZnO-450-2L-95C particles estimated from XRD spectrums

ZnO-50-2L-95C particles				**ZnO-450-2L-95C particles**			
2θ°	**hkl**	**B, radians**	**L, nm**	**2θ°**	**hkl**	**B, radians**	**L, nm**
31.56	(100)	0.3936	37.86	31.83	(100)	0.2460	60.61
34.22	(002)	0.2952	50.82	34.45	(002)	0.2460	61.02
36.03	(101)	0.2952	51.08	36.29	(101)	0.1968	76.67
47.33	(102)	0.3444	45.46	47.58	(102)	0.2460	63.70
56.41	(110)	0.3444	47.24	56.59	(110)	0.1476	110.33
62.57	(103)	0.492	34.10	62.83	(103)	0.4920	34.15
66.12	(200)	0.2952	57.96				
67.73	(112)	0.246	70.20	67.83	(112)	0.3936	43.90
68.86	(201)	0.2952	58.89	69.11	(201)	0.5904	29.49
72.61	(004)	0.3936	45.21	72.72	(004)	0.3936	45.24
81.15	(202)	0.72	26.22				

The unit cell lattice constants were calculated as a(100)= 3.274 A° and c(002) = 5.240 A° (c/a = 1.60) for ZnO-50-2L-95C particles and as a(100)= 3.247 A° and c(002) = 5.210 A° (c/a = 1.60) for ZnO-450-2L-95C particles, according to Bragg's law and lattice geometry as described in section 4.1.4. The calculated values were very similar to those of ZnO-2L-95C particles and to the standard card.

The average crystallite sizes (L) were calculated according to Scherrer equation [98] and the results are given in Table 4.5. Considering the highest intensity peak related to (101) plane, the average crystallite size was increased to L= 51.08 nm for ZnO-50-2L-95C particles and to L= 76.67 nm for ZnO-450-2L-95C particles, compared to the value obtained for ZnO-2L-95C particles (L= 43.81 nm). Increasing CMI concentration increased the average crystallite size of ZnO samples. Since (101) plane shows one of

the equatorial faces, and CMI resulted in an increase in the dimensions of these faces, the increase in the crystallite size was expected.

4.4.2 FTIR Study of the ZnO Particles Synthesized in Presence of CMI

Molecular environment of the ZnO particles synthesized in presence of CMI was investigated with FTIR spectroscopy and compared to that of ZnO-2L-95C particles. The analysis was only applied to the particles synthesized with 50 and 450 ppm CMI addition, since these particles were utilized in the fabrication of PHBV nanocomposites. FTIR characterization of the particles synthesized in presence of 750 ppm CMI were omitted, since these particles were not used in the fabrication of PHBV nanocomposites due to their low aspect ratio. The FTIR spectra of the ZnO-2L-95C, ZnO-50-2L-95C, and ZnO-450-2L-95C particles are given in Figure 4.23. The spectra were obtained after baseline correction and are given in percent transmittance.

The peaks resulting from the stretching vibrations of the Zn-O bond in tetrahedral arrangement was observed to shift from the value observed for ZnO-2L-95C particles (514 cm^{-1}) to 534 cm^{-1} for ZnO-50-2L-95C particles and to 548 cm^{-1} for ZnO-450-2L-95C particles. Similarly, the peak resulting from the vibrations of the Zn-O bonds in octahedral arrangement shifted from 708 to 712 and 680 cm^{-1} for ZnO-50-2L-95C and ZnO-450-2L-95C particles, respectively. Structural environment of the bonds results in small shifts in the frequency [103]. The shifts in the frequencies of the Zn-O bonds were considered to be due to the presence of CMI within the structure. Furthermore, unlike the spectrum of the ZnO-2L-95C particles, the peak resulting from the bonds in octahedral arrangement were observed to be more intense than the peak of bonds in tetrahedral arrangement, in the spectra of CMI containing particles. This suggested that the density of oxygen atoms in the tetrahedral arrangement decreased with the presence of CMI. It can be deduced that, CMI molecules prefer locating on these sites during the synthesis reaction of ZnO, attaching to surrounding Zn^{2+} ions instead of oxygen atoms.

The broad peak at 3375 cm^{-1} of the spectrum of ZnO-2L-95C was assigned to the vibration of hydroxyl (-OH) groups at the ZnO surface due to the adsorption of atmospheric water [127, 129, 130]. The intensity of this peak was observed to increase slightly for ZnO-50-2L-95C particles and significantly for ZnO-450-2L-95C particles. Presence of OH groups within the structure of CMI molecules was responsible for this

increase. The O-H stretching of glucose and fructose units in the backbone of inulin were reported to produce a broad peak at 3277 cm^{-1} [148].

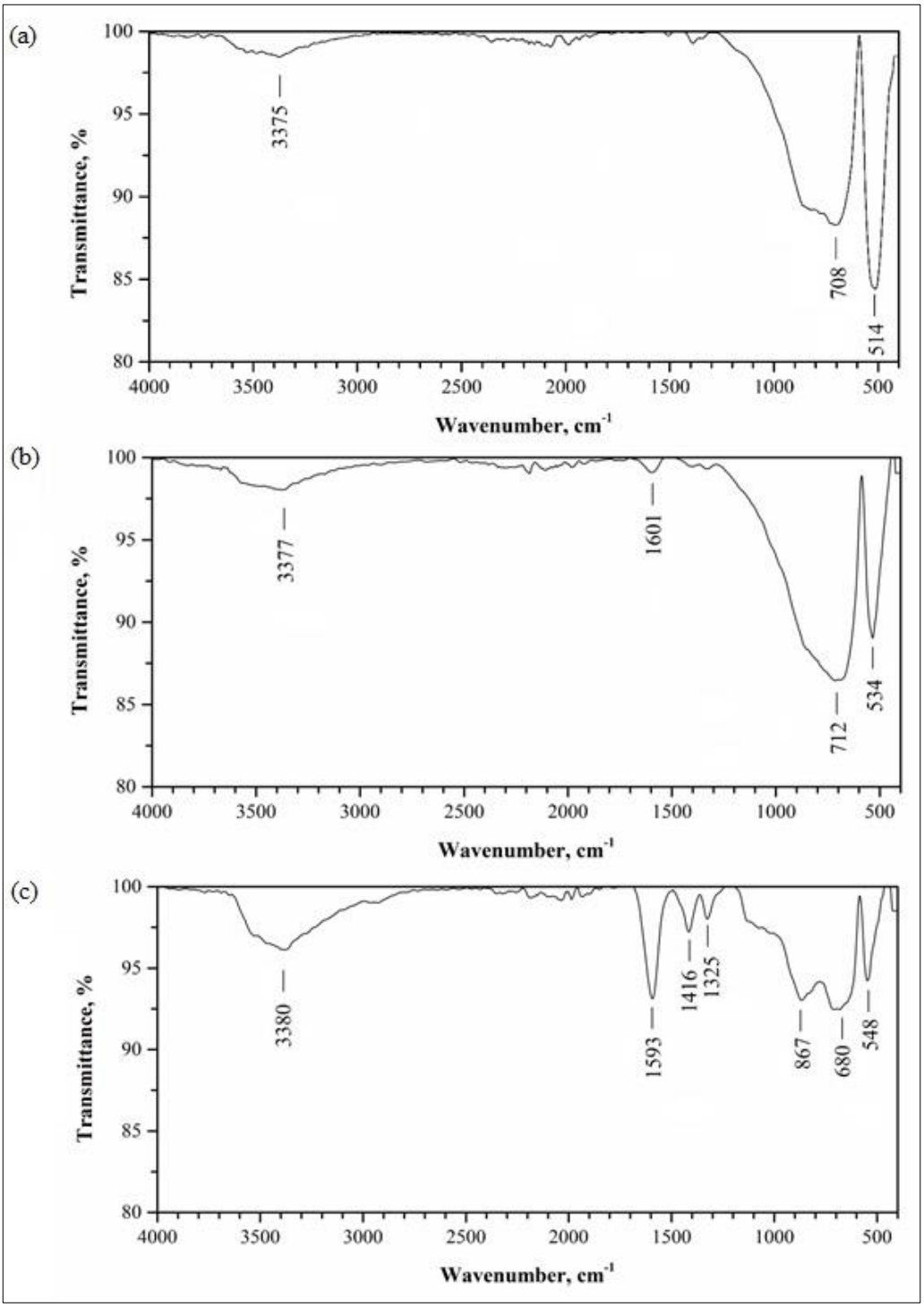

Figure 4.23 FTIR spectra of (a) ZnO-2L-95C, (b) ZnO-50-2L-95C, and (c) ZnO-450-2L-95C

The peak located at 1601 cm^{-1} in the spectrum of ZnO-50-2L-95C particles and at 1593 cm^{-1} in the spectrum of ZnO-450-2L-95C particles result from asymmetric stretching of the carboxylate ($-COO^-$) group of carboxymethyl structure [68, 140, 148]. The intensity

of this peak was observed to increase with increasing CMI concentration. The peak located at 1416 cm^{-1} in the spectrum of ZnO-450-2L-95C particles was produced by the symmetric stretching of carboxylate group of the carboxymethyl [148]. The peak at 1325 cm^{-1} was assigned to the CH_2 bending of the carboxymethyl group [68]. These peaks were only slightly visible in the spectrum of ZnO-50-2L-95C particles. The peak at 867 cm^{-1} and several weak peaks located around this peak are due to the aromatic C-H out-of-plane bending vibrations of inulin [140].

The results of the FTIR study revealed that CMI molecules were adsorbed on the surfaces or were integrated within the structure of ZnO particles. Carboxylate groups of CMI were considered to be adsorbed on the Zn-terminated polar faces of the crystals. FTIR study revealed that the preferred location for the carboxylate groups could be the octahedral interstitial sites.

4.5 Ultrasound Assisted Synthesis of ZnO Particles

The application of ultrasound to chemical reactions is referred to as sonochemical method. Application of ultrasound to a chemical reaction can result in various chemical and physical consequences due to enhanced mass transport, bulk thermal heating, and some other effects on solids [78]. The mentioned effects of ultrasound do not result from acoustic waves themselves but arise from acoustic cavitation which is the formation, growth, and collapse of bubbles within the irradiated liquid [78, 149, 150]. During cavitation, transient local hot spots occur within the reaction liquid for a few seconds due to the intense local heating, high pressures, and very short lifetimes produced by the collapse of bubbles [78, 149]. Hence, the energy created by acoustic cavitation can be acquired by chemical reactions [149]. Application of ultrasound to the synthesis of metal oxides was reported to enhance the reactivity of the metals, increase reaction rate, improve uniformity of size distribution and increase surface area [78].

Application of ultrasonic irradiation to aqueous liquids result in the formation of free radicals $H^{\cdot}$, $OH^{\cdot}$, $\cdot O_2^-$, and $\cdot HO_2$, which are strong oxidants and reductants [151]. Among them, $\cdot O_2^-$ radicals participate the growth reaction by reacting with Zn^{2+} [151]. Among the reaction steps of ZnO synthesis, mentioned in Section 4.1, the application of ultrasound is considered to affect the following reaction steps [149, 151]:

$$Zn(OH)_4^{2-} \overset{)))}{\rightarrow} ZnO + H_2O + 2\,OH^- \qquad (4.14)$$

$$Zn^{2+} + 2\ {\cdot}O_2^- \overset{)))}{\rightarrow} ZnO + \frac{3}{2}\ O_2 \qquad (4.15)$$

where the symbol))) denotes ultrasonic radiation. During the synthesis of ZnO particles with ultrasound assistance; ultrasonic cavitation was suggested to enhance nucleation rate at the beginning of ultrasound application and with further application of ultrasound, the crystals were suggested to grow due to local heating resulting from cavitation [150].

Wet chemical synthesis is a widely used method in ZnO particles synthesis, however they were reported to suffer from polydispersity and encounter difficulty in bringing the rod diameters under 100 nm [152]. The ZnO-2L-95C particles synthesized in this study were considerably monodisperse, having a uniform size distribution. Nevertheless, they suffered from particle agglomeration and the particle diameters were well above 100 nm. Therefore, ultrasound application was incorporated into the wet chemical synthesis method.

Liu and Zeng [152] studied application of ultrasonic pretreatment to the reaction mixture before hydrothermal synthesis of ZnO particles. The precursors mixture of zinc nitrate and NaOH was pretreated in an ultrasonic bath for 20 to 40 minutes and then taken into an autoclave for hydrothermal synthesis. The rod-shaped ZnO particles synthesized at the end of the procedure had an average diameter of 46 nm and an exceptional aspect ratio of 30 to 40. They reported that ultrasonic pretreatment was an important step that generated a suitable amount of cluster nuclei for the hydrothermal synthesis. When they repeated the same procedure, without ultrasonic pretreatment, they could not obtain the same uniform nanorod morphology. Instead, much larger and shorter rods were produced. Nonetheless, they used alcoholic environment and utilized ethylenediamine as capping agent, which were also effective in the inhibition of radial growth.

Wang et al. [79] synthesized ZnO particles in aqueous media from the reaction of zinc nitrate, thiourea, ammonium chloride and ammonia on several substrates. The reaction mixture was pretreated under an ultrasonic bath for 0 to 60 min. They reported that ultrasonic pretreatment had effects on the morphology of the ZnO arrays obtained and tube-like arrays were obtained under the ultrasonic pretreatment for 35 min. When ultrasonic pretreatment time was increased to 60 min, bundle-like morphology was obtained. When the ultrasonic pretreatment was further increased to 2 h, no ZnO

crystals could be obtained on the substrate. Incorporation of thiourea was also reported to be effective on the formation of tube-like structures.

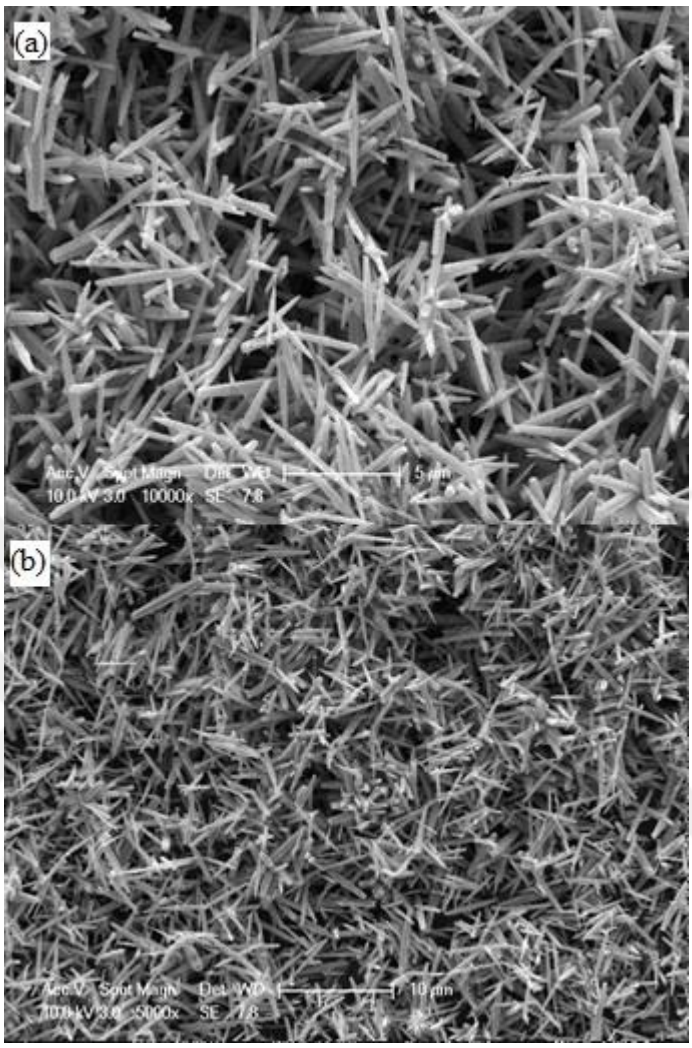

Figure 4.24 SEM micrographs of ZnO-2L-95C-UB40 particles at (a) 10000x and (b) 5000x magnification

Ultrasonic pretreatment was incorporated into the synthesis reaction of ZnO-2L-95C particles in order to observe any possible effects on the structure of the particles. The reaction mixture of zinc nitrate and HMT was treated under an ultrasonic bath for 40 min. At the end of this time, turbidity was observed in the normally clear reaction mixture and the temperature of the mixture was increased to 40 °C. Then the mixture was taken into the reactor and the regular conditions in the synthesis of ZnO-2L-95C particles were applied. The particles synthesized by this procedure were referred as ZnO-2L-95C-UB40 particles and their SEM micrographs are given in Figure 4.24. The ZnO-2L-95C-UB40 particles were hexagonal rod-shaped particles similar to the ones obtained without ultrasonic pretreatment. In other words, ultrasonic pretreatment

did not have an effect on the morphology of the particles. The rod-shaped particles showed tapering along *c*-axis, similar to the particles obtained without ultrasonic pretreatment.

The most prominent effect observed from the SEM micrographs was related to the agglomeration of particles. The ZnO-2L-95C particles synthesized with regular wet chemical synthesis method were observed to form rod arrays that were connected from their central points, resembling and asterisk shape. However, the ZnO-2L-95C-UB40 particles were obtained as homogeneously distributed singular rod particles. Application of ultrasound seemed to affect the self-aggregation mechanism that was previously suggested for the formation of rod arrays. Production of unaggregated ZnO rods was an important result in terms of the homogeneous distribution of the particles within the PHBV matrix.

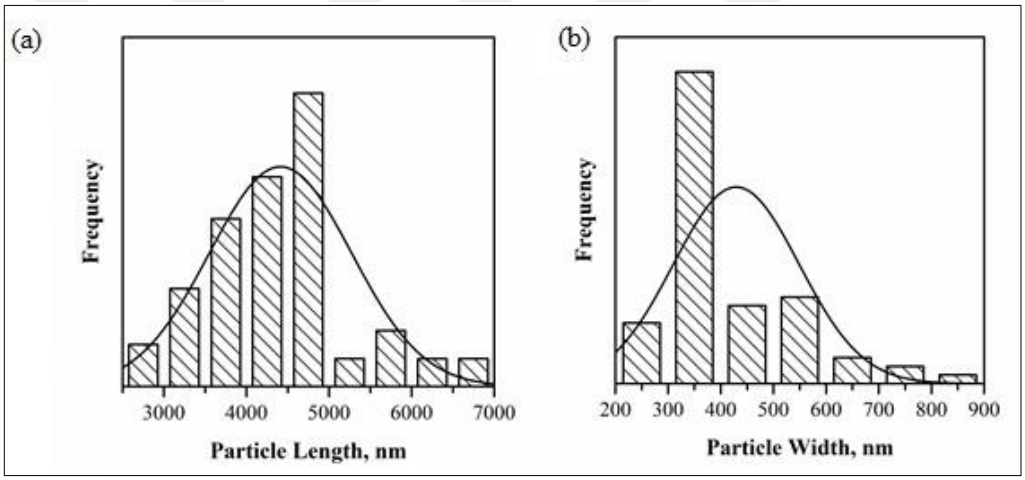

Figure 4.25 Size distribution histograms and Gaussian curves of ZnO-2L-95C-UB40 particles

Size distribution of the ZnO-2L-95C-UB40 particles was obtained by measurement of particle dimensions from the SEM micrographs. Size distribution histograms of the particles are given in Figure 4.25. The mean length of the particles was calculated as 4412.8 ± 862.4 nm and the mean width was calculated as 429.5 ± 119.6 nm. The aspect ratio of the particles was 10.3. When compared to the mean dimensions of the particles obtained without ultrasonic treatment (L = 6183.0 ± 895.2 nm, W = 395.3 ± 75.2 nm), a significant reduction (28.6 %) in particle length was observed together with a smaller (8.7 %) increase in particle diameter. Correspondingly, the aspect ratio of the particles was decreased by 34 %.

In the work of Jung et al. [153], increased ultrasonication time resulted in the formation of smaller-length nanocups instead of nanorods. The increase in the ultrasonication time, which resulted in continuous addition of energy to the reaction, was reported to hinder the growth of nanorods. It was suggested that, nanorod growth was not energetically favorable; but instead, dissolution of the polar surfaces from the synthesized rods was energetically favorable, resulting in shorter particle length and formation of tubular structures. Similarly, the transformation of tower-like ZnO structures into tubes with the application of ultrasonic pretreatment in the work of Wang et al. [79] was probably due to the dissolution of the polar faces of the ZnO tower-like structures, although it was not discussed in the article.

The ZnO nuclei that are formed during the initial growth stage are known to preferentially grow along the c-axis in the polar (001) direction, resulting in the growth of one-dimensional rod-shaped structures. Application of ultrasonic pretreatment to the synthesis reaction of the ZnO particles in this study, might have resulted in the dissolution of ZnO nuclei from the already formed ZnO rods back into the reaction mixture, resulting in a decrease in the length of the particles; since it was more energetically favorable when ultrasound energy was acquired by the reaction mixture.

When the mean values and standard deviations calculated for the dimensions of ZnO-2L-95C-UB40 particles were compared to those of the particles synthesized without ultrasound application, a small loss of monodispersity was observed. Although application of ultrasound to the chemical reaction system is known to increase monodispersity; it is also known that ultrasound can result in the fragmentation of brittle materials such as inorganic oxides due to interparticle collisions [78]. The decrease in monodispersity observed in the particles synthesized by application of ultrasound pretreatment might have resulted from particle fragmentations.

4.5.1 XRD Analysis of the ZnO-2L-95C-UB40 Particles

The crystalline structure of the ZnO-2L-95C-UB40 particles was analyzed by XRD analysis and the diffractogram of the particles is given in Figure 4.26. The diffraction peaks observed in the diffractogram agree with the hexagonal phase of ZnO given in the standard card JCPDS 36-1451. Sharp and clear peaks indicate a well-crystallized structure. The extra peaks observed at 43.65° and 50.93° were assigned to $Zn(OH)_2$ [120] and the small peaks at 42.06° and 49.0° were assigned to impurities.

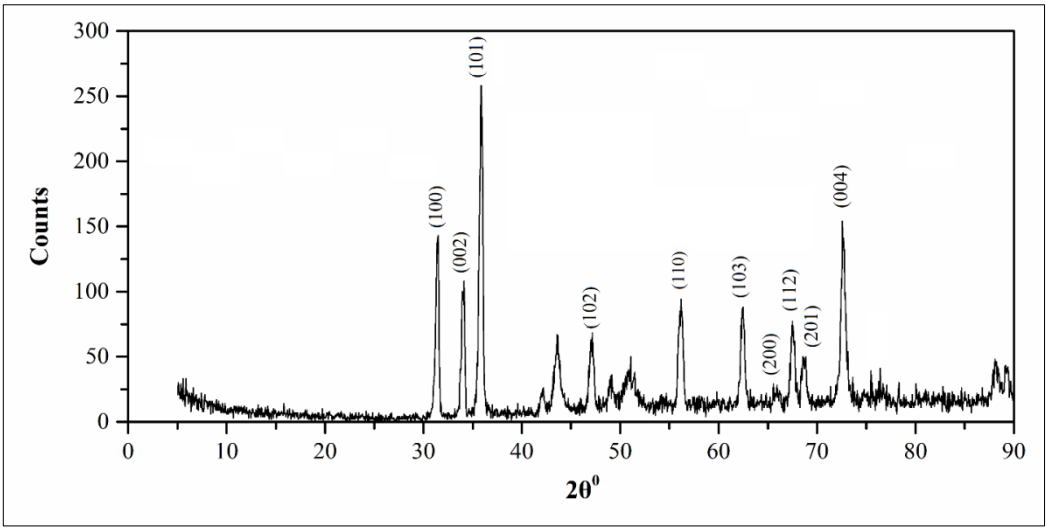

Figure 4.26 XRD diffractogram of the ZnO-2L-95C-UB40 particles

Table 4.6 XRD parameters of ZnO-2L-95C and ZnO-2L-95C-UB40 particles

ZnO-2L-95C particles			**ZnO-2L-95C-UB40 particles**			
2θ°	**I, %**	**d, A°**	**2θ°**	**I, %**	**d, A°**	**hkl**
31.86	52.14	2.8089	31.46	62.75	2.8435	(100)
34.55	36.56	2.5959	34.15	41.28	2.6252	(002)
36.29	100	2.4752	35.91	100	2.5004	(101)
47.60	21.84	1.9103	47.27	17.35	1.9227	(102)
56.60	35.05	1.6259	56.22	32.81	1.6360	(110)
62.96	39.4	1.4763	62.37	31.75	1.4887	(103)
66.42	5.05	1.4075	65.88	3.81	1.4177	(200)
67.93	21.65	1.3798	67.44	24.79	1.3886	(112)
69.19	13.56	1.3578	68.70	13.39	1.3662	(201)
72.68	23.87	1.3010	72.67	56.47	1.3011	(004)

Table 4.6 shows the 2θ peak positions, relative intensities of the peaks (I), lattice spacings (d) and hkl indices data, obtained from XRD analysis. The values of d-spacings were calculated for each peak according to Bragg's law. The data for the particles both synthesized with and without ultrasonic pretreatment are given in the table, for comparison purposes. The significant increase observed in the (004) direction and the smaller increase in (002) direction indicates a preferred c-axis alignment [154].

Unit cell lattice constants were calculated according to Bragg's law and lattice geometry as $a(100)$= 3.283 A° and $c(002)$ = 5.250 A° (c/a = 1.60). The calculated values were slightly higher than the ones given in the standard card. The average crystallite size (L) of the ZnO-2L-95C-UB40 particles were calculated using the Scherrer equation. The calculated values of L for each peak obtained for ZnO-2L-95C-UB40 particles are given in Table 4.7, where B is the full width at half maximum of the peak. Since (101) plane was the highest intensity peak, the average crystallite size of the ZnO-2L-95C-40UB particles was reported as the L value calculated as this plane which was equal to 34.04 nm. This value was lower than that of ZnO-2L-95C particles, which was calculated as 43.81 nm.

Table 4.7 Average crystallite sizes of ZnO-2L-95C-UB40 estimated from XRD spectrum

2θ°	**hkl**	**B, radians**	**L, nm**
31.46	(100)	0.2952	50.46
34.15	(002)	0.3444	43.55
35.92	(101)	0.4428	34.04
47.28	(102)	0.492	31.81
56.22	(110)	0.5904	27.53
62.37	(103)	0.3936	42.58
65.88	(200)	0.5904	28.94
67.45	(112)	0.246	70.08
68.70	(201)	0.492	35.30
72.67	(004)	0.246	72.35

In the work of Carp et al. [128], which studied the synthesis of ZnO by ultrasonic irradiation of the zinc acetate and ammonia mixture in an ultrasonic bath for different time intervals of 3 min to 2h, a white turbidity was reported to be observed as early as 2min of ultrasound treatment. The XRD analysis of the formed particles at this turbidity onset showed a minority phase of ZnO and a majority one identified as orthorhombic α-$Zn(OH)_2$. Pure ZnO phase was not obtained until 15 min of ultrasound application. The calculated lattice volumes of the particles obtained at short periods of ultrasound time

were found to be expanded compared to standards. Smaller crystallite sizes were also calculated. It was reported that, smaller crystalline domain sizes and higher lattice volumes indicated larger density of crystalline defects. Unit cell volumes calculated were same as the standard values after 120 min of ultrasonication, indicating less defected structure.

The XRD data obtained for ZnO-2L-95C-UB40 particles revealed decreased crystallite size, and increased lattice constant values when compared to those of ZnO-2L-95C particles, indicating increased Zn interstitial defects within the crystal structure [128]. The intensities of the impurity peaks assigned to $Zn(OH)_2$ were also increased. The application time of ultrasound was 40 min in this study, and turbidity of the reaction mixture was observed around this time. The temperature of the reaction mixture was 40 °C at this time. During the regular synthesis reaction without ultrasound application, the turbidity onset temperature is far above this temperature value (around 60 °C). Application of ultrasound is known to accelerate the transition of the precursors to ZnO crystals [150] and promote earlier formation of ZnO crystals [79]. Apparently these early-formed crystals exhibit higher defects in their structure. Increased ultrasonication time might have decreased the formation of these defects.

4.5.2 FTIR Study of the ZnO-2L-95C-UB40 Particles

Molecular structure of the ZnO-2L-95C-UB40 particles was investigated by FTIR spectroscopy. The spectrum obtained for the particles is given in Figure 4.27. The peaks observed at 526 cm^{-1} and 697 cm^{-1} were assigned to the stretching vibrations of Zn-O bond [131], similar to the particles obtained without ultrasound application. The second maximum (825 cm^{-1}) observed in the broad peak probably resulted from the increased polarity of the Zn-O bonds in octahedral arrangements [127, 128]. The intensity of the peak related to Zn-O bond in tetrahedral arrangement (526 cm^{-1}) was also observed to decrease when compared to the ZnO-2L-95C particles synthesized without the application of ultrasound.

The broad peak at 3379 cm^{-1} was assigned to the vibrations of -OH groups at the particles surface due to the adsorption of water [130]. The intensity of this peak was slightly increased when compared to the particles synthesized without ultrasound application, indicating slightly higher amount of -OH groups adsorbed.

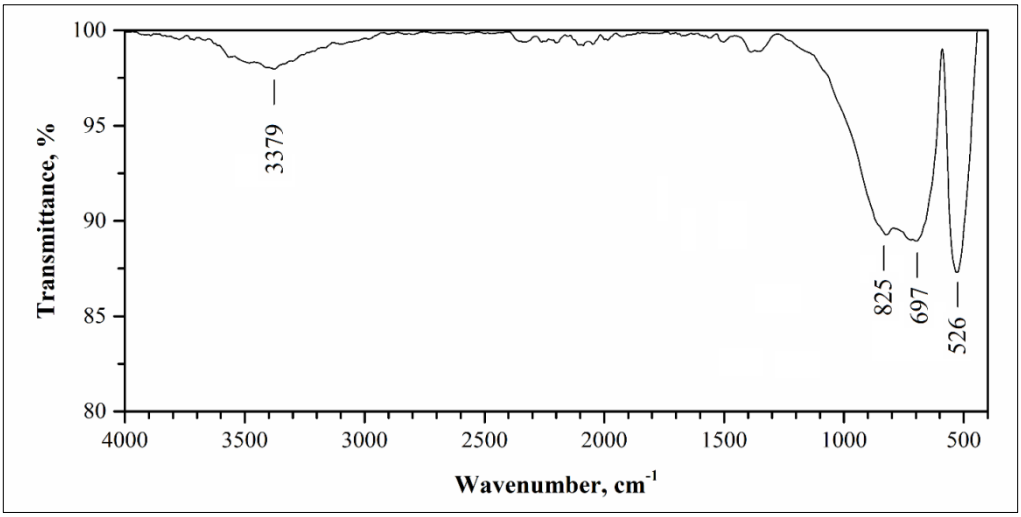

Figure 4.27 FTIR spectrum of the ZnO-2L-95C-UB40 particles

The broad peak at 3375 cm^{-1} of the spectrum of ZnO-2L-95C was assigned to the vibration of hydroxyl (-OH) groups at the ZnO surface due to the adsorption of atmospheric water [130].

4.5.3 Surface Modification of the ZnO-2L-95C-UB40 Particles

Surface modification of ZnO-2L-95C particles was carried out using MPS, as described in the previous sections. For the surface modification of ZnO-2L-95C-UB40 particles, another type of silane was studied, since determination of the most suitable silane for a given composite involves trials with different types of silanes. (Octyl)triethoxy silane ($CH_3(CH_2)_7Si(OC_2H_5)_3$, triethoxy(octyl) silane, OTES), which has an eight-carbon atom chain functional group in its structure (Figure 4.28) was selected for the surface modification of ZnO-2L-95C-UB40 particles. OTES was reported to be more hydrophobic than the various methyl, propyl or butyl-functional silanes. Since PHBV possesses high hydrophobicity [155], OTES was considered to be suitable for utilization in PHBV nanocomposites. Previously, Carli et al. [28] reported enhancement in mechanical properties of PHBV by the incorporation of OTES-modified halloysite clay.

Xu et al. [156] reported that they achieved super-hydrophobic surface of ZnO nanowire films by modifying the surface with OTES. Super-hydrophobic surface refers to a surface which has a contact angle with water larger than 150° and can repel water extremely. The ZnO nanowire film they synthesized was hydrophilic in nature, with a contact angle of almost 0°. After surface modification with OTES, the wettability of the film was changed and super-hydrophobic surface was obtained.

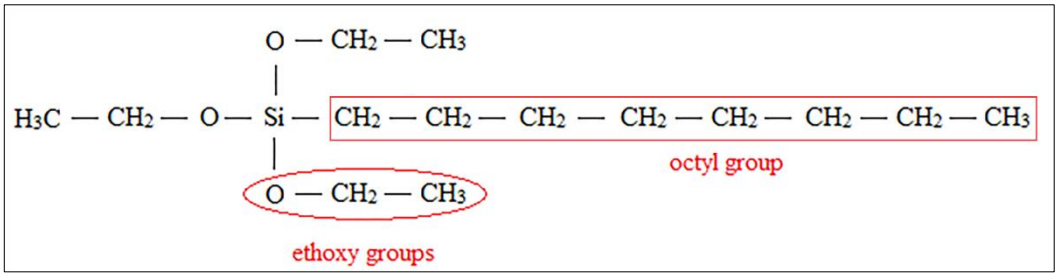

Figure 4.28 Molecular structure of OTES

Ambrozewicz et al. [157] modified the surfaces of silica and magnesium silicate particles using OTES and increased the hydrophobicity of the particles. However, they also reported particle agglomeration with surface modification.

Truong et al. [158] studied surface modification of alumina particles with OTES. It was reported that silylation of alumina particles with OTES resulted in the formation of hydrocarbon groups at the surface of the particles and this resulted an increase in hydrophobicity due to the hydrophobic nature of hydrocarbons. They studied dispersibility of the silane modified particles in syndiotactic polypropylene. The compatibility of the particles with the polymer was reported to be improved by silane modification. Surface-treated particles showed a much better dispersion within the polymer matrix, when compared to untreated particles.

Surface modification of ZnO-2L-95C-UB40 particles with OTES was carried out in an ethanol-water solution with a reaction time of 20 h. The SEM micrographs of the surface-modified particles are given in Figure 4.29. Dispersion quality of the OTES-treated particles was similar to untreated ZnO-2L-95C-UB40 particles (Figure 4.24).

4.5.3.1 Calculation of the Required Amount of OTES for Monolayer Coverage

The surface area of the ZnO-2L-95C particles were determined as 2.86 m^2/g, as described in the section 4.3.1. The surface area of the ZnO-2L-95C-UB40 particles was considered to be slightly lower than this value, considering the dimensions of the particles. The minimum surface coverage area of OTES was reported as 282 m^2/g [87]. Therefore, the required amount of OTES was calculated as 0.01 g per gram of ZnO, from the following equation:

$$Required\ amount\ of\ silane = \frac{(1\ g\ ZnO) * (2.86\ m^2/g)}{282\ m^2/g} \qquad (4.16)$$

Taking into account the multi-layer coverage and the deviation from the theoretical amount, 1 g of OTES was used for 1 gram of ZnO particles.

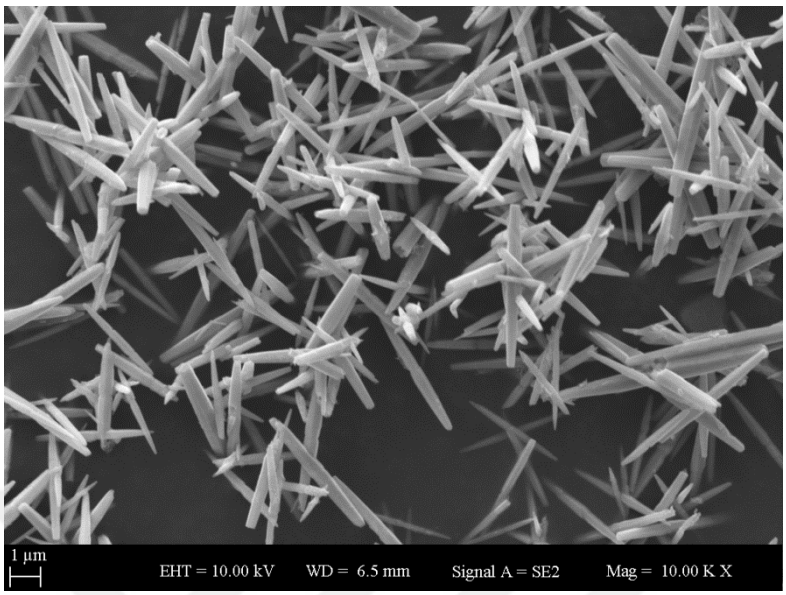

Figure 4.29 SEM micrograph of OTES-treated ZnO-2L-95C-UB40 particles

4.5.3.2 FTIR Study of the OTES-Modified ZnO-2L-95C-UB40 Particles

In order to verify the surface treatment of the ZnO-2L-95C-UB40 particles with OTES, FTIR spectra of the particles were taken and compared with the spectrum of untreated particles. The spectra are given in Figure 4.30. The peaks observed in the spectrum of OTES-treated particles confirm the effectiveness of surface modification.

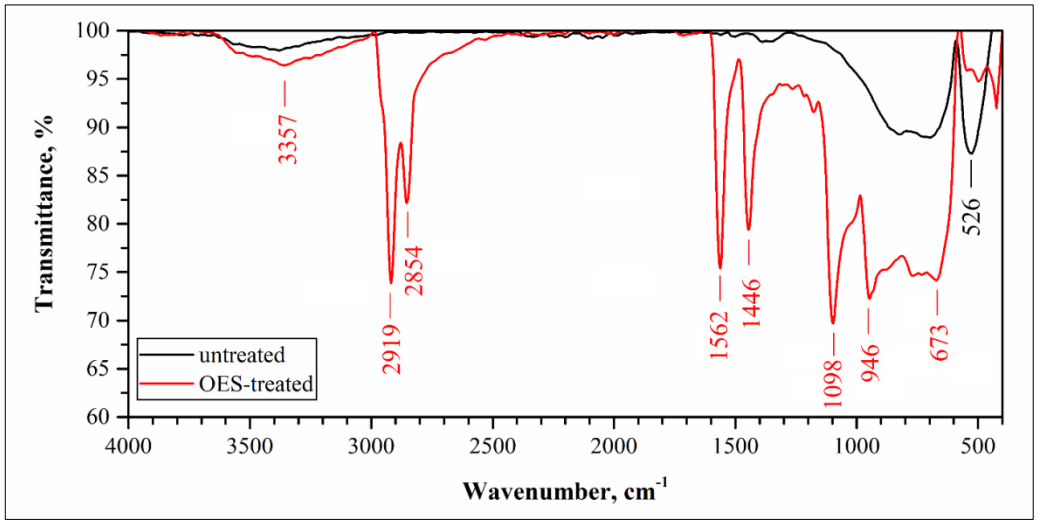

Figure 4.30 FTIR spectra of untreated and OTES-treated ZnO-2L-95C-UB40 particles

The peak point of the broad band assigned to the -OH groups adsorbed on the surface of ZnO-2L-95C-UB40 particles was observed at 3379 cm^{-1}. In the spectrum of OTES-

treated particles, the broad peak of -OH groups showed a maximum 3357 cm^{-1} with slightly higher intensity. Vibrations of H-bonded OH group stretching is known to produce a broad peak between 3200 and 3570 cm^{-1} [140]. The peak assigned to -OH groups in the spectrum of OTES treated particles were considered to be produced by the H-bonded water molecules on the surface silanols [157]. The peaks observed at 2919 cm^{-1} and 2854 cm^{-1} result from methylene C-H asymmetric and symmetric stretching vibrations of the aliphatic octyl group of OTES, respectively. The bending vibrations of these groups were observed at 1446 cm^{-1} [28, 140, 157]. The peak observed at 1562 cm^{-1} was assigned to the formation of C=C-C bonds between the octyl groups of the silane molecules [140].

The intense and broad peak at 1098 cm^{-1} is produced by the Si-O-Si bond formed between OTES molecules [28, 140, 157]. The peak at 946 cm^{-1} was reported to result from the stretching vibrations of the Si-OH groups bonded on the particles [28, 157]. The peak observed at 673 cm^{-1} was reported to be the characteristic symmetric stretching vibrational mode of Zn-O-Si bond [159], established between the particles and the silane molecules.

In the spectrum of the untreated ZnO-2L-95C-UB40 particles, the peak at 526 cm^{-1} was previously assigned to Zn-O bond vibrations. In the spectrum of OTES-treated particles, instead of this peak, two smaller peaks were observed at 498 cm^{-1} and 424 cm^{-1}. The peak at 424 cm^{-1} is known to result from Zn-O bonds [160]. A peak around 470 cm^{-1} was reported to result from Si-O-Si bending vibrations in one study [157] and from Zn-O vibrations in another study [160]. In this study, the peak at 498 cm^{-1} was considered to result from Zn-O vibrations bonded with Si-O-Si molecules.

The reaction sequence for the surface modification of the ZnO particles with OTES progressed in a similar way to the mechanism given in Figure 4.13 for surface modification with MPS. In the first hydrolysis step; three moles of ethanol were produced per mole of OTES, instead of methanol produced in case of MPS. The absence of a peak at 1180 cm^{-1} in the spectrum of OTES-treated particles, which is produced by Si-O-C groups [134, 135] of unhydrolyzed silane, confirmed that hydrolysis step of OTES took place during the reaction. In the second condensation step, silane molecules reacted with each other. The existence of the peak at 1562 cm^{-1} mentioned above, indicated the condensation of silane molecules. Formation of Si-O-Si bonds, indicated by the peak at 1098 cm^{-1}, also confirmed condensation reaction. In the

final reaction step, OTES molecules were bonded to the surface of ZnO particles. Occurrence of this reaction step was verified by the peak located at 673 cm^{-1}.

4.6 Development and Characterization of PHBV/ZnO Nanocomposites

The ZnO particles synthesized with varying reaction conditions as described in previous sections, were incorporated into PHBV matrix by melt-extrusion method. The particles utilized in nanocomposites fabrication were ZnO-2L-95C particles (untreated and MPS-treated, ultrasound separated), ZnO-50-2L-95C particles, ZnO-450-2L-95C particles, and ZnO-2L-95C-UB40 particles (untreated and OTES-treated). In order to evaluate the effects of the addition of ZnO particles on PHBV properties, the fabricated PHBV/ZnO nanocomposites were characterized by various analyses for their structural, thermal, and mechanical properties.

4.6.1 PHBV/ZnO Nanocomposites Fabricated by ZnO-2L-95C Particles

The ZnO-2L-95C particles synthesized by the conditions described in section 4.1.3 were rod-shaped particles with an aspect ratio of 15.6. The particles were obtained as asterisk-shaped rod-arrays connected from their center points and were observed to be severely agglomerated. Since uniform distribution of particles within a polymer matrix is crucial in terms of polymer properties enhancement [105, 106, 158, 161], deagglomeration of the ZnO-2L-95C particles prior to incorporation into polymer matrix was necessary. Surface functionalization and ultrasonic dispersion; two different methods utilized in particle deagglomeration [161], were applied to the particles in order to decrease the level of agglomeration.

The ZnO-2L-95C particles were subjected to direct application of ultrasound for 60 min, as described in section 4.2 and complete deagglomeration of the particles was achieved (Figure 4.6). However, monodispersity and aspect ratio of the particles were negatively affected. Surface functionalization of the particles was performed by hydrophobic surface modification of the particles with MPS, as described in section 4.3. After MPS modification, the asterisk-shaped rod arrays were observed to be broken; however, severe agglomeration of the particles could still be observed (Figure 4.14). Therefore, 60 min of ultrasonic dispersion was applied to MPS-modified particles. Particle agglomeration was significantly decreased but could be completely overcome (Figure 4.16).

Ultrasound-dispersed untreated particles, MPS-treated particles, and ultrasound-dispersed MPS-treated particles were incorporated into PHBV matrix by melt-extrusion method; and the effectiveness of the methods in terms of homogeneous particle distribution was evaluated. The particles were added into PHBV after silanization and/or ultrasonication and the thermal and mechanical properties of the fabrication PHBV/ZnO nanocomposites were investigated. Neat PHBV was also prepared using the same conditions and without addition of the particles, for comparison purpose. The formulations and the sample coding of the nanocomposites are given in Table 4.8. The PHBV/ZnO nanocomposites fabricated were characterized for their structural, thermal, and mechanical properties and were compared to those of neat PHBV.

Table 4.8 Sample codes and formulations of the PHBV/ZnO nanocomposites fabricated from ZnO-2L-95C particles

Sample code	**ZnO content, wt.%**	**PHBV content, wt.%**	**Surface treatment**	**Ultrasound application**
PHBV	-	100	-	-
PHBV/ZnO-US	1	99	-	60 min
PHBV/ZnO-MPS	1	99	MPS	-
PHBV/ZnO-MPS-US	1	99	MPS	60 min

4.6.1.1 Structural Characterization of the PHBV Nanocomposites Fabricated by ZnO-2L-95C Particles

Structural properties of the PHBV nanocomposites fabricated using ultrasound-dispersed and/or MPS-modified ZnO-2L-95C particles were evaluated using SEM analysis. SEM micrographs of the PHBV/ZnO-US, PHBV/ZnO-MPS, and PHBV/ZnO-MPS-US nanocomposites are given in Figures 4.31, 4.32, and 4.33, respectively. In general, the particles were observed to be well dispersed within the PHBV matrix. Areas of small particle agglomerations were observed in all three samples; however, particles were mostly distributed singularly. Other than the distributed ZnO particles, some voids in the shape of particles were also observed on the PHBV matrix. The ZnO particles once attached to the matrix were dislocated during the fracture of the sample prior to SEM analysis, and formed the voids observed in the SEM pictures.

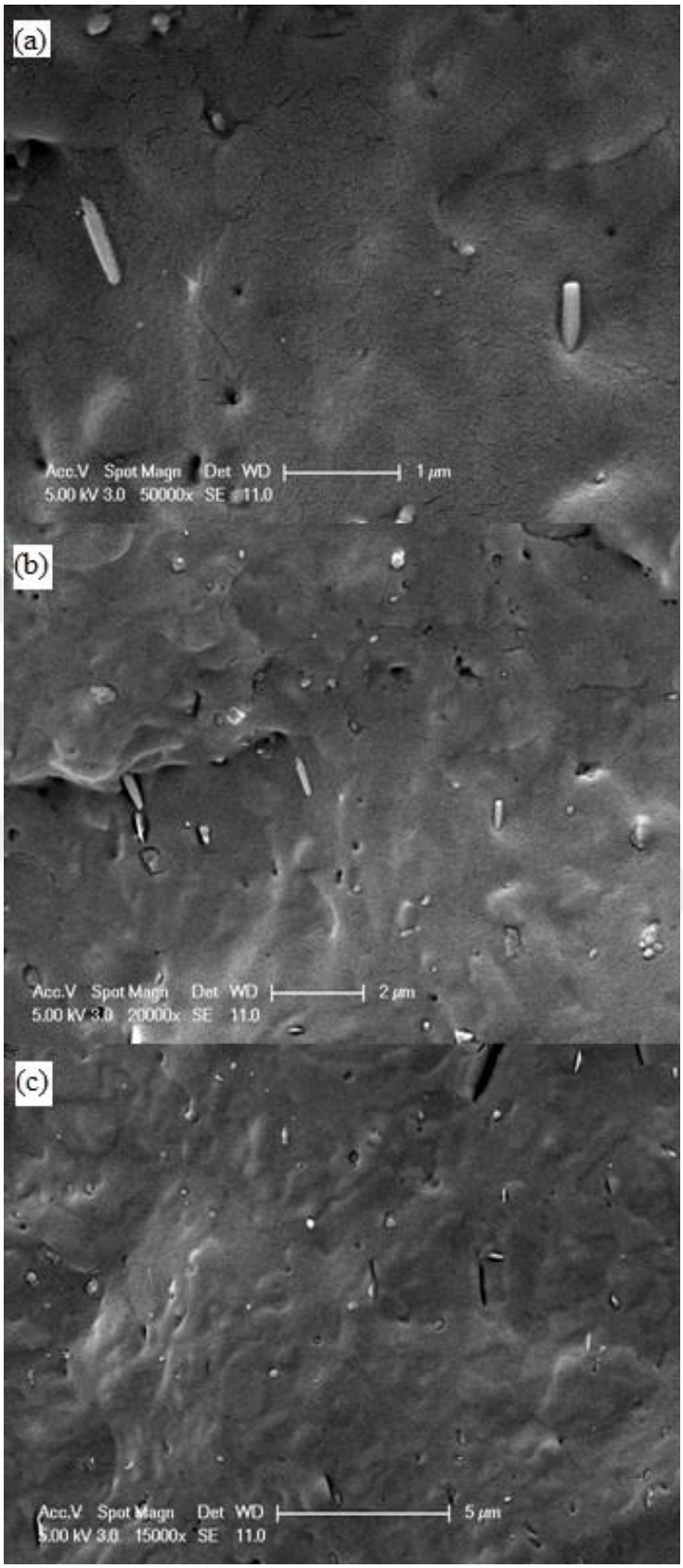

Figure 4.31 SEM micrographs of the PHBV/ZnO-US nanocomposite at (a) 50000x, (b) 20000x, and (c) 15000x magnification

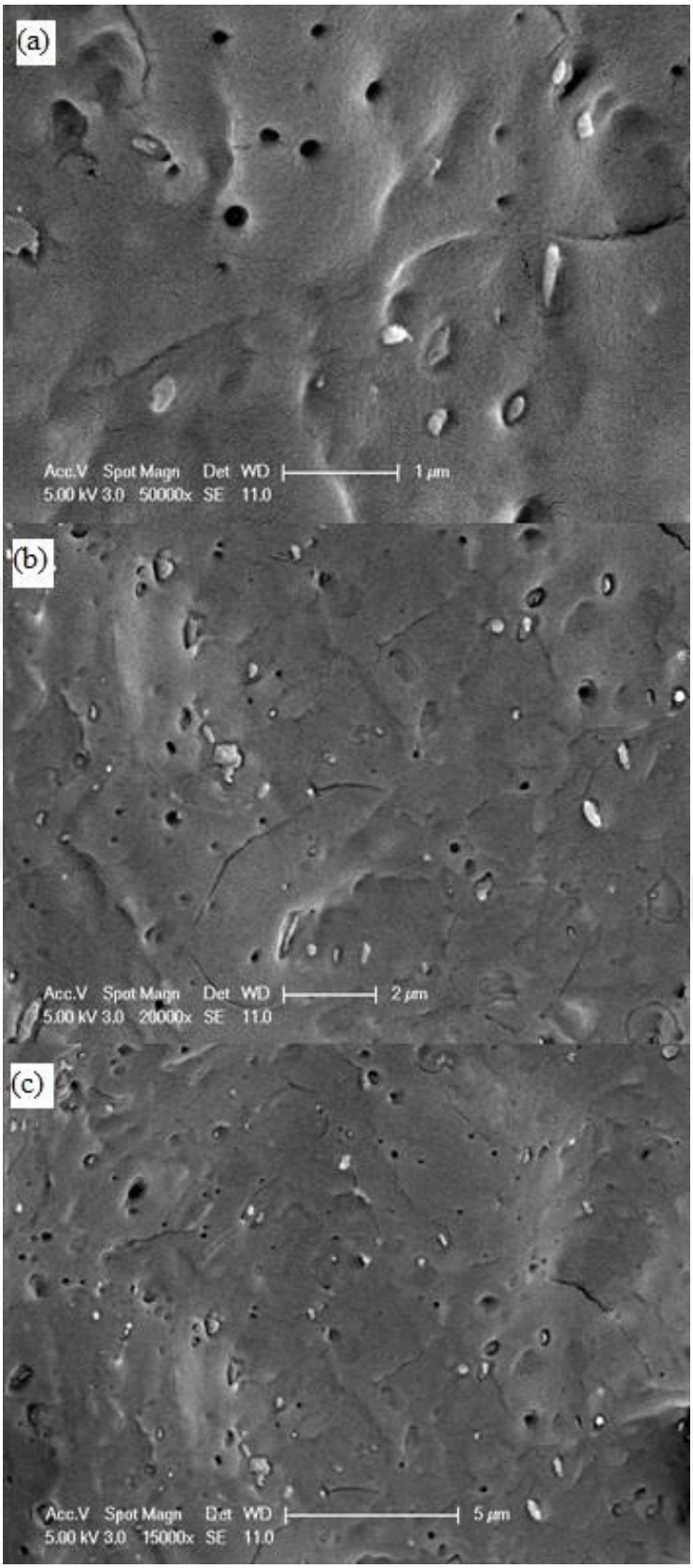

Figure 4.32 SEM micrographs of the PHBV/ZnO-MPS nanocomposite at (a) 50000x, (b) 20000x, and (c) 15000x magnification

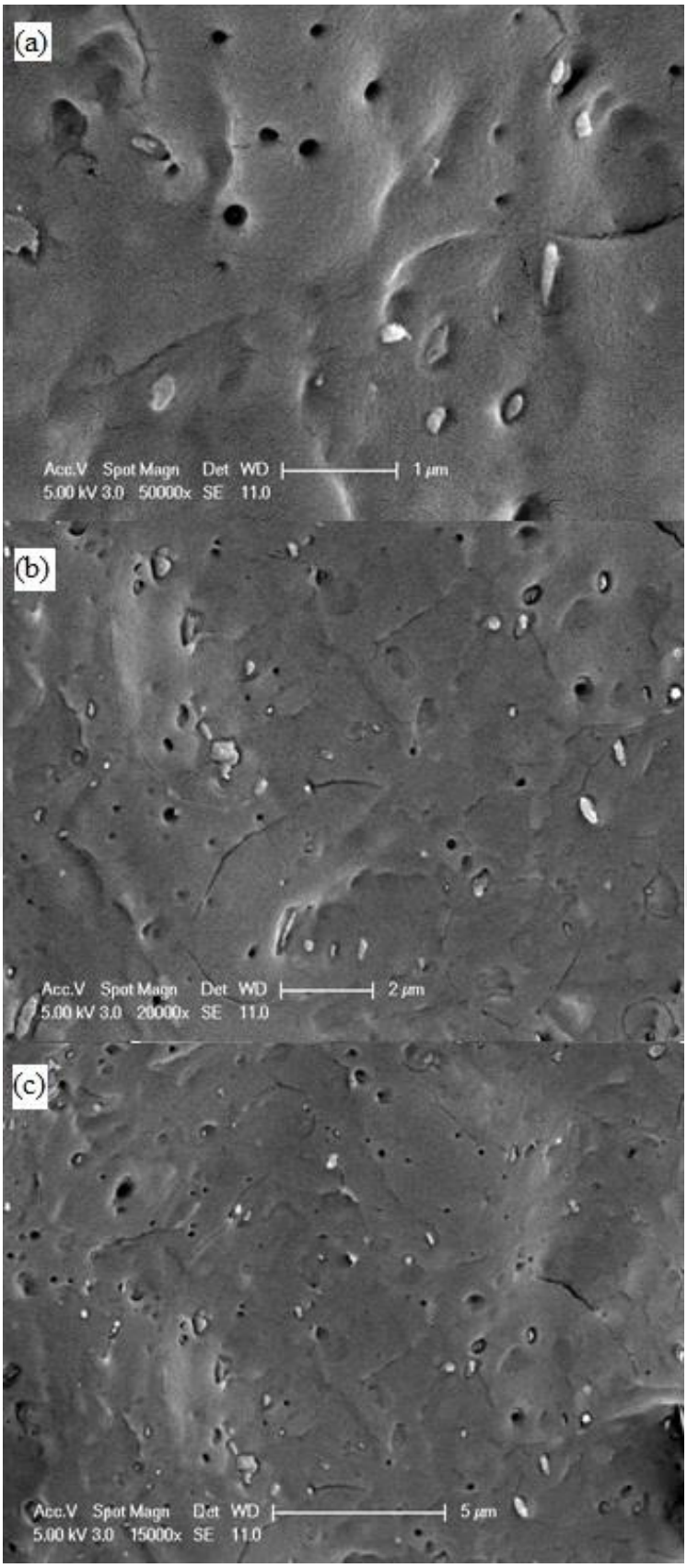

Figure 4.33 SEM micrographs of the PHBV/ZnO-MPS-US nanocomposite at (a) 50000x, (b) 20000x, and (c) 15000x magnification

The properties of a nanocomposite composing of organic polymer matrix and inorganic fillers depend on the individual properties of the polymer and the fillers, the interface between them, and the extent of filler dispersion [106]. In order to achieve desired properties of the polymer nanocomposites, uniform dispersion of the particles within the matrix is essential [105, 106, 158, 161]. The interface between the particles and the polymer matrix also has long-range effects on the surrounding polymer chains [105]. Particle size, loading amount, and level of dispersion were reported to influence the amount of the polymer affected, whereas the structure and chemistry of the particle surface affects the degree of interaction at the interface [105].

The total number of particles observed in a SEM image at a certain magnification was reported to indicate the level of particle dispersion within the matrix [28, 162]. The number of ZnO particles distributed within the PHBV matrix at 15000x magnification was counted in five different SEM images for PHBV/ZnO-US, PHBV/ZnO-MPS, and PHBV/ZnO-MPS-US nanocomposite samples in order to have a quantitative idea on the degree of dispersion. The voids resulting from dislocated particles were included in counting. The results were reported as the average of five different SEM images. The results are given in Table 4.9. The highest number of particles was observed in the SEM images of the PHBV nanocomposite containing both MPS-treated and ultrasound-dispersed particles, indicating a better particle dispersion than the other samples. The average number of particles observed in the sample containing only MPS-treated particles was higher than the number of particles in untreated and ultrasound-dispersed particles.

Table 4.9 Average numbers of particles per SEM image of PHBV nanocomposites fabricated by ultrasound-dispersed and/or MPS-modified ZnO-2L-95C particles

Nanocomposite sample	**Average number of particles observed in SEM micrographs**
PHBV/ZnO-US	99.3
PHBV/ZnO-MPS	142.5
PHBV/ZnO-MPS-US	158.8

The SEM images of the ultrasound-dispersed and/or surface-treated ZnO-2L-95C particles prior to incorporation into PHBV matrix (Figure 4.6, 4.14, and 4.16) indicated that ultrasonic dispersion method produced better results than surface treatment in

deagglomeration of the particles. Severe particle agglomeration was observed after the surface treatment with MPS and even after 60 min of ultrasound application, complete deagglomeration could not be achieved. However, when the particles were added into PHBV matrix; MPS-treated particles exhibited better dispersion within the matrix than the ultrasound-dispersed and untreated particles. This situation resulted from the fact that compatibility of inorganic particles with organic polymer is important in terms of particle dispersion within the matrix [69, 163, 164].

Although nanoparticles are attractive in materials science due to their small dimensions; the same property also causes agglomeration and affects the final properties of the nanocomposites negatively. Nanoparticles tend to form agglomerates due to their small sizes, higher surface areas and higher surface energies. As the particle agglomerates form, they interact with each other instead of interacting with the polymer matrix. When this is the case, existence of particles within the polymer matrix affects the properties of the polymer negatively rather than improving them [105].

Other than the average number of particles within a defined area of the nanocomposite, the distance of any particle from the nearest neighbor particles is an important aspect in terms of distribution uniformity. Shorter distance between neighbor particles means less unaffected areas of the polymer. Therefore, a uniform distribution of particles within the matrix produces better results than a clustered distribution having the same average number of particles [105]. When the SEM images obtained for the nanocomposites fabricated by ZnO-2L-95C particles were considered (Figures 4.31 through 4.33), although the particles mostly appear to be uniformly distributed, some small domains of unaffected polymer could be observed. However, this situation cannot be directly quantified but could rather be evaluated objectively [106]. Therefore, it is difficult to conclude with of the samples exhibits better dispersion than the others, regarding the distance of particles from each other.

4.6.1.2 Thermal Stability of the PHBV Nanocomposites Fabricated by ZnO-2L-95C Particles

PHBV co-polymer has generally better processability than the homopolymer PHB; nevertheless, it still suffers low thermal stability [4, 37, 165]. Thermal degradation of PHBV starts slightly above its melting point, narrowing its processing window during

melt processing [165]. Addition of inorganic particles into PHBV matrix has the possibility of enhancing thermal stability [165].

Exposure to high temperatures, oxygen, or moisture may result in the degradation of polymers and the combination of these factors often accelerates depolymerization [166]. Thermal degradations of PHB and PHBV were reported to proceed through random chain scission of the ester groups by *ß*-hydrogen elimination, considering the typical structures of the pyrolysis products, such as crotonic acid and oligomers with a crotonate end group [166-168]. A gradual decrease of the molecular weight occurs as the thermal degradation proceeds [166].

At high temperatures thermal degradation of PHAs occurs due to the decomposition of carboxylic esters that have *ß*-hydrogen in their structure (at around 160 – 180 ºC, which corresponds to their melting temperature range). Thermal degradation products obtained for PHAs at temperatures between 170 – 200 ºC were reported to be low molecular weight macromolecules that have a carboxylic and an unsaturated end group. The end saturated end group was propenyl for PHB and butenyl for PHV. At moderately high temperatures, the instability of the *ß*-hydrogen results in the degradation to proceed by *cis*-elimination reaction. The degradation mechanism is also referred to as McLafferty rearrangement and produces a six-carbon ring ester intermediate [166]. The random scission mechanism of PHB was proposed to occur between 170 and 300 °C. The complete thermal degradation mechanism of PHAs have not yet been clearly identified [166].

Xiang et al. [166] investigated the thermal degradation of PHBV under nitrogen and air atmospheres. Early stages of the degradation were reported to be insensitive to the atmosphere, indicating that the main reason of the degradation was not oxygen. At the intermediate stages, when the weight loss was higher than 50%, a decrease in activation energy values was observed under air atmosphere. This suggested that the intermediate stages of degradation were sensitive to oxygen. The authors also reported that the sensitivity of the polymer to temperature increased as the degradation temperature increased.

In order to investigate the limiting processing conditions of neat PHBV, thermal stability of PHBV was investigated by dynamic TG analysis under nitrogen atmosphere. TG and DTG curves of PHBV between 25 and 560 °C were obtained (Figure 4.34).

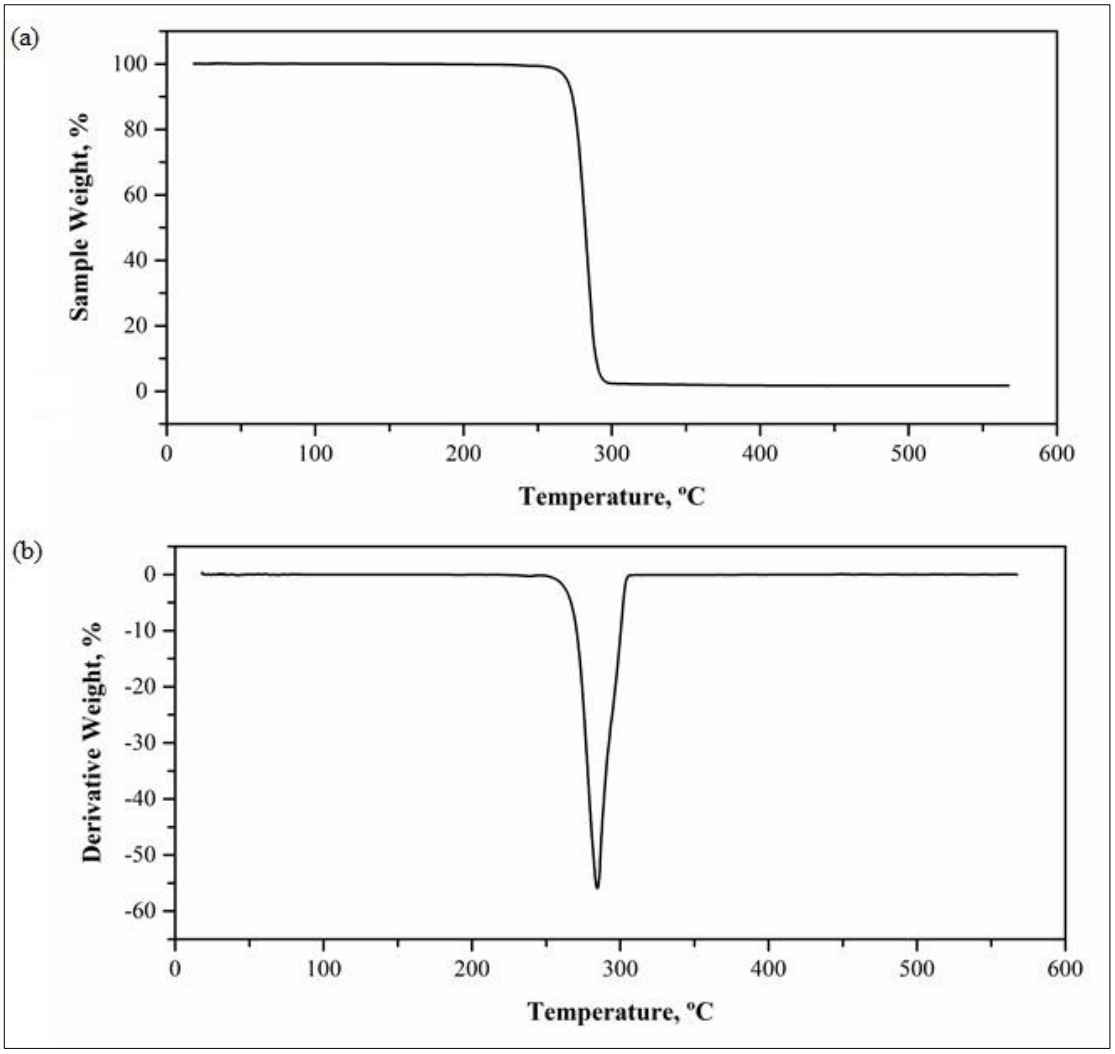

Figure 4.34 Thermogravimetry curves of the extruded neat PHBV sample: (a) weight loss and (b) derivative weight loss curves

Thermal degradation of PHBV was observed to occur in a single step and at a narrow temperature range. In the TG curve after 250 °C, the sample weight was firstly observed to decrease slowly, then decrease rapidly up to a temperature close to 300 °C. At around 300 °C, the curve returned to zero slope as the sample got exhausted. Similar degradation behavior was obtained for neat PHBV previously in the literature [26, 33, 37, 41].

The TG curves obtained for the PHBV nanocomposites fabricated with ultrasound-dispersed and/or silane-modified ZnO-2L-95C particles are given in Figures 4.35 to 4.37. The weight and derivative weight curves obtained for neat PHBV are also shown in the figures for comparison purpose. TG curves of the nanocomposites showed a single-step, narrow temperature range decomposition behavior, similar to neat PHBV. However, the curves were observed to slightly shift towards left, indicating a slight

decrease in thermal stability, compared to neat PHBV. The TG and DTG curves of the neat PHBV and its nanocomposites are given together in Figure 4.38 in a narrower temperature range around the degradation zone. No particular difference could be observed on the TG curves between the different nanocomposite samples. On DTG curves, the shift of the T_{max} to lower temperatures could be observed for the nanocomposite samples.

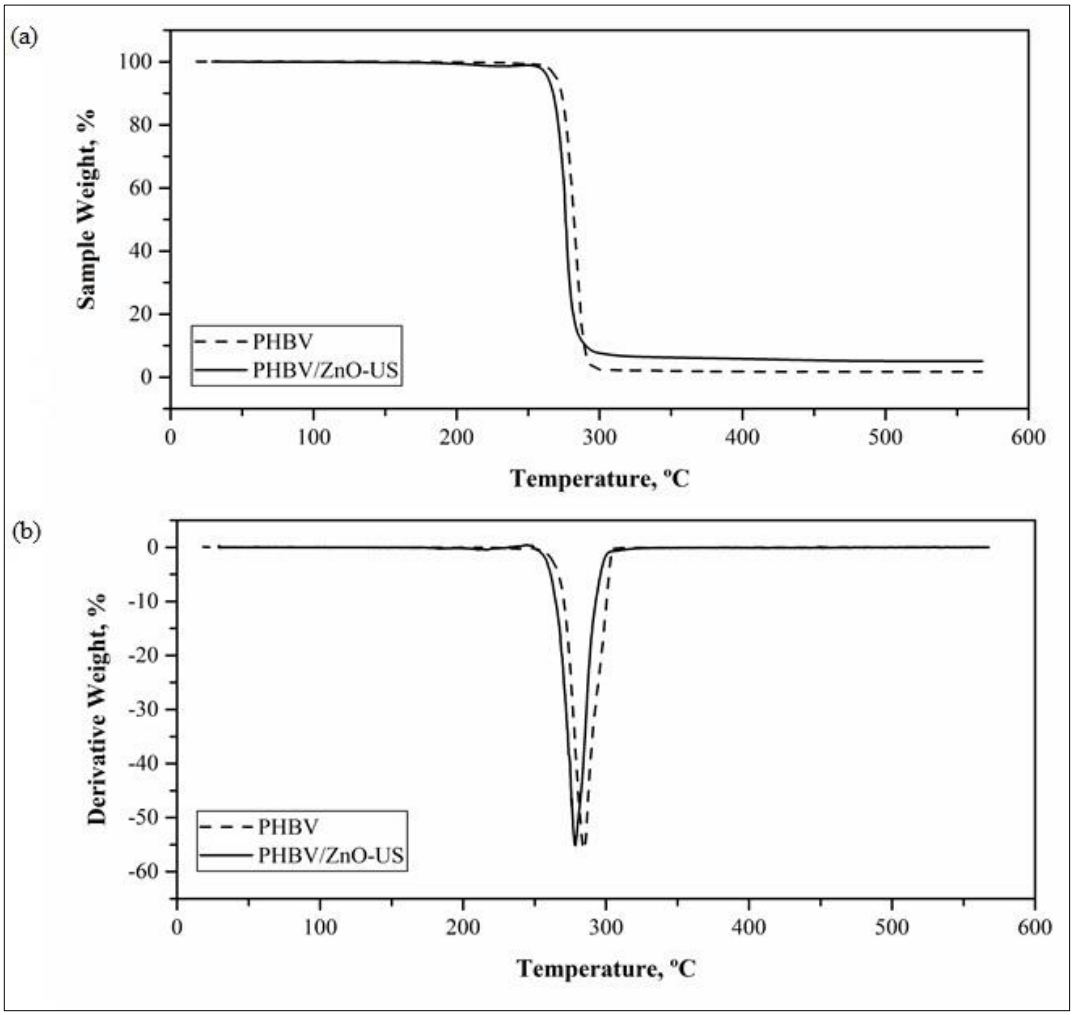

Figure 4.35 Thermogravimetry curves of neat PHBV and PHBV/ZnO-US samples: (a) weight loss and (b) derivative weight loss curves

The maximum degradation temperature (T_{max}) was determined as the temperature at which the rate of thermal degradation is the highest [35]. T_{max} values calculated from the DTG curves of the neat PHBV and its nanocomposites are given in Table 4.10. Other characteristic degradation temperatures $T_{x\%}$ were determined as the temperatures at which the sample weight equals to the (100-x) % of the sample [27]. The values of $T_{x\%}$ temperatures calculated for neat PHBV and its nanocomposites are given in Table 4.10.

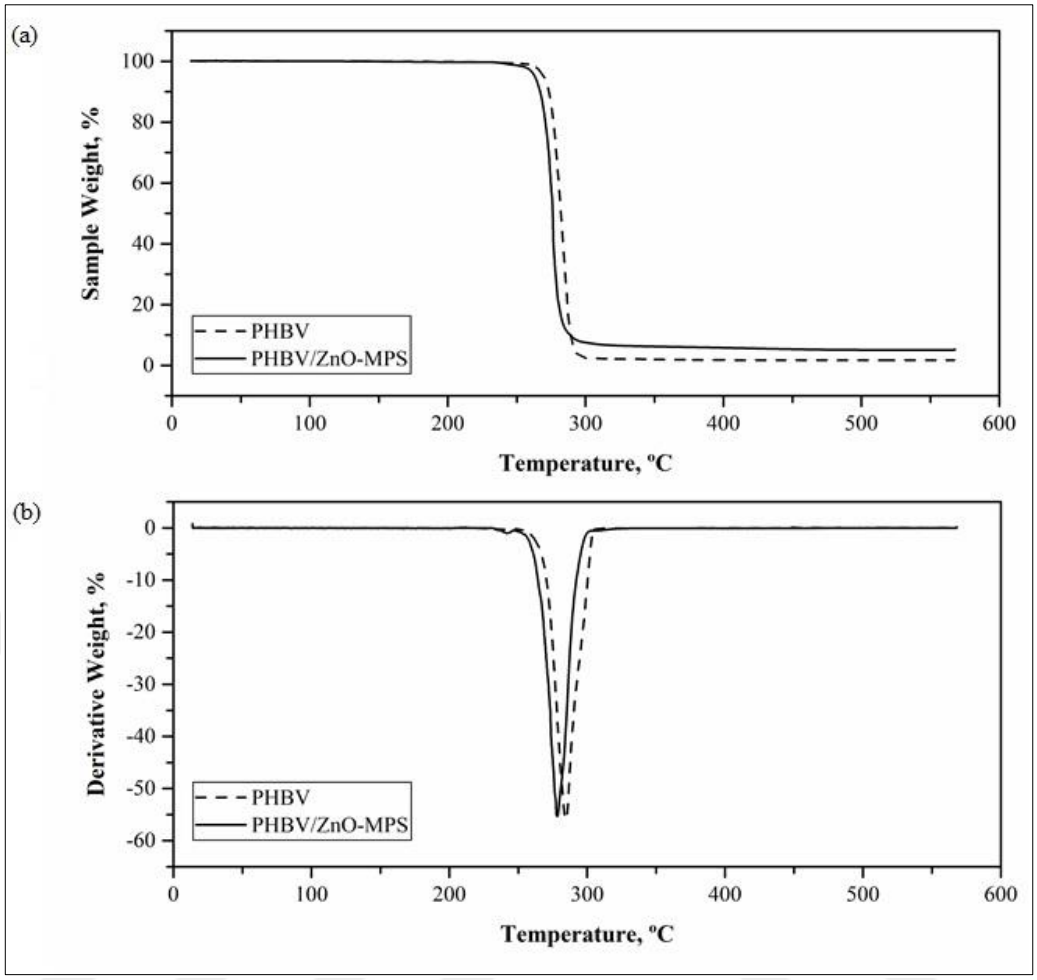

Figure 4.36 Thermogravimetry curves of neat PHBV and PHBV/ZnO-MPS samples: (a) weight loss and (b) derivative weight loss curves

The characteristic degradation temperatures calculated for the nanocomposites were observed to decrease about 6 – 8 °C, compared to neat PHBV sample. Considering the initial decomposition temperature as the $T_{2\%}$, where the 2% of the initial weight was lost, the processing window of the polymer was slightly narrowed by the addition of ZnO-2L-95C particles. The processing window indicates the temperature interval between the melting temperature of the polymer and its initial decomposition temperature, and the melting temperature value given by the manufacturer company was 150 °C. Therefore, despite the slight decrease in the initial decomposition temperature, the processing window was still quite wide to allow melt processing and the slight decrease was not significant.

The percent char residues remaining by the end of thermal degradation are also given in Table 4.10. The value of the char residue was 1.74 % for the neat PHBV sample, whereas it increased by about 3.4 % for the PHBV/ZnO-2L-95C nanocomposite

samples. Since the nanocomposite samples contained 1 % of ZnO particles by weight, the remaining portion of the increased char (2.4 %) should have been coming from the polymer. This suggests that incorporation of ZnO might have blocked the transfer of the volatile thermal decomposition products from the bulk to the gaseous state [43].

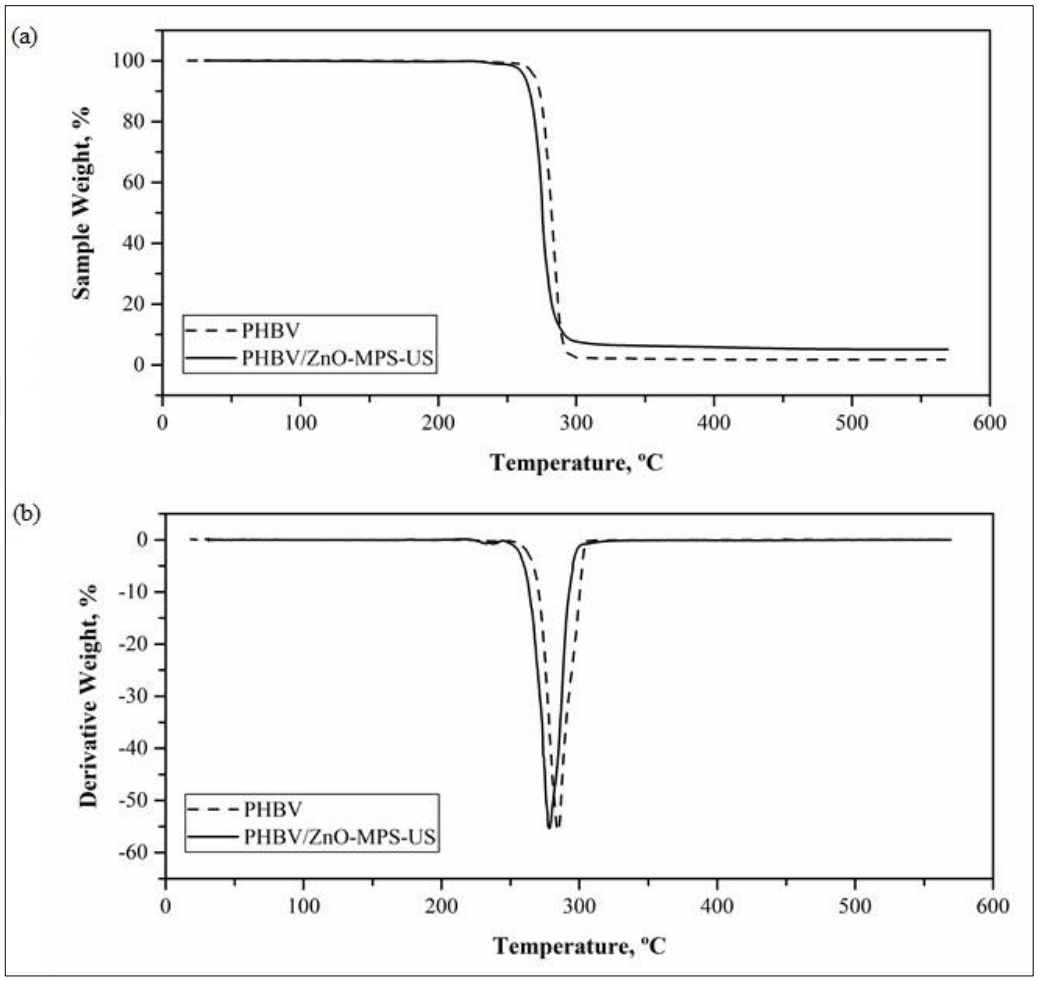

Figure 4.37 Thermogravimetry curves of neat PHBV and PHBV/ZnO-MPS-US samples: (a) weight loss and (b) derivative weight loss curves

Decrease in initial and maximum thermal degradation temperatures were previously reported in the literature for incorporation of lignosulfonate [41], cellulose nanowhiskers [39], lignin [42], and graphene [31] particles into PHBV matrix. The possible reason for this effect was reported as the high thermal conductivity of the particles [31, 39].

Diez-Pascual and Diez-Vicente [43] studied incorporation of ZnO particles into PHBV matrix by solution casting method. In their study, addition of the ZnO particles increased the thermal stability of PHBV and the value of T_{max} increased with increasing ZnO content. They reported that the heat resistance of the matrix could have increased

due to the barrier effect created by ZnO particles and the transfer of decomposition products from the bulk to the gas phase was hindered. Hydrogen bonding between the polymer and the particles due to good dispersion and strong interactions was considered to create this barrier effect. They also suggested that the high thermal conductivity of the ZnO particles would facilitate the dissipation of heat throughout the matrix and therefore enhance thermal stability.

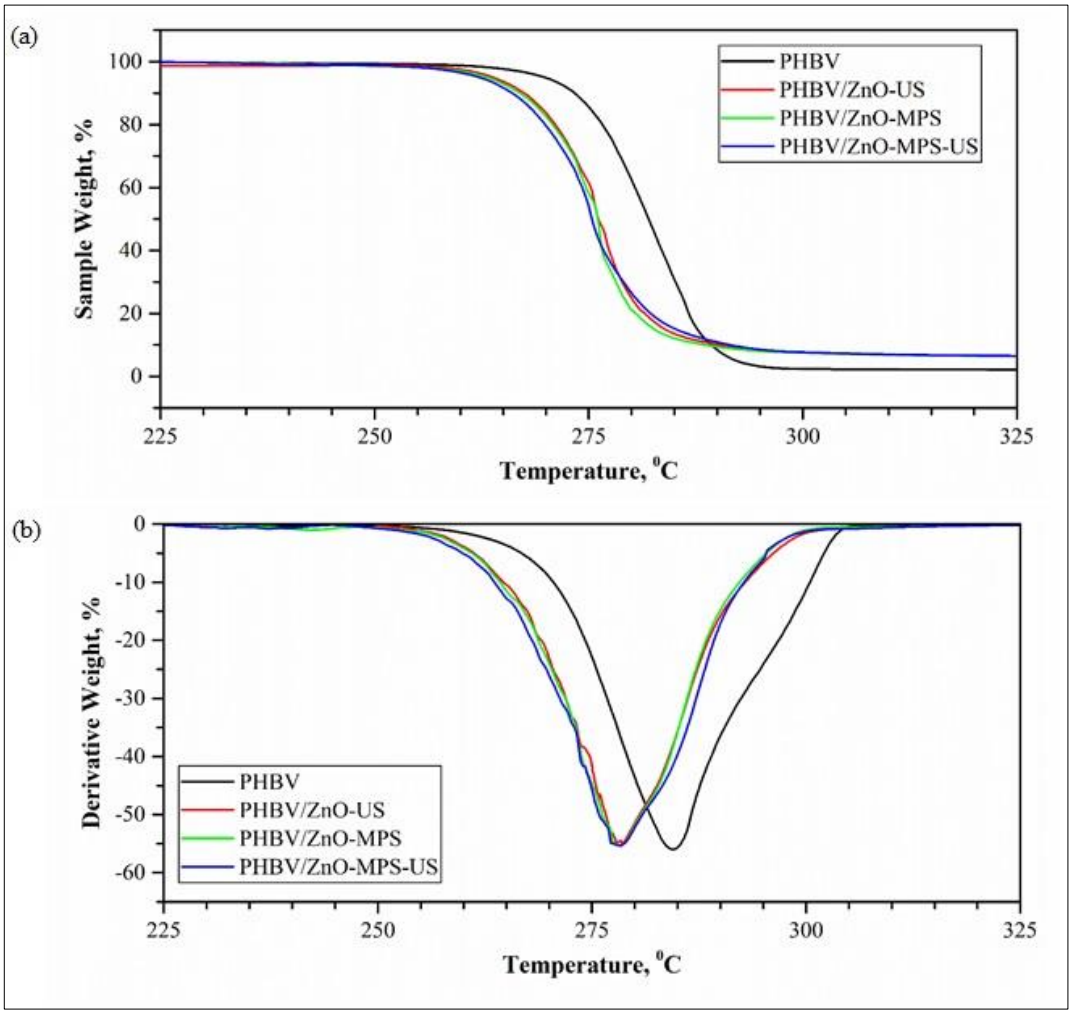

Figure 4.38 Thermogravimetry curves of neat PHBV and PHBV/ZnO-2L-95C nanocomposites at a narrower temperature range: (a) weight loss and (b) derivative weight loss curves

In another study related to the incorporation of ZnO particles into PHBV matrix by electrospinning method [46], the thermal stability of the polymer was reported to decrease with the addition of the ZnO particles, similar to our study. They mentioned the high heat conductivity and catalytic properties of ZnO nanoparticles as the possible reason for the decrease in thermal stability.

The results of our study, together with the works of Diez-Pascual and Diez-Vicente [10, 43] and Castro-Mayorga and co-workers [46], suggest that; among particle dispersion and polymer-particle interaction, processing method might also be an important parameter in the final thermal properties of the fabricated nanocomposite. ZnO nanoparticles were found to enhance thermal stability of PHBV when the nanocomposite fabrication method was solution casting; whereas they were found to impair thermal stability when the method was electrospinning or melt-extrusion. In melt-processing techniques such as extrusion, polymer is subjected to local high temperatures and shear friction and this could result in the scission of the polymeric chain and pre-mature onset of degradation [35, 169]. Solution casting method, on the other hand, does not include such applications that could lead to thermal degradation.

Table 4.10 Parameters of thermal degradation calculated for the neat extruded PHBV and the PHBV/ZnO-2L-95C nanocomposites

Sample	**$T_{2\%}$, °C**	**$T_{5\%}$, °C**	**$T_{10\%}$, °C**	**$T_{20\%}$, °C**	**$T_{80\%}$, °C**	**T_{max}, °C**	**Char, %**	**Ea, kJ/mole**
PHBV	264.0	270	273.3	276.6	286.7	284.5	1.74	480.8
PHBV/ZnO-US	258.6	263.8	267.4	271	281.2	278.1	5.05	470.7
PHBV/ZnO-MPS	256.5	263.2	266.9	270.7	280.2	278.4	5.18	481.0
PHBV/ZnO-MPS-US	255.9	262.2	266.0	269.9	282	278.3	5.06	460.1

The increase in the char residue of PHBV observed in our study indicated that the barrier effect of ZnO particles suggested by Diez-Pascual and Diez-Vicente [10, 43] might have taken place during the thermal degradation process, hindering the transfer of thermal degradation products into the gas phase. Nevertheless, the high thermal conductivity of the ZnO particles might have played different roles in different fabrication methods. Since the melt-extrusion and electrospinning methods included application of high temperatures, the suffering of the polymer from high temperatures repeatedly might have accelerated chain scission and further degradation. This effect might not have observed in the solution cast samples. Another possibility is the better dispersion of the particles achieved by solution casting method facilitated heat dissipation through the matrix and enhanced thermal stability; whereas poorer dispersion resulted in increased thermal degradation.

The activation energy for thermal decomposition of PHBV and PHBV/ZnO-2L-95C nanocomposites were calculated according to the Horowitz-Metzger method [42, 170] using the following equation:

$$ln\left[ln\left(\frac{W_0}{W_T}\right)\right] = \frac{E_a\theta}{RT_{max}^2} \quad (4.17)$$

where W_0 is the initial weight and W_T is the remaining weight of PHBV at temperature T, θ is equal to $T-T_{max}$, and R is the universal gas constant. The graphs of $\ln[\ln(W_0/W_T)]$ values against the θ values were plotted (Figure 4.39) and the values of E_a were calculated from the slopes and reported in Table 4.10. The E_a value calculated for neat PHBV was similar to the value previously reported in the literature [42]. The E_a values calculated for the PHBV/ZnO-2L-95C nanocomposites were also close to that of neat PHBV.

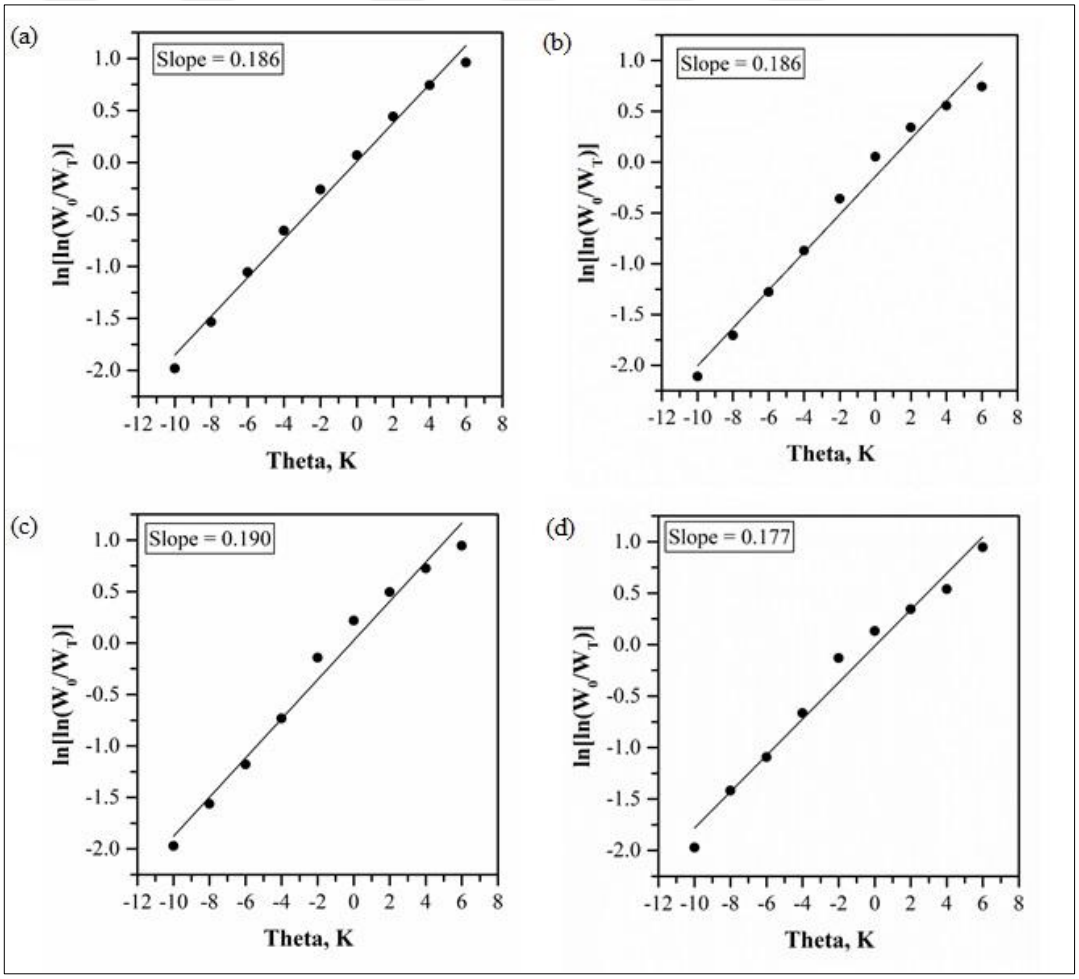

Figure 4.39 Calculation of the E_a values for neat PHBV and PHBV/ZnO-2L-95C nanocomposites by the Horowitz-Metzger method: (a) neat PHBV, (b) PHBV/ZnO-US, (c) PHBV/ZnO-MPS, and (d) PHBV/ZnO-MPS-US

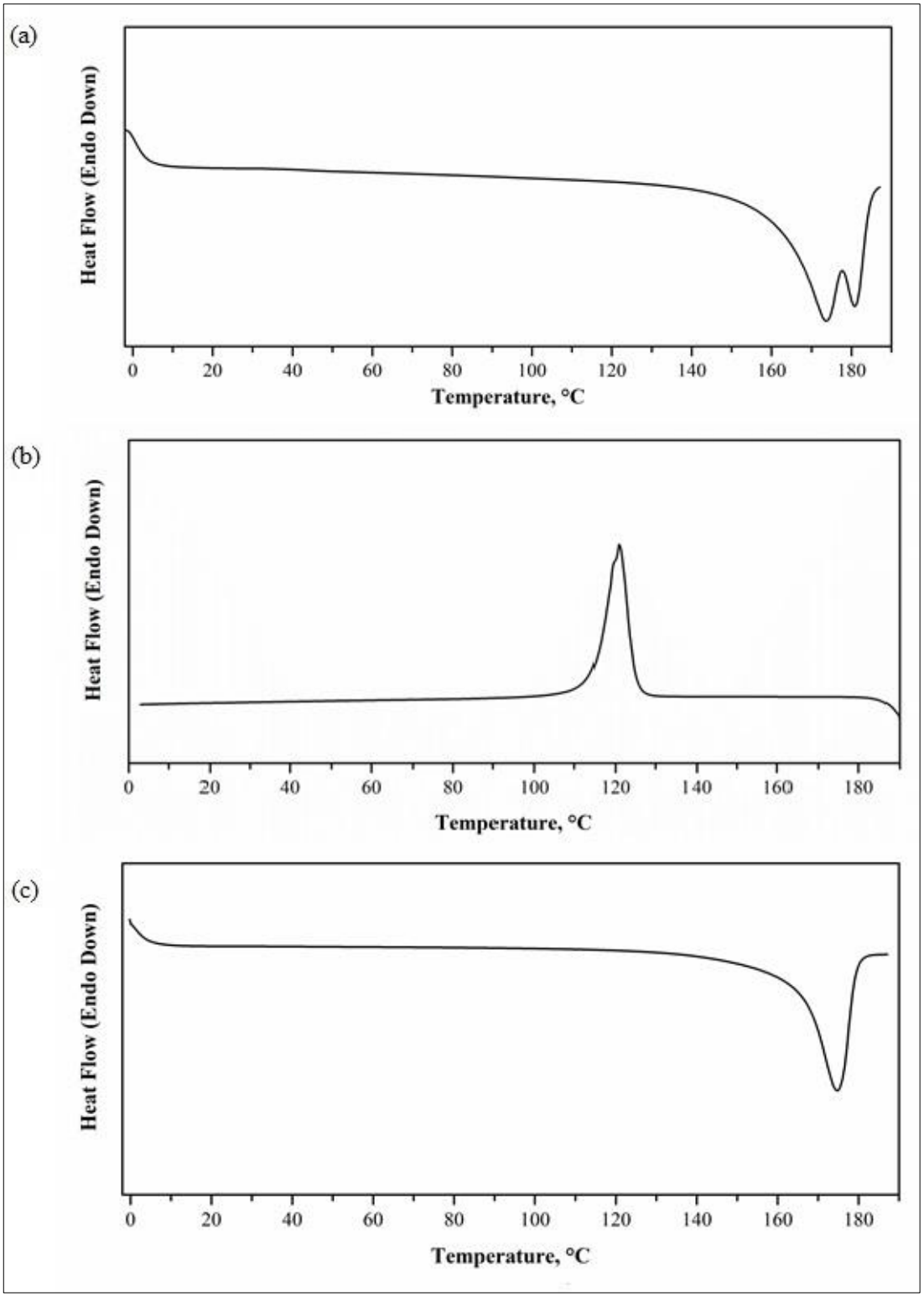

Figure 4.40 DSC scans of neat extruded PHBV (a) 1st heating scan, (b) cooling scan, and (c) 2nd heating scan

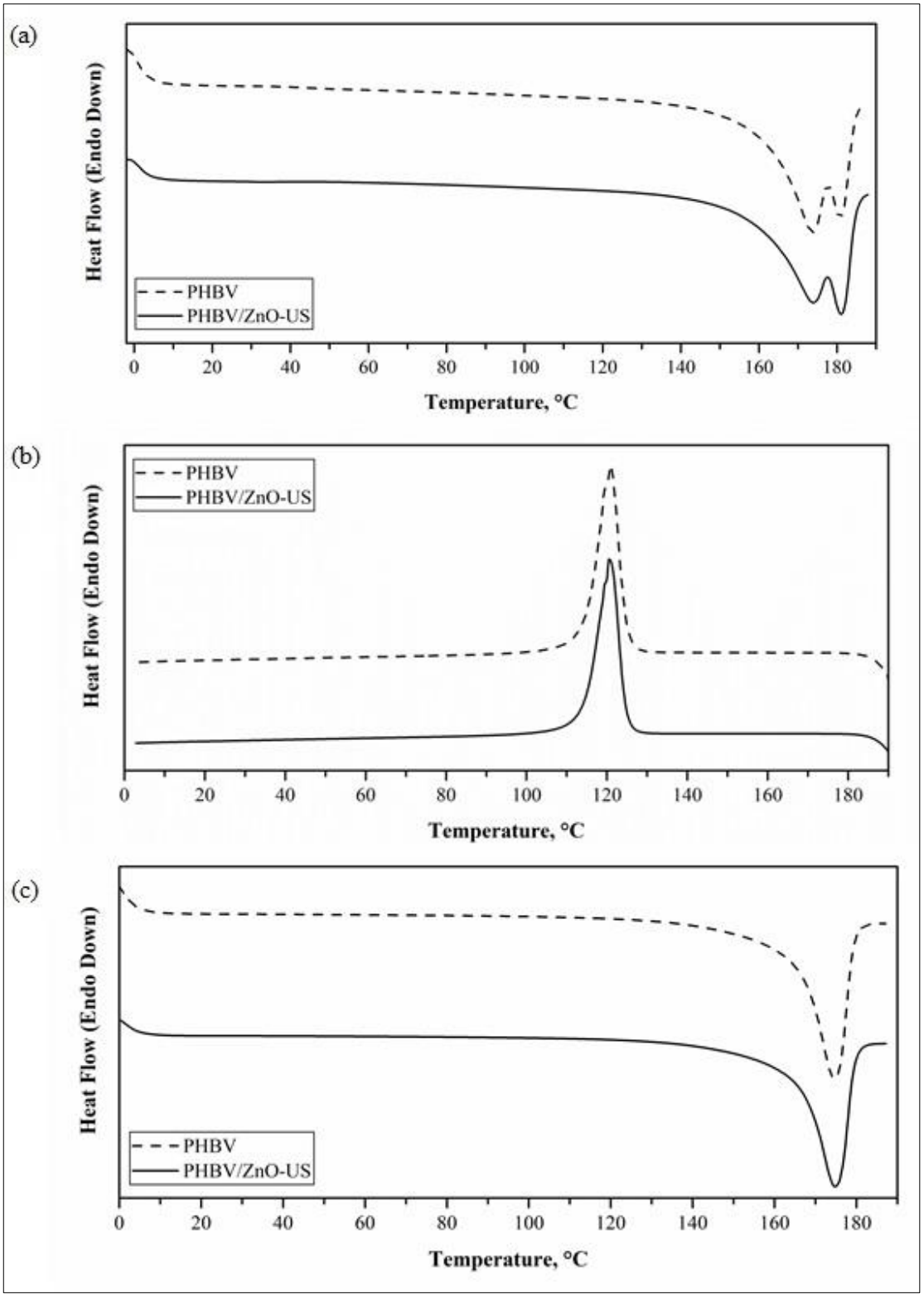

Figure 4.41 DSC scans of the PHBV/ZnO-US nanocomposite shown together with neat PHBV (a) 1st heating scans, (b) cooling scans, and (c) 2nd heating scans

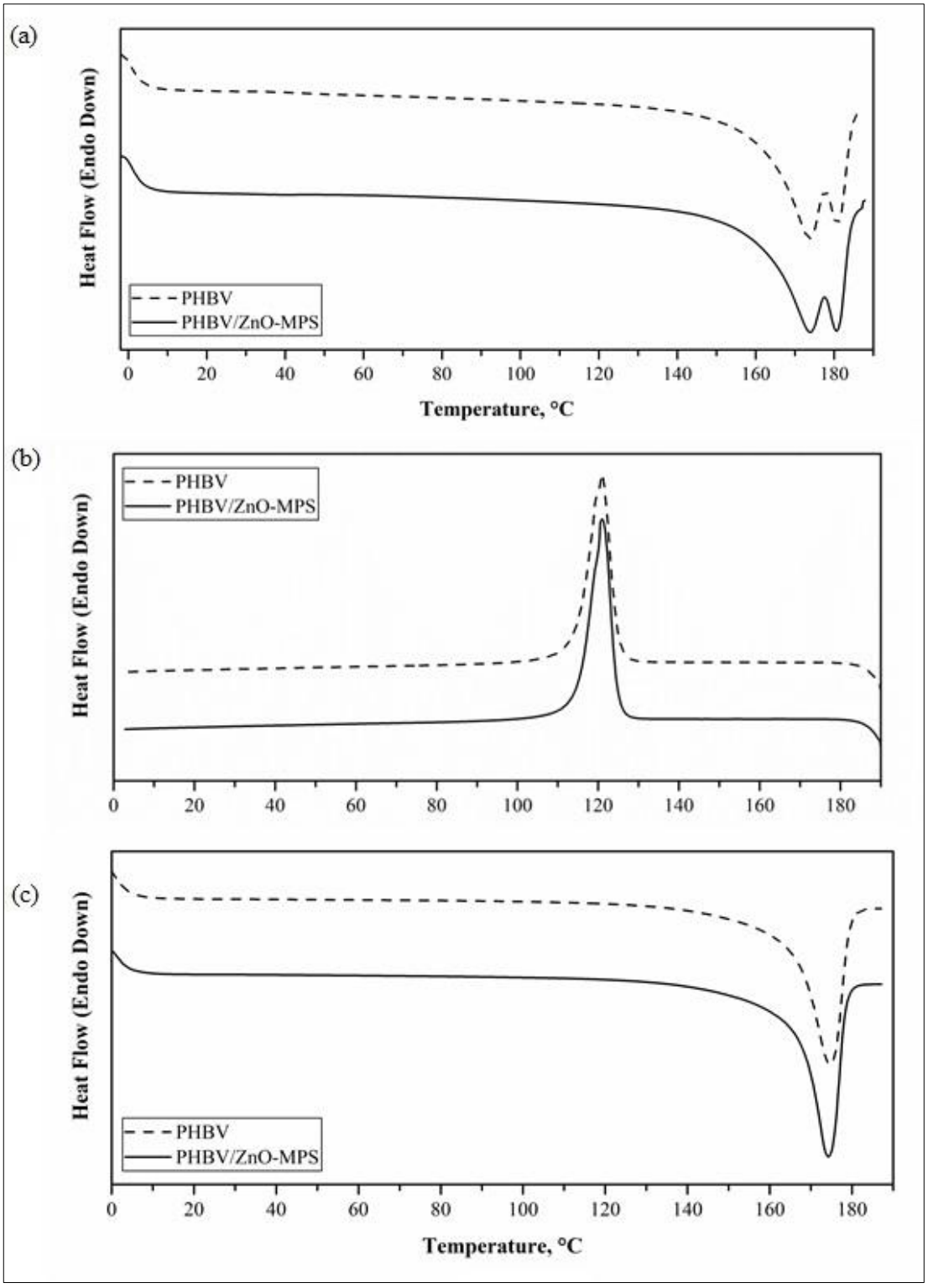

Figure 4.42 DSC scans of the PHBV/ZnO-MPS nanocomposite shown together with neat PHBV (a) 1st heating scans, (b) cooling scans, and (c) 2nd heating scans

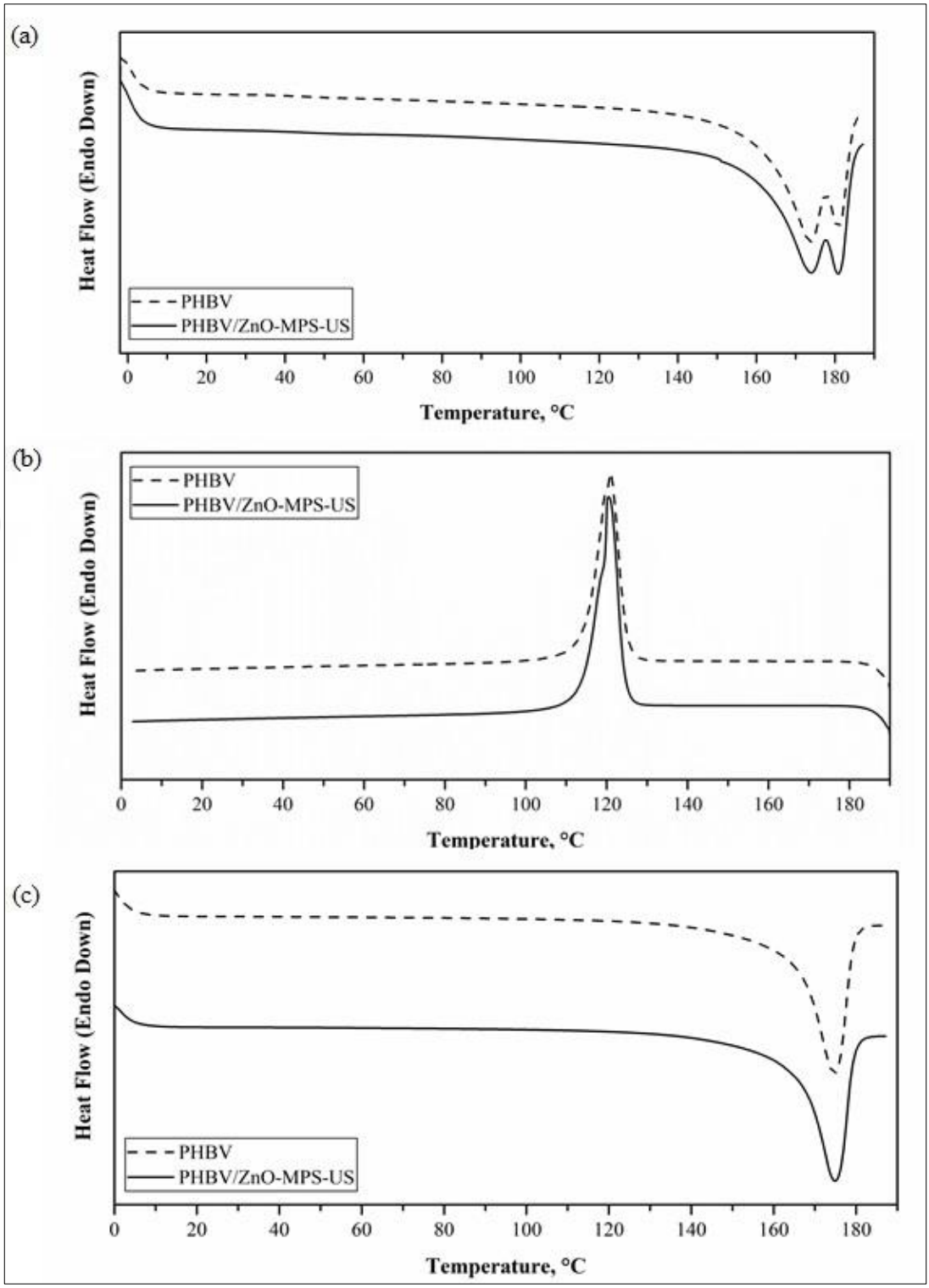

Figure 4.43 DSC scans of the PHBV/ZnO-MPS-US nanocomposite shown together with neat PHBV (a) 1st heating scans, (b) cooling scans, and (c) 2nd heating scans

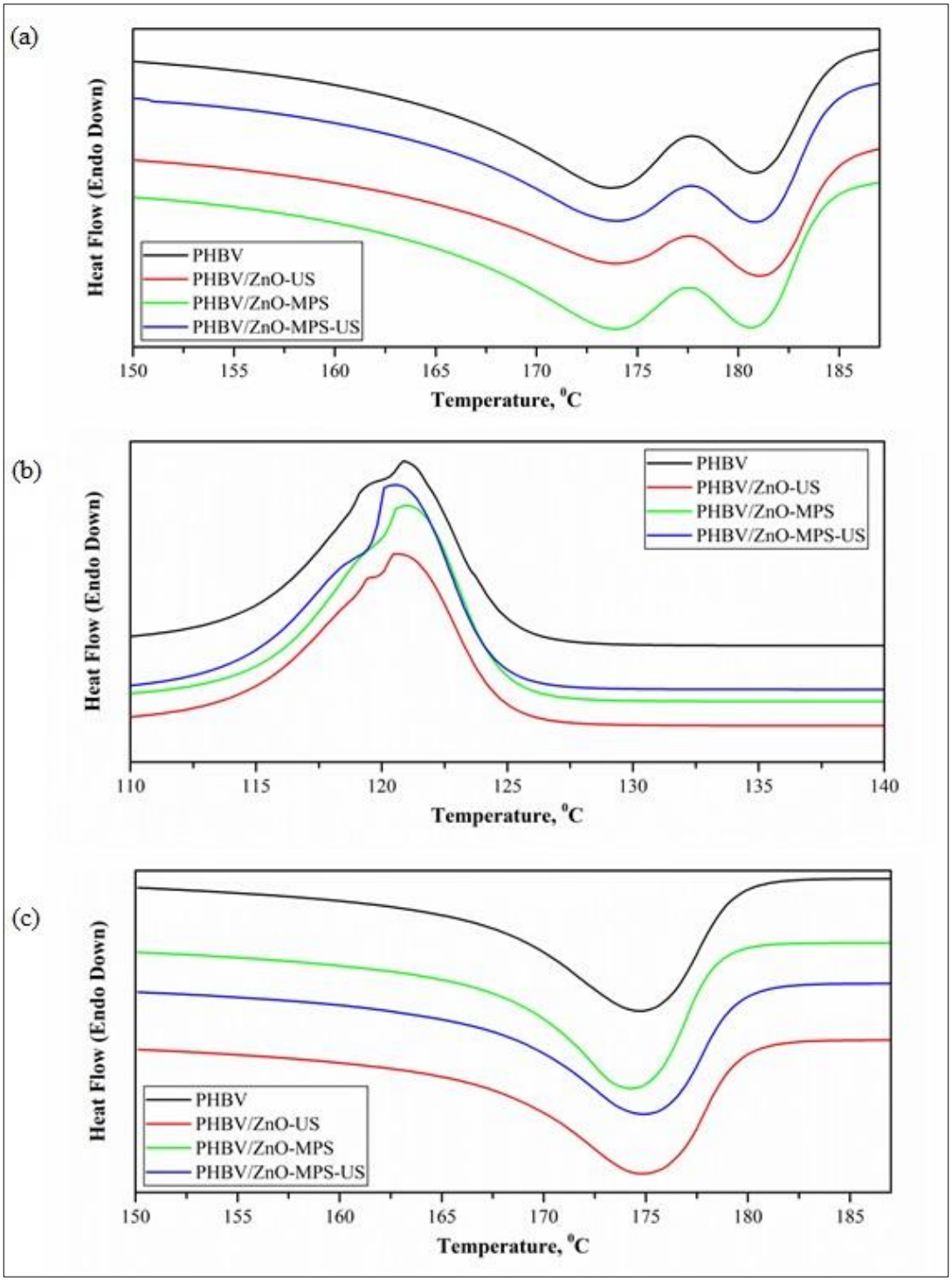

Figure 4.44 DSC scans of the neat PHBV and the PHBV/ZnO-2L-95C nanocomposites shown together at a narrower temperature range (a) 1st heating scans, (b) cooling scans, and (c) 2nd heating scans

4.6.1.3 Melting and Crystallization Behavior of the PHBV Nanocomposites Fabricated by ZnO-2L-95C Particles

PHBV inherently possesses high crystallinity (>50 %) for the entire range of different hydroxyvalerate contents [35, 112]. Since the crystalline regions of a polymer make the material strong but brittle, and the amorphous regions gives toughness to the polymer [109]; high crystallinity of PHBV causes stiffness and brittleness [171]. In spite of the advantages of PHBV like being fully bio-based and bio-degradable, commercial applications of it are limited due to its properties like high crystallinity and brittleness, and narrow processing window [4, 35]. Another drawback of PHBV is its slow crystallization kinetics that require long mold processing cycles [35].

Thermal transition temperatures of polymers, such as melting, crystallization, and glass transition temperatures, are other important aspects that determine the temperature limits of industrial applications. Melting temperatures of PHBV are generally high, while the glass transition temperatures are low [171].

Melting and crystallization behavior of neat PHBV and the PHBV/ZnO-2L-95C nanocomposites were studied by DSC analysis. For this purpose, the samples were first heated to 190 °C (1st heating run), then cooled to 0 °C (cooling run), and then heated again to 190 °C (2nd heating run). The 1st heating, cooling, and 2nd heating DSC curves of neat PHBV are given in Figure 4.40. The DSC curves of the PHBV/ZnO-US, PHBV/ZnO-MPS, and PHBV/ZnO-MPS-US nanocomposites are given in Figures 4.41, 4.42, and 4.43, respectively; together with the curves of neat PHBV for comparison. The curves of all four samples were combined in a single graph at a narrower temperature range in Figure 4.44.

Since melting is an endothermic process, the melting of the polymer is observed as an endothermic peak in the DSC thermograms. In the 1st heating runs of the neat PHBV and its nanocomposites, melting of the polymer is observed as two adjacent endothermic peaks. This double-peak melting behavior was also reported in the literature by many authors [27-29, 31, 33, 34, 37, 39].

Some authors suggested that the double-peak melting behavior was the result of the melting-recrystallization-remelting process [27, 29, 31, 33, 39]. Since PHBV has a slow crystallization rate, the crystallization was not completed during melt processing and the crystals formed had less perfection and less stability. During DSC scans with

sufficiently low heating rates, these less perfect crystals are more prone to undergo melting and recrystallizing into more stable crystals. Remelting of these more stable crystals produces the second melting peak. The first melting peak observes in the DSC 1st heating scan therefore resulted from the melting of the crystals formed during melt processing, while the second peak resulted from the melting of new crystals formed during heating process of DSC analysis.

Wang and co-workers suggested that homogeneous nucleation of PHBV starting by chain aggregation below the melting point produced the first melting peak, while heterogeneous nucleation of PHBV produced the second peak [26, 31]. Carli and co-workers suggested that thermal degradation of the polymer during processing could affect the formation of the crystals. The formation of low molecular weight chains due to the degradation could lead to the formation of less perfect crystals of various sized, and thus the multiple-peak melting behavior [28]. Another opinion is that compositional heterogeneity due to HV-rich regions and HB-rich regions could have resulted in the formation of multiple melting peaks [34, 172]. Other possibilities were reported as presence of multiple crystal modifications, physical ageing, different morphologies, relaxation of the amorphous fraction, different molecular weight species, and orientation effects [37, 172].

The double-peak melting behavior was observed for both neat PHBV and all the PHBV/ZnO-2L-95C nanocomposites. The intensity of the lower-temperature melting peak was observed to decrease when compared to the higher temperature melting peak for the PHBV/ZnO-US and PHBV/ZnO-MPS-US nanocomposites (Figure 4.44a). If the melting-recrystallization-remelting mechanism is taken into consideration, it can be said that the formation of the aforementioned less-perfect crystals during melt-processing was lower for these nanocomposites, and the amount of more perfect crystals were higher. If the compositional heterogeneity theory is taken into consideration, it can be said that the amount of HB-rich regions was slightly higher than the HV-rich regions for these two nanocomposites.

Melting temperatures (T_m) obtained for neat PHBV and its nanocomposites from the 1st heating run are given in Table 4.11. The lower temperature peak of the double melting peaks observed was shown as T_{m1}, and the higher temperature melting peak observed was shown as T_{m2}. The melting enthalpy (ΔH_m) values were calculated as the area under the melting peaks. Percent crystallinity (X_c) was calculated by the equation:

$$X_c, \% = \frac{\Delta H_m}{\Delta H^0 * w} * 100 \quad (4.18)$$

where ΔH^0 is the melting enthalpy of 100 % crystalline PHBV and w is the weight fraction of PHBV in the blend. The value of ΔH^0 was taken as 146.6 J/g due to the low valerate content of PHBV [42, 113]. The values of X_c calculated from the 1st heating runs are given in Table 4.11.

Table 4.11 Melting parameters of neat PHBV and PHBV/ZnO-2L-95C nanocomposites calculated from the DSC 1st heating runs

Sample	**T_{m1}, °C**	**T_{m2}, °C**	**ΔH_m, J/g**	**X_c, %**
PHBV	173.7	181.0	111.3	75.9
PHBV/ZnO-US	174.2	181.1	101.0	69.6
PHBV/ZnO-MPS	173.9	180.8	102.9	70.9
PHBV/ZnO-MPS-US	174.0	180.8	107.9	74.4

The melting temperature of the polymer is related to the layer thickness and perfection of crystals. An increase in the melting temperature would indicate higher layer thickness and better crystal perfection [27, 173]. There were no significant differences in the lower and higher melting temperatures of neat PHBV and the PHBV/ZnO-2L-95C nanocomposites. This suggested that the ZnO-2L-95C nanoparticles added into PHBV matrix did not affect the layer thickness and perfection of the PHBV crystals. However, changes in the ΔH_m and X_c values were observed. Percent crystallinity of PHBV decreased by 1.5 – 6 % with the addition of ZnO-2L-95C particles. Therefore, it was deduced that the ZnO particles hindered crystallization of PHBV without affecting the size and the structure of the crystals. The effect was most prominent for the ultrasound-dispersed and untreated ZnO-US particles, for the 1st heating run.

The glass transition of a polymer is the transition of the amorphous sections of the polymer from a hard and brittle state into a rubber like molten state and it is observed as a sudden shift in the DSC plot towards the endothermic direction [110]. The endothermic shift due to glass transition of PHBV was observed between -1 and 4 °C for the neat PHBV and the nanocomposites (Figure 4.45). Glass transition temperature (T_g) of PHBV was taken as the middle point of the shift as 1.5 °C. This value was similar to the values reported in the literature (0 – 1 °C) [27, 41, 173]. No particular difference was observed for the value of T_g between the neat PHBV and the

nanocomposites, except it shifted to slightly lower values for the PHBV/ZnO-MPS-US nanocomposite. Since the analysis was carried out for temperatures higher than -2 °C, the exact value of T_g could not be observed for this nanocomposite.

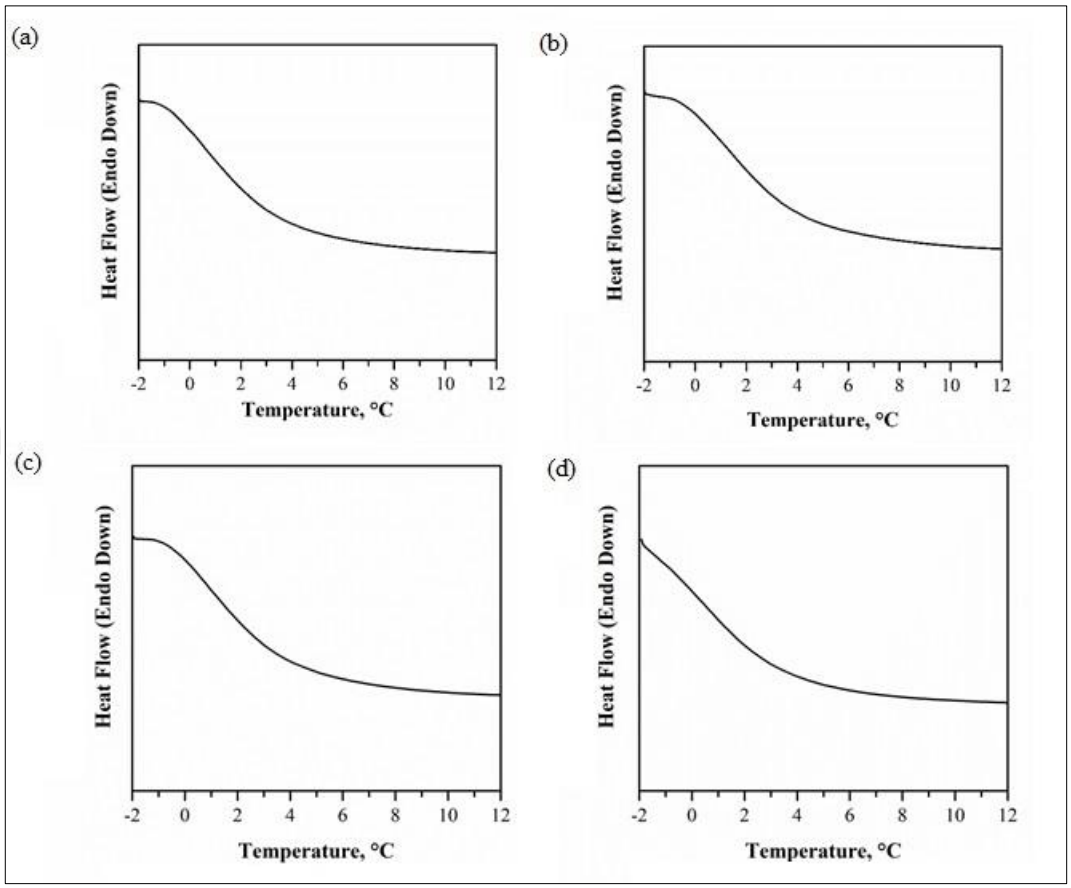

Figure 4.45 Glass transition temperatures of the (a) neat PHBV, (b) PHBV/ZnO-US, (c) PHBV/ZnO-MPS, and (d) PHBV/ZnO-MPS-US samples from the DSC 1st heating curves

At a certain temperature, polymers crystallize into ordered arrangements by giving off energy and this behavior can be observed as an exothermic peak on the DSC graph. The crystallization peaks of the neat PHBV and the nanocomposites can be seen in the cooling curves of the DSC scan (Figures 4.40 to 4.43). The maximum temperatures of the crystallization peaks were taken as the crystallization temperature (T_c) and the results are given in Table 4.12. The onset temperature of crystallization was shown as $T_{c,onset}$ and the end temperatures were shown as $T_{c,end}$.

The enthalpy of crystallization (ΔH_c) was calculated from the area under the crystallization peak and the results are also given in Table 4.12. The value of T_c was observed to be 120.9 °C for the neat PHBV and was not changed significantly for the nanocomposites. ΔH_c values on the other hand, were observed to decrease with the

addition of ZnO-2L-95C particles. The lowest value was obtained for the PHBV/ZnO-US nanocomposite, by a 13 % decrease compared to the crystallization enthalpy of the neat PHBV. This result was consistent with the lowest X_c value obtained for this nanocomposite from the 1st heating scan.

Table 4.12 Crystallization parameters of neat PHBV and PHBV/ZnO-2L-95C nanocomposites calculated from the DSC cooling runs

Sample	**$T_{c,\,onset}$, °C**	**T_c, °C**	**$T_{c,\,end}$, °C**	**$T_{c,\,onset}$ - T_c, °C**	**ΔH_c, J/g**
PHBV	124.9	120.9	116.0	4.0	-107.2
PHBV/ZnO-US	124.8	120.6	116.9	4.2	-93.3
PHBV/ZnO-MPS	124.9	121.1	117.3	3.8	-99.2
PHBV/ZnO-MPS-US	124.6	120.6	118.5	4.0	-97.6

The value of $T_{c,onset} - T_c$ was reported to be a measure of the crystallization rate [40, 174]. Smaller difference would indicate a greater rate of crystallization. When the values of $T_{c,onset} - T_c$ calculated for neat PHBV and the nanocomposites, it was observed that the values were not significantly different from each other. This suggested that there was no significant change in the crystallization rate of PHBV with the addition of ZnO-2L-95C particles.

The cooling curves of neat PHBV and the nanocomposites are given in Figure 4.44b together and at a narrower temperature scale. The crystallization process appeared to occur in two successive steps, since two shoulders can be observed on the crystallization peaks. The reason for this situation could be due to multiple crystal modifications, physical ageing, different morphologies, relaxation of the amorphous fraction, different molecular weight species, or orientation effects, similar to the reasons mentioned for the double-peak melting behavior [37, 172].

The second heating scan of the DSC analysis reveals thermal transitions information regardless of the effects of melt processing, since the thermal histories due to processing are erased during the 1st heating run [37]. The 2nd heating curves of the neat PHBV and the nanocomposites are given in Figures 4.40 to 4.43. Double-peak melting behavior observed in the 1st heating scans was not observed in the 2nd heating scans of neat PHBV and the nanocomposites. It was deduced that the double-peak melting behavior was probably the result of the melting-recrystallization-remelting mechanism, where

less perfect crystals were formed during melt-processing and higher perfection crystals during 1st heating of the DSC scan. As this thermal stress history was erased during the 1st heating scan of DSC, this behavior was not observed during the 2nd heating scan. The 2nd heating curves of the neat PHBV and the nanocomposites are given in Figure 4.44c together and at a narrower temperature scale. No particular difference could be observed between the melting behavior of the neat PHBV and the nanocomposites.

The melting temperatures (T_m) obtained from the 2nd heating scan for neat PHBV and the nanocomposites are given in Table 4.13. The onset and end temperatures of melting were shown as $T_{m,onset}$ and $T_{m,end}$, respectively. ΔH_m values were calculated from the area under the melting curves. X_c values were calculated from the ΔH_m values by the same equation as in the 1st heating scan. The values are given in Table 4.13. The melting temperatures of neat PHBV and the nanocomposites did not show any significant difference in the 2nd heating scan, similar to the results obtained in 1st heating and cooling scans. ΔH_m and X_c values were observed to decrease for the nanocomposites compared to neat PHBV, similar to the 1st heating scan. The lowest crystallinity value was again obtained for the PHBV/ZnO-US nanocomposite.

Table 4.13 Melting parameters of neat PHBV and PHBV/ZnO-2L-95C nanocomposites calculated from the DSC 2nd heating runs

Sample	**$T_{m,\ onset}$, °C**	**T_m, °C**	**$T_{m,\ end}$, °C**	**ΔH_m, J/g**	**X_c, %**
PHBV	165.5	174.7	179.3	112.7	76.9
PHBV/ZnO-US	166.0	174.9	179.6	99.0	68.2
PHBV/ZnO-MPS	167.2	174.3	178.5	104.5	72.0
PHBV/ZnO-MPS-US	166.1	174.9	179.5	100.8	69.5

Decrease in the crystallinity of PHBV was previously reported in the literature with the addition of hydroxyapatite and halloysite particles [28, 175]. Öner and İlhan [175] reported that formation of covalent bonds between the polymer and the particles would increase crystallinity whereas non-covalent interactions would decrease or would not affect the crystallinity. When the non-covalent bonds are strong attractions, the crystallinity would be inhibited due to the constraining of polymer molecules. When the non-covalent bonds are weak attractions, little or no effect would be created on

crystallinity. Carli et al. [28] suggested that the thermal degradation of the polymer during processing would influence crystal formation.

Diez-Pascual and Diez-Vicente reported an increase in T_c and X_c values of PHB [43] and PHBV [10] with the incorporation of ZnO particles by solution casting method. Homogeneous dispersed ZnO nanofillers were reported to act as nucleating agents for PHBV, accelerating the crystallization rate by heterogeneous nucleation effect.

On the contrary, Castro-Mayorga et al. [34] and Yu et al. [173] reported a decrease in X_c of PHBV with the addition of ZnO particles by electrospinning method. Yu et al. [173] suggested that H-bonds were formed between the hydroxyl (-OH) groups of ZnO particles and the carbonyl (C=O) groups of PHBV, and the regularity of the PHBV molecular chains were disturbed by the ZnO particles, decreasing the crystallinity.

The addition of ZnO particles into PHBV matrix by different methods, produced controversial results in the crystalline structure of PHBV, as well as in its thermal stability, as it was discussed in the previous section. The reason for these differences in the crystallinity and thermal stability were considered to be arising from the different effects caused by different processing methods. Better particle dispersion achieved by solution casting or thermal degradation caused by melt-extrusion and electrospinning might have caused these variational results.

4.6.1.4 Mechanical Properties of the PHBV Nanocomposites Fabricated by ZnO-2L-95C Particles

Polymers have the ability to improve their properties by the addition of nanofillers while maintaining their characteristics [176]. Nanoparticles can improve the mechanical properties of polymers even with very low loadings and when the aspect ratio of the particles is higher this effect is more pronounced [177, 178, 180].

Mechanical properties of PHBV/ZnO-2L-95C particles were investigated and compared with those of neat PHBV. Uniaxial tensile testing was applied to the nanocomposite samples and stress-strain curves of the samples were obtained. Tensile strength, offset yield strength, elastic modulus, elongation at break, and toughness values of the samples were calculated from the stress-strain curves.

The stress-strain curves obtained for neat PHBV and the nanocomposites are given in Figure 4.46. The curves show five different specimens repeated for each sample. The

first linear section of the curves corresponds to the elastic deformation region whereas the second curved part is the plastic deformation region [114, 115]. For neat PHBV and the PHBV/ZnO-MPS nanocomposite, the plastic deformation region was quite small, indicating brittle fracture behavior. For the nanocomposites PHBV/ZnO-US and PHBV/ZnO-MPS, plastic deformation region was wider, probably due to the increased ductility. For these two nanocomposites, the maximum stress and strain values were also observed to increase.

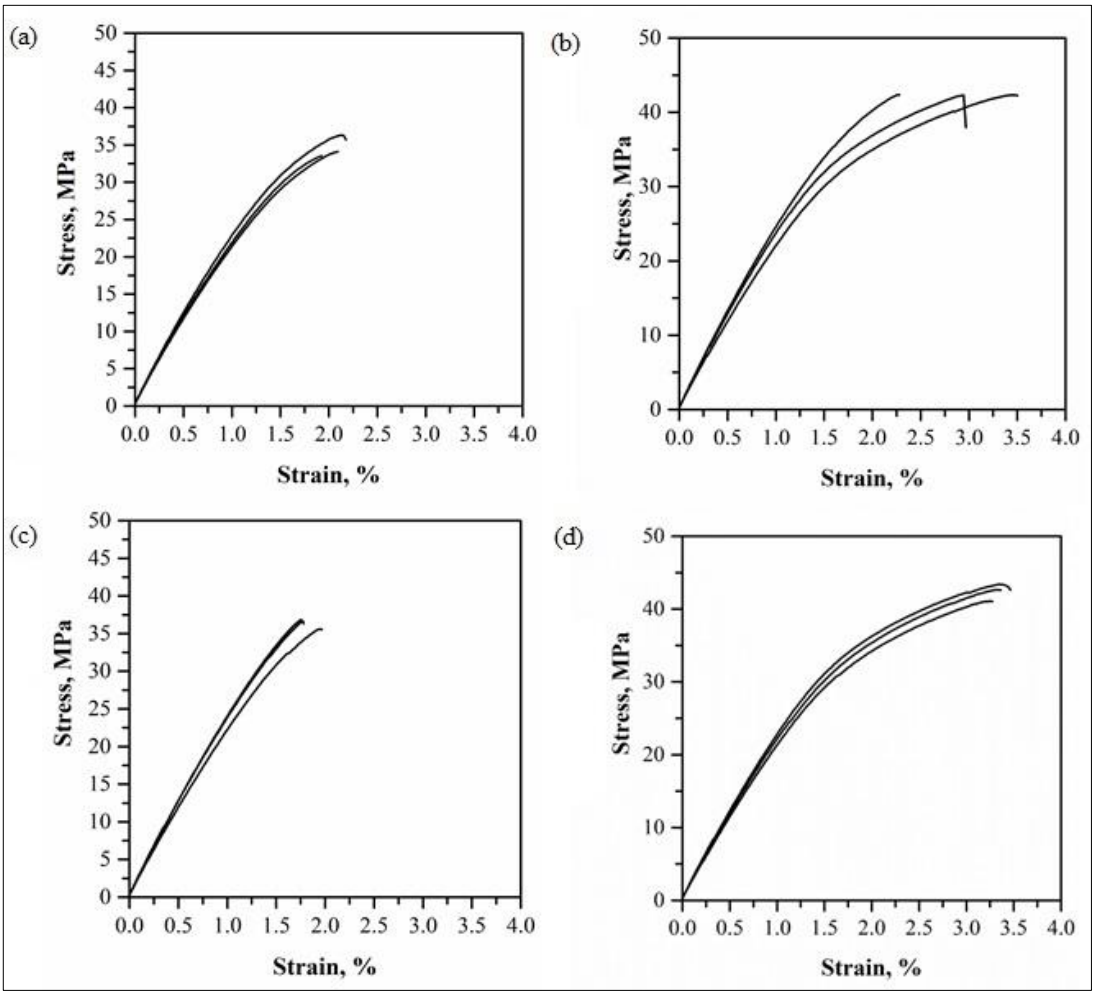

Figure 4.46 Stress-strain curves of (a) neat PHBV, (b) PHBV/ZnO-US, (c) PHBV/ZnO-MPS, and (d) PHBV/ZnO-MPS-US nanocomposites obtained from tensile testing

The tensile strength (σ) values of neat PHBV and the nanocomposites were calculated as the highest value of stress that the samples could withstand. Elastic moduli (E) of the samples were calculated from the slope of the linear elastic deformation region. Percent elongation (%El) values were calculated by dividing the displacement values of the samples to the initial lengths. Toughness values of the samples were calculated from the area under the stress-strain curves. The calculated values of the mechanical parameters

are given in Table 4.14. The changes in the mechanical properties can be observed in Figure 4.47 in graphical form.

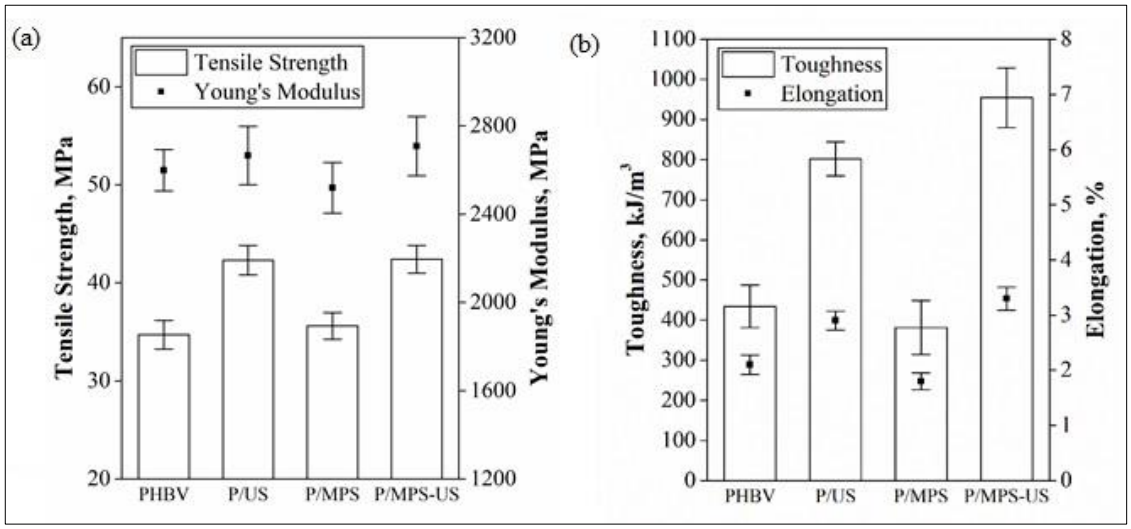

Figure 4.47 Mechanical properties of neat PHBV and the PHBV/ZnO-2L-95C nanocomposites: (a) tensile strength and elastic modulus and (b) elongation at break and toughness

Table 4.14 Mechanical properties of neat PHBV and the PHBV/ZnO-2L-95C nanocomposites

Sample	**Tensile strength, MPa**	**Elongation, %**	**Elastic modulus, MPa**	**Toughness, kJ/m^3**
PHBV	34.7±1.5	2.1±0.2	2440.8±93.5	434.6±52.9
PHBV/ZnO-US	42.3±1.5	2.9±0.2	2562.3±132.2	801.9±42.4
PHBV/ZnO-MPS	35.6+1.4	1.8±0.1	2533.6±114.7	381.2±67.5
PHBV/ZnO-MPS-US	42.4±1.4	3.3±0.2	2356.3±134.0	954.7±74.7

The nanocomposites PHBV/ZnO-US and PHBV/ZnO-MPS-US showed remarkable increase (about 22 %) in tensile strength compared to neat PHBV. On the other hand, the tensile strength value of the PHBV/ZnO-MPS nanocomposite was not significantly changed, compared to neat PHBV. ZnO nanoparticles incorporated into the PHBV matrix could improve the strength of the material only when ultrasonic dispersion was applied to them. Surface modification of the ZnO particles with silane did not seem to have an effect on the strength of PHBV.

Elongation at break values of the PHBV/ZnO-US and PHBV/ZnO-MPS-US nanocomposites were also increased compared to neat PHBV, similar to the tensile

strength results. The increase in percent elongation was 38 % and 57 % for the PHBV/ZnO-US and PHBV/ZnO-MPS-US nanocomposites, respectively. A decrease of 14 % was observed for the PHBV/ZnO-MPS nanocomposite compared to neat PHBV. Similar results were obtained for toughness values, where the increase was 85 % for PHBV/ZnO-US and 120 % for PHBV/ZnO-MPS-US. The decrease was 12 % for PHBV/ZnO-MPS. These results also demonstrated the importance of effective particle dispersion on the strength and ductility of the material. Unlike tensile strength, silane modification seemed to have an effect on the elongation value. For the treated particles that were not dispersed by ultrasound, elongation was negatively affected, whereas surface treated and dispersed particles produced better results than ultrasound-dispersed but untreated particles. These results suggest that, in terms of ductility of the material, a combination of effective particle dispersion and surface modification can produce the best results. In order to silane be effective on mechanical properties, homogeneous dispersion of the particles in required. When the particles are heavily agglomerated, surface modification can even produce negative results on the mechanical properties of the polymer.

The results obtained for elastic modulus values showed a different trend from tensile strength, elongation and toughness values. Elastic modulus of the PHBV/ZnO-US and PHBV/ZnO-MPS samples were increased by 5 % and 4 %, respectively, when compared to neat PHBV. The elastic modulus of the PHBV/ZnO-MPS-US nanocomposite was decreased by 3 %. Nevertheless, these changes were very small and it can be said that the elastic modulus value of PHBV was not significantly changed with the incorporation of ZnO particles.

The improvement or impairing of the mechanical properties of a polymer nanocomposite is depends on filler dispersion, crystallinity, and the interface compatibility [10, 175]. The best results obtained in terms of strength and ductility was obtained for the both ultrasound-dispersed and silane treated particles, emphasizing the importance of both particle dispersion and polymer-particle compatibility. The elastic modulus was observed to slightly decrease for this nanocomposite probably due to the decreased crystallinity, since higher crystallinity would restrict the movement of polymer chains.

In the work of Castro-Mayorga et al. [34] where PHBV/ZnO nanocomposites were fabricated by electrospinning method, ZnO particles were reported to decrease strength

and toughness and show no significant effect on the elongation and stiffness. Diez-Pascual and Diez-Vicente [10] reported an increase in both tensile strength and elastic modulus by the incorporation of ZnO particles into PHBV matrix by solution casting method at low particle loadings. Elongation at break value on the other hand, was decreased with increasing ZnO content. As it was previously mentioned in the thermal properties section, processing method may result in different final properties of the nanocomposite.

4.6.2 PHBV/ZnO Nanocomposites Fabricated by CMI Containing ZnO Particles

CMI biopolymer was incorporated in the wet chemical synthesis reaction of ZnO particles as it was described in Section 3.1.1. Hexagonal rod-shaped particles were obtained with different aspect ratios for different CMI contents. The ZnO particles that were synthesized without the addition of CMI (ZnO-2L-95C particles) had an aspect ratio of 15.6. This value was decreased to 11.2 for the particles synthesized in presence of 50 ppm CMI and to 4.5 for the particles synthesized with 450 ppm CMI. Aspect ratio and the polymer-particle compatibility are two important phenomena in polymer nanocomposite properties. Even though the aspect ratio was negatively affected by the incorporation of CMI into ZnO particles, it could have increased the particle compatibility with the polymer matrix, since CMI is also a biopolymer. Therefore, the effects of CMI containing ZnO particles on the thermal and mechanical properties of PHBV were investigated.

ZnO-50-2L-95C particles and ZnO-450-2L-95C particles were incorporated into PHBV in a ratio of 1 wt. %. The results obtained for thermal and mechanical analyses were compared to those of ZnO-2L-95C particle that do not contain any CMI. As it was described in the previous sections, ZnO-2L-95C particles exhibited severe agglomeration and thus were dispersed using direct ultrasound. Severe agglomeration was also observed for 50 ppm CMI containing particles and these particles were dispersed with 60 min of ultrasound application. 450 ppm CMI containing particles showed no agglomeration, however, 60 min of ultrasound was also applied to these particles for comparison purposes. Surface modification was not applied to these particles, since CMI was believed to provide the surface compatibility between the particles and the polymer. The formulations and the sample coding of the nanocomposites are given in Table 4.15. The PHBV/ZnO nanocomposites fabricated

were characterized for their structural, thermal, and mechanical properties and were compared to those of neat PHBV.

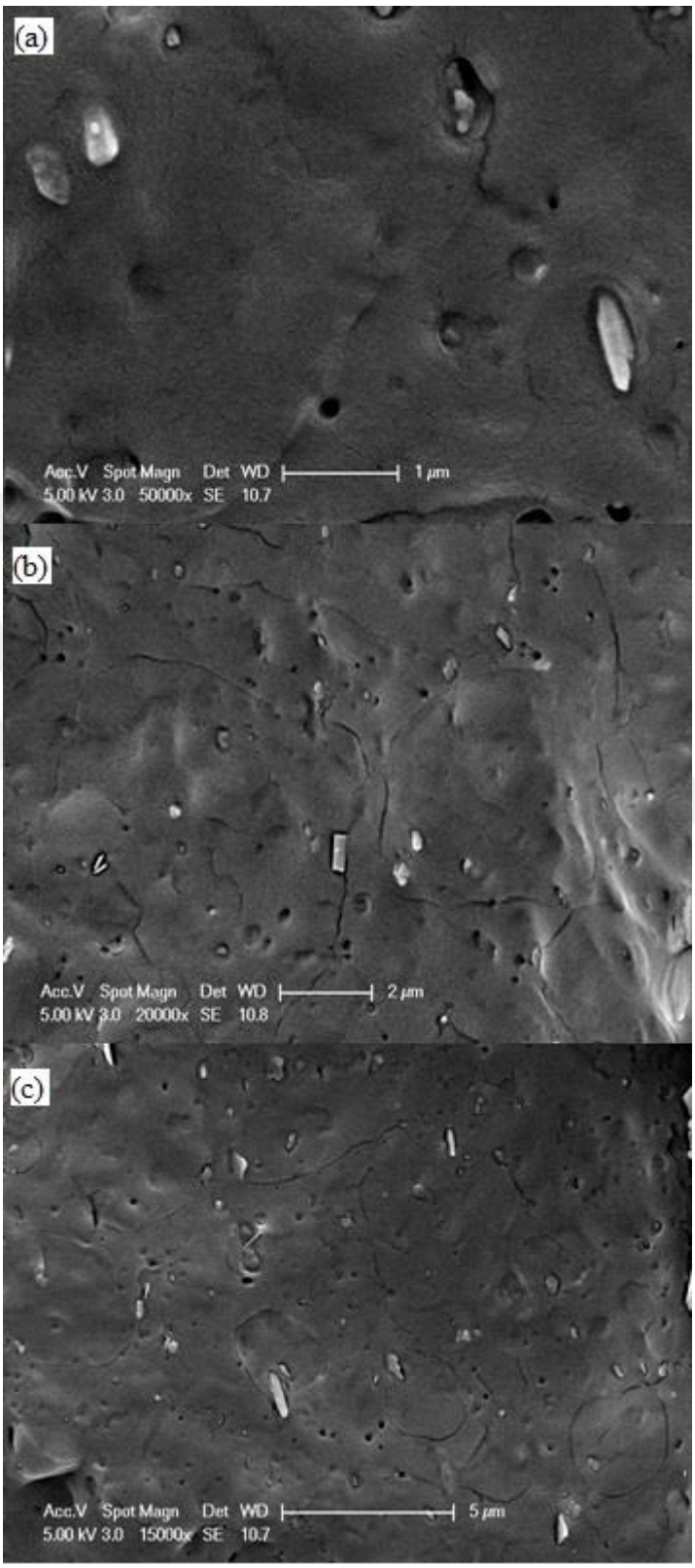

Figure 4.48 SEM micrographs of the PHBV/ZnO(50) nanocomposite at (a) 50000x, (b) 20000x, and (c) 15000x magnification

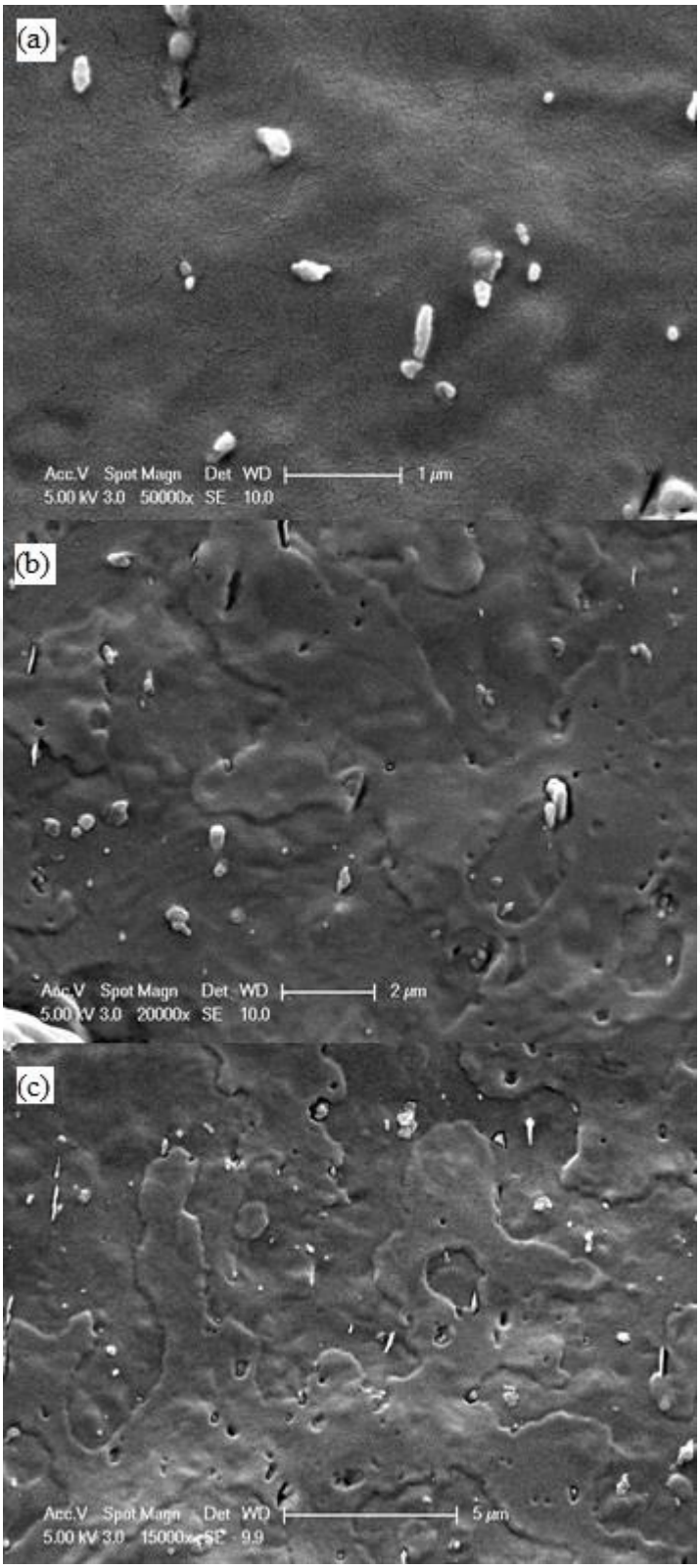

Figure 4.49 SEM micrographs of the PHBV/ZnO(450) nanocomposite at (a) 50000x, (b) 20000x, and (c) 15000x magnification

Table 4.15 Sample codes and formulations of the PHBV/ZnO nanocomposites fabricated from CMI containing ZnO particles

Sample code	**ZnO content, wt.%**	**PHBV content, wt.%**	**CMI content, ppm**
PHBV/ZnO(50)	1	99	50
PHBV/ZnO(450)	1	99	450

4.6.2.1 Structural Characterization of the PHBV Nanocomposites Fabricated by CMI Containing ZnO Particles

Structural characterization of the nanocomposites was performed by SEM analysis. SEM micrographs of the PHBV/ZnO(50) and PHBV/ZnO(450) nanocomposites are given in Figures 4.48 and 4.49, respectively. The particles were generally well dispersed within the matrix except some small areas of agglomeration. The voids observed in SEM images resulted from dislocated ZnO particles during fracturing prior to the analysis.

Table 4.16 Average numbers of particles per SEM image of PHBV nanocomposites fabricated by CMI containing ZnO particles

Nanocomposite sample	**Average number of particles observed in SEM micrographs**
PHBV/ZnO(50)	171.1
PHBV/ZnO(450)	116.6
PHBV/ZnO-US	99.3
PHBV/ZnO-MPS-US	158.8

One indication of the level of particle dispersion within the matrix was reported as the total number of particles observed in a SEM image [28, 162]. The number of ZnO particles observed in the 15000x magnification SEM images of PHBV/ZnO(50) and PHBV/ZnO(450) nanocomposites were counted for five different images. The results were reported in Table 4.16 together with the results previously obtained for PHBV/ZnO-US and PHBV/ZnO-MPS-US nanocomposites for comparison. The best particle dispersion was obtained for the PHBV/ZnO(50) among the nanocomposite samples, indicating that CMI might increase the compatibility between the PHBV matrix and ZnO particles at low concentrations. The particles containing higher amount

of CMI (450 ppm) showed poorer dispersion than the MPS-treated particles. Even though CMI is a hydrophilic polymer, the carbonyl groups in its structure might be the reason for the interface compatibility.

4.6.2.2 Thermal Stability of the PHBV Nanocomposites Fabricated by CMI Containing ZnO Particles

Thermal stability of the nanocomposites was investigated by dynamic TGA under nitrogen atmosphere. TG and DTG curves of the PHBV/ZnO(50) and PHBV/ZnO(450) nanocomposite samples were obtained between 25 and 560 °C (Figures 4.50 and 4.51).

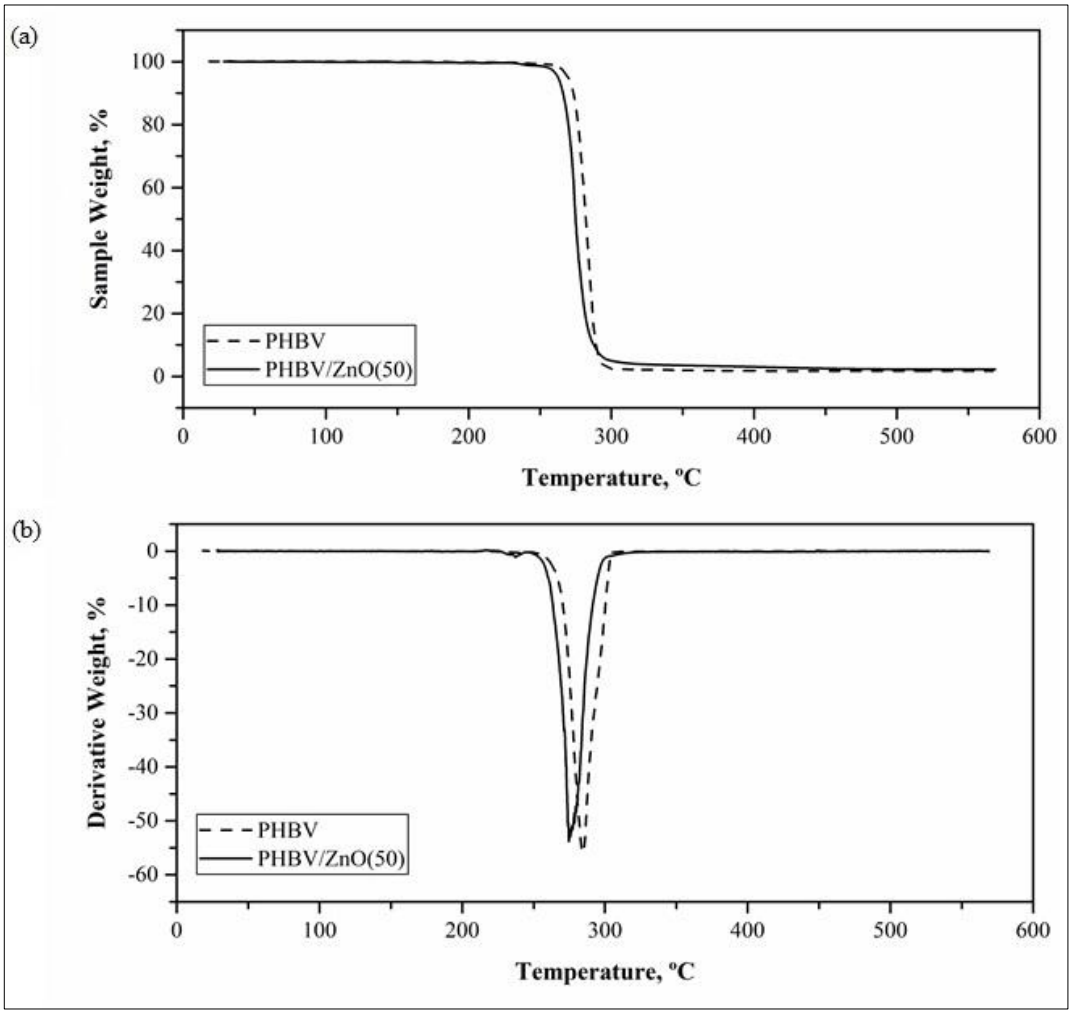

Figure 4.50 Thermogravimetry curves of neat PHBV and PHBV/ZnO(50) samples: (a) weight loss and (b) derivative weight loss curves

Thermogravimetry curves of neat PHBV were also included in the graphs for comparison. Thermal degradation of the nanocomposite samples was observed to occur in a single step and at a narrow temperature range, similar to the neat PHBV sample. The curves were slightly shifted towards lower temperatures indicating a slight decrease

in thermal stability compared to neat PHBV. The TG and DTG curves of the nanocomposites and the neat PHBV are given together in Figure 4.52 in a narrower temperature range around the degradation zone. No particular difference could be observed between the TG and DTG curves of the two nanocomposite samples, except the curve of the PHBV/ZnO(50) sample was slightly shifted left compared to the curve of PHBV/ZnO(450) sample.

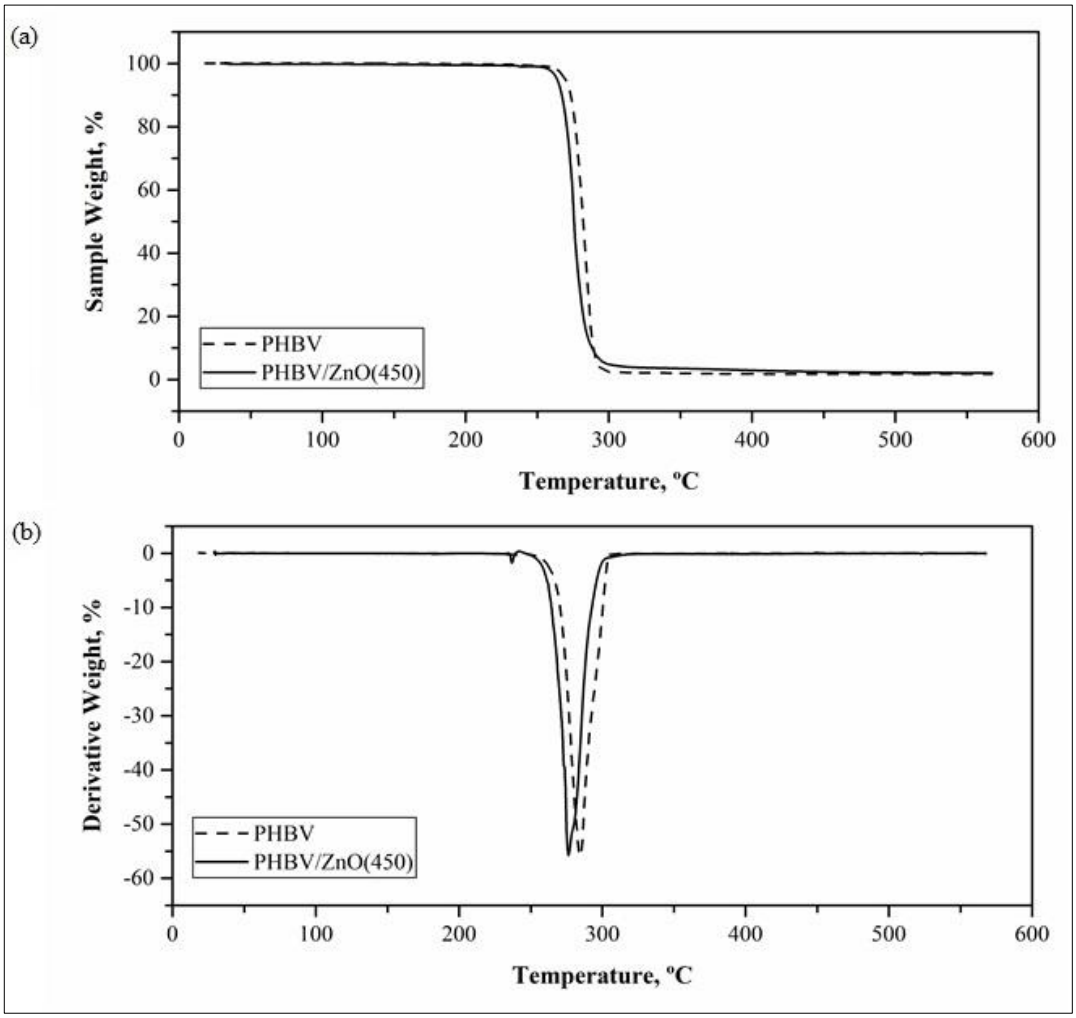

Figure 4.51 Thermogravimetry curves of neat PHBV and PHBV/ZnO(450) samples: (a) weight loss and (b) derivative weight loss curves

T_{max} values calculated from the DTG curves of the nanocomposites are given in Table 4.17, together with other characteristic degradation temperatures ($T_{x\%}$). The values previously calculated for the neat PHBV sample are also given in the table for comparison. The T_{max} values and the other degradation temperatures calculated for the nanocomposites were observed to decrease about 9 °C when compared to the temperatures of the neat PHBV. This indicated a small decrease in the thermal stability, probably due to the high thermal conductivity of ZnO particles [43, 46]. Considering the

initial decomposition temperature as the $T_{2\%}$, the processing window of the polymer was slightly narrowed by the addition of ZnO particles containing CMI. However, degradation temperature was still far above its melting point, allowing some processing window. Char residues were around 2 % for both nanocomposite samples.

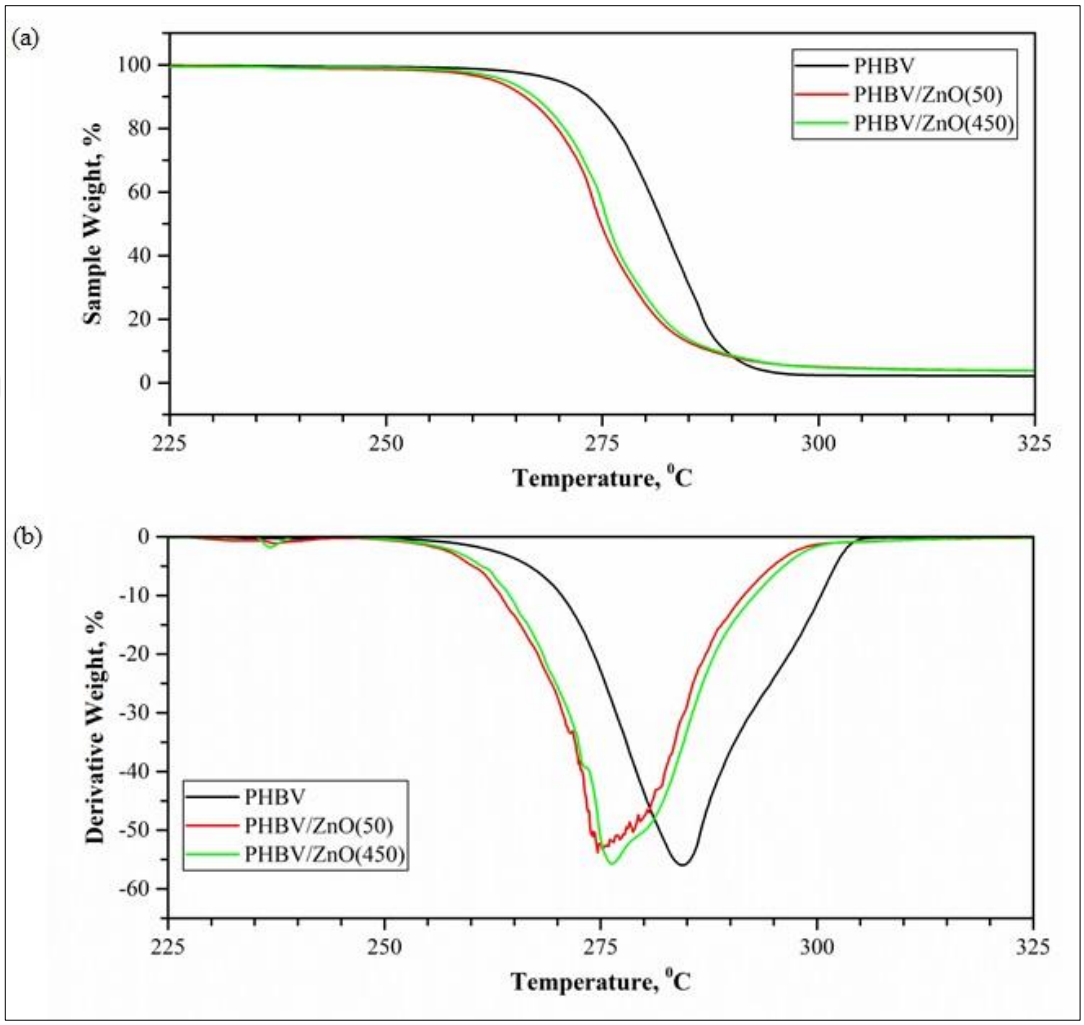

Figure 4.52 Thermogravimetry curves of neat PHBV, PHBV/ZnO(50) and PHBV/ZnO(450) nanocomposites at a narrower temperature range: (a) weight loss and (b) derivative weight loss curves

The activation energy for thermal decomposition was calculated for the PHBV/ZnO(50) and PHBV/ZnO(450) nanocomposites using the Horowitz-Metzger method [170]. The graphs of $\ln[\ln(W_0/W_T]$ values against the θ values were plotted (Figure 4.53) and the values of E_a were calculated from the slopes and reported in Table 4.17. The E_a value calculated for the PHBV/ZnO(50) nanocomposite was higher than that of neat PHBV. This suggested that well-distributed ZnO particles increased the activation energy and retarded degradation. However, due to the high thermal conductivity of the particles,

heat was dissipated throughout the nanocomposite rapidly and thermal stability was decreased [43, 46].

Table 4.17 Parameters of thermal degradation calculated for neat PHBV, PHBV/ZnO(50) and PHBV/ZnO(450) samples

Sample	**$T_{2\%}$, °C**	**$T_{5\%}$, °C**	**$T_{10\%}$, °C**	**$T_{20\%}$, °C**	**$T_{80\%}$, °C**	**T_{max}, °C**	**Char, %**	**Ea, kJ/mole**
PHBV	264.0	270	273.3	276.6	286.7	284.5	1.74	480.8
PHBV/ZnO(50)	256.1	262.5	266.0	269.7	281.4	275.2	2.27	494.5
PHBV/ZnO(450)	258.5	263.8	267.1	270.5	282.1	276.3	2.08	474.1
PHBV/ZnO-US	258.6	263.8	267.4	271	281.2	278.1	5.05	470.7

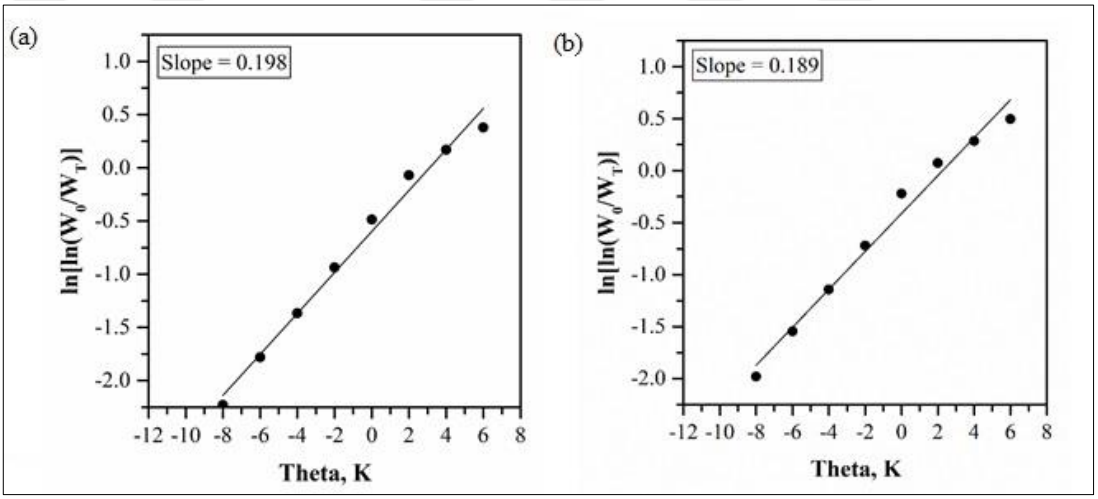

Figure 4.53 Calculation of the E_a values for (a) PHBV/ZnO(50) and (b) PHBV/ZnO(450) nanocomposites by the Horowitz-Metzger method

4.6.2.3 Melting and Crystallization Behavior of the PHBV Nanocomposites Fabricated by CMI Containing ZnO Particles

Melting and crystallization behavior of the PHBV/ZnO(50) and PHBV/ZnO(450) nanocomposites were studied by DSC analysis. The samples were heated to 190 °C (1st heating run), cooled to 0 °C (cooling run) and heated again to 190 °C (2nd heating run). The 1st heating, cooling, and 2nd heating curves obtained for the two nanocomposites are given in Figures 4.54 and 4.55. The curve previously obtained for neat PHBV was also shown in these plots for comparison. The curves of all three samples were combined in a single graph at a narrower temperature range in Figure 4.56.

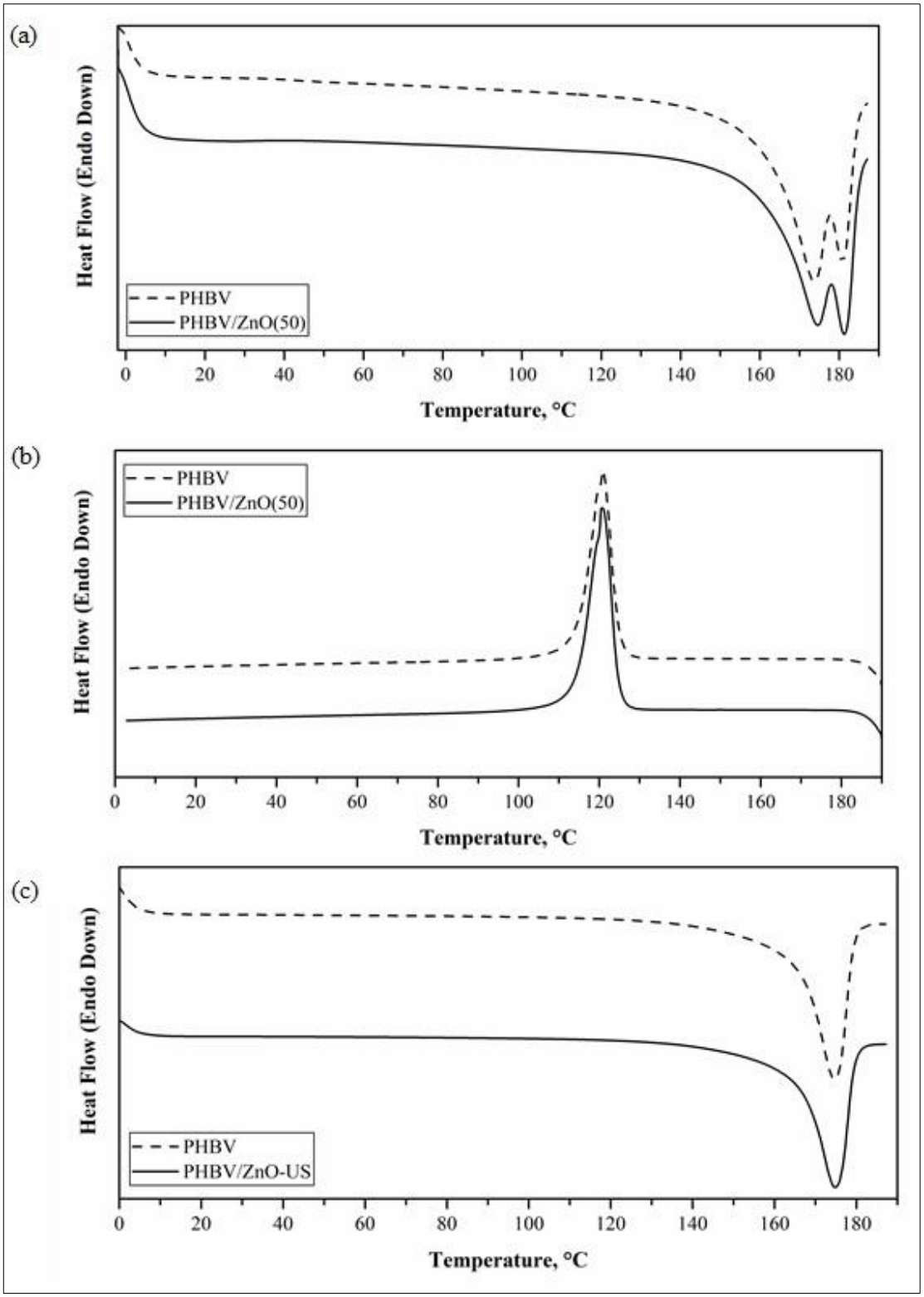

Figure 4.54 DSC scans of the PHBV/ZnO(50) nanocomposite shown together with neat PHBV (a) 1st heating scans, (b) cooling scans, and (c) 2nd heating scans

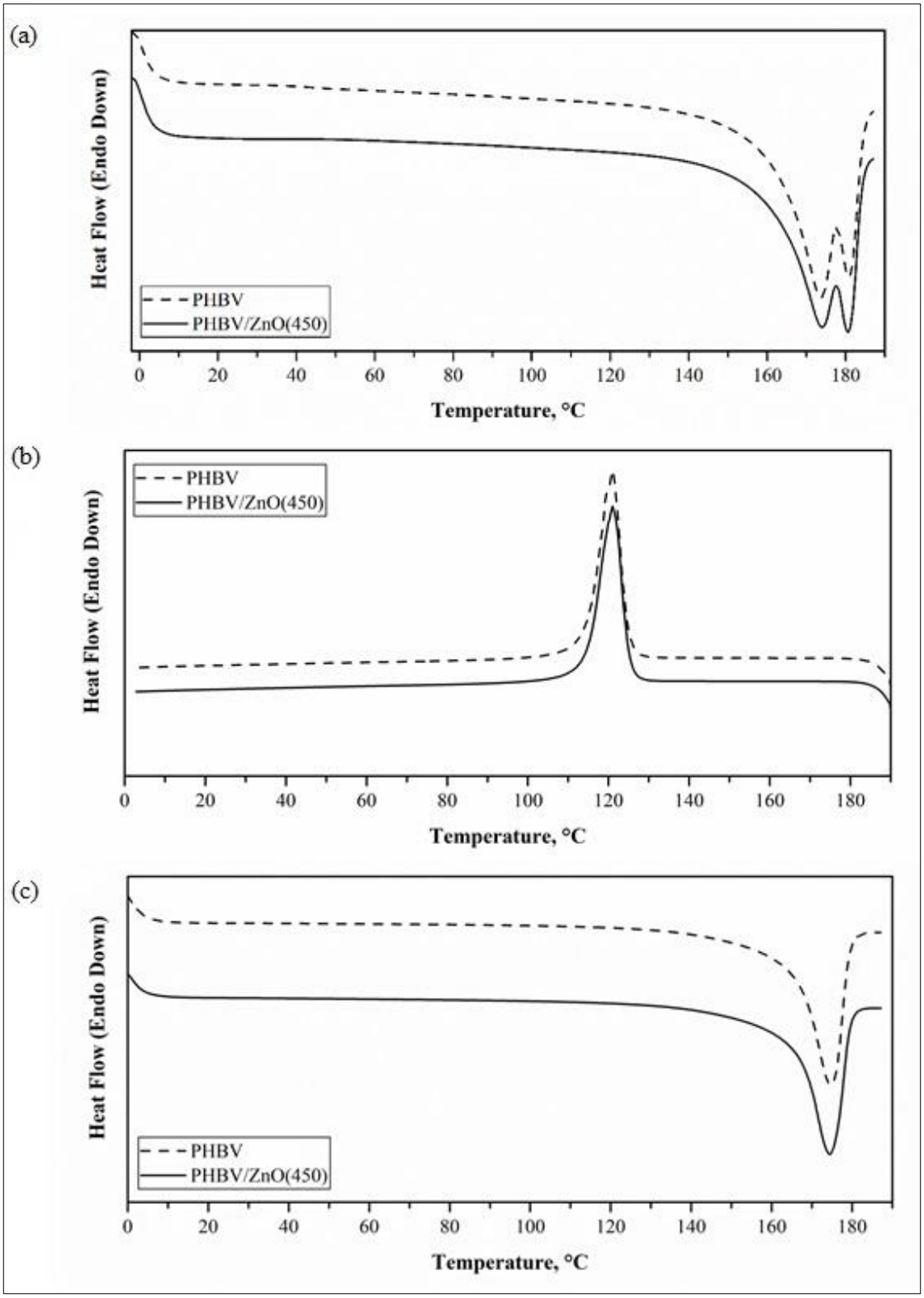

Figure 4.55 DSC scans of the PHBV/ZnO(450) nanocomposite shown together with neat PHBV (a) 1st heating scans, (b) cooling scans, and (c) 2nd heating scans

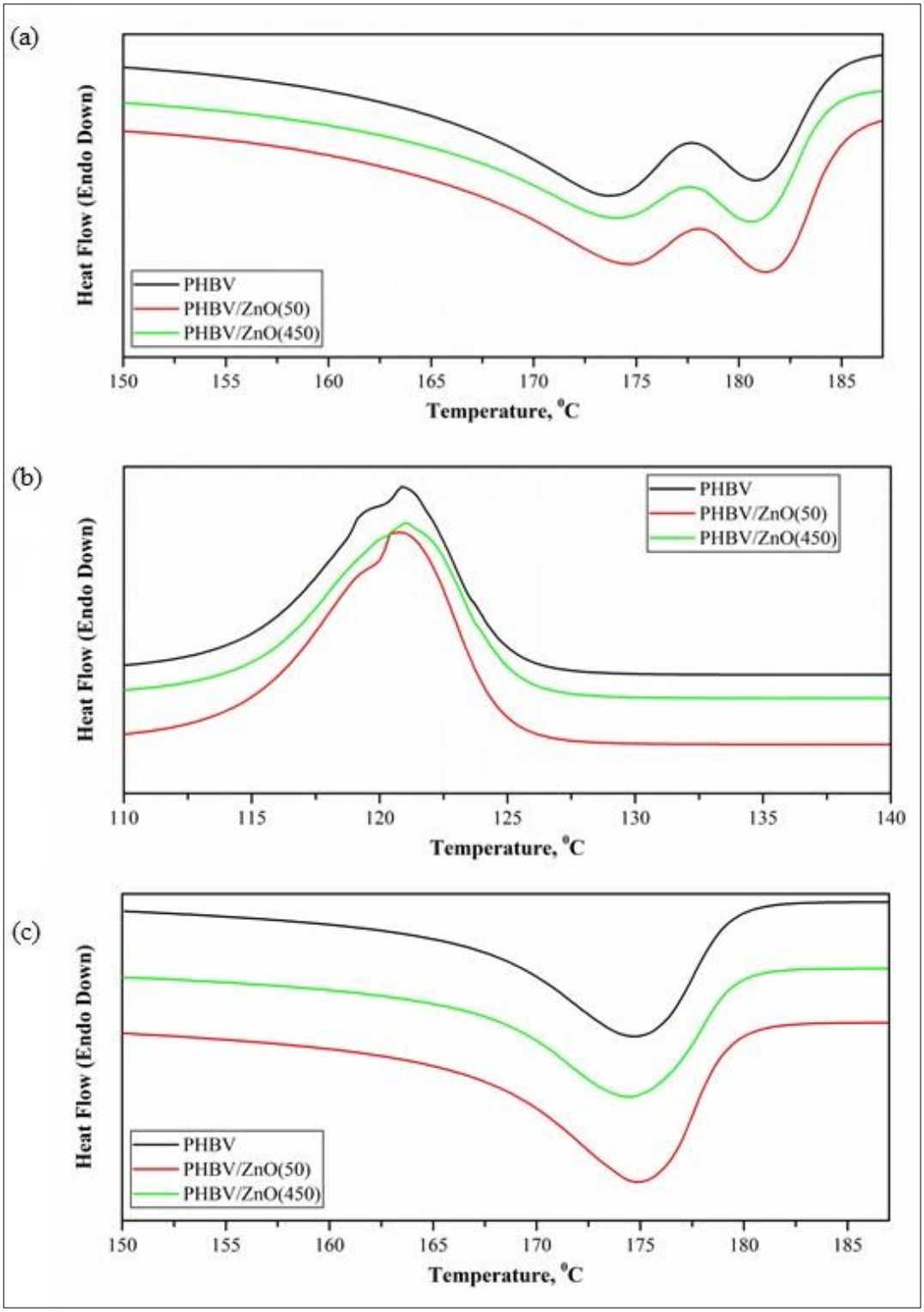

Figure 4.56 DSC scans of neat PHBV, PHBV/ZnO(50), and PHBV/ZnO(450) shown together at a narrower temperature range (a) 1st heating scans, (b) cooling scans, and (c) 2nd heating scans

Double-peak melting behavior was observed for both nanocomposites similar to neat PHBV, as discussed in the previous sections. In comparison to neat PHBV, the intensity of the lower-temperature melting peak was decreased for the nanocomposites while the

intensity of the higher temperature melting peak was increased (Figures 4.54a and 4.55a). Melting temperatures (T_m) obtained for the nanocomposites and neat PHBV from the 1st heating runs are given in Table 4.18. The lower temperature peak of the double melting peaks observed was shown as T_{m1}, and the higher temperature melting peak observed was shown as T_{m2}. The calculated values of ΔH_m and X_c are also given in Table 4.18.

Table 4.18 Melting parameters of neat PHBV, PHBV/ZnO(50) and PHBV/ZnO(450) calculated from the DSC 1st heating runs

Sample	**T_{m1}, °C**	**T_{m2}, °C**	**ΔH_m, J/g**	**X_c, %**
PHBV	173.7	181.0	111.3	75.9
PHBV/ZnO(50)	174.4	181.3	102.3	70.5
PHBV/ZnO(450)	173.7	180.6	101.3	69.8
PHBV/ZnO-US	174.2	181.1	101.0	69.6

There were no significant differences in the lower and higher melting temperatures of the nanocomposites and the neat PHBV. Therefore, it can be said that the CMI-containing ZnO particles added into PHBV matrix did not affect the crystal layer thickness or perfection. The decreases in the ΔH_m and X_c values suggested that the CMI-containing ZnO particles hindered crystallization of PHBV without affecting the size and the structure of the crystals. Percent crystallinity of the nanocomposite samples were decreased by about 5 – 6 %, compared to neat PHBV. The melting parameters obtained for PHBV/ZnO(50) and PHBV/ZnO(450) from the DSC 1st heating runs did not show any particular difference than the PHBV/ZnO-US nanocomposite.

The endothermic shift due to glass transition was observed between -2 and 4 °C for the PHBV/ZnO(50) nanocomposite and between -1 and 4 °C for PHBV/ZnO(450). The T_g values calculated for PHBV/ZnO(50) and PHBV/ZnO(450) were 1 °C and 1.5 °C, respectively (Figure 4.57). The values were similar to the values obtained for neat PHBV and the values reported in the literature [27, 41, 173].

The exothermic crystallization peaks of the two nanocomposites together with neat PHBV can be seen in the cooling curves given in Figures 4.54b and 4.55b. The calculated parameters for crystallization are given in Table 4.19.

Table 4.19 Crystallization parameters of neat PHBV, PHBV/ZnO(50), PHBV/ZnO(450), and PHBV/ZnO-US nanocomposites calculated from the DSC cooling runs

Sample	**$T_{c,\ onset}$, °C**	**T_c, °C**	**$T_{c,\ end}$, °C**	**$T_{c,\ onset}$ - T_c, °C**	**ΔH_c, J/g**
PHBV	124.9	120.9	116.0	4.0	-107.2
PHBV/ZnO(50)	124.9	120.7	117.1	4.2	-104.4
PHBV/ZnO(450)	125.1	121.0	114.8	4.1	-94.2
PHBV/ZnO-US	124.8	120.6	116.9	4.2	-93.3

The value of T_c obtained for PHBV/ZnO(50) and PHBV/ZnO(450) nanocomposites were almost the same as neat PHBV and the PHBV/ZnO-US nanocomposite. The value of $T_{c,\ onset}$ - T_c, indicating crystallization rate, was also not changed. The ΔH_c values on the other hand, were slightly decreased (2.6 %) for the PHBV/ZnO(50) sample, and decreased by 12.1 % for the PHBV/ZnO(450) nanocomposite.

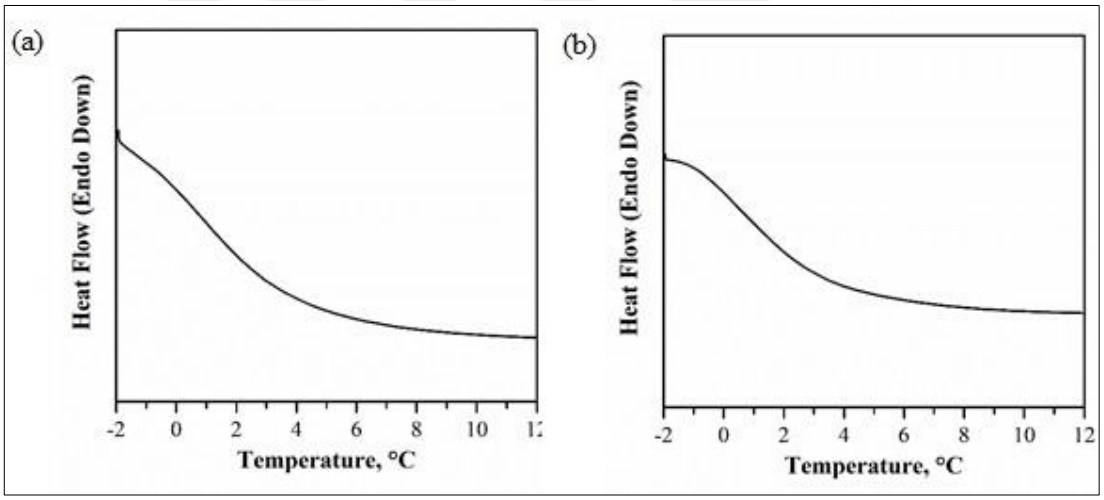

Figure 4.57 Glass transition temperatures of the (a) PHBV/ZnO(50) and (b) PHBV/ZnO(450) nanocomposite samples from the DSC 1st heating curves

The cooling curves of the two nanocomposites were given together with neat PHBV and at a narrow temperature scale in Figure 4.56b. For neat PHBV and the PHBV/ZnO(50) samples, the crystallization process appeared to occur in two successive steps and two shoulders could be observed on the crystallization peaks. The reason could be multiple crystal modifications or orientation effects [37]. The two shoulders were not apparent in the cooling curve of the PHBV/ZnO(450) sample.

The 2nd heating curves of the two samples were given in Figures 4.54c and 4.55c. Double-peak melting behavior observed in the 1st heating scans was not observed in the

2nd heating scans. This could be the result of the melting-recrystallization-remelting mechanism. As the thermal history was erased during the 1st heating scans, this behavior was not observed in the 2nd heating scans. The 2nd heating curves of the two samples and neat PHBV are given in Figure 4.56c together and at a narrower temperature scale. No particular difference could be observed between the melting behavior of the samples.

The melting temperatures (T_m) obtained from the 2nd heating scans of the two nanocomposites are given in Table 4.20, together with neat PHBV and PHBV/ZnO-US sample. The melting temperatures obtained from the 2nd heating curves of PHBV/ZnO(50) and PHBV/ZnO(450) did not show any significant difference from neat PHBV and PHBV/ZnO-US samples. ΔH_m and X_c values were not changed significantly for the PHBV/ZnO(50) samples, whereas they were decreased by about 7 % for the PHBV/ZnO(450) sample. The particle distribution observed for PHBV/ZnO(50) sample was the best distribution among all samples given in this section and the previous section. The good dispersion of the particles probably hindered the movement of the polymer chains, preventing a decrease in percent crystallinity.

Table 4.20 Melting parameters of neat PHBV, PHBV/ZnO(50), PHBV/ZnO(450), and PHBV/ZnO-US samples calculated from the DSC 2nd heating runs

Sample	**$T_{m,\ onset}$, °C**	**T_m, °C**	**$T_{m,\ end}$, °C**	**ΔH_m, J/g**	**X_c, %**
PHBV	165.5	174.7	179.3	112.7	76.9
PHBV/ZnO(50)	165.4	174.8	179.3	112.1	77.2
PHBV/ZnO(450)	165.8	174.5	179.6	104.0	71.7
PHBV/ZnO-US	166.0	174.9	179.6	99.0	68.2

4.6.2.4 Mechanical Properties of the PHBV Nanocomposites Fabricated by CMI Containing ZnO Particles

The stress-strain curves obtained for PHBV/ZnO(50) and PHBV/ZnO(450) nanocomposites by uniaxial tensile testing are given in Figure 4.58. The nonlinear plastic deformation section obtained was larger than that of neat PHBV for the nanocomposites, indicating more ductile behavior. The maximum stress and strain values were also increased compared to neat PHBV. Mechanical parameters calculated for the two nanocomposites are given in Table 4.21, together with neat PHBV and

PHBV/ZnO-US sample. The changes in the mechanical properties can be observed in Figure 4.59 in graphical form.

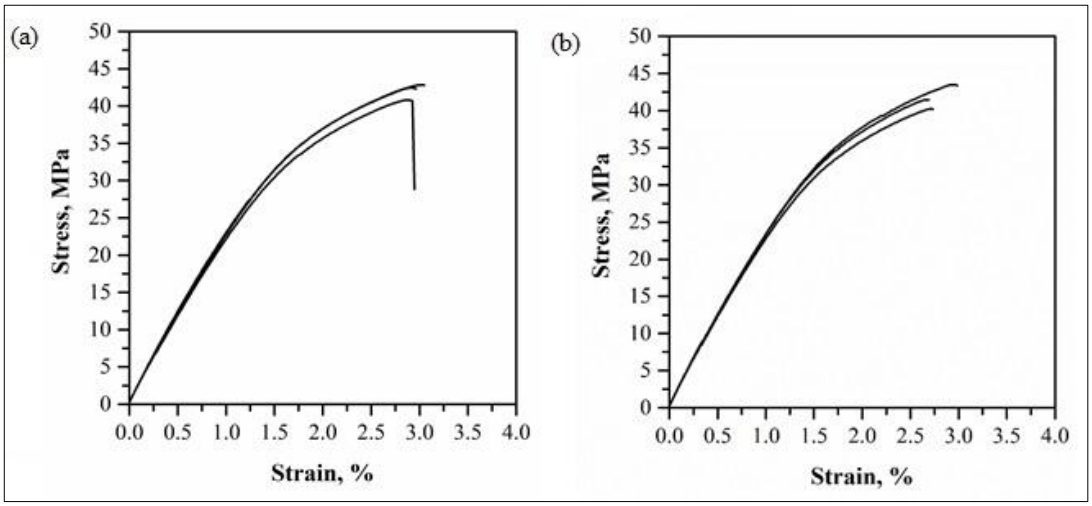

Figure 4.58 Stress-strain curves of (a) PHBV/ZnO(50) and (b) PHBV/ZnO(450) nanocomposites obtained from tensile testing

Table 4.21 Mechanical properties of neat PHBV, PHBV/ZnO(50), PHBV/ZnO(450), and PHBV/ZnO-US

Sample	**Tensile strength, MPa**	**Elongation, %**	**Elastic modulus, MPa**	**Toughness, kJ/m^3**
PHBV	34.7±1.5	2.1±0.2	2440.8±93.5	434.6±52.9
PHBV/ZnO(50)	42.5±1.5	3.0±0.2	2476.2±132.2	818.4±42.4
PHBV/ZnO(450)	41.7±1.4	2.8±0.1	2532.1±114.7	754.1±67.5
PHBV/ZnO-US	42.3±1.4	2.9±0.2	2562.3±134.0	801.9±74.7

PHBV/ZnO(50) and PHBV/ZnO(450) showed 22.5 % and 20.2 % increase in tensile strength, respectively, when compared to neat PHBV. The tensile strength of these nanocomposites was close to each other and to the tensile strength value of the PHBV/ZnO-US nanocomposite. Elongation at break value was increased by 43 % for PHBV/ZnO(50) and by 38 % for PHBV/ZnO(450). Decrease in brittleness (increase in ductility) was verified by both the plastic deformation region in the stress-strain graphs and by the increase in elongation and toughness values. Toughness of PHBV was increased by 88 % for PHBV/ZnO(50) and 73.5 % for PHBV/ZnO(450). Elastic modulus value of PHBV was only slightly increased for the nanocomposite samples. Among the three nanocomposites, the best results in mechanical properties was

obtained for the PHBV/ZnO(50) sample. This was probably due to the best particle dispersion achieved for this nanocomposite.

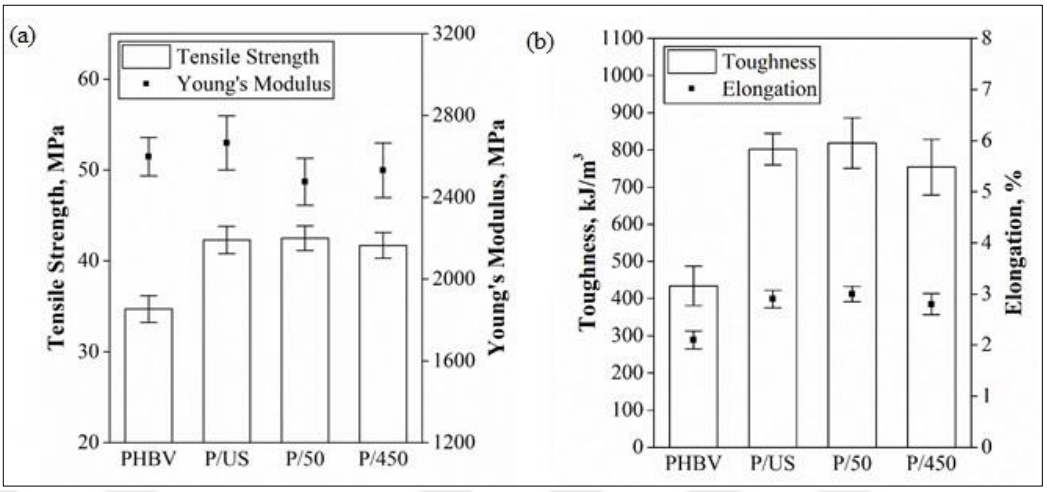

Figure 4.59 Mechanical properties of PHBV/ZnO(50), PHBV/ZnO(450), and PHBV/ZnO-US nanocomposites: (a) tensile strength and elastic modulus and (b) elongation at break and toughness

Table 4.22 Sample codes and formulations of the PHBV/ZnO nanocomposites fabricated from Sonochemically synthesized ZnO particles

Sample code	**ZnO content, wt.%**	**PHBV content, wt.%**	**Surface modification**
PHBV/UB(1)	1	99	-
PHBV/UB-OTES(0.5)	0.5	99.5	OTES
PHBV/UB-OTES(1)	1	99	OTES
PHBV/UB-OTES(3)	3	97	OTES

4.6.3 PHBV Nanocomposites Fabricated by Sonochemically Synthesized ZnO Particles

Application of ultrasound was incorporated into wet chemical synthesis of the ZnO particles and ZnO-2L-95C-UB40 particles were obtained as it was described in sections 3.1.2 and 4.5. The particles were hexagonal rods and their aspect ratio was 10.3. ZnO-2L-95C-UB40 particles were surface modified with OTES silane in order to increase surface compatibility of the particles with the PHBV matrix. Surface-modified particles were sample coded as ZnO-2L-95C-UB40-OTES. Unmodified and surface modified particles were added into PHBV matrix by melt-extrusion method in 1 wt. % ratio. The

results obtained for thermal and mechanical analysis were compared to those of neat PHBV and to each other. Since OTES-modified particles produced better results in terms of mechanical properties, the study was continued using OTES-modified particles. ZnO-2L-95C-UB40-OTES particles were incorporated into PHBV matrix in varying ratios (0.5 and 3 wt. %). Formulations and sample coding of the fabricated nanocomposites are given in Table 4.22. Thermal and mechanical properties of the nanocomposites were measured and compared to neat PHBV.

4.6.3.1 XRD Analysis of the PHBV Nanocomposites Fabricated by Sonochemically Synthesized ZnO Particles

The structure of PHBV and its nanocomposites were investigated by XRD analysis between 2θ angles of 0 to 60º. The resulting diffractograms are given in Figures 4.60 and 4.61. The peaks observed at 13.4, 16.9, 19.6, 21.3, and 22.4º in the diffraction patters of neat PHBV (Figure 4.60a) were associated with (020), (110), (021), (111), and (121) planes, respectively and were in agreement with the literature [29, 31, 37, 174, 175]. All peaks observed in the diffractogram of neat PHBV are given in Table 4.23. The high intensity peak was observed at 26.7º was associated with barium nitrate particles added by the supplier company. The peaks of the nanocomposites that belong to PHBV did not show any significant difference from neat PHBV. Among peaks that were previously associated with ZnO crystal structure, the peaks at 31.5 and 56.2, corresponding to (100) and (110) planes, were prominent in the diffractograms of the nanocomposites. The intensities of these two peaks were increased as the concentration of ZnO was increased, as expected. All of the X-ray diffraction peaks obtained for the neat PHBV and PHBV/UB(1) and PHBV/UB-OTES(1) nanocomposites are also given in Table 4.23.

Although the angles of the reflections did not change with the addition of ZnO particles, changes in the intensity of the (002) and (110) peaks were observed between neat PHBV and the nanocomposites. This suggested that the ZnO particles affected the ordering of PHBV molecular chains. The crystallite sizes (L) of the neat PHBV and the nanocomposites were calculated using Scherrer's equation. Crystallite size was calculated as 73.4 for neat PHBV and 58.7 for all of the nanocomposites. This indicated that addition of the ZnO particles decreased crystallite size of PHBV, affecting PHBV crystallinity.

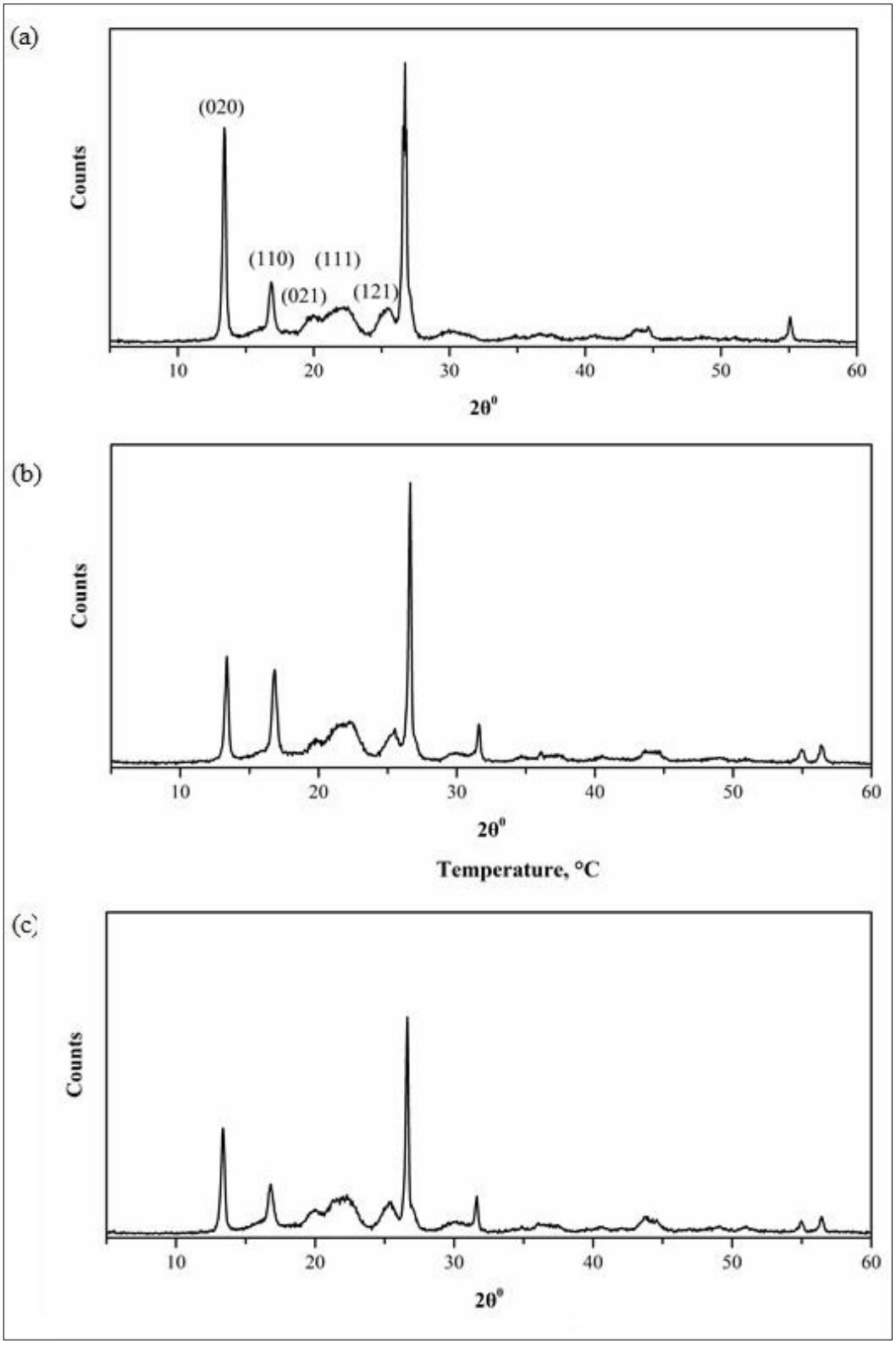

Figure 4.60 X-ray diffraction patterns of (a) neat PHBV, (b) PHBV/UB(1), and (c) PHBV/UB-OTES(1) samples

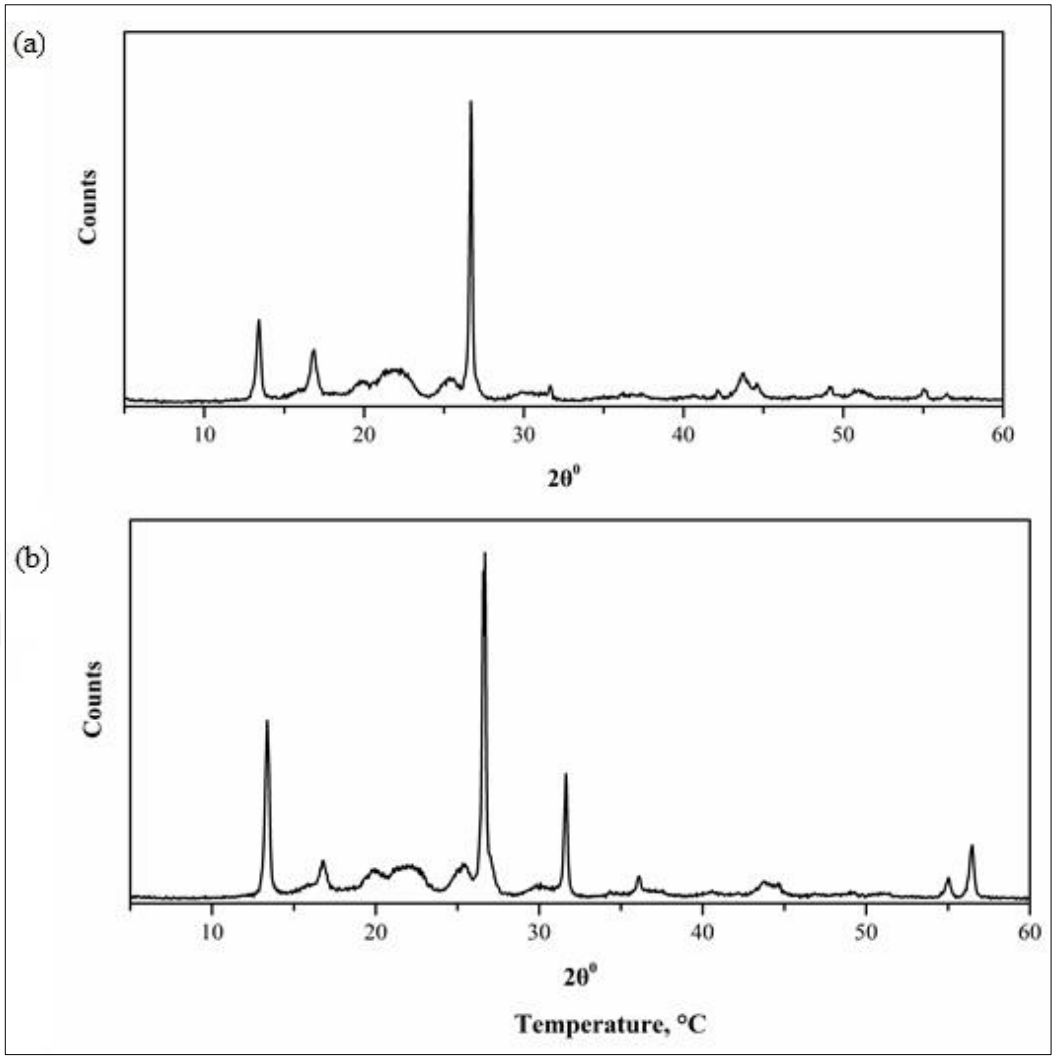

Figure 4.61 X-ray diffraction patterns of (a) PHBV/UB-OTES(0.5) and (b) PHBV/UB-OTES(3) samples

4.6.3.2 FTIR Analysis of the PHBV Nanocomposites Fabricated by Sonochemically Synthesized ZnO Particles

Molecular structures of the neat PHBV and the nanocomposites were investigated by FTIR spectrometry. The resulting spectra of the samples are given in Figures 4.62 and 4.63. The transmittance peaks observed in the spectrum of neat PHBV (Figure 4.62a) and the associated bonds are given in Table 4.24. There were no significant differences in the wavenumbers of the peaks observed in the spectra of the nanocomposites, suggesting that molecular structure of PHBV was not changed significantly with the addition of the ZnO particles. The peak in the inorganic region of the spectrums (459 cm^{-1}) was considered to be arising from the inorganic impurity added by the supplier company, as it was detected in XRD patterns. The peak of added ZnO could not be

observed in the spectra of the nanocomposites probably due to overlapping with the peak of the inorganic impurity.

Table 4.23 X-ray diffraction patterns of neat PHBV, PHBV/UB(1), and PHBV/UB-OTES(1)

PHBV			**PHBV/UB(1)**			**PHBV/UB-OTES(1)**			
2θ	**I, %**	**d, Aº**	**2θ**	**I, %**	**d, Aº**	**2θ**	**I, %**	**d, Aº**	**hkl**
3.37	17.94	26.25	3.33	41.72	26.51	3.36	53.43	26.26	
13.44	34.89	6.59	13.38	36.95	6.62	13.38	48.17	6.62	(020)
16.91	8.10	5.24	16.80	30.46	5.28	16.77	19.39	5.29	(110)
19.74	2.23	4.5	19.80	4.54	4.48	20.00	7.04	4.44	(021)
22.65	3.53	3.93	22.35	11.49	3.98	22.40	13.08	3.97	(111)
25.59	4.18	3.48	25.49	9.89	3.49	25.43	11.66	3.50	(121)
26.71	100	3.34	26.62	100.00	3.35	26.63	100.00	3.35	
			31.61	13.22	2.83	31.62	16.69	2.83	
36.52	0.61	2.46	36.14	3.11	2.49	36.04	3.45	2.49	
			56.42	5.56	1.63	56.41	6.90	1.63	

4.6.3.3 Thermal Stability of the PHBV Nanocomposites Fabricated by Sonochemically Synthesized ZnO Particles

In order to investigate the limiting processing conditions of PHBV and the nanocomposites, thermal stability was investigated by dynamic TG analysis under nitrogen atmosphere. TG and DTG curves of PHBV and the nanocomposites were obtained between 25 and 560 °C, and are given in Figures 4.64 and 4.65, respectively. The TG and DTG plots of the samples were shown together and at a narrower temperature range than the analysis temperature range. Thermal degradation of neat PHBV and the nanocomposites were observed to occur in a single step and at a narrow temperature range. In the TG curve of neat PHBV, after 250 °C the sample weight was first observed to decrease slowly, then decrease rapidly up to a temperature around 300 °C.

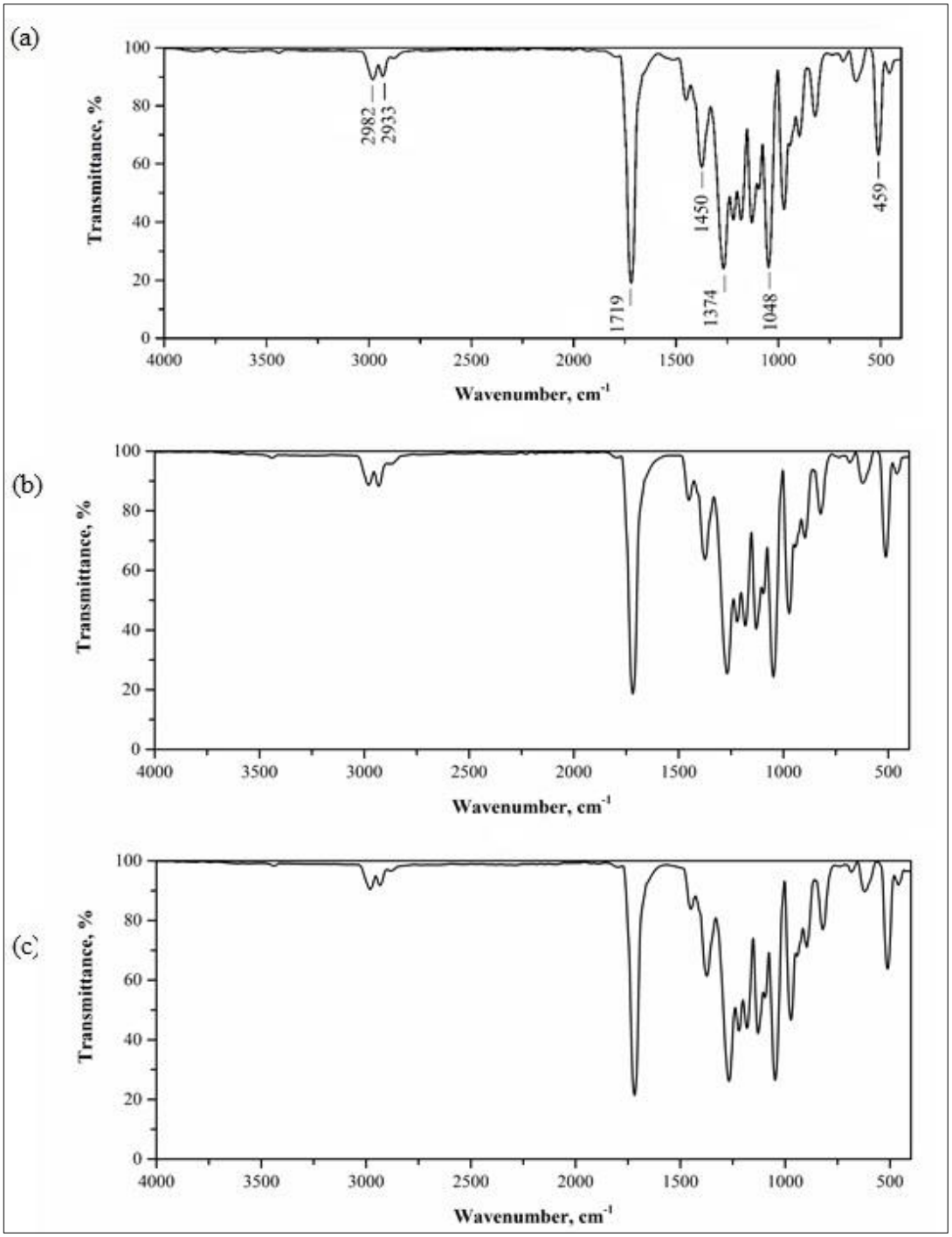

Figure 4.62 FTIR spectra of (a) neat PHBV, (b) PHBV/UB(1), and (c) PHBV/UB-OTES(1) samples

At around 300 °C, the curve returned to zero slope as the sample got exhausted. The same degradation behavior was also observed for the nanocomposite samples; however, the temperatures were shifted to lower temperatures, indicating a slight decrease in the thermal stability. In DTG curves, the shift of the T_{max} to lower temperatures could be observed for the nanocomposite samples. The decrease in thermal stability was lowest for the PHBV/UB-OTES(0.5) sample and the highest for the PHBV/UB-OTES(3)

sample. The untreated and treated PHBV/UB(1) and PHBV/UB-OTES(1) samples produced approximately the same results. Lower loadings of ZnO resulted in a lower decrease in thermal stability. The decrease in thermal stability was considered to be the result of high thermal conductivity of the ZnO particles, as it was discussed in the previous sections. Increasing ZnO content probably increased the heat conductance within the samples, decreasing thermal stability [43, 46].

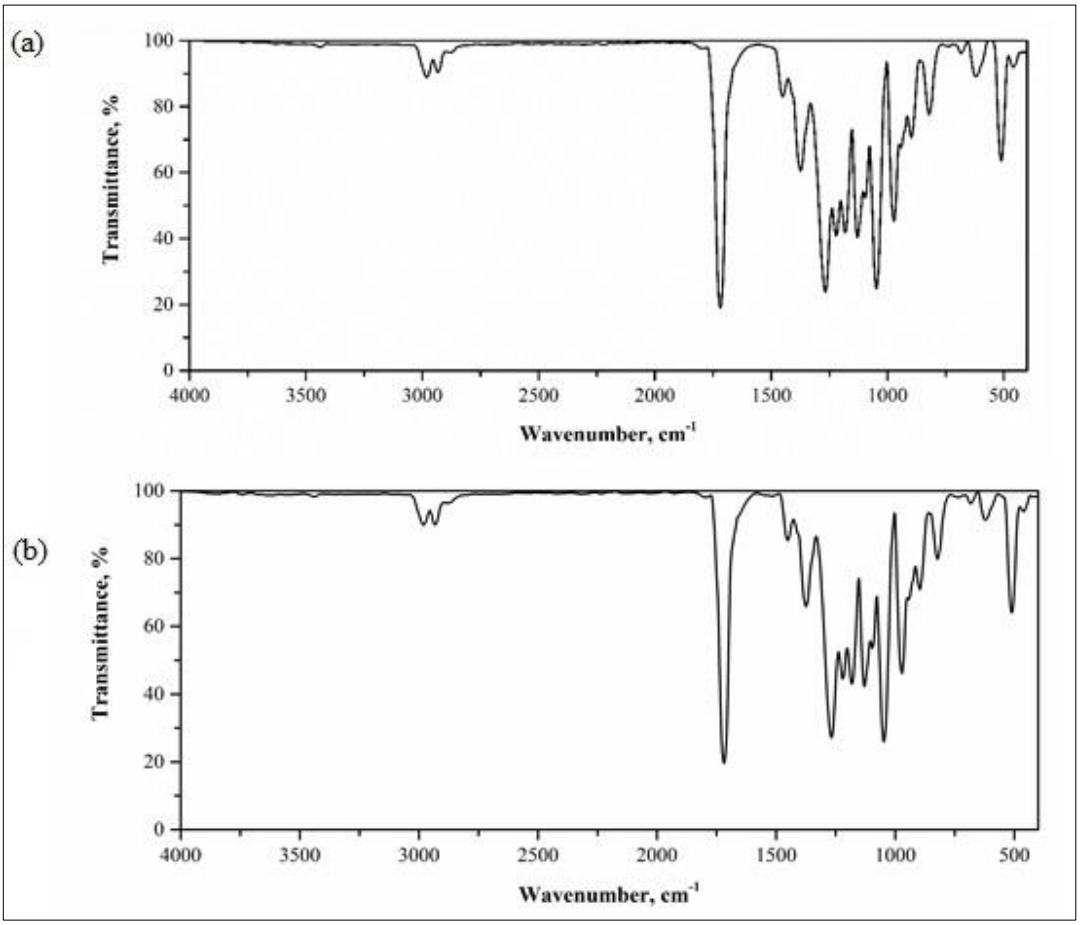

Figure 4.63 FTIR spectra of (a) PHBV/UB-OTES(0.5) and (b) PHBV/UB-OTES(3) samples

T_{max} was determined as the temperature at which the thermal degradation was the highest [35] and the values were given in Table 4.25. Other characteristic degradation temperatures $T_{x\%}$ calculated for neat PHBV and the nanocomposite samples are also given in Table 4.25. The characteristic degradation temperatures calculated for the nanocomposites were observed to decrease about 10 – 17 °C, compared to the neat PHBV sample. The processing window of the polymer was slightly narrowed by the addition of the ZnO particles; however, it was still sufficiently wide to allow melt processing.

Table 4.24 Transmittance peaks observed in the FTIR spectrum of neat PHBV and the molecular bonds associated with the peaks

Wavenumber, cm^{-1}	**Molecular bonds [140]**
2981.9	Methyl C – H asymmetric stretching
2933.0	Methylene C – H asymmetric stretching
1719.4	Carbonyl group
1450.2	C = C – C stretching
1374.7	C – C skeletal vibrations
1268.6	C – C skeletal vibrations
1219.7	C – C skeletal vibrations
1183.0	C – C skeletal vibrations
1129.9	C – C skeletal vibrations
1095.3	C – C skeletal vibrations
1048.4	C – C skeletal vibrations
972.9	C – C skeletal vibrations
944.3	C – C skeletal vibrations
822.0	C – C skeletal vibrations
458.9	Inorganic impurity

The activation energy for thermal decomposition of PHBV and the nanocomposites were calculated according to the Horowitz-Metzger method [170]. The graphs of $\ln[\ln(W_0/W_T)]$ values against the θ values were plotted (Figure 4.66) and the values of E_a were calculated from the slopes and reported in Table 4.25. The E_a value calculated for neat PHBV was similar to the value previously reported in the literature [42]. For the PHBV/UB(1) sample, which was prepared by untreated ZnO particles, the E_a value was decreased to 425.7 kJ, indicating an easier and faster thermal degradation. This was consistent with the TG and DTG results given in Figures 4.64 and 4.65. The E_a values of the nanocomposites prepared by OTES treated particles were higher than the value of neat PHBV.

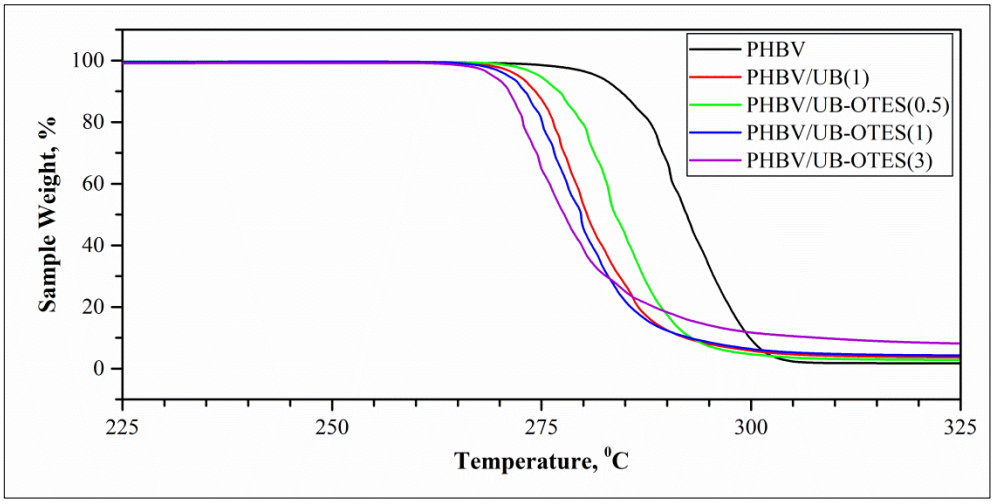

Figure 4.64 TG curves of neat PHBV, PHBV/UB(1), PHBV/UB-OTES(0.5), PHBV/UB-OTES(1) and PHBV/UB-OTES(3) samples together and at a narrow temperature scale

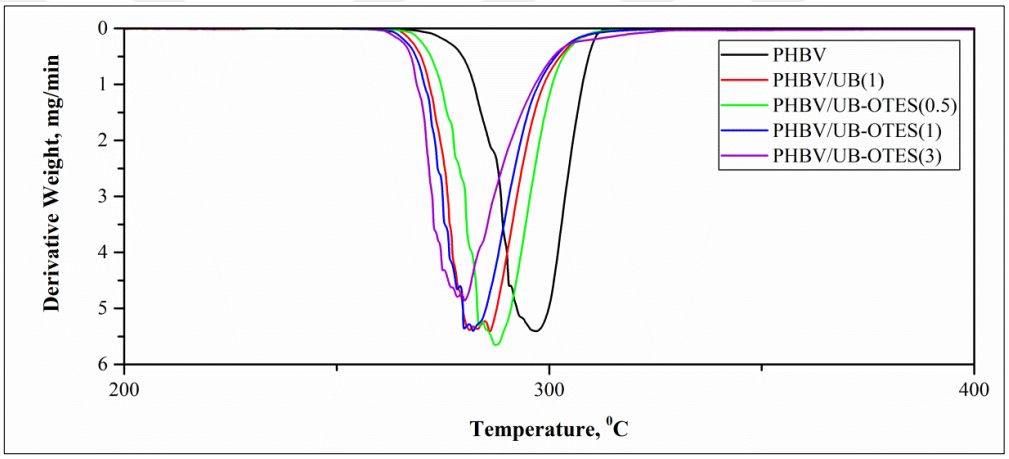

Figure 4.65 DTG curves of neat PHBV, PHBV/UB(1), PHBV/UB-OTES(0.5), PHBV/UB-OTES(1) and PHBV/UB-OTES(3) samples together and at a narrow temperature scale

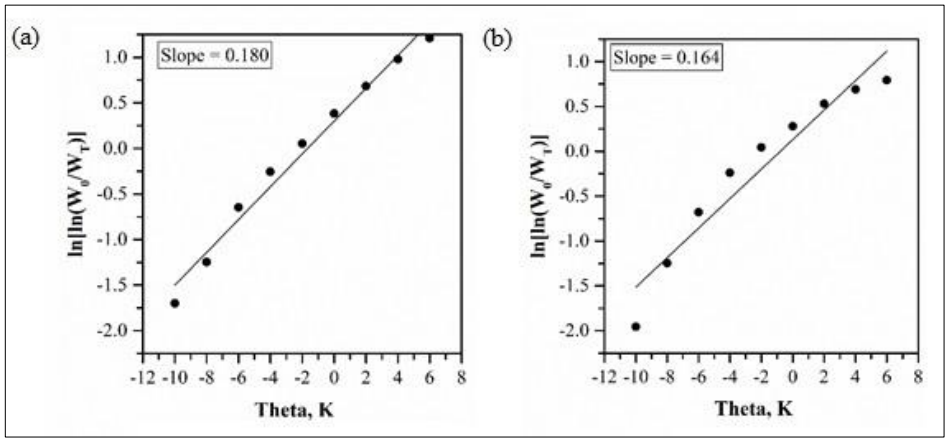

Figure 4.66 Calculation of the E_a values for (a) neat PHBV, (b) PHBV/UB(1), (c) PHBV/UB-OTES(0.5), (d) PHBV/UB-OTES(1) and (e)PHBV/UB-OTES(3) by the Horowitz-Metzger method

Table 4.25 Parameters of thermal degradation calculated for neat PHBV, PHBV/UB(1), PHBV/UB-OTES(0.5), PHBV/UB-OTES(1) and PHBV/UB-OTES(3) samples

Sample	**$T_{2\%}$, °C**	**$T_{5\%}$, °C**	**$T_{10\%}$, °C**	**$T_{20\%}$, °C**	**$T_{80\%}$, °C**	**T_{max}, °C**	**Char, %**	**Ea, kJ/mole**
PHBV	276.7	281.6	284.2	287.9	297.4	296.8	1.11	485.9
PHBV/UB(1)	269.4	272.2	274.2	276.4	286.7	285.1	2.44	425.7
PHBV/UB-OTES(0.5)	271.4	274.7	277.1	279.8	289.2	287.5	2.02	490.5
PHBV/UB-OTES(1)	268.2	271.0	272.9	275.1	285.6	282.1	2.86	563.1
PHBV/UB-OTES(3)	266.5	269.1	271.1	272.8	288.1	280.1	1.65	509.4

Higher E_a value is an indication of higher thermal stability; nevertheless, the T_{max} values of these nanocomposites were observed to be lower than that of neat PHBV. This suggested that, even though the ZnO particles were helpful in enhancing the thermal stability of PHBV, high thermal conductivity of the particles resulted in an overall decrease in the thermal stability [43,46]. Highest E_a value was obtained for the PHBV/UB-OTES(1) nanocomposite as 563.1 kJ. The E_a value of PHBV/UB-OTES(3) nanocomposite was calculated as 509.4 kJ. At the ZnO content of 3%, the value of E_a was probably decreased due to particle agglomeration.

4.6.3.4 Melting and Crystallization Behavior of the PHBV Nanocomposites Fabricated by Sonochemically Synthesized ZnO Particles

Melting and crystallization behavior of the OTES-modified nanocomposites were studied by DSC analysis. The samples were heated to 190 °C (1st heating run), cooled to 0 °C (cooling run) and heated again to 190 °C (2nd heating run). The 1st heating, cooling, and 2nd heating curves obtained for the nanocomposites are given in Figures 4.67 to 4.69. The curves of all nanocomposite samples were combined in a single graph at a narrower temperature range in Figure 4.70.

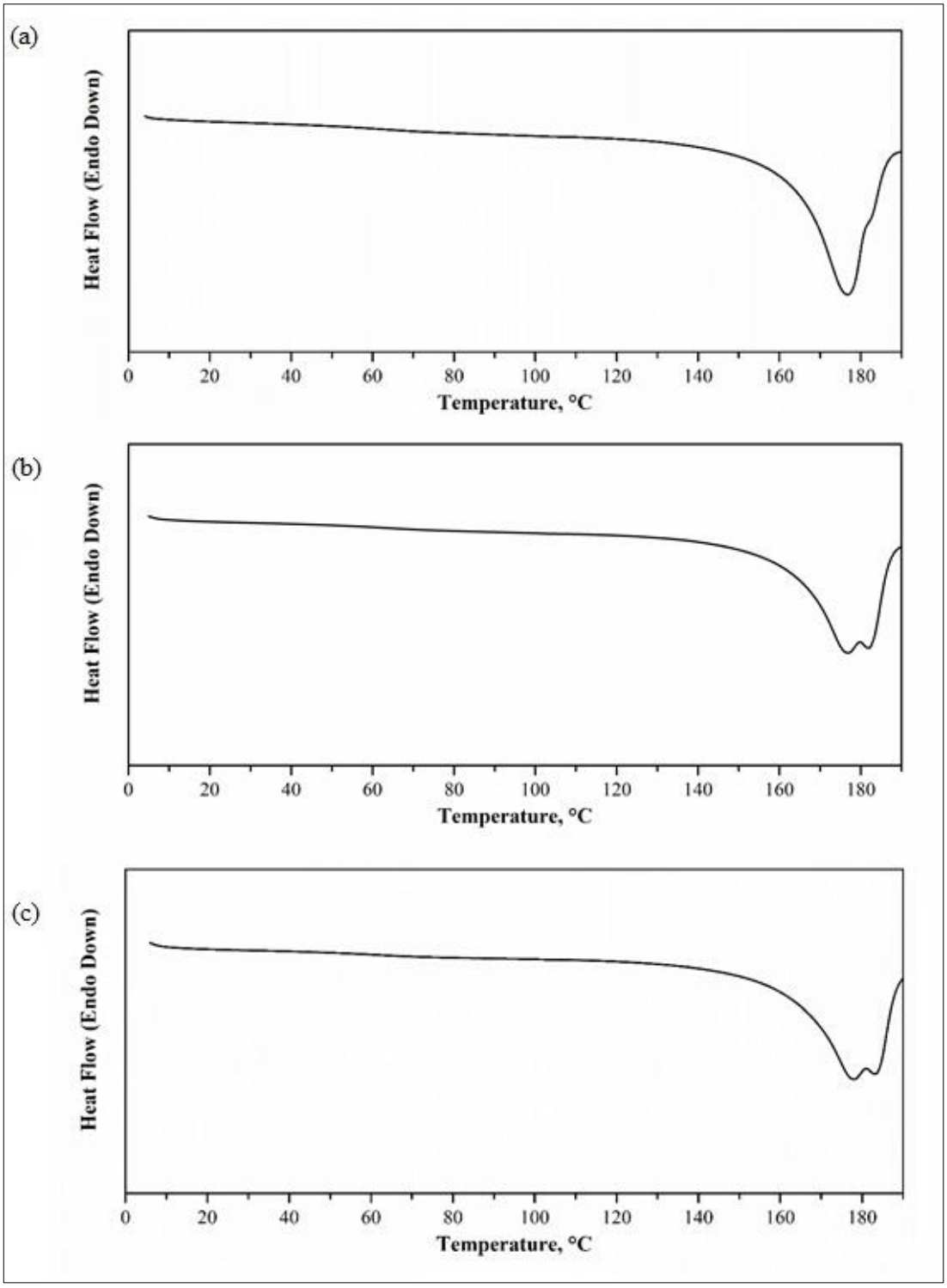

Figure 4.67 DSC 1st heating curves of the (a) PHBV/UB-OTES(0.5), (b) PHBV/UB-OTES(1), and (c) PHBV/UB-OTES(3) samples

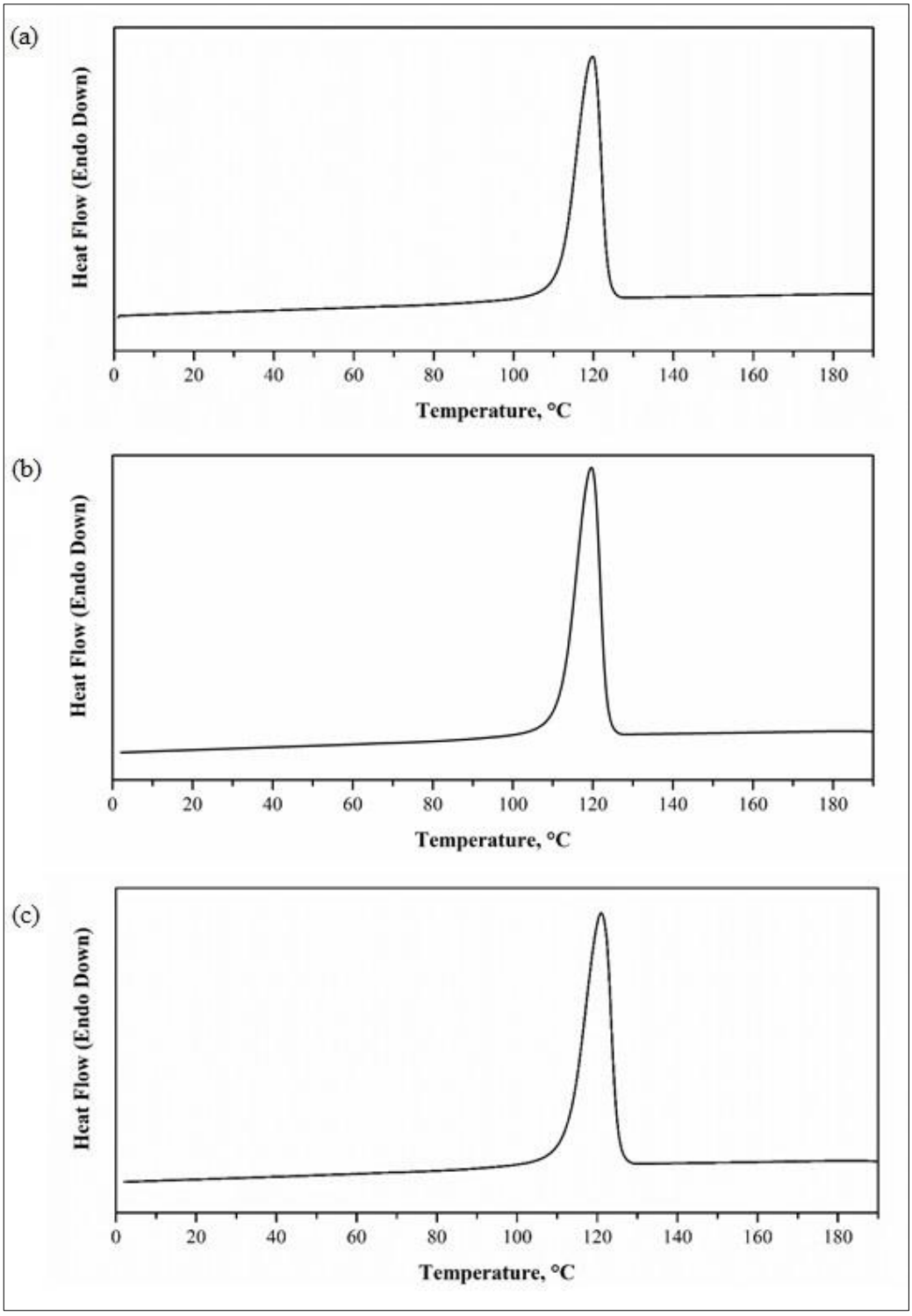

Figure 4.68 DSC cooling curves of the (a) PHBV/UB-OTES(0.5), (b) PHBV/UB-OTES(1), and (c) PHBV/UB-OTES(3) samples

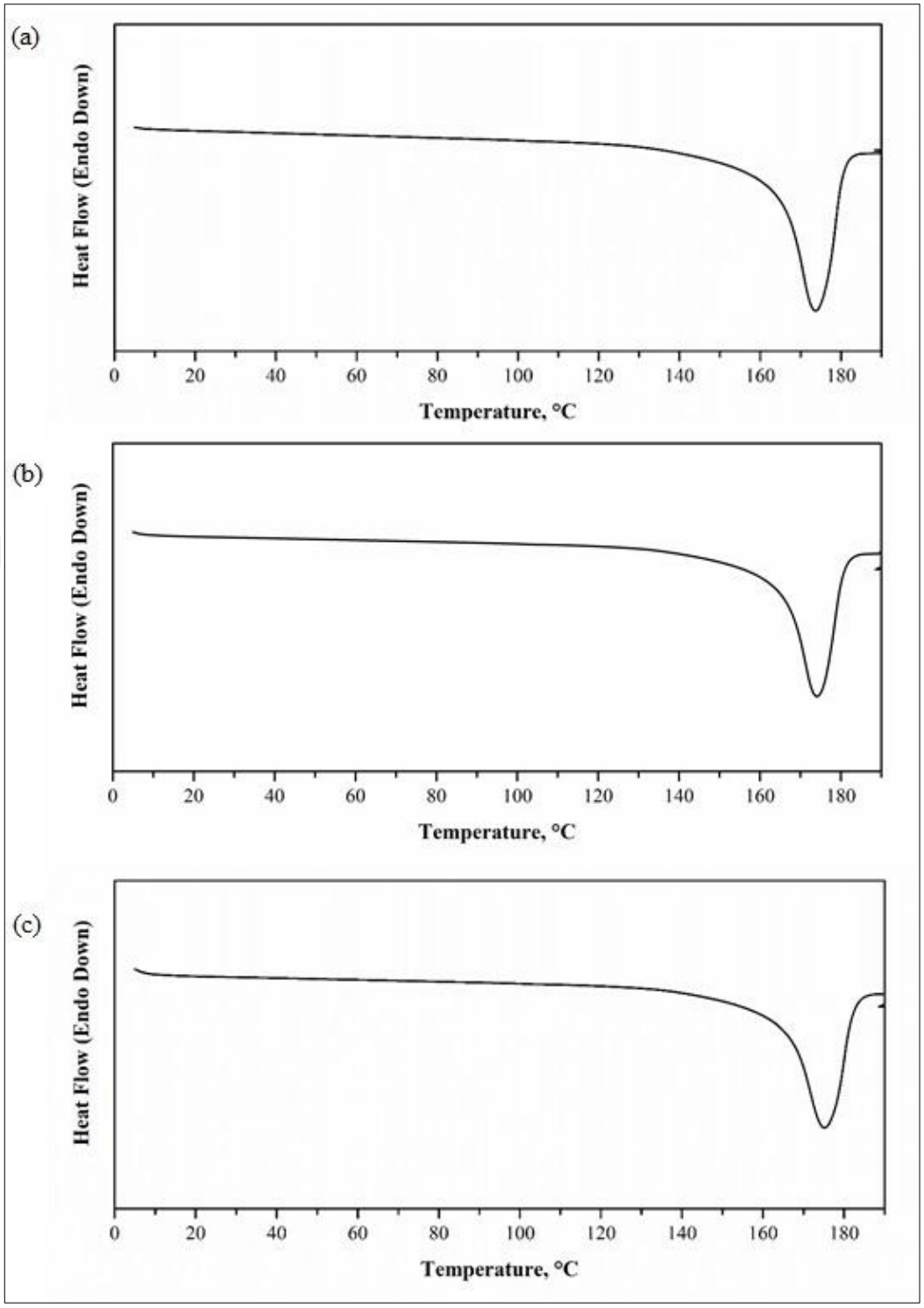

Figure 4.69 DSC 2nd heating curves of the (a) PHBV/UB-OTES(0.5), (b) PHBV/UB-OTES(1), and (c) PHBV/UB-OTES(3) samples

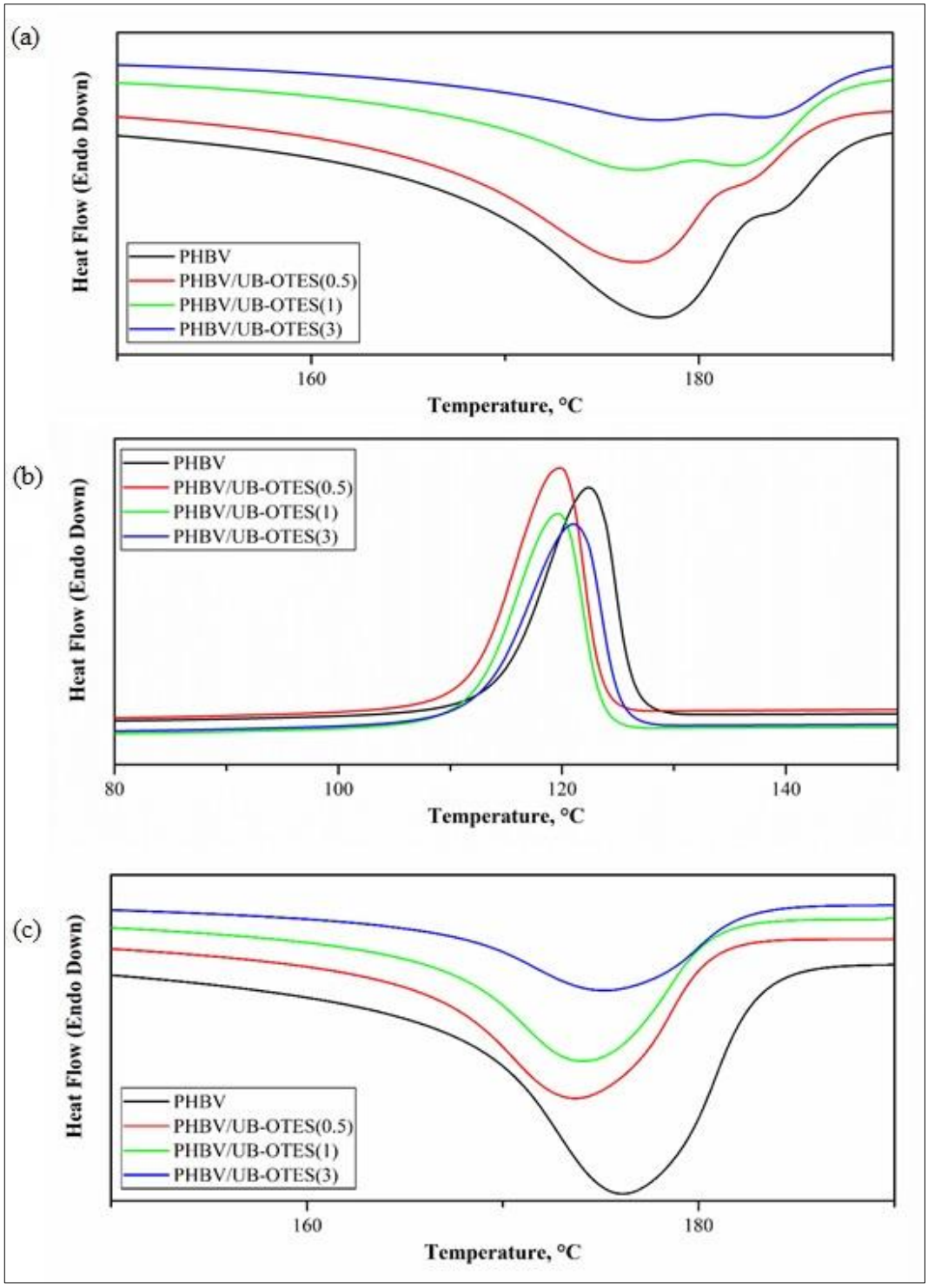

Figure 4.70 DSC scans of neat PHBV, PHBV/UB-OTES(0.5), PHBV/UB-OTES(1) and PHBV/UB-OTES(3) shown together at a narrower temperature range (a) 1st heating scans, (b) cooling scans, and (c) 2nd heating scans

In the 1st heating runs of neat PHBV and the nanocomposites, melting of the polymer was observed as two adjacent endothermic peaks, which is referred to as double-peak melting behavior. The first melting peaks observed in the 1st heating scans resulted from the melting of crystals formed during melt processing, while the second melting peak

resulted from the melting of new crystals formed during heating process of DSC analysis. The formation of less perfect crystals that undergo melting-recrystallization-remelting were observed to be higher for neat PHBV and PHBV/UB-OTES(0.5) samples. The intensity of the first melting peak, therefore the formation of less perfect crystals during melt processing [27, 29, 31] was lower for the PHBV/UB-OTES(1) and PHBV/UB-OTES(3) nanocomposites. If the compositional heterogeneity theory is taken in the formation of the double-peak melting behavior, then it can be said that HB-rich regions were higher than HV-rich regions for the PHBV/UB-OTES(1) and PHBV/UB-OTES(3) nanocomposites.

Table 4.26 Melting parameters of neat PHBV, PHBV/UB-OTES(0.5), PHBV/UB-OTES(1), and PHBV/UB-OTES(3) nanocomposites calculated from the DSC 1st heating runs

Sample	**T_{m1}, °C**	**T_{m2}, °C**	**ΔH_m, J/g**	**X_c, %**
PHBV	177.9	182.2	87.9	60.0
PHBV/UB-OTES(0.5)	176.7	180.9	88.1	60.4
PHBV/UB-OTES(1)	176.9	181.8	83.0	57.2
PHBV/UB-OTES(3)	178.0	183.1	80.8	56.8

Melting temperatures (T_m) obtained for neat PHBV and the nanocomposites from the 1st heating run are given in Table 4.26. The lower temperature melting peak was shown as T_{m1}, and the higher temperature melting peak was shown as T_{m2}. The melting enthalpy (ΔH_m) values were calculated as the area under the melting peaks. Percent crystallinity (X_c) was calculated by the equation $(\Delta H_m * 100)/(\Delta H^0 * w)$ where ΔH^0 is the melting enthalpy of 100 % crystalline PHBV and w is the weight fraction of PHBV in the blend. The value of ΔH^0 was taken as 146.6 J/g due to the low valerate content of PHBV [42, 113]. The values of X_c calculated from the 1st heating runs are given in Table 4.26.

The melting temperature of the polymer is related to the layer thickness and perfection of crystals. There were no significant changes in the 1st and 2nd melting temperatures of the nanocomposite samples in the 1st heating run, compared to neat PHBV. This suggested that the ZnO particles did not affect the layer thickness or crystal perfection of PHBV. X_c value was not significantly affected by the addition of ZnO particles by 0.5 wt.%. When the amount of ZnO particles were further increased, the value of X_c decreased with increasing ZnO content.

The crystallization peaks of the neat PHBV and the nanocomposites can be observed in the cooling curves in Figure 4.68 and 4.70b. The maximum temperatures of the crystallization peaks were taken as the crystallization temperature (T_c) and the results are given in Table 4.27. The onset temperatures of crystallization were shown as $T_{c,\ onset}$ and the end temperatures were shown as $T_{c,\ end}$. The enthalpy of crystallization (ΔH_c) was calculated from the area under the crystallization peak and the results are also given in Table 4.27.

Table 4.27 Crystallization parameters of neat PHBV, PHBV/UB-OTES(0.5), PHBV/UB-OTES(1), and PHBV/UB-OTES(3) nanocomposites calculated from the DSC cooling runs

Sample	**$T_{c,\ onset}$, °C**	**T_c, °C**	**$T_{c,\ end}$, °C**	**$T_{c,\ onset}$ - T_c, °C**	**ΔH_c, J/g**
PHBV	126.4	122.4	99.6	4.0	84.2
PHBV/UB-OTES(0.5)	127.1	119.8	95.6	7.3	85.1
PHBV/UB-OTES(1)	126.6	119.6	100.9	7.0	79.3
PHBV/UB-OTES(3)	129.2	121.0	99.6	8.2	77.8

The value of T_c was observed to be 122.4 °C for the neat PHBV sample and was not changed significantly for the nanocomposites. ΔH_c value was not significantly changed for the PHBV/UB-OTES(0.5) sample, whereas it was decreased for the PHBV/UB-OTES(1) and PHBV/UB-OTES(3) samples. These results were consistent with the X_c values calculated for the samples from the 1st heating scans. The value of $T_{c,\ onset}$ - T_c is a measure of the crystallization rate and the smaller the difference the greater the rate of crystallization. The crystallization rate of PHBV was decreased by the addition of the ZnO particles.

The 2nd heating scan reveals thermal transitions information regardless of the effects of melt processing. The 2nd heating curves of the neat PHBV and the nanocomposites are given in Figures 4.69 and 4.70c. The double-peak melting behavior observed in the 1st heating scans was not observed in the 2nd heating curves. Slight decrease in the melting temperature was observed for the nanocomposites compared to neat PHBV.

The melting temperatures obtained from the 2nd heating scan for neat PHBV and the nanocomposites are given in Table 4.28. The onset and end temperatures of melting were shown as $T_{m,\ onset}$ and $T_{m,\ end}$, respectively. ΔH_m values were calculated from the

area under the melting curves. X_c values were calculated from the ΔH_m values by the same equation as in the 1st heating scans. The values are given in Table 4.28.

Table 4.28 Melting parameters of neat PHBV, PHBV/UB-OTES(0.5), PHBV/UB-OTES(1), and PHBV/UB-OTES(3) nanocomposites calculated from the DSC 2nd heating runs

Sample	**$T_{m,\ onset}$, °C**	**T_m, °C**	**$T_{m,\ end}$, °C**	**ΔH_m, J/g**	**X_c, %**
PHBV	133.4	176.1	186.8	94.4	64.4
PHBV/UB-OTES(0.5)	134.5	173.6	187.2	94.3	64.6
PHBV/UB-OTES(1)	140.6	174.1	184.8	84.1	57.9
PHBV/UB-OTES(3)	138.7	175.2	190.6	85.3	60.0

The melting temperatures of neat PHBV and the nanocomposites did not show any significant difference in the 2nd heating scan, except for the increase in $T_{m,\ onset}$ value for the PHBV/UB-OTES(1) and PHBV/UB-OTES(3) samples.

ΔH_m and X_c values were not significantly changed for the PHBV/UB-OTES(0.5) sample, whereas they were decreased for the PHBV/UB-OTES(1) and PHBV/UB-OTES(3) samples when compared to neat PHBV. These results were consistent with the results obtained from the 1st heating and cooling scans.

4.6.3.5 Mechanical Properties of the PHBV Nanocomposites Fabricated by Sonochemically Synthesized ZnO Particles

The stress-strain curves obtained for PHBV/UB(1), PHBV/UB-OTES(0.5), PHBV/UB-OTES(1), and PHBV/UB-OTES(3) nanocomposites are given in Figure 4.71. Nonlinear plastic deformation section obtained for the nanocomposites containing OTES-treated particles was larger than that of the nanocomposite containing untreated particles. This suggested that nanocomposites with surface-treated particles exhibited more ductile behavior. Mechanical properties of the nanocomposites are given in Table 4.29, together with neat PHBV for comparison. The changes in the mechanical properties can be observed in graphical form in Figure 4.72.

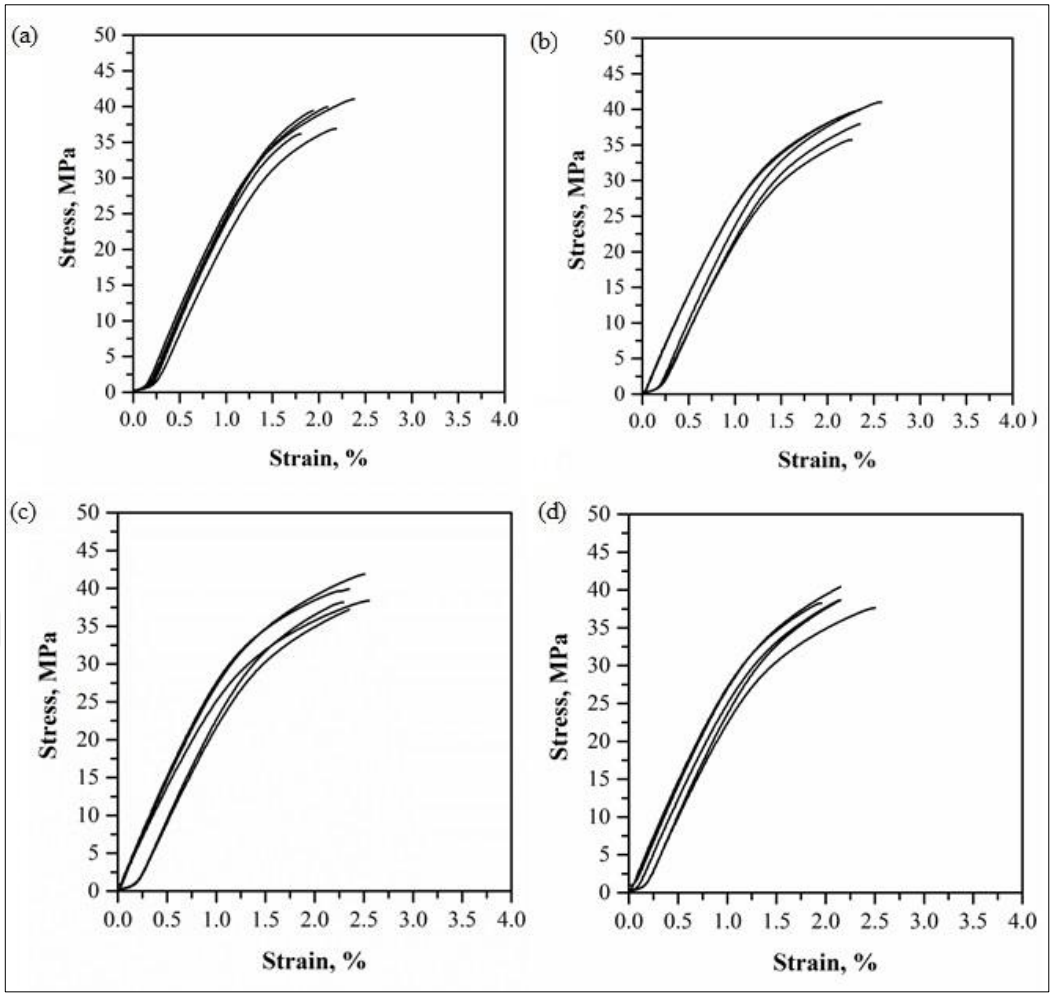

Figure 4.71 Stress-strain curves of (a) PHBV/UB(1), (b) PHBV/UB-OTES(0.5), (c) PHBV/UB-OTES(1), and (d) PHBV/UB-OTES(3) nanocomposites obtained from tensile testing

PHBV/UB(1) nanocomposite showed 8.7% increase in tensile strength, PHBV/UB-OTES(0.5) showed 9.0% increase, PHBV/UB-OTES(1) and PHBV/UB-OTES(3) showed 10.4% increase, when compared to neat PHBV. Tensile strength value was higher for the nanocomposites containing treated particles than the nanocomposite containing untreated particles. Tensile strength was observed to increase with addition of treated surface particles for up to 1% particle content, and then it remained the same for 3% particle content. Elongation at break value was decreased by 2.3% for the nanocomposite containing untreated particles. It was increased by 10.8% for PHBV/UB-OTES(0.5), 14.5% for PHBV/UB-OTES(1), and 9.4% for PHBV/UB-OTES(3). Elongation at break value was observed to increase with the addition of treated particles for up to 1% particle content and then decrease for 3% particle content. The decrease in brittleness (increase in ductility) was determined by the increase in both elongation and toughness values for the nanocomposites containing OTES-treated

particles. Toughness was increased by 22.9% for PHBV/UB-OTES(0.5), 32.9% for PHBV/UB-OTES(1), and 22.6% for PHBV/UB-OTES(3), while it remained almost the same for PHBV/UB(1). Toughness value increased with addition of OTES-treated particles for up to 1% particle content and then decreased for 3% particle content. Elastic modulus values were only slightly increased for the nanocomposites compared to neat PHBV. Among all nanocomposites, the best results were obtained for the PHBV/UB-OTES(1) nanocomposite. This was probably due to the best particle dispersion achieved for this nanocomposite.

Table 4.29 Mechanical properties of neat PHBV, PHBV/UB(1), PHBV/UB-OTES(0.5), PHBV/UB-OTES(1) and PHBV/UB-OTES(3) nanocomposites

Sample	**Tensile strength, MPa**	**Elongation, %**	**Elastic modulus, MPa**	**Toughness, kJ/m^3**
PHBV	35.6±1.5	2.13±0.2	2769.6±93.5	460.8±52.9
PHBV/UB(1)	38.7±1.5	2.08±0.2	2855.0±82.2	463.3±42.4
PHBV/UB-OTES(0.5)	38.8±1.4	2.36±0.1	2903.9±94.7	566.4±67.5
PHBV/UB-OTES(1)	39.3±1.4	2.44±0.2	2910.3±94.0	612.5±74.7
PHBV/UB-OTES(3)	39.3±1.4	2.33±0.1	2922.5±80.9	564.8±63.5

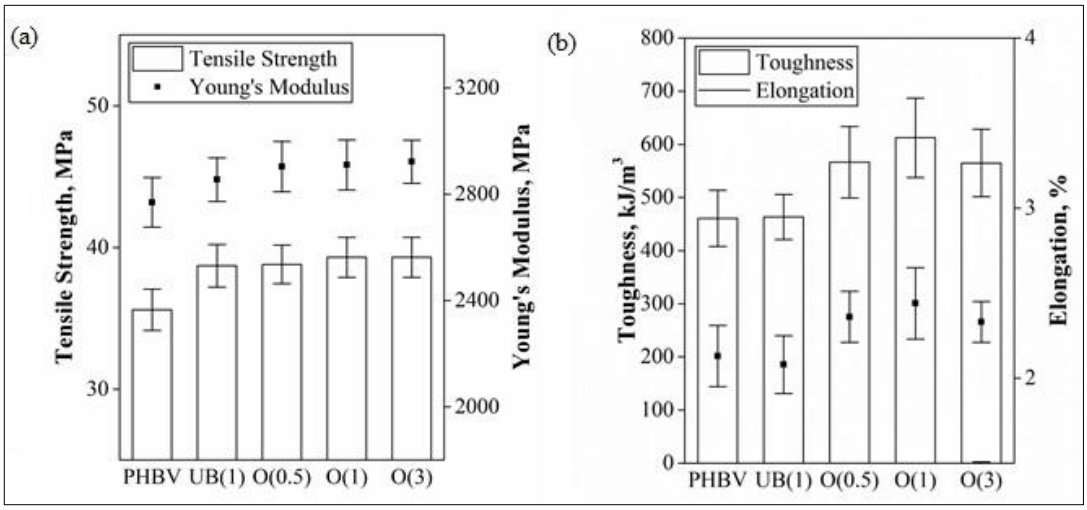

Figure 4.72 Mechanical properties of PHBV, PHBV/UB(1), PHBV/UB-OTES(0.5), PHBV/UB-OTES(1) and PHBV/UB-OTES(3) nanocomposites: (a) tensile strength and elastic modulus and (b) elongation at break and toughness

CHAPTER 5

CONCLUSION AND RECOMMENDATIONS

Various morphologies of ZnO particles were synthesized with different reaction parameters of wet chemical synthesis method, using zinc nitrate hexahydrate and HMT as reaction precursors. The aim of this part of the study was synthesis of high quality, monodisperse and rod-shaped particles for the purpose of incorporation into PHBV matrix.

Effects of reaction parameters such as precursor concentrations, reaction temperature, and reactor volume were investigated. When precursor concentrations were increased from 0.03M to 0.06M, an increase in particle density was observed. The number of particles produced in one batch was increased. Change in precursor concentrations did not result in any changes in particle morphology and rod-shaped particles were observed. Particle size was also not affected significantly.

The reaction temperature was increased from 75 ºC to 95 ºC, keeping reactor volume at 1L and precursor concentrations at 0.06 M. Change of particle morphology from nanorods to nanotubes was observed for some particles. There were no significant changes in the aspect ratio of the particles. ZnO nanorods could be obtained by the increase in reactor volume from 1 L to 2 L, keeping reaction temperature at 95 ºC and precursor concentrations at 0.06. These particles were sample coded as ZnO-2L-95C. The ZnO particles synthesized at these conditions resulted in well-developed hexagonal, one-dimensional rod-shaped crystals. Highest aspect ratio was obtained for the particles synthesized with these conditions. These results suggested that the morphology and uniformity of the ZnO particles synthesized strongly depended on reaction parameters.

ZnO-2L-95C particles were utilized for the fabrication of PHBV/ZnO nanocomposites and other particles that used previously mentioned reaction parameters were omitted. The ZnO particles were first structurally characterized before incorporation into

polymer matrix. The diffraction peaks obtained in XRD analysis were in agreement with the hexagonal phase of ZnO given in standard cards. Sharp, strong and clear peaks indicated that the ZnO particles synthesized were well characterized. FTIR analysis confirmed fabrication of pure ZnO structures since specific peaks for ZnO were obtained.

SEM analysis revealed formation of rod array structures resembling an asterisk shape by the self-aggregation mechanism. Therefore ultrasonic dispersion was utilized for homogeneous dispersion of the particles. Complete deagglomeration of the particles was achieved. Surface modification was applied as another method in obtaining uniform particle dispersion. MPS was the type of silane that was used in this part of the study. FTIR analysis confirmed successful modification of the ZnO surfaces with MPS; however, SEM images revealed strong particle agglomeration. Ultrasonic dispersion was applied to the particles; however, complete deagglomeration could not be achieved.

The ultrasound-dispersed untreated particles, MPS-treated particles, and ultrasound dispersed and MPS-treated ZnO-2L-95C particles were incorporated into PHBV matrix by the melt-extrusion method in a ratio of 1 wt. %. The nanocomposites produced were coded as PHBV/ZnO-US, PHBV/ZnO-MPS, and PHBV/ZnO-MPS-US, respectively. SEM images showed that best particle dispersion was obtained for PHBV/ZnO-MPS-US and the poorest dispersion was obtained for PHBV/ZnO-US particles. Combination of ultrasound dispersion and surface modification showed the best results in terms of uniform particle dispersion.

When thermal stability of the nanocomposites fabricated with ZnO-2L-95C was analyzed with TGA, thermal degradation temperature of PHBV was observed to decrease slightly with the addition of particles. This indicated a slight decrease in the thermal stability of PHBV. However, processing window was not significantly affected since the decrease was small. Thermal degradation temperatures obtained for PHBV/ZnO-US, PHBV/ZnO-MPS, and PHBV/ZnO-MPS-US nanocomposites were almost the same.

Melting and crystallization behavior of PHBV/ZnO-2L-95C nanocomposites were investigated by DSC analysis. Melting temperature of PHBV did not change significantly with the addition of particles. However, a decrease in percent crystallinity was observed. Highest crystallinity value was obtained for the PHBV/ZnO-MPS-US

nanocomposite and the lowest crystallinity for the PHBV/ZnO-US nanocomposite. The crystallization temperature of PHBV also did not change significantly with the addition of particles.

Mechanical properties of PHBV/ZnO-2L-95C nanocomposites were investigated by uniaxial tensile testing. Tensile strength, elongation at break, elastic modulus, and toughness values of the nanocomposites were measured. Best results were obtained for the PHBV/ZnO-MPS-US nanocomposite while poorest results were obtained for the PHBV/ZnO-MPS nanocomposite. This indicated that uniform particle dispersion is very important in improvement of mechanical properties. Combination of uniform particle dispersion with surface modification produced the best results.

Addition of CMI, a water-soluble biopolymer, into ZnO synthesis reaction was studied. Concentrations of CMI added into the reaction were 50, 450, and 750 ppm. The length of the rod-shaped particles was decreased while the width of the particles was increased, with increasing CMI concentration. Consequently, the aspect ratio of the nanorods was decreased as concentration of added CMI was increased. Self-aggregated rod arrays observed in particles synthesized without CMI addition was also observed for the particles containing 50 ppm of CMI. However, for 450 and 750 ppm of CMI, agglomeration was not observed and singular particles were obtained. The particles synthesized were sample coded as ZnO-50-2L-95C, ZnO-450-2L-95C, and ZnO-750-2L-95C, according to their CMI content. ZnO-50-2L-95C and ZnO-450-2L-95C particles were utilized for fabrication of PHBV/ZnO nanocomposites. ZnO-750-2L-95C particles were not used in nanocomposites due to their low aspect ratio. XRD analysis of ZnO-50-2L-95C and ZnO-450-2L-95C particles showed diffraction peaks that agree well with standard cards. Sharp and clear peaks indicated well-crystallized structure. The average crystallite size of ZnO particles calculated from XRD analysis was increased with increasing CMI concentration. FTIR analysis revealed that CMI molecules were adsorbed on the surfaces or were integrated within the structure of ZnO particles.

ZnO-50-2L-95C and ZnO-450-2L-95C particles were subjected to ultrasonic dispersion and then were added into PHBV matrix in a ratio of 1 wt. %. The nanocomposites fabricated were coded as PHBV/ZnO(50) and PHBV/ZnO(450). Structural, thermal, and mechanical properties of these nanocomposites were measured and compared to

neat PHBV. The results were also compared to PHBV/ZnO-US sample which was also ultrasonically dispersed but did not contain CMI.

In SEM analysis, best particle dispersion was obtained for PHBV/ZnO(50) sample. Both PHBV/ZnO(50) and PHBV/ZnO(450) samples showed better dispersion than the PHBV/ZnO-US sample, indicating CMI might be the reason for better dispersion. TGA revealed that addition of CMI-containing particles slightly decreased thermal degradation temperature of PHBV. In DSC analysis, melting temperatures of PHBV did not change significantly but the crystallinity was decreased. Lowest crystallinity was obtained for the PHBV/ZnO-US nanocomposite while the highest was obtained for PHBV/ZnO(450). Crystallization temperature also did not change with the addition of CMI-containing particles. In mechanical analysis, best results were obtained for the PHBV/ZnO(50) sample which showed the best particle dispersion among samples.

Combination of sonochemical synthesis method and wet chemical synthesis method was studied. There were no changes in the morphology and size of the particles; however, dispersion of particles was affected. ZnO-2L-95C-UB40 particles synthesized with ultrasound assistance were obtained as homogeneously distributed singular rod particles. XRD analysis of the particles showed good agreement with the standard cards of hexagonal wurtzite structure. Average crystallite size calculated was lower than that of ZnO-2L-95C particles. FTIR study showed specific peaks of ZnO structure. Surface modification was also applied to ZnO-2L-95C-UB40 particles using OTES silane. FTIR analysis confirmed successful modification of particle surfaces. SEM images showed that uniformly dispersed particles were obtained after surface modification.

Untreated ZnO-2L-95C-UB40 particles were added into PHBV matrix by 1 wt. % ratio and the nanocomposite sample was coded as PHBV/UB(1). OTES-treated particles were added in 1 wt. % ratio and were coded as PHBV/UB-OTES(1). Since OTES-treated particles provided better results in mechanical analysis, these particles were also added in 0.5 and 3 wt. % ratios and the samples were coded as PHBV/UB-OTES(0.5) and PHBV/UB-OTES(3), respectively.

XRD analysis of the nanocomposites showed that ZnO particles affected the ordering of PHBV chains. Crystallite size calculated was also decreased with the addition of particles, compared to neat PHBV. FTIR analysis of the nanocomposite samples

suggested that the molecular structure of PHBA did not change significantly with the addition of ZnO particles.

The thermal degradation temperature of PHBV was decreased with the addition ZnO particles. Highest decrease was obtained for PHBV/UB-OTES(3) sample and the lowest was obtained for PHBV/UB-OTES(0.5) sample. The melting temperatures of PHBV did not change with the addition of particles but the crystallinity was decreased. Lowest crystallinity was obtained for PHBV/UB-OTES(3) sample and the highest was obtained for PHBV/UB-OTES(0.5) sample. The crystallization temperature of PHBV did not change significantly with addition of particles.

In the mechanical analysis, OTES-treated particles produced better results than untreated particles. Among nanocomposites containing treated particles, best results for mechanical analysis were obtained for the PHBV/UB-OTES(1) sample. When particle content was increased from 1 to 3 wt. %, decrease in mechanical properties was observed. This was probably due to the agglomeration of particles with increased particle content.

In this study, ZnO particles synthesized with various reaction conditions were added into PHBV matrix. In general, particles showed good dispersion within the polymer. Thermal stability of PHBV was observed to decrease slightly with the addition of particles. This was probably due to the high thermal conductivity of particles. Melting and crystallization temperatures of PHBV did not change significantly with the addition of particles. However, percent crystallinity was decreased. Since high crystallinity is related to brittleness, decreased crystallinity resulted in increased toughness and decreased brittleness. Since one of the most important drawbacks of PHBV is its brittleness, the increase in ductility and toughness of the nanocomposites were important in terms of enhancing industrial usage of PHBV. Tensile strength, elastic modulus, elongation at break, and toughness values of PHBV could be increased with ZnO particles addition.

In order to achieve improvement in polymer properties, uniform particle dispersion and surface compatibility are the essential factors. Surface modification using silane agents produces relatively better results than using untreated particles. Utilization of biopolymers like CMI both affects crystal morphology and dispersion of particles within PHBV matrix. Utilization of ultrasound in dispersion of synthesized particles and

in particle synthesis allows obtaining homogeneously dispersed particles and enhancement of nanocomposite properties.

In future studies, various morphologies of ZnO particles could be synthesized by changing reaction conditions and addition of crystal growth modifiers. These particles could be added into PHBV matrix in varying ratios and the effects on thermal and mechanical properties could be studied. Uniform particle dispersion within PHBV matrix and surface compatibility between the particles and the polymer should be achieved. Ultrasonic dispersion and silane modification could be used for dispersion and compatibility. Different ultrasonication times and different silane types could be studied.

REFERENCES

[1] Anjum, A., Zuber, M., Zia, K.M., Noreen, A., Anjum, M.N. and Tabasum S., (2016). "Microbial Production of Polyhydroxyalkanoates (PHAs) and Its Copolymers: A Review of Recent Advancements", International Journal of Biological Macromolecules, 89:161–174.

[2] Zinn, M., Witholt, B. and Egli, T., (2001). "Occurrence, Synthesis and Medical Application of Bacterial Polyhydroxyalkanoate", Advanced Drug Delivery Reviews, 53:5–21.

[3] Rhim, J., Park, H., and Ha, C., (2013). "Bio-Nanocomposites for Food Packaging Applications", Progress in Polymer Science, 38:1629–1652.

[4] Bordes, P., Pollet, E. and Avérous, L, (2009). "Nano-Biocomposites: Biodegradable Polyester/nanoclay Systems", Progress in Polymer Science, 34:125–155.

[5] Michael, C. and Aeschelmann F., (2016). "Bio-Based Building Blocks and Polymers Imprint Bio-Based Building Blocks and Polymers – Global Capacities and Trends", European Bioplastics.

[6] Scarfato, P., Di Maio, and Incarnato, L.L., (2015). "Manufacturing of Advanced Biodegradable Polymeric Components", Journal of Applied Polymer Science, 132(48):1-11.

[7] Verlinden, R.A.J., Hill, D.J., Kenward, M., Williams, C.D. and Radecka, I., (2007). "Bacterial Synthesis of Biodegradable Polyhydroxyalkanoates", Journal of Applied Microbiology, 102:1437–1449.

[8] Lenz, R.W. and Marchessault, R.H., (2005). "Bacterial Polyesters: Biosynthesis, Biodegradable Plastics and Biotechnology", Biomacromolecules, 6(1):1–8.

[9] Ublekov, F., Baldrian, J. and Nedkov, E., (2009). "Crystalline B-Structure of PHBV Grown Epitaxially on Silicate Layers of MMT", Journal of Polymer Science: Part B: Polymer Physics, 2: 751–755.

[10] Diez-Pascual, A.M. and Diez-Vicente, A.L., (2014). "ZnO-Reinforced Poly(3-Hydroxybutyrate-co-3-Hydroxyvalerate) Bionanocomposites with Antimicrobial Function for Food Packaging.", ACS Applied Materials and Interfaces, 6(12):9822–9834.

[11] Yuxian, A., Dong, L., Xing, P. Zhuang, Y., Mo, Z. And Feng, Z., (1997). "Crystallization Kinetics And Morphology Of Poly (B -Hydroxybutyrate) and Poly (Vinyl Acetate) Blends", European Polymer Journal, 33(9):1449–1452.

[12] Chiu, H.J., Chen, H.L. and Lin, J.S., (2001). "Crystallization Induced Microstructure of Crystalline/Crystalline Poly(Vinylidene-Uoride)/ Poly(3-Hydroxybutyrate) Blends Probed by Small Angle X-Ray Scattering", Polymer, 42:5749-5754.

[13] Furukawa, T., Sato, H., Murakami, R., Zhang, J., Noda, I., Ochiai, S. And Ozaki, Y., (2007). "Comparison of Miscibility and Structure of poly(3-Hydroxybutyrate-Co-3-Hydroxyhexanoate)/poly(l-Lactic Acid) Blends with Those of poly(3-Hydroxybutyrate)/poly(l-Lactic Acid) Blends Studied by Wide Angle X-Ray Diffraction, Differential Scanning Calorimetry", Polymer, 48(6): 1749–1755.

[14] Wasantha, L.M., Gunaratne, K. and Shanks, R.A., (2008). "Miscibility, Melting, and Crystallization Behavior of Poly(hydroxybutyrate) and Poly(D,L-Lactic Acid) Blends", Polymer Engineering and Science, 47:21–25.

[15] Hinüber, C. Haussler, L., Vogel, R., Brunig, H., Heinrich, G. And Werner, C., (2011). "Hollow Fibers Made from a poly(3-Hydroxybutyrate)/poly-ε-Caprolactone Blend", Express Polymer Letters, 5(7):643–652.

[16] Reddy, K.R., Sato, H., Takahashi, I., and Ozaki, Y., (2015). "Intermolecular Hydrogen Bondings İn The Poly(3-Hydroxybutyrate) And Chitin Blends: Their Effects On The Crystallization Behavior And Crystal Structure Of Poly(3-Hydroxybutyrate)", Polymer, 75:141–150.

[17] Qiu, Z., Ikehara, T. and Nishi, T., (2003). "Miscibility And Crystallization Behaviour Of Biodegradable Blends Of Two Aliphatic Polyesters. Poly(3-Hydroxybutyrate-Co-Hydroxyvalerate) And Poly(Butylene Succinate) Blends", Polymer, 44(24):7519–7527.

[18] Gracida, J., Alba, J., Cardoso, J. and Perez-Guevara, F., (2004). "Studies Of Biodegradation Of Binary Blends Of Poly(3-Hydroxybutyrate-Co-3-Hydroxyvalerate) (PHBHV) With Poly(2-Hydroxyethylmetacrilate) (PHEMA)", Polymer Degradation and Stability, 83(2):247–253.

[19] Reis, K.C., Pereira, J., Smith, A.C., Carvalho, C.W.P., Wellner, N. and Yakimets, I., (2008). "Characterization Of Polyhydroxybutyrate-Hydroxyvalerate (PHB-HV)/Maize Starch Blend Films", Journal of Food Engineering, 89(4):361–369.

[20] Veleirinho, B., Ribeiro-Do-Valle, R. M., and Lopes-Da-Silva, J. A., (2011). "Processing Conditions And Characterization Of Novel Electrospun Poly (3-Hydroxybutyrate-Co-Hydroxyvalerate)/Chitosan Blend Fibers", Materials Letters, 65(14):2216–2219.

[21] Bianco, A., Calderone, M., and Cacciotti, I., (2013). "Electrospun PHBV/PEO Co-Solution Blends: Microstructure, Thermal And Mechanical Properties", Materials Science and Engineering C, 33(3):1067–1077.

[22] Zembouai, I., Kaci, M., Bruzaud, S., Benhamida, A., Corre, Y. M., and Grohens, Y., (2013). "A Study Of Morphological, Thermal, Rheological And Barrier Properties Of Poly(3-Hydroxybutyrate-Co-3- Hydroxyvalerate) /Polylactide Blends Prepared By Melt Mixing", Polymer Testing, 32(5):842–851.

[23] Li, L., Huang, W., Wang, B., Wei, W., Gu, Q. and Chen, P., (2015). "Properties And Structure Of Polylactide/Poly(3-Hydroxybutyrate-Co-3-Hydroxyvalerate) (PLA/PHBV) Blend Fibers", Polymer, 68:183–194.

[24] Yu, W., Lan, C.H., Wang, S.J., Fang, P.F. and Sun, Y.M., (2010). "Influence Of Zinc Oxide Nanoparticles On The Crystallization Behavior Of Electrospun Poly(3-Hydroxybutyrate-Co-3-Hydroxyvalerate) Nanofibers", Polymer, 51(11):2403–2409.

[25] Chen, G., Hao, G. and Guo, T., (2002). "Structure And Mechanical Properties Of Poly (3-Hydroxybutyrate-Co-3-Hydroxyvalerate)(PHBV)/Clay Nanocomposites", Journal of Materials, 21:1587–1589.

[26] Wang, S., Song, C., Chen, G., Guo, T., Liu, J., Zhang, B. and Takeuchi, S., (2005). "Characteristics And Biodegradation Properties Of Poly(3-Hydroxybutyrate-Co-3-Hydroxyvalerate)/Organophilic Montmorillonite (PHBV/OMMT) Nanocomposite", Polymer Degradation and Stability, 87(1):69–76.

[27] Correa, M.C.S., Branciforti, M.C., Pollet, E., Agnelli, J.A.M., Nascente, P.A.P. and Avérous, L., (2011). "Elaboration and Characterization of Nano-Biocomposites Based on Plasticized Poly(Hydroxybutyrate-Co-Hydroxyvalerate) with Organo-Modified Montmorillonite", Journal of Polymers and the Environment, 20(2):283–290.

[28] Carli, L.N., Daitx, T.S., Soares, G.V., Crespo, J.S. and Mauler, R.S., (2014). "The Effects Of Silane Coupling Agents On The Properties Of PHBV/Halloysite Nanocomposites", Applied Clay Science, 87:311–319.

[29] Shan, G.F., Gong, X., Chen, W.P., Chen, L. and Zhu, M.F., (2011). "Effect Of Multi-Walled Carbon Nanotubes On Crystallization Behavior Of Poly(3-Hydroxybutyrate-Co-3-Hydroxyvalerate)", Colloid and Polymer Science, 289(9):1005–1014.

[30] Khankrua, R., Pivsa-Art, S., Hiroyuki, H. and Suttiruengwong, S., (2013). "Thermal and Mechanical Properties of Biodegradable Polyester/Silica Nanocomposites", Energy Procedia, 34(3):705–713.

[31] Ambrosio-Martin, J., Gorrasi, G., Lopez-Rubio, A., Fabra, MJ., Mas, L.C., Lopez-Manchado, M.A. and Lagaron, J.M., (2015). "On The Use Of Ball Milling To Develop Poly(3-Hydroxybutyrate-Co-3-Hydroxyvalerate)-Graphene Nanocomposites (I) - Morphology, Thermal Properties, And Thermal Stability", Journal of Applied Polymer Science, 132(29):1–11.

[32] Ambrosio-Martin, J., Gorrasi, G., Lopez-Rubio, A., Fabra, M.J., Mas, L.C., Lopez-Manchado, M.A. and Lagaron, J.M., (2015). "On The Use Of Ball Milling To Develop Poly(3-Hydroxybutyrate-Co-3-Hydroxyvalerate)-Graphene Nanocomposites (II) - Mechanical, Barrier, And Electrical Properties", Journal of Applied Polymer Science, 132(29):1–10.

[33] Min, M., Shi, Y., Ma, H., Huang, H., Shi, J., Chen, X. and Wang, L., (2015). "Polymer-Nanoparticle Composites Composed of Poly(3-hydroxybutyrate-co-3-hydroxyvalerate) and Coated Silver Nanoparticles", Journal of Macromolecular Science, Part B, 54(4):411–423.

[34] Castro-Mayorga, J.L., Fabra, M.J. and Lagaron, J.M., (2016). "Stabilized Nanosilver Based Antimicrobial Poly(3-Hydroxybutyrate-Co-3-Hydroxyvalerate) Nanocomposites Of Interest In Active Food Packaging", Innovative Food Science and Emerging Technologies, 33(2016):524–533.

[35] Silverman, T., Naffakh, M., Marco, C. and Ellis, G., (2016). "Morphology And Thermal Properties Of Biodegradable Poly(Hydroxybutyrate-Co-Hydroxyvalerate)/Tungsten Disulphide Inorganic Nanotube Nanocomposites", Materials Chemistry and Physics, 170:145–153.

[36] Öner, M. and İlhan, B. (2016). "Fabrication Of Poly(3-Hydroxybutyrate-Co-3-Hydroxyvalerate) Biocomposites With Reinforcement By Hydroxyapatite Using Extrusion Processing", Materials Science and Engineering: C, 65:19–26.

[37] Öner, M., Çöl, A.A., Pochat-Bohatier, C. and Bechelany, M., (2016). "Effect of incorporation of boron nitride nanoparticles on the oxygen barrier and thermal properties of poly(3-hydroxybutyrate-co-hydroxyvalerate)", RSC Advances, 6(93):90973–90981.

[38] Javadi, A., Srithep, Y., Pilla, S., Lee, J., Gong, S. and Turng, L.S., (2010). "Processing and Characterization Of Solid And Microcellular PHBV/Coir Fiber Composites", Materials Science and Engineering C, 30(5):749–757.

[39] Ten, E., Turtle, J., Bahr, D., Jiang, L. and Wolcott, M., (2010). "Thermal And Mechanical Properties Of Poly(3-Hydroxybutyrate-Co-3-Hydroxyvalerate) /Cellulose Nanowhiskers Composites", Polymer, 51(12):2652–2660.

[40] Yu, H.Y., Qin, Z.Y., Liu, Y.N., Chen, L., Liu, N. and Zhou, Z., (2012). "Simultaneous Improvement Of Mechanical Properties And Thermal Stability Of Bacterial Polyester By Cellulose Nanocrystals", Carbohydrate Polymers, 89(3):971–978.

[41] Lemes, A.P., Soto-Oviedo, M.A., Waldman, W.R., Innocentini-Mei, L.H. and Duran, N., (2010). "Effect of Lignosulfonate on the Thermal and Morphological Behavior of Poly(3-hydroxybutyrate-co-3-hydroxyvalerate)", Journal of Polymers and the Environment, 18(3):250–259.

[42] Shichao, W., Hengxue, X., Renlin, W., Zhe, Z. and Meifang, Z., (2015). "Influence Of Amorphous Alkaline Lignin On The Crystallization Behavior And Thermal Properties Of Bacterial Polyester", Journal of Applied Polymer Science, 132:41325.

[43] Diez-Pascual, A.M. and Diez-Vicente, A.L., (2014). "Poly(3-Hydroxybutyrate) /Zno Bionanocomposites With Improved Mechanical, Barrier And Antibacterial Properties", International Journal of Molecular Sciences, 15:10950–10973.

[44] Naphade, R. and Jog, J., (2012). "Electrospinning of PHBV/ZnO membranes: Structure and properties", Fibers and Polymers, 13(6):692–697.

[45] Abdalkarim, S.Y.H., Yu, H.Y., Wang, D. and Yao, J., (2017). "Electrospun Poly(3-Hydroxybutyrate-Co-3-Hydroxy-Valerate)/Cellulose Reinforced Nanofibrous Membranes With Zno Nanocrystals For Antibacterial Wound Dressings", Cellulose, 24(7):2925–2938.

[46] Castro-Mayorga, J.L., Fabra, M.J., Pourrahimi, A.M., Olsson, R.T. and Lagaron, J.M., (2017). "The Impact Of Zinc Oxide Particle Morphology As An

Antimicrobial And When Incorporated In Poly(3-Hydroxybutyrate-Co-3-Hydroxyvalerate) Films For Food Packaging And Food Contact Surfaces Applications", Food and Bioproducts Processing, 101:32–44.

[47] Wang, Z.L., (2004). "Nanostructures of zinc oxide", Materials Today, 7(6):26–33.

[48] Kolodziejczak-Radzimska, A. and Jesionowski, T., (2014). "Zinc Oxide-From Synthesis To Application: A Review", Materials, 7(4):2833–2881.

[49] Kawano, T. and Imai, H., (2010). "Nanoscale Morphological Design Of Zno Crystals Grown In Aqueous Solutions", Journal of the Ceramic Society of Japan, 118(1383):969–976.

[50] Vayssieres, L., Keis, K., Lindquist, S.E. and Hagfeldt, A., (2001). "Purpose-Built Anisotropic Metal Oxide Material: 3D Highly Oriented Microrod Array of ZnO", The Journal of Physical Chemistry B, 105(17):3350–3352.

[51] Baruah, S. and Dutta, J., (2009). "Hydrothermal Growth of ZnO Nanostructures", Science and Technology of Advanced Materials, 10:13001.

[52] Xu, S. and Wang, Z.L., (2011). "One-Dimensional ZnO Nanostructures: Solution Growth And Functional Properties", Nano Research, 4(11):1013–1098.

[53] Sepulveda-Guzman, S., Reeja-Jayan, B., Rosa, E., Torres-Castro, A., Gonzalez-Gonzalez, V. and Jose-Yacaman, M., (2009). "Synthesis of Assembled Zno Structures By Precipitation Method In Aqueous Media", Materials Chemistry and Physics, 115(1):172–178.

[54] Fujita, K., Murata, K, Nakazawa, T. and Kayama I., (1984). "Crystal Shapes of Zinc Oxide Prepared Method by Homogeneous Precipitation", Yogyo Kyokai Shi 92:227-230.

[55] Zhou, Z. and Deng, Y., (2009). "Kinetics Study of ZnO Nanorod Growth in Solution", Journal of Physical Chemistry, 113:19853–19858.

[56] Liu, B. and Zeng, H.C., (2004). "Room Temperature Solution Synthesis of Monodispersed Single-Crystalline ZnO Nanorods and Derived Hierarchical Nanostructures Room Temperature Solution Synthesis of Monodispersed Single-Crystalline ZnO Nanorods and Derived Hierarchical Nanostructures", Langmuir, 20:4196–4204.

[57] Garcia, S.P. and Semancik, S., (2007). "Controlling The Morphology Of Zinc Oxide Nanorods Crystallized From Aqueous Solutions: The Effect Of Crystal Growth Modifiers On Aspect Ratio", Chemistry of Materials, 19(16):4016–4022.

[58] Jitianu, M. and Goia, D. V., (2007). "Zinc Oxide Colloids with Controlled Size, Shape, and Structure", Journal of Colloid and Interface Science", 309(1):78–85.

[59] Preda, N., Enculescu, M. and Enculescu, I., (2014). "Polysaccharide-Assisted Crystallization of Zno Micro/Nanostructures", Materials Letters, 115(2014):256–260.

[60] Panigrahy, B., Aslam, M., Misra, D.S. and Bahadur, D., (2009). “Polymer-Mediated Shape-Selective Synthesis Of Zno Nanostructures Using A Single-Step Aqueous Approach”, CrystEngComm, 11(9):1920.

[61] Gao, Y.F., Miao, H.Y., Luo, H.J. and Nagai, M., (2008). “Precipitation Of Zno Powders From Aqueous Solutions With Water-Soluble Polymers”, Crystal Growth and Design, 8(7):2187–2193.

[62] Akin, B. and Oner, M., (2012). “Aqueous Pathways For Formation Of Zinc Oxide Particles In The Presence Of Carboxymethyl Inulin”, Research on Chemical Intermediates, 38(7):1511–1525.

[63] Boels, L. and Witkamp, G.J., (2011). “Carboxymethyl Inulin Biopolymers: A Green Alternative for Phosphonate Calcium Carbonate Growth Inhibitors”, Crystal Growth and Design, 11(9):4155–4165.

[64] Verraest, D.L., Peters, J.A., Bekkum, H. and Rosmalen, G.M., (1996). “Carboxymethyl Inulin: A New Inhibitor for Calcium Carbonate Precipitation”, Journal of the American Oil Chemists’ Society, 73(1):55–62.

[65] Kirboga, S. and Öner, M., (2016). “Investigating The Effect Of Ultrasonic Irradiation On Synthesis Of Calcium Carbonate Using Box-Behnken Experimental Design”, Powder Technology, 308:442–450.

[66] Akın, B., Öner, M., Bayram, Y. and Demadis, K. D., (2008). “Effects of Carboxylate-Modified, “Green” Inulin Biopolymers on the Crystal Growth of Calcium Oxalate”, Crystal Growth & Design, 8(6):1997–2005.

[67] Dogan, O., Oner, M. and Cinel, O., (2010). “The Inhibitory Effects Of Inulin Biopolymers On The Seeded Growth Of Hydroxyapatite”, Journal of the Ceramic Society of Japan, 118(1379):579–586.

[68] Öner, M. and Uysal, U., (2013). “Synthesis Of Hydroxyapatite Crystals Using Carboxymethyl Inulin For Use As A Delivery Of Ibuprofen” Materials Science and Engineering C, 33(1):482–489.

[69] Tang, E., Tian, B., Zheng, E. and Fu, C., (2008). “Preparation of Zinc Oxide Nanoparticle Via Uniform Precipitation Method and Its Surface Modification By Methacryloxypropyltrimethoxysilane”, Chemical Engineering Communications, 6445:37–41.

[70] Nicolay, A., Lanzutti, A., Poelman, M., Ruelle, B., Fedrizzi, L., Dubois, P. and Olivier, M.G., (2015). “Elaboration And Characterization Of A Multifunctional Silane/ZnO Hybrid Nanocomposite Coating”, Applied Surface Science, 327:379–388.

[71] Posthumus, W., Magusin, P.C.M.M., Brokken-Zijp, J.C.M., Tinnemans, A.H.A. and Linde, R., (2004). “Surface Modification Of Oxidic Nanoparticles Using 3-Methacryloxypropyltrimethoxysilane”, Journal of Colloid and Interface Science, 269(1):109–116.

[72] Brochier Salon, M.C. and Belgacem, M.N., (2011). “Hydrolysis-Condensation Kinetics of Different Silane Coupling Agents. Phosphorus, Sulfur, and Silicon and the Related Elements”, Phosphorus, Sulfur and Silicone, 186(2):240–254.

[73] Sterman, S. and Marsden, J.G., (1966). “Silane Coupling Agents”, Industrial & Engineering Chemistry, 58(3):33–37.

[74] Kango, S., Kalia, S., Celli, A., Njuguna, J., Habibi, Y. and Kumar, R., (2013). "Surface Modification Of Inorganic Nanoparticles For Development Of Organic-Inorganic Nanocomposites - A Review", Progress in Polymer Science, 38(8):1232–1261.

[75] Kumar, R., Umar, A., Kumar, G., Nalwa, H. S., Kumar, A. and Akhtar, M. S., (2017). "Zinc Oxide Nanostructure-Based Dye-Sensitized Solar Cells", Journal of Materials Science, 52(9):4743–4795.

[76] Zhong, Q. and Matijevic, E., (1996). "Preparation Of Uniform Zinc Oxide Colloids By Controlled Double-Jet Precipitation", Journal of Materials Chemistry, 6(3):443.

[77] Xu, S., Lao, C., Weintraub, B. and Wang, Z. L., (2008). "Density-Controlled Growth Of Aligned Zno Nanowire Arrays By Seedless Chemical Approach On Smooth Surfaces", Journal of Materials Research, 23(8):2072–2077.

[78] Suslick, K. S. and Price, G. J., (1999). "Applications of Ultrasound to Materials Chemistry" Annu. Rev. Mater. Sci., 29:295–326.

[79] Wang, Z., Qian, X., Yin, J. and Zhu, Z., (2004). "Large-Scale Fabrication of Tower-like, Flower-like, and Tube-like ZnO Arrays by a Simple Chemical Solution Route", Langmuir, 20(8):3441–3448.

[80] Parker, A. A Technical Review of Organosilanes and Adhesion, http://www.famastechnology.com/pdf/silanes_techpaper-parker.pdf, 17 March 2018.

[81] Abboud, M., Turner, M., Duguet, E. and Fontanille, M., (1997). "PMMA-Based Composite Materials with Reactive Ceramic Fillers. Part 1.—Chemical Modification and Characterization of Ceramic\Nanoparticles", Journal of Materials Chemistry, 7(8):1527.

[82] Miller, J. D. and Ishida, H., (1984). "Quantitative Monomolecular Coverage Of Inorganic Particulates By Methacryl-Functional Silanes", Surface Science, 148(2–3):601–622.

[83] Brinker, C.J., (1988). "Hydrolysis and Condensation of Silicates: Effects on Structure", Journal of Non-Crystalline Solids, 100:31–50.

[84] Zhang, Y., Fang, F., Wang, C., Wang, L., Wang, X., Chu, X. and Wang, X., (2014). "Hydrophobic Modification Of Zno Nanostructures Surface Using Silane Coupling Agent", Polymer Composites, 35(6):1204-1211.

[85] Witucki, G.L., (1993). "A Silane Primer: Chemistry and Applications of Alkoxy Silanes", Journal of Coatings Technology, 65(822):57–60.

[86] UCT Unites Chemical Technologies, (2012). Silane Coupling Agent Guide, Bristol.

[87] Shin-Etsu Chemical Ltd. (2015). Silane Coupling Agents, Tokyo.

[88] Ilyas, S.U., Pendyala, R. and Marneni, N., (2014). "Dispersion Behaviour and Agglomeration Effects Of Zinc Oxide Nanoparticles In Ethanol–Water Mixtures", Materials Research Innovations, 18:179–183.

[89] Chung, S. J., Leonard, J.P., Nettleship, I., Lee, J.K., Soong, Y., Martello, D.V. and Chyu, M. K., (2009). "Characterization Of Zno Nanoparticle Suspension

In Water: Effectiveness Of Ultrasonic Dispersion", Powder Technology, 194(1–2):75–80.

[90] Graves, J.E., Sugden, M., Litchfield, R.E., Hutt, D.A., Mason, T.J. and Cobley, A.J., (2016). "Ultrasound Assisted Dispersal Of A Copper Nanopowder For Electroless Copper Activation", Ultrasonics Sonochemistry, 29:428–438.

[91] Hwang, N., and Barron, A.R., (2011). "BET Surface Area Analysis of Nanoparticles", OpenStax-CNX Module:m38278.

[92] Matshitse, R., Brunauer-Emmett-Teller (BET) Surface Area Analysis, https://www.ru.ac.za/media/rhodesuniversity/content/nanotechnology/documents/BET Refilwe Matshitse.pdf, 17 March 2018.

[93] Johannesson, B., (2000). "Verification of the BET-theory by Experimental Investigations on the Heat of Adsorption", Lund University Report TVBM Vol.3096.

[94] Dutrow, B.L. and Clark, C.M., (2016). "X-ray Powder Diffraction (XRD)", Geochemical Instrumentation and Analysis, 1–4.

[95] Rupp, B., What is X-ray Crystallography. Crystallography 101 - An Introductory Course, http://www.ruppweb.org/Xray/101index.html, 17 March 2018.

[96] University of California Santa Barbara, X-ray Generation & Properties, http://www.mrl.ucsb.edu/centralfacilities/x-ray/basics, 17 March 2018.

[97] Laing, M. (1981), "An Introduction to the Scope, Potential and Applications of X-ray Analysis" Teaching Pamphlets, Commission on Crystallographic Teaching.

[98] Patterson, A.L., (1939). "The Scherrer Formula for X-Ray Particle Size Determination", Physical Review, 56(10):978–982.

[99] Swapp, S., Scanning electron microscopy (SEM), https://doi.org/10.13140/RG.2.2.20113.22889, 17 March 2018.

[100] University of Iowa, Scanning Electron Microscopy, https://doi.org/10.1016/B0-12-227410-5/00674-8, 17 March 2018.

[101] Doyle, W.M., (1992). "Principles and applications of Fourier transform infrared (FTIR) process analysis", Technical Note AN-906 Rev. C, 2, 11–41.

[102] Thermo-Nicolet Corporation, Introduction to Fourier Transform Infrared Spectrometry, https://doi.org/10.1016/j.rser.2015.05.073, 17 March 2018.

[103] University of Pennsylvania, FTIR Spectroscopy, http://www.sas.upenn.edu/~carrolld/SpecProjectPages/FTIR.html, 17 March 2018.

[104] Gable, K.P., FTIR Spectroscopy, https://chemistry.oregonstate.edu/courses/ch361-464/ch362/irinterp.htm, 17 March 2018.

[105] Khare, H. S. and Burris, D. L., (2010). "A Quantitative Method for Measuring Nanocomposite Dispersion", Polymer, 51(3):719–729.

[106] Saheb, N., Qadir, N.U., Siddiqui, M.U., Arif, A.F.M., Akhtar, S.S. and Al-Aqeeli, N., (2014). "Characterization of nanoreinforcement dispersion in inorganic nanocomposites: A review", Materials, 7(6):4148–4181.

[107] Gabbot, P. (2008). Principles and Applications of Thermal Analysis, Blackwell Publishing, New Delhi.

[108] Mohomed, K., Thermogravimetric Analysis (TGA) Theory and Applications, http://:www.tainstruments.com/wp-content/uploads/CA-2016-TGA.pdf, 17 March, 2018.

[109] Mathias, L.J., The Glass Transition, http://pslc.ws/macrog/tg.htm, 17 March 2018.

[110] Kodre, K.V., Attarde, S.R.,R., Patil, R.Y. and Barge, V. U., (2014). "Differential Scanning Calorimetry: A Review", Research and Reviews: Journal of Pharmaceutical Analysis, 3(3):11–22.

[111] Gill, P., Moghadam, T.T. and Ranjbar, B., (2010). "Differential Scanning Calorimetry Techniques: Applications In Biologyy And Nanoscience", Journal of Biomolecular Techniques, 21(4)-167–93.

[112] Laycock, B., Halley, P., Pratt, S., Werker, A. and Lant, P., (2014). "The Chemomechanical Properties Of Microbial Polyhydroxyalkanoates", Progress in Polymer Science, 39(2):397–442.

[113] Barham, P.J., Keller, A., Otun, E.L. and Holmes, P.A. (1984). "Crystallization And Morphology Of A Bacterial Thermoplastic: Poly-3-Hydroxybutyrate", Journal of Materials Science, 19(9):2781–2794.

[114] ASM International, Introduction to Tensile Testing, Tensile Testing, https://doi.org/10.1017/CBO9781107415324.004, 17 March 2018.

[115] Laitila, E. A, Tensile Test Experiment, http://www.mtu.edu/materials/k12/experiments/tensile/, 17 March, 2017.

[116] ASTM D882-12, (2012) Standard Test Method For Tensile Properties Of Thin Plastic Sheeting, ASTM, Philadelphia.

[117] Wei, A., Sun, X.W., Xu, C.X., Dong, Z.L., Yang, Y., Tan, S.T. and Huang, W., (2006). "Growth Mechanism Of Tubular Zno Formed In Aqueous Solution", Nanotechnology, 17:1740–1744.

[118] Pacholski, C., Kornowski, A. and Weller, H., (2002). "Self-assembly of ZnO: From Nanodots To Nanorods", Angewandte Chemie, 41(7):1188–1191.

[119] Zhang, H., Yang, D., Ji, Y.J., Ma, X.Y., Xu, J. and Que, D.L., (2004). "Low Temperature Synthesis of Flowerlike ZnO Nanostructures by Cetyltrimethylammonium Bromide-Assisted Hydrothermal Process", The Journal of Physical Chemistry B, 108(13):3955–3958.

[120] Pung, S.Y., Lee, W.P. and Aziz, A., (2012). "Kinetic Study of Organic Dye Degradation Using ZnO Particles with Different Morphologies as a Photocatalyst", International Journal of Inorganic Chemistry, 2012:1–9.

[121] Parra, M.R. and Haque, F.Z., (2015). "Poly(Ethylene Glycol) (PEG)-Assisted Shape-Controlled Synthesis Of One-Dimensional ZnO Nanorods", Optik, 126(18):1562–1566.

[122] Foo, K., Hashim, U., Muhammad, K. and Voon, C., (2014). “Sol–Gel Synthesized Zinc Oxide Nanorods And Their Structural And Optical Investigation For Optoelectronic Application”, Nanoscale Research Letters, 9(1):429.

[123] Kurda, A.H., Hassan, Y.M. and Ahmed, N.M., (2015). “Controlling Diameter, Length and Characterization of ZnO Nanorods by Simple Hydrothermal Method for Solar Cells”, World Journal of Nano Science and Engineering, 5:34–40.

[124] Jitianu, M. and Goia, D. V., (2007). “Zinc Oxide Colloids With Controlled Size, Shape, And Structure”, Journal of Colloid and Interface Science, 309(1):78–85.

[125] Thirugnanam, T., (2013). “Effect of polymers (PEG and PVP) on sol-gel synthesis of microsized zinc oxide”, Journal of Nanomaterials, 2013:362175.

[126] Newport Corporation, FT-IR Spectroscopy, https://assets.newport.com/webDocuments/images/FTIR_Spectroscopy.pdf, 19 March 2018.

[127] Sharma, D. and Jha, R., (2017). “Transition Metal (Co, Mn) Co-Doped ZnO Nanoparticles: Effect on Structural and Optical Properties”, Journal of Alloys and Compounds, 698:532–538.

[128] Carp, O., Tirsoaga, A., Ene, R., Ianculescu, A., Negrea, R.F., Chesler, P. and Birjega, R., (2017). “Facile, High Yield Ultrasound Mediated Protocol for ZnO Hierarchical Structures Synthesis: Formation Mechanism, Optical and Photocatalytic Properties”, Ultrasonics Sonochemistry, 36(2017):326–335.

[129] Hernandez, A., Maya, L., Sanchez-Mora, E. and Sanchez, E.M., (2007). “Sol-Gel Synthesis, Characterization and Photocatalytic Activity of Mixed Oxide ZnO-Fe2O3”, Journal of Sol-Gel Science and Technology, 42(1):71–78.

[130] Christobel, G.J., (2016). “Vibrational Spectroscopy”, International Journal of Science and Research, 5(6):2228–2230.

[131] Djaja, N.F., Montja, D.A. and Saleh, R., (2013). “The Effect of Co Incorporation into ZnO Nanoparticles”, Advances in Materials Physics and Chemistry, 3(1):33–41.

[132] Noriega, R., Goris, L., Rivnay, J., Scholl, J., Thompson, L.M., Palke, A. C. and Salleo, A., (2009). “Transport and Structural Characterization of Solution-Processable Doped Zno Nanowires”, Proceedings of SPIE, 7411:74110N-6.

[133] Hausmann, A. and Schallenberger, B., (1978). “Interstitial Oxygen in Zinc Oxide Single Crystals”, Zeitschrift Für Physik B Condensed Matter, 31(3):269–273.

[134] Ma, S.R., Shi, L.Y., Feng, X., Yu, W.J. and Lu, B., (2008). “Graft Modification of Zno Nanoparticles with Silane Coupling Agent KH570 in Mixed Solvent”, Journal of Shanghai University, 12(3):278–282.

[135] Tang, E., Liu, H., Sun, L., Zheng, E. and Cheng, G., (2007). “Fabrication of Zinc Oxide/Poly(Styrene) Grafted Nanocomposite Latex and Its Dispersion”, European Polymer Journal, 43(10):4210–4218.

[136] Rhodes, R., Horie, M., Chen, H., Wang, Z., Turner, M.L. and Saunders, B.R. (2010). "Aggregation Of Zinc Oxide Nanoparticles: From Non-Aqueous Dispersions To Composites Used As Photoactive Layers In Hybrid Solar Cells", Journal of Colloid and Interface Science, 344(2):261–271.

[137] Mandzy, N., Grulke, E. and Druffel, T., (2005). "Breakage of Tio2 Agglomerates in Electrostatically Stabilized Aqueous Dispersions", Powder Technology, 160(2):121–126.

[138] Ilyas, S.U., Pendyala, R. and Marneni, N., (2014). "Preparation, Sedimentation, and Agglomeration of Nanofluids", Chemical Engineering and Technology, 37(12):2011–2021.

[139] Yu, W. and Xie, H., (2012). "A Review on Nanofluids: Preparation, Stability Mechanisms, and Applications", Journal of Nanomaterials, 2012:435873.

[140] Coates, J., (2000). "Interpretation of Infrared Spectra, A Practical Approach" Encyclopedia of Analytical Chemistry, 10815–10837.

[141] Joshi, S.S., (2012). "Crystal Habit Modification Using Habit Modifiers", Modern Aspects of Bulk Crystal and Thin Film Preparation, 413–436.

[142] Zhang, H.P., Luo, X., Lin, X., Tang, P., Lu, X., Yang, M. and Tang, Y., (2016). "Biodegradable Carboxymethyl Inulin As A Scale Inhibitor For Calcite Crystal Growth: Molecular Level Understanding" Desalination, 381:1–7.

[143] Biswas, K., Das, B. and Rao, C.N.R., (2008). "Growth Kinetics of ZnO Nanorods: Capping-Dependent Mechanism and Other Interesting Features", Journal of Physical Chemistry C, 112(7):2404–2411.

[144] Golovko, D.S., Munoz-Espi, R. and Wegner, G., (2007). "Interaction Between Poly (Styrene-Acrylic Acid) Latex Nanoparticles And Zinc Oxide Surfaces", Langmuir, 23(7):3566–3569.

[145] Das, S., Dutta, K. and Pramanik, A., (2013). "Morphology Control of ZnO With Citrate: A Time and Concentration Dependent Mechanistic Insight", CrystEngComm, 15(32):6349.

[146] Cho, S., Jang, J., Jung, S., Lee, B. R., Oh, E. and Lee, K., (2009). "Precursor Effects of Citric Acid and Citrates on ZnO Crystal Formation Precursor Effects of Citric Acid and Citrates on ZnO Crystal Formation", Langmuir, (27):3825–3831.

[147] Viswanatha, R. and Sarma, D.D., (2006). "Study Of The Growth Of Capped Zno Nanocrystals: A Route To Rational Synthesis", Chemistry - A European Journal, 12(1):180–186.

[148] Rahul, R., Jha, U., Sen, G. and Mishra, S., (2014). "Carboxymethyl Inulin: A Novel Flocculant For Wastewater Treatment", International Journal of Biological Macromolecules, 63:1–7.

[149] Pholnak, C., Sirisathitkul, C., Danworaphong, S. and Harding, D.J., (2012). "Sono-Synthesized Sword-Like Zinc Oxide and Its Use as a Filler in Polyurethane Composites", Journal of Optoelectronics and Advanced Materials, 14(5–6):441–447.

[150] Qian, D., Jiang, J.Z. and Hansen, P.L., (2003). "Preparation of ZnO Nanocrystals via Ultrasonic Irradiation", Chemical Communications (9):1078–1709.

[151] Deng, C., Hu, H., Shao, G. and Han, C., (2010). "Facile Template-Free Sonochemical Fabrication of Hollow ZnO Spherical Structures" Materials Letters, 64(7):852–855.

[152] Tang, E., Liu, H., Sun, L., Zheng, E. and Cheng, G., (2007). "Fabrication Of Zinc Oxide/Poly(Styrene) Grafted Nanocomposite Latex And Its Dispersion", European Polymer Journal, 43(10):4210–4218.

[153] Jung, S., Oh, E., Lee, K., Yang, Y., Park, C.G., Park, W. and Jeong, S., (2008). "Sonochemical Preparation of Shape-Selective ZnO Nanostructures Sonochemical Preparation of Shape-Selective ZnO Nanostructures", Crystal Growth and Design, 8:265-269.

[154] Akiyama, J., Hashimoto, M., Takadama, H., Nagata, F., Yokogawa, Y., Iwai, K. and Asai, S., (2006). "Formation of C-Axis Aligned Polycrystal Hydroxyapatite Using a High Magnetic Field With Mechanical Sample Rotation", Nippon Kinzoku Gakkaishi/Journal of the Japan Institute of Metals, 70(5):412–414.

[155] Liu, Q., Zhu, M. and Chen, Y., (2010). "Synthesis and characterization of multi-block copolymers containing poly [(3-hydroxybutyrate)-co-(3-hydroxyvalerate)] and poly(ethylene glycol)", Polymer International, 59(6):842–850.

[156] Xu, C.L., Fang, L., Wu, F., Huang, Q. L. and Yin, B., (2014). "Wetting Behavior of Triethoxyoctylsilane Modified ZnO Nanowire Films", Colloids and Surfaces A: Physicochemical and Engineering Aspects, 444:48–53.

[157] Ambrozewicz, D., Ciesielczyk, F., Nowacka, M., Karasiewicz, J., Piasecki, A., MacIejewski, H. and Jesionowski, T. (2013). "Fluoroalkylsilane versus Alkylsilane as Hydrophobic Agents for Silica and Silicates", Journal of Nanomaterials, 2013:631938.

[158] Truong, L.T., Larsen, A., Holme, B., Diplas, S., Hansen, F.K., Roots, J. and Jørgensen, S., (2010). "Dispersibility of Silane-Functionalized Alumina Nanoparticles in Syndiotactic Polypropylene", Surface and Interface Analysis, 42(6–7):1046–1049.

[159] Samsudin, N.F., Matori, K.A., Liew, J.Y.C., Fen, Y.W., Mohd Zaid, M.H. and Alassan, Z.N., (2015). "Investigation on Structural and Optical Properties of Willemite Doped Mn2+ Based Glass-Ceramics Prepared by Conventional Solid-State Method", Journal of Spectroscopy, 2015:730753.

[160] Shahid, M.U., Deen, K.M., Ahmad, A., Akram, M.A., Aslam, M. and Akhtar, W. (2015). "Formation of Al-Doped ZnO Thin Films On Glass By Sol–Gel Process And Characterization", Applied Nanoscience, 2015:235–241.

[161] Faure, B., Salazar-Alvarez, G., Ahniyaz, A., Villaluenga, I., Berriozabal, G., De Miguel, Y. R. and Bergström, L., (2013). "Dispersion and Surface Functionalization of Oxide Nanoparticles for Transparent Photocatalytic and UV-Protecting Coatings And Sunscreens", Science and Technology of Advanced Materials, 14(2):23001.

[162] Dennis, H.R., Hunter, D.L., Chang, D.,Kim, S., White, J.L., Cho, J.W. and Paul, D. R., (2001). "Effect Of Melt Processing Conditions On The Extent Of Exfoliation In Organoclay-Based Nanocomposites", Polymer, 42(23):9513–9522.

[163] Kalia, S. and Haldorai, Y., (2015). Organic –Inorganic Hybrid Nanomaterials, Springer, Switzerland.

[164] Abdolmaleki, A., Mallakpour, S. and Borandeh, S., (2012). "Effect Of Silane-Modified Zno On Morphology And Properties Of Bionanocomposites Based On Poly(Ester-Amide) Containing Tyrosine Linkages" Polymer Bulletin, 69(1):15–28.

[165] Duan, B., Wang, M. and Zhou, W., (2011). "Nonisothermal Melt-Crystallization Behavior Of Calcium Phosphate/Poly(3-Hydroxybutyrate-Co-3-Hydroxyvalerate) Nanocomposite Microspheres", Polymer Engineering and Science, 51(8):1580–1591.

[166] Xiang, H., Wen, X., Miu, X., Li, Y., Zhou, Z. and Zhu, M. (2016). "Thermal depolymerization mechanisms of poly(3-hydroxybutyrate-co-3-hydroxyvalerate)", Progress in Natural Science: Materials International, 26(1):58–64.

[167] Ariffin, H., Nishida, H., Shirai, Y. and Hassan, M.A., (2008). "Determination Of Multiple Thermal Degradation Mechanisms Of Poly(3-Hydroxybutyrate)", Polymer Degradation and Stability, 93(8):1433–1439.

[168] Doi, Y., Kanesawa, Y., Kunioka, M. and Saito, T., (1990). "Biodegradation Of Microbial Copolyesters: Poly(3-Hydroxybutyrate-Co-3-Hydroxyvalerate) And Poly(3-Hydroxybutyrate-Co-4-Hydroxybutyrate)", Macromolecules, 23(1):26–31.

[169] Pachekoski, W.M., Dalmolin, C. and Agnelli, J.A.M., (2013). "The Influence of The Industrial Processing on The Degradation Of Poly(Hidroxybutyrate) – PHB", Materials Research, 16(2):237–332.

[170] Horowitz, H.H. and Metzger, G., (1963). "A New Analysis of Thermogravimetric Traces", Analytical Chemistry, 35(10):1464–1468.

[171] Mozejko-Ciesielska, J. and Kiewisz, R., (2016). "Bacterial Polyhydroxyalkanoates: Still Fabulous?", Microbiological Research, 192(2016):271–282.

[172] Arcos-Hernandez, M.V., Laycock, B., Donose, B.C., Pratt, S., Halley, P., Al-Luaibi, S. and Lant, P. A., (2013). "Physicochemical and Mechanical Properties of Mixed Culture Polyhydroxyalkanoate (PHBV)", European Polymer Journal, 49(4):904–913.

[173] Yu, W., Lan, C.H., Wang, S.J., Fang, P.F. and Sun, Y.M., (2010). "Influence Of Zinc Oxide Nanoparticles On The Crystallization Behavior Of Electrospun Poly(3-Hydroxybutyrate-Co-3-Hydroxyvalerate) Nanofibers", Polymer, 51(11):2403–2409.

[174] Yu, H., Yan, C. and Yao, J., (2014). "Fully Biodegradable Food Packaging Materials Based On Functionalized Cellulose Nanocrystals/Poly(3-Hydroxybutyrate-Co-3-Hydroxyvalerate) Nanocomposites", RSC Advances, 4:59792–59802.

[175] Öner, M. and İlhan, B., (2016). "Fabrication Of Poly(3-Hydroxybutyrate-Co-3-Hydroxyvalerate) Biocomposites With Reinforcement By Hydroxyapatite Using Extrusion Processing", Materials Science and Engineering: C, 65:19–26.

[176] Abraham, R., Thomas, S.P., Kuryan, S., Isac, J., Varughese, K.T. and Thomas, S., (2009). "Mechanical Properties of Ceramic-Polymer Nanocomposites", Express Polymer Letters, 3(3):177–189.

[177] Hu, H., Onyebueke, L. and Abatan, A., (2010). "Characterizing and Modeling Mechanical Properties of Nanocomposites- Review and Evaluation", Journal of Minerals & Materials Characterization & Engineering, 9(4):275–319.

[178] Tjong, S.C., (2006). "Structural and Mechanical Properties of Polymer Nanocomposites", Materials Science and Engineering R: Reports, 53(3–4):73–197.

[179] Valavala, P.K. and Odegard, G.M., (2005). "Modeling Techniques for Determination of Mechanical Properties Of Polymer Nanocomposites", Reviews on Advanced Materials Science, 9(1):34–44.

CURRICULUM VITAE

PERSONAL INFORMATION

Name Surname : Tuğçe BEKAT

Date of birth and place : 21.12.1982 İzmir

Foreign Languages : English, Italian

E-mail : tugcebekat@gmail.com

EDUCATION

Degree	**Department**	**University**	**Date of Graduation**
Master	Chemical Engineering	Izmir Institute of Technology	2012
Undergraduate	Food Engineering	Ege University	2008
High School		Bornova Anat. High School	2000

WORK EXPERIENCE

Year	**Corporation/Institute**	**Enrollment**
2012	Yıldız Technical University	Research Assistant
2009	Izmir Institute of Technology	Research Assistant

PUBLISHMENTS

Papers

1. Bekat T., Oner M., ‘Effects of ZnO crystals synthesized in presence of CMI biopolymer on PHBV properties’, Pure and Applied Chemistry 89 (1), 89-96 (2017).

2. Bekat T., Oner M., ‘Effects of surface modification and ultrasonic agitation on the properties of PHBV/ZnO nanocomposites’, Pure and Applied Chemistry 88 (10-11), 1027-1035 (2016).

3. Bekat T., Inal F., ‘Effects of reactor pressure and inlet temperature on n-butane/dimethyl ether oxidation and the formation pathways of the aromatic species’, Environmental Progress & Sustainable Energy 35 (1), 230-240 (2016).

4. Atayev P., Bekat T., Oner M., ‘The effects of zinc oxide and clay nanoparticles on thermal, barrier, and mechanical properties of polypropylene and high density polyethylene’, Sigma Journal of Engineering and Natural Sciences 33 (1), 16-21 (2015).

5. Bekat T., Inal F., ‘Effects of Dimethyl Ether on n-Butane Oxidation’, Fuel 115, 861-869 (2014).

6. Bekat T., Erdogan M., Inal F., Genc A., ‘Prediction of the Bottom Ash Formed in a Coal-Fired Power Plant Using Artificial Neural Networks’, Energy 45 (1), 882-887 (2012).

Conference Papers

1. Bekat T., Oner M., ‘Incorporation of silane modified and ultrasound dispersed ZnO particles into PHBV matrix’, European Materials Research Society 2017 Spring Meeting, Strasbourg, France, Accepted as Oral Presentation (May, 2017).

2. Bekat T., Oner M., ‘Effects of ZnO crystals synthesized in presence of CMI biopolymer on PHBV properties’, 16th International Conference on Polymer and Organic Chemistry, Crete, Greece, Poster Presentation (June, 2016).

3. Bekat T., Oner M., ‘Effects of surface modification and ultrasonic agitation on the

properties of PHBV/ZnO nanocomposites', 16th International Conference on Polymer and Organic Chemistry, Crete, Greece, Poster Presentation (June, 2016).

4. Bekat T., Oner M., 'Thermal, mechanical, and gas barrier properties of PHBV/ZnO nanocomposites', 5th International Conference on Biobased and Biodegradable Polymers, Donostia-San Sebastian, Spain, Poster Presentation (October, 2015).

5. Oner M., Ilhan B., Bekat T., 'Preparation and Characterization of Hydroxyapatite Reinforced Polyhydroxyalkanoate Composites', 39th International Conference and Exposition on Advanced Ceramics and Composites, Florida, USA, Oral Presentation (January, 2015).

6. Bekat T., Oner M., 'The effects of ZnO crystals on the barrier properties of LDPE polymer', Chemtech'14 Chemical Technologies and Chemical Engineering Conference, Istanbul, Turkey, Oral Presentation (October, 2014).

7. Bekat T., Ilhan B., Yardim T., Oner M., 'The effects of ZnO crystals synthesized in the presence of carboxymethyl inunlin biopolymer on the properties of HDPE polymer', 2nd International Conference on Bioinspired and Biobased Chemistry & Materials, Nice, France, Poster Presentation (October, 2014).

8. Bekat T., Inal F., 'Effects of Dimethyl Ether on n-Butane Oxidation', 1st International Symposium on Energy Challenges and Mechanics, Aberdeen, Scotland, Oral Presentation (July, 2014).

9 Atayev P., Bekat T., Akin M.B., Oner M., 'Effects of Surface Modification and Particle Morphology on the Oxygen Permeability of HDPE/Nanoclay and HDPE/Nanoclay/ZnO Nanocomposites', IUPAC 44th World Chemistry Congress, Istanbul, Turkey, Oral Presentation (August, 2013).

10 Bekat T., Inal F., 'Effects of Dimethyl Ether and Equivalence Ratio on n-Butane Oxidation', 12th International Combustion Symposium, Kocaeli, Turkey, Oral Presentation (May, 2012).

11. Bekat T., Inal F., 'Detailed Chemical Kinetic Modeling of the Effects of Dimethyl Ether on n-Butane Oxidation', 18th National Heat Science and Technology

Congress, Zonguldak, Turkey, Oral presentation (September, 2011).

12. Bekat T., Erdogan M., Inal F., Genc A., ‘Determination of Bottom Ash Amount in Pulverized Coal-Fired Power Plants Using Artificial Neural Networks’, 18th National Heat Science and Technology Congress, Zonguldak, Turkey, Oral presentation (September, 2011).

13. Akinci Z.S., Bekat T., Ozdemir S.K., Okur S., ‘Atomic Force Microscopy And Kelvin Probe Study Of Emulsifier Incorporated Phospholipids’, 6th International Nanoscience and Nanotechnology Conference, Izmir, Turkey, Poster presentation (June, 2010).

14. Akinci Z.S., Bekat T., Ozdemir E., Okur S., Ozdemir S.K., ‘Development of Microbubbles for Ultrasound Imaging’, 9th National Chemical Engineering Congress, Ankara, Turkey, Oral Presentation (June, 2010).